NASA SP-136

Significant Achievements in

Space Science 1965

NATIONAL AERONAUTICS AND SPACE ADMINISTRATION

NASA SP-136

Significant Achievements in

Space Science 1965

Scientific and Technical Information Division
OFFICE OF TECHNOLOGY UTILIZATION 1967
NATIONAL AERONAUTICS AND SPACE ADMINISTRATION
Washington, D.C.

For Sale by the Superintendent of Documents,
U.S. Government Printing Office, Washington, D.C. 20402
Price $1.00

Foreword

THIS VOLUME IS ONE OF A SERIES which summarizes the achievements made in the scientific and technical disciplines involved in the Space Science and Applications Program of the United States. The contribution made by the National Aeronautics and Space Administration is highlighted against the background of the overall progress in these disciplines. Succeeding issues will document the results from later years.

The achievements during the period 1958 to 1964 in the following areas were reported in NASA Special Publications 91 to 100: Astronomy, Bioscience, Communications and Navigation, Geodesy, Ionospheres and Radio Physics, Meteorology, Particles and Fields, Planetary Atmospheres, Planetology, and Solar Physics.

This volume describes the significant scientific progress in 1965 in the following areas: Astronomy, Ionospheres and Radio Physics, Particles and Fields, Planetary Atmospheres, Planetology, and Solar Physics. A companion volume (NASA SP–137) summarizes the progress in space applications in 1965 in the following areas: Communications, Geodesy, and Meteorology.

Although we do not here attempt to name all those who have contributed to the NASA program during 1965, both in the experimental and theoretical research, and in the analysis, compilation, and reporting of these results, nevertheless we wish to acknowledge all the contributions to a very fruitful program in which this country may take justifiable pride.

HOMER E. NEWELL
Associate Administrator for
Space Science and Applications, NASA

Preface

A SCIENTIFIC ACCOMPLISHMENT may be defined as an increase in human understanding of the universe, of life, or of the laws by which they are governed. Human understanding may increase in a variety of ways. A scientist may use a new instrument or a new technique to discover a new phenomenon or to measure a known phenomenon to a new accuracy which measurably increases knowledge of that phenomenon. A sudden insight may enable a theoretical physicist to understand and be able to formulate a new law of nature which will relate to and resolve many puzzling aspects of a particular area of research. In these cases, man's understanding of nature suddenly increases by a substantial amount through the efforts of one scientist, and one can say that prior to this particular instant in history, man did not know, and afterward, he did know. Prior to the receipt of the pictures from Mariner IV, man did not know what the surface of another planet really looked like. Immediately after receipt of the pictures, man's knowledge increased by a significant amount.

Human understanding does not always increase so suddenly or dramatically. Sometimes progress is made by a deliberate step-by-step gathering of data and use of those data to prove a hunch or to test a hypothesis. In other cases, the technique of research is the systematic accumulation and analysis of data over several years by many scientists to develop a complete picture and understanding of a complex phenomenon such as the magnetosphere. Though the progress of this routine of scientific research is often not spectacular, it is sure and direct, and in the long term revolutionizes our thinking just as much as the individual dramatic scientific breakthrough.

For NASA, 1965 was a year in which there was both the sudden dramatic increase in human understanding by individual scientists or by a group of scientists and engineers working together on a single mission and the slow steady accumulation of knowledge in broad areas through the efforts of a large number of scientists and engineers working on several missions. These scientific accomplishments and reports of progress are grouped by discipline or area of research rather than by mission. In many cases data from several missions

were used together to provide new or deeper insight into a problem.

The major increase in our knowledge concerning the planet Mars was the most significant scientific accomplishment of 1965. At the beginning of the year, man knew very little about the nature of the surface of Mars. He thought the surface pressure was about 20 to 40 millibars (2 to 4 percent that of Earth). Before 1965, nothing was known about the nature of either the ionosphere or the magnetic field of Mars.

By the end of 1965, 21 pictures of the planet had been taken by Mariner IV and had been interpreted by R. B. Leighton and his colleagues to show that the surface of Mars is quite similar to that of the Moon. There are about the same number of craters per unit area on the Moon as on Mars. The surface of Mars shows little evidence of erosion by wind or dust and none by rainfall. In the area which was photographed, which was less than 1 percent of the surface of the planet, there was no evidence of mountain ranges similar to the Rockies or the Himalayas. The surface pressure was shown to be much less than previous estimates (5 to 10 millibars or 0.5 percent that of the Earth). An ionosphere was found on the sunlit side of Mars, but there was no detectable magnetic field or radiation belt at the point of closest approach of Mariner IV, 9656 kilometers.

Although Mariner IV provided the most significant accomplishments, the many other significant advancements made in 1965 are also reported herein.

Contents

SPACE ASTRONOMY

A. G. W. CAMERON
Institute for Space Studies
Goddard Space Flight Center, NASA

J. K. GLEIM
Physics and Astronomy Programs
Office of Space Science and Applications, NASA

F. T. HADDOCK
University of Michigan
Radio Astronomy Observatory

A. G. W. CAMERON
Institute for Space Studies
Goddard Space Flight Center, NASA

X-RAY ASTRONOMY

The principal efforts in the field of X-ray astronomy during 1965 were directed toward analyzing results obtained from rockets flown during the latter part of 1964. More quantitative special distribution measurements and more precise position determinations of discrete X-ray sources were the objects of rocket flights made toward the end of 1965. The final results from Explorer XI, the gamma-ray telescope, were also published during this year.

X-RAY ASTRONOMY is a new and significant field of research. The first observations of stellar X-ray sources were made in 1962 with experiments flown on Aerobee rockets. Stellar X-rays are absorbed below about 120 000 feet and hence can be observed only with balloons or rockets. X-ray astronomy is significant because astronomers do not understand the mechanisms by which stars can generate X-rays of such an intensity that they can be detected at the Earth.

The principal efforts in this field at present are aimed at surveying the sky to detect X-ray sources and then locating them precisely so they can be identified with known astronomical objects and their extent can be determined. Both rockets and balloons are being used for this purpose. Satellites will be used in the future to increase the observing time. Another important element of the work is the measurement of the spectra of the sources. This is important because the spectra indicate the nature of the mechanism which produces the X-rays. There is also a vigorous effort by theoretical physicists to develop theories to explain the processes which produce the X-rays.

In 1965 there were published reports of the analyses of data obtained in 1964 during several rocket flights which had been made to locate accurately X-ray sources and to measure the spectra. An instrumented Aerobee flown from White Sands, N. Mex., on October 26, 1964, provided data which G. Clark, G. Garmire, M. Oda, and M. Wada used to determine the location of X-ray sources. The positions of three sources in Scorpio and Sagittarius were determined to within an uncertainty of 1 to 3 square degrees (Clark et al., 1965). Two alternative positions for Sco X–1 were found to be within the uncertainty circle of 2° radius around the position given by U.S. Naval Research Laboratory group (Bowyer et al., 1965), and one of the two positions was found to be within ½° of that given by P. Fisher et al. (to be published). The X-ray detectors were four banks of Geiger tubes, having sensitive areas of 70 cm² each, beryllium windows 9 mg

cm^{-2} thick, and 5.4 mg cm^{-2} of argon. Three of the banks had slat collimators with rectangular fields of view of 3° × 30° or 3° × 40°. The fourth bank employed a modulation collimator with a sawtooth response function in the direction perpendicular to the rocket equator and a triangular response function in the direction parallel to the rocket equator.

Two other flights were made at White Sands, one on August 28, 1964, and one on October 26, 1964, by R. Giacconi, H. Gursky, and J. Waters to measure the spectra in the energy region from 1 to 25 keV for X-rays emitted along the Galactic equator, near the galactic center and from the known X-ray source Sco X–1. Twelve Geiger counters similar to those used by Clark et al. were used for the first two flights. Pulse-height analysis using a sodium iodide scintillator was added for the October flight. The pulse-height distribution for Sco X–1 suggests a cutoff in the spectrum at about 15 keV, but shows approximately equal intensity above and below 2.5 keV which is in disagreement with the observations of Fisher. Radiation from the galactic equator extends to higher energies with a possible peak at 20 keV. Comparison of the scintillator results with the Geiger-counter data appears to eliminate the possibility that the Sco X–1 radiation is from a blackbody (Giacconi et al., 1965).

P. C. Fisher of Lockheed Missiles & Space Co. flew an Aerobee 150 rocket on October 1, 1965, to make quantitative spectral measurements and to determine the location of discrete X-ray sources. Four or five X-ray sources near the galactic center were seen, but analysis of the data has not been completed.

Chodil and his colleagues at the Lawrence Radiation Laboratory of the University of California flew a proportional counter and a special telemetry system on a rocket to measure the spectrum of Sco XR–1 with high resolution between 2 and 20 keV (Chodil et al., 1965). Significant flux as high as 20 keV was found. A good fit to the results could be made for bremsstrahlung from a plasma at a temperature of about 5 keV (5.8×10^7 °K). To fit a synchrotron spectrum to the data, spectral indices of about −0.9 between 2 and 8 keV and of −2 between 8 and 20 keV are required. Blackbody radiation from an object with a single temperature does not fit the data well.

Goddard Space Flight Center personnel flew an X-ray telescope spectrometer sensitive to the 20- to 100-keV region on December 6, 1965, on a balloon launched from Holloman Air Force Base, Alamogordo, N. Mex. The general operation of the equipment was quite satisfactory and preliminary examination of the data indicates that the system is suitable for X-ray astronomy. Five additional flight units are in preparation.

Peterson, Jacobson, and Pelliny of the University of California, San Diego, conducted an experiment to detect X-rays in the range from 16 to 120 keV from the Crab Nebula. On September 23, 1965, a balloon was launched from Palestine, Tex., carrying a sodium iodide crystal 5 millimeters thick surrounded by an anticoincidence collimator to reject background cosmic-ray events. The detector area was 9.4 cm^2. Resolution at "full width half maximum" (FWHM) was 54 percent of the central energy at 30 keV (i.e., the uncertainty of an energy measurement is 54 percent$\times$30 keV=16 keV). A peak of X-ray intensity was found within about $\pm 2°$ right ascension and $\pm 4°$ declination of the Crab Nebula. The spectral index was found to be -0.91 ± 0.10 over the spectral range studied. A synchrotron mechanism with an appropriate time-dependent source of 10^4 BeV electrons in a 10^{-4} gauss field can produce the observed photon spectrum.

Burbidge, Gould, and Tucker (1965) discussed four mechanisms which might be responsible for X-ray production; namely, (*a*) neutron stars, (*b*) inverse Compton scattering, (*c*) bremsstrahlung, and (*d*) synchrotron emission. Neutron stars do not emit sufficient X-rays to explain the observations, and inverse Compton scattering of low-energy photons by high-energy electrons, at least in the Crab Nebula, cannot account for the observed flux. For synchrotron emission, the source must be continuously active, and the X-ray flux would then arise in a very small volume, with an upper limit of about 1 parsec in extent. They offer as an attractive hypothesis an alternative model, in which an outburst gives rise to a small, very hot cloud which continues to emit hard radiation as part of the thermal bremsstrahlung.

Morrison and Sartori (1965) propose, as a model for sources of X-rays, remnants of Type I supernovas. The X-ray sources are hot, low density gas clouds, very rich in high-Z elements, radiating principally by bremsstrahlung. Such a cloud at the center of an SN–I remnant contains heavy isotopes formed in the explosion, and has been heated to a temperature of 1 to 10 keV per particle by the kinetic energy released in radioactive decay over a long period of time.

Kraushaar et al. (1965) reported the final results obtained from Explorer XI which orbited a telescope designed to detect gamma rays with energies over 50 MeV. This radiation is believed to result principally from collisions of cosmic-ray particles with gas. These collisions produce π^0 mesons which in turn decay into gamma rays. An average gamma-ray intensity of 3×10^{-4} cm^{-2} sec^{-1} sr^{-1} was observed. During the 7 months that the instrument was turned on and working, a total of only 141 hours, or 3 percent of the time, was accepted as useful observing time. This was because the satellite was within range

of a receiving station only 20 percent of the time, was below the radiation belts only 30 percent of the time, and had subnormal voltages for much of the fifth, sixth, and seventh months. Only 31 events were recorded as coming from an attitude such that they were likely to be cosmic in origin. Although the statistical sample was small, a careful analysis revealed that the data are consistent with an isotropic cosmic distribution. An upper limit to the gamma-ray flux from a number of possible discrete sources was calculated and is given in table I. The intensity is not consistent with what one would expect from cosmic-ray collisions with interstellar atomic hydrogen, but can be accounted for if a modest intensity of high-energy electrons in intergalactic space is assumed.

Table I.—*Approximate Gamma-ray Flux Upper Limits for Possible Discrete Sources*

Source	Flux upper limit $\times 10^{-4}$ cm^{-2} sec^{-1}
Andromeda	16
Small Magellanic cloud	11
Large Magellanic cloud	9.4
Taurus A	6.6
Hydra A	1.7
Virgo A	2.7
Centaurus A	3
Hercules A	3.4
Cygnus A	5
Cassiopeia A	23
Galactic Center	5.3

A search for point sources of gamma rays was made by C. Fichtel and D. Kniffen of Goddard Space Flight Center. Using oriented nuclear emulsions in high-altitude balloons, they examined the energy range from 10 to 2×10^3 MeV. Their detection efficiency in the 10- to 50-MeV region averaged about 10 percent, greater by a factor of almost 10 than previous experiments using counter systems.

BIBLIOGRAPHY

BOWYER, S.; BYRAM, E. T.; CHUBB, T. A.; AND FRIEDMAN, H.: Cosmic X-ray Sources. Science, vol. 147, 1965, p. 394.

BURBIDGE, G. R.; GOULD, R. J.; AND TUCKER, W. H.: Galactic X-ray Sources. Phys. Rev. Let., vol. 14, 1965, p. 771.

CHODIL, G.; JAPSON, R. C.; MARK, HANS; SEWARD, F. D.; AND SWIFT, C. D.: X-ray Spectra from Scorpius (SCO–XR–1) and the Sun Observed Above the Atmosphere. Phys. Rev. Let., vol. 15, 1965, p. 605.

CLARK, G.; GARMIRE, G.; ODA, M.; AND WADA, M.: Positions of Three Cosmic X-Ray Sources in Scorpio and Sagittarius. Nature, vol. 207, 1965, p. 584.

GIACCONI, R.; GURSKY, H.; AND WATERS, J. R.: Spectral Data From the Cosmic X-Ray Sources in Scorpius and Near the Galactic Center. Nature, vol. 207, 1965, p. 572.

KRAUSHAAR, W.; CLARK, G. W.; GARMIRE, G.; HELMKEN, H.; HIGBIE, P.; AND AGOGINO, M.: Explorer XI Experiment on Cosmic Gamma Rays. Astrophysical J., vol. 141, 1965, p. 845.

MORRISON, P.; AND SARTORI, L.: X-Ray Emission From Remnants of Type-I Supernovas. Phys. Rev. Let., vol. 14, No. 19, 1965, p. 771.

J. K. GLEIM
Physics and Astronomy Programs
Office of Space Science and Applications, NASA

ULTRAVIOLET ASTRONOMY

On June 2, 1965, an Aerobee rocket flight from White Sands recorded the first absorption-line spectra of stars in the ultraviolet region. Improved models for the atmospheres of early-type stars were derived. Technological progress included the completion of fabrication and final tests on the ultraviolet instrumentation to be flown aboard the first orbiting Astronomical Observatory in early 1966.

BECAUSE OF THE TOTAL ABSORPTION of radiation below 3000 Å by the Earth's atmosphere, any astronomical observations made in this region must be made in space. Since 1955 rocket flights have been flown to perform photometric and low-resolution spectrophotometric sky surveys. These flights were flown on spinning rockets but in 1965 three-axis-stabilized astronomical rocket experiments were flown.

The ultraviolet spectral region holds great promise for astronomical observations. Current estimates of the total energy output of stars must be made on the basis of limited observations in the visual spectral region. For stars significantly hotter than the Sun this can be a dangerous extrapolation. However, the total energy output can be measured directly from satellites. This information is important to theories of both interior energy generation and atmospheric structure. The hot stars, most of whose energy is emitted in the ultraviolet, are of particular interest because of their rapid evolution which makes them useful as gages of the time scale of stars. Recent rocket results have caused a downward revision of the temperature of the hot stars.

The ultraviolet regions are being studied initially by means of broadband spectrophotometry and photometry. These observations will provide the statistical data needed to understand the major characteristics of many types of stars. These studies will be followed by surveys from the Orbiting Astronomical Observatory, which is capable of greatly increased spatial and spectral resolution and extended observing time.

A team directed by Donald C. Morton of Princeton University obtained the first photographic spectra of stars in the vacuum ultraviolet and the first spectra of stars in this region showing absorption lines on a historic flight on June 2, 1965. The instrumentation con-

sisted of two objective-grating spectrographs mounted on a roll-stabilized platform. Pitch-and-yaw gyros provided orientation within 2° of target, with 0.6° drift, and ±0.2° jitter for 4 minutes. Each spectrograph used plane gratings with 1200 lines per millimeter followed by f/2 Schmidt cameras with 100-millimeter focal lengths and 10°-diameter fields. One corrector was made of calcium fluoride, transmitting down to about 1250 Å and thus eliminating the Lyman-α night airglow. The other corrector was quartz which transmitted down to about 1700 Å. Dispersions at the center of the fields were 67.1 Å/mm for the calcium fluoride camera and 64.0 Å/mm for the quartz camera. Although the parachute failed and the instrument was smashed beyond repair in the June flight, it was subsequently found that the last exposure of the calcium fluoride camera showed weak spectra of two stars, later identified as δ and π Scorpii. Twenty-three lines in the δ Scorpii spectrum and 18 lines in the π Scorpii spectrum were identified. The far UV lines in these early B-type stars are all absorption lines, rather than emission lines as those in the Sun are. This result agrees with theory, since it is difficult to imagine a nonequilibrium process which enhances a chromospheric line above the UV continuum which carries most of the flux in a hot star.

On October 6, 1965, Morton obtained spectra of six early-type stars in Orion. The attitude control system, fine-stabilization system, and astronomical instrumentation were similar to that of the June flight, except that the quartz corrector in one of the two Schmidt cameras was replaced by one of lithium fluoride. The other corrector was of calcium fluoride, as before. The rocket reached an altitude of 114 miles and directed the spectrographs to within 1° of ϵ Orionis. An exposure of 180 seconds gave the best spectra of the six OB stars, with a resolution of 4 Å (compared to 1-Å resolution for the earlier flight). Absorption lines were visible in the spectra of five of the six stars, with the lines of Si IV at 1394 Å and 1403 Å and C IV at 1549 Å particularly strong in δ, ϵ, and ζ Orionis. Emission features are visible on the long-wavelength edges of these lines in ϵ and ζ Orionis.

On November 29, 1965, Goddard Space Flight Center personnel obtained spectrophotometric data for stars in the southern half of Orion and the northern parts of Lupus and Canis Major. The spectra extended below 1400 Å with 8- to 10-Å resolution. Two absorption features near 1500 Å were found in some of the spectra. Detailed reduction of the spectrograms is still in progress.

Stecher (ref. 1) used scanning spectrometer data for five pairs of reddened and unreddened stars to derive an interstellar scattering curve which confirmed a preliminary report by Stecher (ref. 2) and the two-color results of Boggess and Borgman (ref. 3). In general,

the extinction coefficient increases down to about $1/\lambda = 6.2\ \mu^{-1}$, with a peak at $4.4\ \mu^{-1}$. The magnitude of this peak shows considerable variation from one star to the next, but the peak appears to be an intrinsic feature of the scattering curve, and is suggestive of graphite particles. Mie-scattering calculations have been carried out using optical constants for graphite. The calculations fit the observations, except at short wavelengths where a dielectric scattering component must be added. However, since graphite is strongly anisotropic, it may be possible to attribute the dielectric scattering to graphite also, by postulating its existence in flakes randomly oriented with respect to the incident radiation.

Theoretical ultraviolet spectra from 911.6 to 3000 Å of two early B stars (types B2 V and B0 V) were computed in detail by Morton (ref. 4). All lines expected to be wider than 2 Å were included. It was found that the overlapping lines absorb one-half or more of the continuum flux between 911.6 and 1040 Å, between 1060 and 1090 Å, and between 1165 and 1220 A. For the hotter star, the overlapping wings of the absorption lines reduce the continuum flux below 1410 Å by 20 percent; for the cooler star, by 31 percent. This study formed the basis for a more detailed analysis by Mihalas and Morton (ref. 5) of a model for a B1.5 V star with line blanketing.

Hallam flew an ultraviolet spectrophotometer in the wheel section of OSO II, launched in February 1965. The instrumentation, which included a 6-inch telescope, was designed to give stellar spectra in the 1500 to 3000-Å region. Technical problems have prevented the obtaining of results to date, but the data are still being analyzed in order to find out if useful information can be derived.

Bashkin and his associates at the University of Arizona used a beam of high-speed particles from a Van de Graaff accelerator as a high-purity source of neutral and ionized atoms for spectral analysis. The particles are excited electronically by passage through a thin foil of carbon. Spectra have been obtained for deuterium, helium, nitrogen, and oxygen in the wavelength range 2700 to 6600 Å. The wavelengths of many of the nitrogen and oxygen lines agree satisfactorily with the wavelengths given in the standard multiplet tables, but many unreported lines were observed also.

REFERENCES

1. Stecher, T. P.: Interstellar Extinction in the Ultraviolet. Astrophys. J., vol. 142, 1965, p. 1683.
2. Stecher, T. P.: Observed Interstellar Extinction in the UV. Astron. J., vol. 69, 1964, p. 558.

3. BOGGESS, A.; AND BORGMAN, J.: Interstellar Extinction in the Middle Ultraviolet. Astrophys. J., vol. 140, 1964, p. 1636.
4. MORTON, D. C.: Theoretical Line Profiles in the Ultraviolet Spectra of Early-Type Stars. Ap. J., vol. 141, 1965, p. 73.
5. MIHALAS, D. M.; AND MORTON, D. C.: A Model for a B1V Star With Line Blanketing. Ap. J., vol. 142, 1965, p. 253.

J. K. GLEIM
Physics and Astronomy Programs
Office of Space Science and Applications, NASA

F. T. HADDOCK
University of Michigan
Radio Astronomy Observatory

RADIO ASTRONOMY

During 1965 the main events of interest to low-frequency radio astronomy were the launching of two U.S. satellites: OGO II, launched October 14, 1965, and Alouette II, launched November 29, 1965. Cosmic background noise measurements made by use of the U.S.S.R. Electron II and IV satellites were reported by the Soviets.

RADIO ASTRONOMY HAS GROWN RAPIDLY since the discovery of radio waves from the Milky Way in 1937. A succession of rapid advances has occurred since then, largely as a result of new instruments with greater and greater resolving power. However, ground-based radio observations are prevented in both the long wave and short wave portion of the spectrum. At wavelengths greater than 300 meters (1 MHz) the ionosphere prevents radiation from reaching the Earth. At wavelengths less than 10 mm (300 GHz) the atmosphere absorbs extraterrestrial radiation.

The principal space efforts in this field have been to develop instrumentation to be carried aloft by a satellite. The early long-wave experiments, because of the short antennae employed, have been nondirectional. These experiments were mainly for the purpose of measuring sky brightness. This information is needed to understand the mechanism of emission and absorption of radio waves within the galaxy. There is some indication that absorption by ionized hydrogen at 2–3 MHz has been detected.

Future goals, when higher resolution is possible, are to measure radiation from the Sun and planetary objects and galactic and extragalactic sources. The Sun and other objects in the solar system will be studied intensively at the shorter wavelengths. Temperature and surface characteristics of these objects will be explored. Radio sources, quasi-stellar sources and red stars are particularly intriguing subjects to study at the shorter wavelengths.

At the Sixth Space Science Symposium organized by COSPAR in Buenos Aires, May 1965, Steinberg read a paper by a group from the State University at Gorky. He reported results of measurements of

cosmic background noise at 0.725 and 1.525 MHz obtained with direct-amplification receivers and a 3.75-meter rod antenna aboard the U.S.S.R. Electron II satellite. The satellite was launched June 30, 1964, into an eccentric orbit with an apogee of 70 000 kilometers and an inclination of 61°. The paper reported values for the average flux density over the sky of 5.1×10^{-21} and 8.7×10^{-21} W/m²/cps/sr. In addition, it reported measurements obtained from the Electron IV satellite launched July 11, 1964, into a similar orbit, but with receivers operating at 1.11 and 2.29 MHz. Values obtained for the intensity were 8.4×10^{-21} and 10.2×10^{-21} W/m²/cps/sr, respectively, with an estimated error of 30 percent. No details were given of instrumentation or methods of calibration. Sporadic enhanced radio emission at 0.725 and 1.525 MHz was also observed, with the maximum intensity at geomagnetic latitudes of +45° and 0 at the geomagnetic equator. Sporadic radio emission was observed more frequently at 0.725 MHz at intensities 10 times greater than at 1.525 MHz. The sporadic emission increased the total emission level by more than a hundredfold. It was concluded that the sporadic radio emission is generated by electron streams in the upper ionosphere and has many features in common with radio bursts from the Sun and Jupiter.

Early on the morning of June 30, 1965, University of Michigan radio astronomers obtained a successful measurement similar to their 1962 measurement of mean cosmic noise near 1 MHz. The Journeyman rocket lofted a 130-pound payload to the same maximum altitude (1708 kilometers). The most important improvement was obtained by increasing the overall antenna length from 40 to 70 feet and by the measurement of both the real and imaginary components of the antenna impedance at the two lower frequencies. Although the data analysis is still in progress, the first preliminary indications are that the 1962 intensities at 2.0 and 1.22 MHz were confirmed and that the 0.75 MHz value is consistent with these.

The OGO II satellite was launched on October 14, 1965, into a polar orbit with perigee of 414 kilometers and apogee of 1510 kilometers, and inclination of 87.5°. The University of Michigan had a radio-astronomy experiment mounted in the same location as on OGO I and with a similar antenna which, however, was self-erected and twice as long. The purpose of this experiment is to obtain a moderate-resolution map of cosmic background noise at 2.5 MHz using the ionosphere as a large lens to focus the incoming radio waves into a moderate-sized beam. The experiment seems to be functioning properly, although the receiver noise level is rather high because of interference from sources on the spacecraft itself.

In October 1965, J. L. Steinberg and his coworkers at the Meudon Observatory in Paris conducted a rocketborne radio-astronomy experiment on a two-stage solid-fuel rocket, called "Rubis," launched from the French Sahara test range. It carried a 40-kilogram payload to 1700 kilometers maximum altitude. Two receivers, each switching between two frequencies, provided calibrated measurements of cosmic noise at 1.8, 2.13, 3.5, and 6.0 MHz. The electric dipole antenna used was 120 feet tip to tip and its impedance was measured during flight. Preliminary verbal reports indicated that the experiment was successful.

Alouette II, like Alouette I, was prepared by the Defence Research Telecommunications Establishment of the Canadian Defence Research Board and was primarily designed to study the ionosphere. It was launched as part of a double payload from the Western Test Range on November 29, 1965, into an 80° inclination orbit, with perigee of 500 kilometers and apogee of 3000 kilometers, approximately. The measurement of cosmic noise in the 0.2- to 14.8-MHz range is also included in the experiment objectives. All systems are working well, but no results are yet available.

A few groups in the United States are carrying out preliminary studies on large orbiting antenna systems in order to obtain relatively high angular resolution in the 1-MHz band. Thompson Ramo Wooldridge (TRW), Inc., is studying a spin-stabilized system of filaments supporting a rhombic antenna a few thousand feet in diameter to obtain resolution over this same band. The University of Michigan radio-astronomy group has also begun an engineering feasibility study of a kilometer-wave orbiting telescope (KWOT) which in the present state of conception consists of a spin-stabilized double-layered web, 10 kilometers in diameter, made of conducting and nonconducting filaments attached to four subsatellites which are equally spaced around the perimeter of the 10-kilometer-diameter web. This web is attached to a large-diameter spinning central observatory. The system will spin with a period of about 2 hours and the spin axis will be changed in a programed way by microrockets on the subsatellites and central observatory so that a map of the whole sky can be obtained within a year or so. The size of this system was chosen to give sufficient angular resolution at a frequency of 1 MHz to make accurate flux density measurements of several dozen extragalactic and galactic radio sources. It will also be possible to map the cosmic background noise of the full sky at a number of frequencies from 0.1 to 10 MHz.

BIBLIOGRAPHY

ALEXANDER, J. K.; AND STONE, R. G.: Rocket Measurements of Cosmic Noise Intensities Below 5 Mc/s. NASA-Goddard Space Flight Center Report X-615-65-185, Apr. 1965.

BENEDIKTOV, E. A.; GETMANTSEV, G. G.; MITJAKOV, N. A.; RAPOPORT, V. O.; SAZONOV, J. A.; AND TARASOV, A. F.: Intensity Measurements of Radiation at Frequencies 725 and 1525 Kc/s by Means of the Receiver on the Satellite Electron-2. COSPAR Symposium, Buenos Aires, Argentina, May 1965 (unpublished).

FINK, D. E.: Radio Astronomy Explorer to Utilize 750–1000 Foot Antennas. Aviation Week & Space Technology, vol. 83, 1965, p. 106.

HARVEY, C. C.: Results From the UK-2 Satellite. Ann. d'Ap., vol. 28, 1965, p. 248.

HUGILL, J.: Some Measurements of Aerial Impedance in the Ionosphere. Ann. d'Ap., vol. 28, 1965, p. 255.

HUGUENIN, G. R.; AND PAPAGIANNIS, M. D.: Spaceborne Observations of Radio Noise From 0.7 to 7.0 MHz and Their Dependence on the Terrestrial Environment. Ann. d'Ap., vol. 28, 1965, p. 239.

LUDWIG, G. H.: Relative Advantages of Small Observatory Type Satellites. NASA-Goddard Space Flight Center Report X-611-65-189, May 1965.

WALSH, D.; AND HADDOCK, F. T.: Antenna Impedance in a Plasma: Problems Relevant to Radio Astronomy Measurements From Space Vehicles. Ann. d'Ap., vol. 28, 1965, p. 605.

WEIL, H.; AND WALSH, D.: Radiation Resistance of an Elementary Loop Antenna in a Magnetoionic Medium. IEEE Trans., Antennas and Propagation. AP-13, 1965, p. 21.

IONOSPHERES AND RADIO PHYSICS

E. R. SCHMERLING
Physics and Astronomy Programs
Office of Space Science and Applications, NASA

PRECEDING PAGE BLANK NOT FILMED.

Ionospheres and Radio Physics

INTRODUCTION

IN THE IONOSPHERES AND RADIO PHYSICS discipline, the most important event in 1965 was undoubtedly the occultation measurement of the Martian atmosphere and ionosphere performed by Mariner IV on July 15. Careful observations on Earth of the phase of the spacecraft telemetry transmitter not only resulted in considerable revisions of the generally accepted values for the atmospheric surface pressure of Mars, but also produced the first electron-density profile ever obtained from a planetary ionosphere—truly a notable return for a zero-weight experiment.

In other respects 1965 was a year of steady, if unspectacular, progress. The NASA Mobile Launch Range Expedition produced considerable data, but more time is needed for a final analysis of the results. Early results do show a definite latitude effect on the lower D-region (C-region), but opposite in sense from what would be expected for a cosmic ray origin. Some progress has been made in identifying the ions in the D-region, in understanding the distribution of electrons near the geomagnetic equator, and in developing VLF resonance phenomena as a powerful tool for investigating the ionic composition of the topside.

Table I presents a list of the major spacecraft launchings of 1965 with experiments primarily of interest to ionospheres and radio physics. The twin launch of ISIS–X, consisting of Alouette II with a topside sounder and Explorer XXXI with direct-measurement experiments, provided valuable data. Preliminary indications from identical Langmuir probes in both spacecraft are that direct-measurement experiments can probably be made from the same satellite as a sounder equipped with long antennas. Early data from the two-frequency propagation experiment on Pioneer VI set an upper limit for average plasma densities in interplanetary space at 10 electrons per cubic centimeter.

THE IONOSPHERIC REGIONS

The Lower Ionosphere

In an important series of rocket experiments, Bowhill and Smith (ref. 1) measured the electron density near sunrise. They found that

Table I.—*U.S. Satellite and Space Probe Launchings in 1965 of Interest in Ionospheres and Radio Physics Research*

Satellite space probe	Launch date	Perigee, km	Apogee, km	Inclination, deg	Items of ionospheric interest
Explorer XXVII (BE–C)	Apr. 29, 1965	939	1318	41.2	Langmuir probe and multifrequency beacon for electron content and irregularities.
OGO–II	Oct. 14, 1965	407	1510	87.4	VLF receivers; ion spectrometers.
Explorer XXX (Naval Research Laboratory).	Nov. 19, 1965	709	883	59.7	Solar X-ray monitors.
ISIS–X (Alouette II+Explorer XXXI) (Canadian-U.S.)	Nov. 29, 1965	501	2983	79.8	Dual launching of Alouette II (topside sounder, VLF receivers) with Explorer XXXI (direct measurements).
FR–1 (French-U.S.)	Dec. 6, 1965	743	773	75.9	Independent measurement of VLF electric and magnetic fields.
Pioneer VI	Dec. 16, 1965	----------	----------	----------	Two-frequency propagation experiment for interplanetary plasma studies. Faraday cup plasma probe. To 0.81 AU.

the ionization below 80 kilometers increases quite rapidly at a solar zenith angle of 95°. This ionization is frequently called the C-layer. Absorption considerations indicate that solar ultraviolet radiation in the range from 1800 to 2900 angstroms penetrates to those levels at that time. Since the C-layer is believed to be formed by cosmic rays, the results are interpreted in terms of photodetachment from negative ions. The ion O_2^- had previously been suggested as the dominant negative ion; but since photodetachment from O_2^- occurs with visible light, the electron density would have been seen to increase earlier. It is consequently concluded that the dominant negative ion in the C-layer must be one, such as O_3^- or NO_2^-, with a photodetachment threshold below 2900 Å.

Some preliminary results of Bowhill and Smith (ref. 1) obtained on the NASA Mobile Launch Range Expedition during the first half of 1965 indicate a marked variation with latitude of the low-altitude electron density profile. This effect is, however, opposite in sense from what would be expected for a cosmic ray origin if the incident cosmic ray flux remained constant during the period of measurement. Figure 1 shows the electron density profiles taken

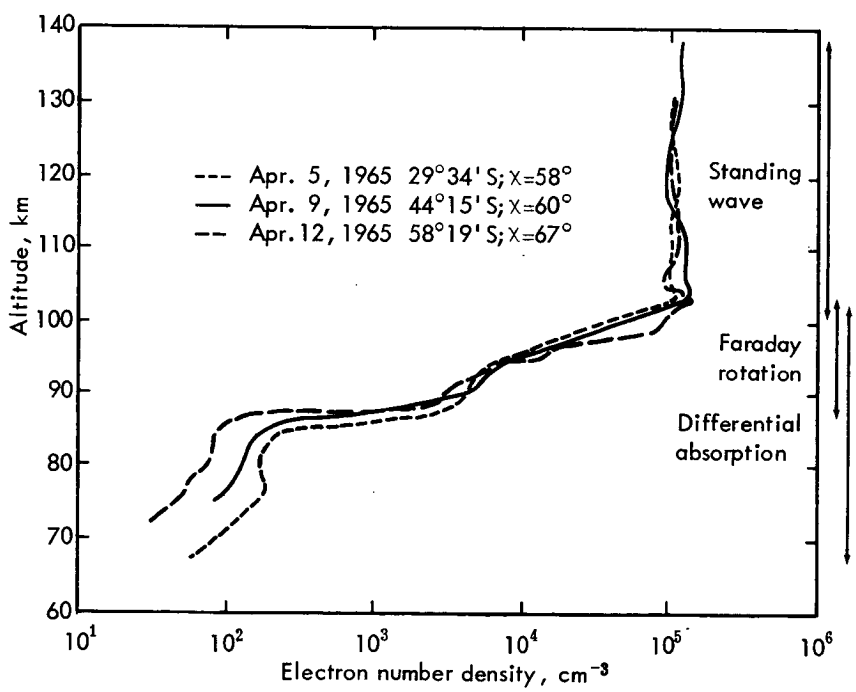

Figure 1.—**Electron density-height profiles from mobile launch range rocket series (Bowhill and Smith, ref. 1).**

at nearly the same solar zenith angle, but at different latitudes. Above 90 kilometers the profiles are nearly coincident, but below 90 kilometers the electron densities decrease with latitude.

The first direct measurements of ion composition in the region from 64 to 112 kilometers were reported by Narcisi and Bailey (ref. 2); they were made with a cooled zeolite-pumped quadrupole mass spectrometer at noon. The results, presented in figure 2, were surprising in several respects. Below 82 kilometers, the dominant positive ions were reported to have mass numbers in excess of 37. According to Narcisi, H_3O^+ and $H_5O_2^+$ were major constituents; NO^+ was reported to comprise less than 10 percent of the ionization, and O_2^+ even less. Above 82 kilometers, NO^+ and O_2^+ were found to be the main constituents. In addition, metallic ions were detected in a sharply layered structure, with concentration maxima near 95 kilometers and minima near 105 kilometers.

The Middle Ionosphere (Photoequilibrium Region)

Smith, Accardo, Weeks, and McKinnon (ref. 3) analyzed data from a series of rocket flights during the solar eclipse of July 20, 1963. The electron density profiles, measured up to 200 kilometers, showed smooth distributions at all times without the development of valleys predicted by some workers. In the range from 90 to 200 kilometers, the electron density was reduced by the same factor during the eclipse. No significant changes of electron temperature were found in this altitude range. As in previous eclipse observations, the magnitude and the time of the minimum observed electron density could not both be reconciled with a solar-radiation source of ionization proportional to the visible disk. The results were, however, consistent with a model having a considerable contribution from the solar corona, and with an ionization source for the E-region proportional to the radiation measured in the 44- to 60-Å range on the same rockets. It is unlikely that

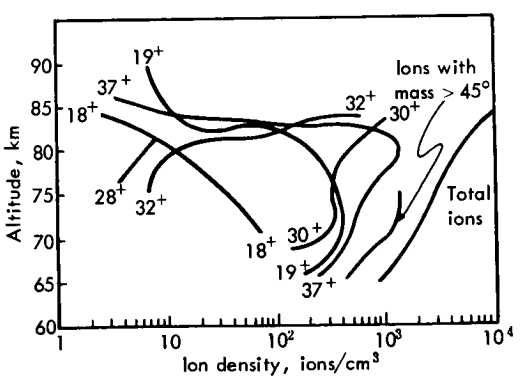

Figure 2.—**Positive ion concentrations (Narcisi and Bailey, ref. 2).**

the 44-Å to 60-Å radiation itself is responsible for the bulk of the E-region ionization, since Thomas, Venables, and Williams (ref. 4) report that the radiation in this region, as monitored by satellite, did not correlate well with fluctuations in the critical frequency of the E-layer.

The resonance rectification probe described by Miyazaki et al. (1960, ref. 5) as a possible tool for measuring electron density and temperature has been subjected to further tests. Bain and Davies (1965, ref. 6) found the situation to be quite complex: The existence of resonant structure in the records depended markedly on the shape of the probe, and spherical probe resonances appeared at several frequencies, none of which were consistently at the plasma frequency or at a fixed multiple of the plasma frequency.

The Upper Ionosphere

The theory of the electron distribution near the magnetic equator (magnetic anomaly) has been further refined, and computations which take into account electron production, loss, diffusion, and electromagnetic drift have been described by Moffett and Hanson (ref. 7) and Bramley and Peart (ref. 8). Goldberg (ref. 9) has, in addition, related the electron distribution to the ionospheric current system. Independent verification of the current, electric field, or vertical drift velocity is still needed.

Evans (ref. 10) has compared electron temperature measurements made by several different techniques involving rockets, satellites, and backscatter sounders. Although a few surprising discrepancies remain, there is general agreement that the electron temperature exceeds the neutral temperature in the F-region both by day and by night, and that the electron temperature increases monotonically with altitude at night for the sunspot minimum period discussed. As a result of the electron temperature changes observed, two anomalies in the F-region critical frequency at sunspot minimum can be explained in terms of the motion of electrons from high altitudes. These are the midlatitude winter night increase (Evans, ref. 11) and the midlatitude summer evening increase (Evans, ref. 12). Similar considerations serve to explain the increase in F-region critical frequency sometimes observed during a solar eclipse at high magnetic latitudes (Evans, ref. 13). Evans' work was based primarily on data obtained from a backscatter sounder on the ground. This type of equipment is uniquely suited for observing the detailed, diurnal changes in electron temperature and density at a fixed location, and has provided a valuable complement to the data obtained from rockets and satellites.

The Topside Ionosphere

Alouette I, launched September 29, 1962, continues to perform remarkably well. Figure 3 shows two ionograms, one taken 1 day after launch; the other, 3½ years later.

The Alouette I sounder continues to reveal details of ionospheric structure never seen before since the satellite sounder can provide data at much closer intervals than the existing ground-based sounders. This is of particular importance in the polar regions, where sur-

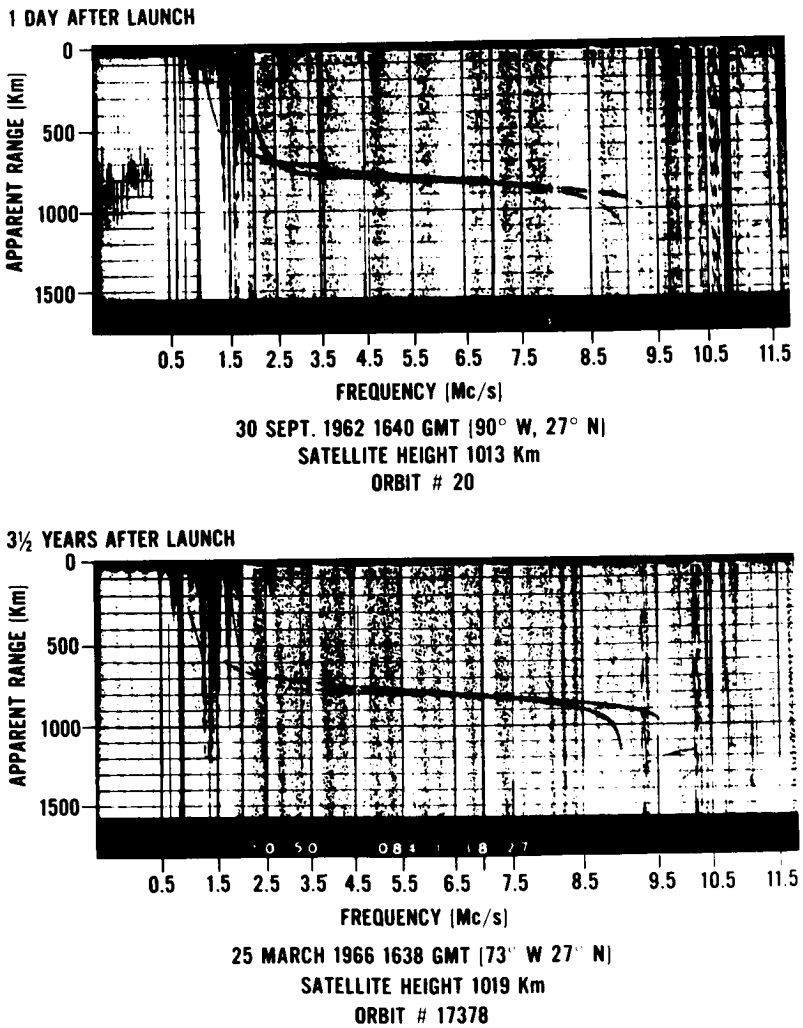

Figure 3.—Alouette I ionograms.

prisingly rapid variations of electron density with latitude have been observed, and a number of "troughs" and "cliffs" show a systematic behavior indicative of particle interactions which are, as yet, not properly understood. Muldrew (ref. 14) has investigated the variation of the extraordinary critical frequency, f_xF2. This quantity is simply related to the peak electron density in the F-region, which would show substantially the same structure. An example is given in figure 4.

Some attention has been given by Doupnik and Schmerling (ref. 15) to refinements in techniques for reducing ionograms to electron density profiles. These refinements are likely to become of increasing importance as topside sounders are orbited at ever higher altitudes.

The new VLF phenomena discovered in 1964 have become very useful tools in the determination of ion composition. The theory of ion cyclotron whistlers has been worked out in some detail by Gurnett, Shawhan, Brice, and Smith (ref. 16) who show, in particular, how the "crossover frequency" on a proton whistler may be used to deter-

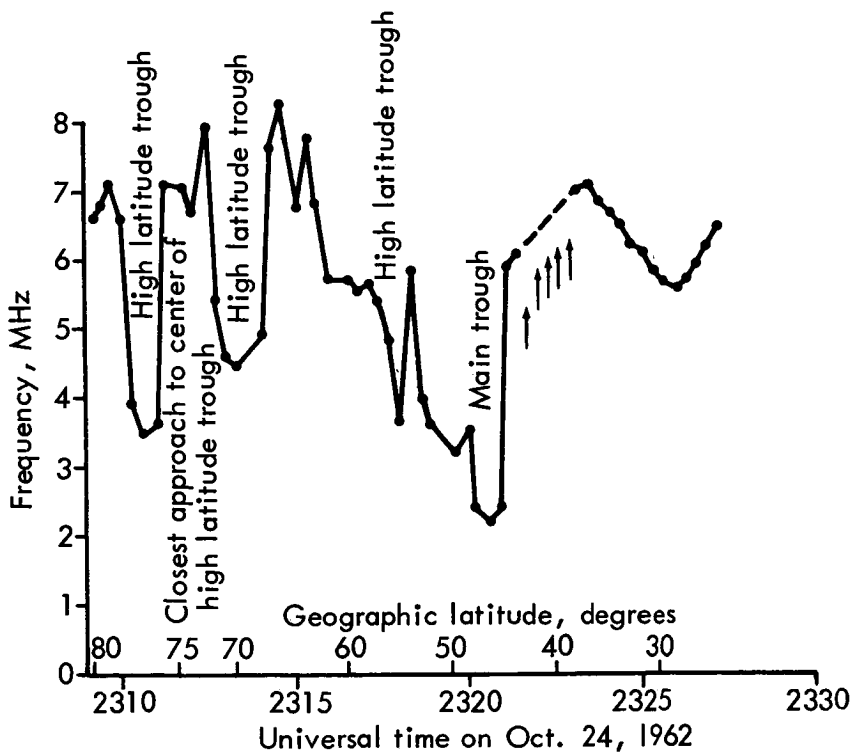

Figure 4.—Frequency f_xF2 from Alouette I as a function of latitude (Muldrew, ref. 14).

245-015 O—67——3

mine the fractional concentration of protons near the satellite. Alouette II, launched on November 29, 1965, is equipped with a VLF receiver sensitive to lower frequencies. Helium whistlers have been discovered on Alouette II VLF records. These helium whistlers are analogous to proton whistlers, and they enable the fractional concentration of helium ions in the vicinity of the satellite to be determined.

A band of noise found on the Alouette I VLF records has been further investigated by Brice and Smith (ref. 17) and Barrington, Belrose, and Nelms (ref. 18). These scientists have shown that the low-frequency cutoff of this band is due to the lower hybrid plasma resonance, which defines a cutoff frequency for propagation transverse to the Earth's magnetic field. Observation of this cutoff, together with independently obtained values of the plasma frequency, enable the harmonic-mean mass of the positive ions near the satellite to be computed. Belrose and Barrington (ref. 19) describe how such noise bands can be triggered by whistlers (both upgoing and downcoming), and they discuss the timing, which indicates that triggering occurs in the vicinity of the satellite.

The theory of these VLF tools seems to be quite well established, apart from the questions of the detailed excitation mechanism, but it is still desirable to obtain some direct comparisons of the ion composition deduced by both VLF measurements and more direct means. Attempts are being made to provide cross-checks using rendezvous opportunities with other satellites that contain ion mass spectrometers and with rockets similarly equipped. A more detailed series of direct comparisons is planned for OGO–II and ISIS–A, where ion mass spectrometers and VLF receivers will be available on the same satellite.

Evidence of significant departures from diffusive equilibrium at altitudes above 1000 kilometers is now emerging from several sources. Taylor, Brinton, and Smith (ref. 20) obtained ion spectra on OGO–I in the altitude range from 1500 to 30 000 kilometers. Over this entire range, they found that the concentrations of H^+ and He^+ decreased with altitude at about the same rate, with the concentration of H^+ 100 times that of He^+. Similar results are beginning to appear from the preliminary analysis of topside ionograms taken from Alouette II. The results from Alouette II show, on some occasions, remarkably low electron densities of the order of 20 electrons/cm^3 at altitudes near 2000 kilometers over the polar regions. This result is likely to prove important in relation to the sudden decrease in electron density over the equator at altitudes of 4 Earth radii, and in relation to the maintenance of the nighttime ionosphere at low altitudes in the polar regions.

INTERPLANETARY PLASMA

Pioneer VI was launched on December 16, 1965. V. R. Eshleman of Stanford University is conducting an experiment in which a transmitter on the spacecraft radiates harmonically related frequencies of about 50 and 400 megahertz. By a phase comparison of the received signals on the ground, the total electron content between the observer and the spacecraft can be obtained. Subtraction of the electron content of the Earth's ionosphere then yields a measure of the interplanetary electron content. Preliminary results indicate that the average interplanetary electron density is below 10 electrons/cm^3.

PLANETARY ATMOSPHERES AND IONOSPHERES

During the occultation of Mars by Mariner IV on July 15, 1965, careful observations of the phase of the spacecraft transmitter enabled the refractive effects of the planet's ionosphere and neutral atmosphere to be made. In order to perform this measurement, the predictable phase shifts caused by the motion of the Earth, the spacecraft, and perturbations due to the Earth's ionosphere had to be subtracted from the raw data with great precision. As reported by Kliore, Cain, Levy, Eshleman, Fjeldbo, and Drake (ref. 21), the maximum phase shifts at immersion due to the atmosphere and the ionosphere amounted to 30 and 10 cycles, respectively. The precision of the observations was, therefore, equivalent to that of measuring a radio-path perturbation of a few meters at a total distance of 2×10^{11} meters. It is extremely unlikely that perturbations in the Earth's ionosphere over an observing station during the occultation period affected the results, since good agreement was obtained by stations in both the United States and Australia.

The theory of the occultation experiment has been described by Fjeldbo and Eshleman (ref. 22) and Fjeldbo, Eshleman, Garriott, and Smith (ref. 23). At immersion, the surface pressure was 5 ± 1 millibars and the temperature, $180°\pm20°$ K. The electron density profile is shown in figure 5.

These conditions correspond, approximately, to winter noon. Emersion occurred at local night and no ionosphere was detected, leading to the conclusion that nighttime peak electron densities at that time were below about 10^4 electrons/cm^3. Surface pressures deduced at emersion were several millibars higher than at immersion, suggesting that there might be a significant effect due to the altitudes of the occulting regions above the gravitational equipotential surface.

CONCLUSIONS AND OUTLOOK

The year 1965 was one of steady progress. The major contributions were made by rockets and satellites, supplemented by data from

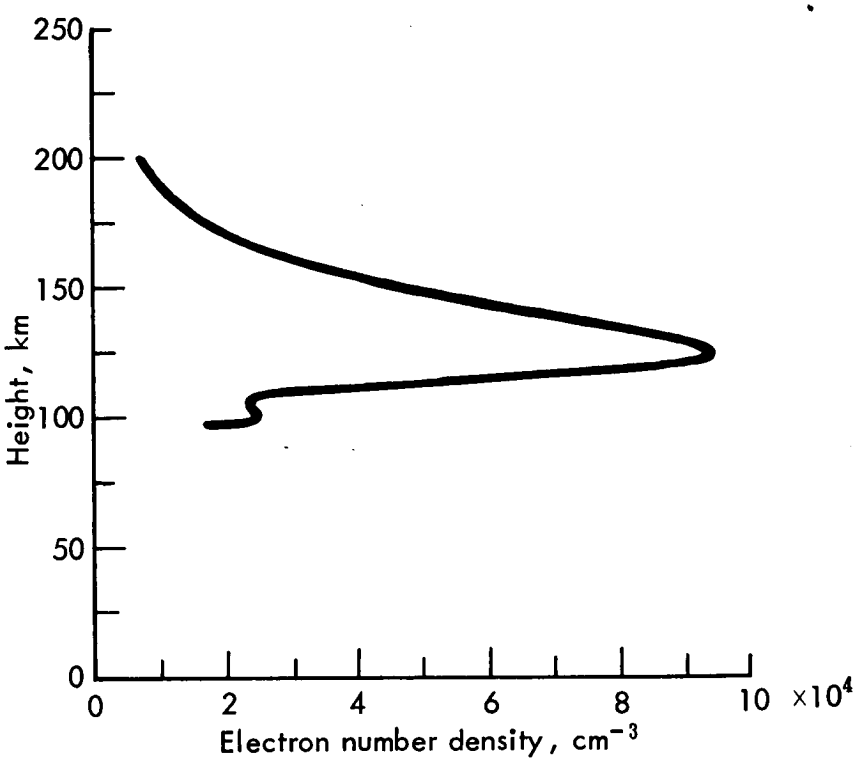

Figure 5.—**Martian electron density profile above Electris at time and location corresponding to immersion into occultation. Latitude, 50° S; longitude, 177° E; 1300 local time; late winter; solar zenith angle, 67°.**

ground-based incoherent backscatter sounders with the unique capability of making continuous observations at fixed locations. This capability is likely to become of increasing importance with the realization that the ionosphere cannot be considered as a static medium, and the increased emphasis consequently being placed on its dynamic behavior. At this time, the important question of heat transfer is being examined by relating the detailed diurnal temperature changes at fixed locations as revealed by the backscatter sounders to the global variations sampled by satellites, and a fresh look is being taken at the large-scale irregularity structure similarly observed by these complementary techniques.

The unexpectedly low electron densities observed at high altitudes over the polar regions are likely to shed new light on the question of the maintenance of the lower ionosphere during the 6-month winter

night. Concurrently, the influence of particle ionization is being studied from balloons, rockets, and satellites.

The important but difficult problem of electric fields in the ionosphere is being tackled by three methods. Firstly, experiments are scheduled to measure potential differences between long insulated booms on spacecraft. Secondly, the observation of a stream of particles ejected from a satellite is planned; and thirdly, the separation of a stream of neutral and ionized gases released from a rocket has already been observed. These important experiments offer a reasonable possibility of measuring the electric fields which are thought to be a major factor in controlling the dynamical behavior of the Earth's ionosphere.

The unexpected variation of electron densities with latitude observed in the lower ionosphere underlines the importance of extending these measurements and of including cosmic ray monitoring in order to test the hypothesis of ionization production by cosmic rays.

An auspicious beginning was made in 1965 on ionospheric studies outside the Earth's magnetosphere, and some results were made available both on the total ionization in interplanetary space and, for the first time, on the ionosphere of a planet. The results on the ionosphere of a planet, in particular, illustrate the power of the radio technique in obtaining a large amount of information from a remarkably simple experiment. Further studies of the Martian ionosphere are of extreme interest, as these represent an opportunity of investigating the behavior of the ionosphere of a planet without a significant magnetic field. The same techniques hopefully can also be applied to studies of the solar corona.

REFERENCES

1. Bowhill, S. A.; and Smith, L. G.: Rocket Observations of the Lowest Ionosphere at Sunrise and Sunset. In: Space Research VI, R. L. Smith-Rose, ed., Spartan Books, 1965.
2. Narcisi, R. S.; and Bailey, A. D.: Mass Spectrometric Measurements of Positive Ions at Altitudes From 64–112 Kilometers. J. Geophys. Res., vol. 70, 1965, pp. 3687–3700.
3. Smith, L. G.; Accardo, C. A.; Weeks, L. H.; and McKinnon, P. J.: Measurements in the Ionosphere During the Solar Eclipse of 20 July 1963. J. Atmospheric Terrest. Phys., vol. 27, 1965, pp. 803–829.
4. Thomas, L.; Venables, F. H.; and Williams, K. M.: Measurements of Solar X-Ray Fluxes by the U.S. Naval Research Laboratory Satellite 1964–01–D. Planetary Space Sci., vol. 13, 1965, pp. 807–822.
5. Miyazaki, S.; Kirao, K.; Aono, Y.; Takayama, K.; Ikegami, H.; and Ichiyama, T.: Resonance Probe—A New Probe Method for Measuring Electron Density and Electron Temperature in the Ionosphere. Rept. of Ionosphere and Space Res. in Japan, vol. 14, 1960, pp. 148–159.
6. Bain, W. C.; and Davies, P. G.: Resonance Rectification. Planetary Space Sci., vol. 13, 1965, pp. 725–726.

7. MOFFETT, R. J.; AND HANSON, W. B.: Effect of Ionization Transport of the Equatorial F Region. Nature, vol. 206, 1965, pp. 705–706.
8. BRAMLEY, E. N.; AND PEART, M.: Diffusion and Electromagnetic Drift in the Equatorial F2 Region. J. Atmospheric Terrest. Phys., vol. 27, 1965, pp. 1201–1211.
9. GOLDBERG, R. A.: Equatorial Geomagnetic Anomaly and Its Associated Current System. J. Geophys. Res., vol. 70, 1965, pp. 5417–5424.
10. EVANS, J. V.: A Comparison of Rocket, Satellite and Radar Determinations of Electron Temperature at Midlatitudes. J. Geophys. Res., vol. 70, 1965, pp. 4365–4374.
11. EVANS, J. V.: Midlatitude Winter Night Increase in f_0F_2. J. Geophys. Res., vol. 70, 1965, pp. 4331–4345.
12. EVANS, J. V.: Cause of the Mid-Latitude Evening Increase in f_0F_2. J. Geophys. Res., vol. 70, 1965, pp. 1175–1185.
13. EVANS, J. V.: On the Behavior of f_0F_2 During Solar Eclipses. J. Geophys. Res., vol. 70, 1965, pp. 733–738.
14. MULDREW, D. B.: F-Layer Ionization Troughs Deduced From Alouette Data. J. Geophys. Res., vol. 70, 1965, pp. 2635–2650.
15. DOUPNIK, J. R.; AND SCHMERLING, E. R.: The Reduction of Ionograms from the Bottomside and Topside. J. Atmospheric Terrest. Phys., vol. 27, 1965, pp. 917–941.
16. GURNETT, D. A.; SHAWHAN, S. D.; BRICE, N. M.; AND SMITH, R. L.: Ion Cyclotron Whistlers. J. Geophys. Res., vol. 70, 1965, pp. 1665–1688.
17. BRICE, N. M.; AND SMITH, R. L.: Lower Hybrid Resonance Emissions. J. Geophys. Res., vol. 70, 1965, pp. 71–80.
18. BARRINGTON, R. E.: BELROSE, J. S.: AND NELMS, G. L.: Ion Composition and Temperatures at 1000 km as Deduced From Simultaneous Observations of a VLF Plasma Resonance and Topside Sounding Data From the Alouette I Satellite. J. Geophys. Res., vol. 70, 1965, pp. 1647–1664.
19. BELROSE, J. S.; AND BARRINGTON, R. E.: VLF Noise Bands Observed by the Alouette I Satellite. Radio Sci., vol. 69D, 1965, pp. 69–76.
20. TAYLOR, H. A.; BRINTON, H. C.; AND SMITH, C. R.: Positive Ion Composition in the Magnetoionosphere Obtained From the OGO–A Satellite. J. Geophys. Res., vol. 70, 1965, pp. 5769–5781.
21. KLIORE, A.; CAIN, D. L.; LEVY, G. S.; ESHLEMAN, V. R.; FJELDBO, G.; AND DRAKE, F. D.: Mariner IV Occultation Experiment: Results of the First Direct Measurement of Mars' Atmosphere and Ionosphere. Science, vol. 149, 1965, pp. 1243–1248.
22. FJELDBO, G.; AND ESHLEMAN, V. R.: The Bistatic Radar Occultation Method for the Study of Planetary Atmospheres. J. Geophys. Res., vol. 70, 1965, pp. 3217–3225.
23. FJELDBO, G.; ESHLEMAN, V. R.; GARRIOTT, O. K.; AND SMITH, F. L., III: The Two-Frequency Bistatic Radar-Occultation Method for the Study of Planetary Ionospheres. J. Geophys. Res., vol. 70, 1965, pp. 3701–3710.

PARTICLES AND FIELDS

ALOIS W. SCHARDT AND ALBERT G. OPP
Physics and Astronomy Programs
Office of Space Science and Applications, NASA

Particles and Fields

INTRODUCTION

THE ACCOMPLISHMENTS IN SPACE SCIENCE during any given year consist of two rather different contributions. Foremost, the accomplishments should be measured in terms of new discoveries and the insight gained into the processes shaping our environment. Of importance for the continued health of space science are, however, the observations and measurements which are conducted during the year. The analysis of these data is in general difficult; as a result many scientific consequences are not discovered for several years. In order to cover both aspects, this paper contains a short summary of spacecraft operations before the discussion of scientific areas in the particles and fields discipline which were particularly active during the year.

The space data taken during the year can be described fully only in terms of a multidimensional matrix involving time of observation, spatial position, and type of observation. The periods of operation and the parts of space explored with spacecraft which carried primarily investigations in the particles and fields area are summarized in table I and figures 1 to 3. A listing of the physical parameters observed with these spacecraft is given in appendix A. The spatial coverage is difficult to describe because the satellite orbits are generally not in the plane of the ecliptic. In figure 1 the actual apogee distances are shown in units of Earth radii (R_e) and the projection, on the plane of the ecliptic, of the Sun-Earth probe (SEP) angle. The line of apsides for the OGO I satellite was on the average 35° above (north) the plane of the ecliptic and that of IMP II about 20° below (south). This means that the crossings of the shock front or magnetopause do not necessarily occur near the magnetic equator. The orbits of the Vela spacecraft are nearly circular and are inclined 60° to the plane of the ecliptic (fig. 2); consequently these orbits map out a quite different part of the magnetosphere than does OGO I.

During much of the year, several spacecraft were operating simultaneously. Even though telemetry from these spacecraft was not monitored 100 percent of the time, it will be possible to find periods of simultaneous observations at different locations in space. Correlations between measurements by Mariner IV, located as shown in

Table I.—*Major Particles and Fields Spacecraft Operating During 1965* [a]

Spacecraft	Launch	Perigee altitude, km	Apogee altitude, km	Inclination, deg	Period, min.	Months operated J	F	M	A	M	J	J	A	S	O	N	D
APOGEE LESS THAN 8 EARTH RADII [b]																	
1963—38C	28 Sep 63	1 074	1 136	90	107												
Relay II (1964—3A)	21 Jan 64	2 079	7 420	46	195												
Injun IV or Explorer XXV (1964—76B).	21 Nov 64	529	2 495	81	116												
EPE IV or Explorer XXVI (1964—86A).	21 Dec 64	300	25 936	20	452												
Proton I (1965—54A).	16 Jul 65	189	624	64	92												
OV I-2 (1965—78A)	5 Oct 65	413	3 451	144	126												
OGO II [c] (1965—81A).	14 Oct 65	420	1 511	87	104												
Proton II (1965—87A).	2 Nov [c] 65	160	312	63	89												
APOGEE GREATER THAN 8 EARTH RADII																	
Vela IIa (1964—40A).	17 Jul 64	102 551	103 947	38	6020												

Vela IIb (1964—40B).	17 Jul	64	90 918	115 142	40	6003
OGO I (1964—54A)[c]	5 Sep	64	4 930	144 824	41	3842
IMP II or Explorer XXI (1964—60A).	4 Oct	64	917	94 288	34	2080
IMP III or Explorer XXVIII (1965—42A).	29 May	65	196	264 247	34	8559
Vela IIIa (1965—58A).	20 Jul	65	106 367	115 839	35	6679
Vela IIIb (1965—58B).	20 Jul	65	100 569	122 079	34	6698
ERS 17 (1965—58C)	20 Jul	65	566	111 793	37	2595

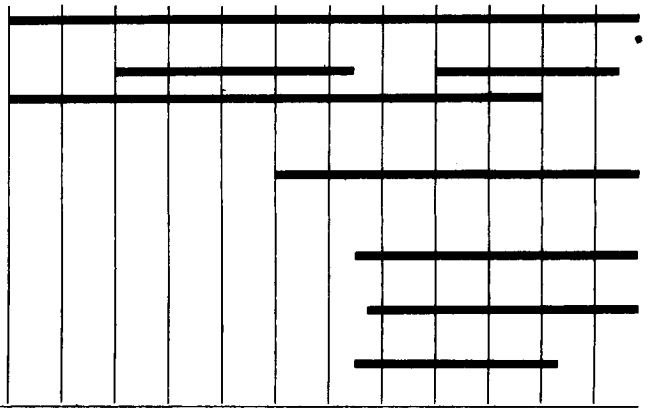

PLANETARY AND INTERPLANETARY PROBES

Mariner IV (1964—77A).	28 Nov	64	Mars flyby, launched at 248° from Earth-Sun line
Pioneer VI (1965—105A).	16 Dec	65	To investigate interplanetary medium in to 0. 81 AU, launched at 85° from Earth-Sun line

[a] Prepared from the Satellite Situation Report, Goddard Space Flight Center, Document X–537–217.

[b] In addition to Proton I and Proton II, the U.S.S.R. launched the following spacecraft during 1964 and 1965. Since no definitive information was available on the data return from these spacecraft, they were not included in the table.

Elektron I and II—30 Jan 1964
Elektron III and IV—11 Jul 1964
27 Cosmos Satellites—1964
52 Cosmos Satellites—1965
2 planetary probes (Zond I and II)—1964
1 deep space probe (Zond III)—1965
2 planetary probes (Venera II and III)—1965

[c] Due to exhaustion of stabilization gas approximately 3 weeks after launch, OGO II has gathered data on an intermittent basis since that date.

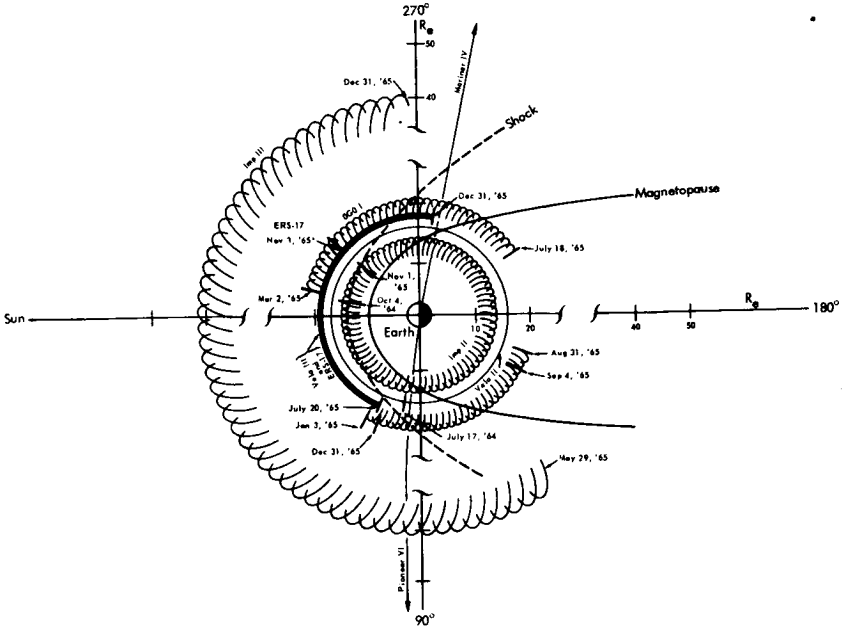

Figure 1.—**Orbits of various eccentric "near-equatorial" satellites and space probes shown in the equatorial plane.**

figure 3, and IMP or OGO I measurements near Earth have permitted the first direct study of the spatial extent of solar proton events. Simultaneous measurements in different parts of the magnetosphere will shed light on the propagation of geomagnetic disturbances through this region and their effects on the trapped-particle population of the radiation belts.

The scientific research during 1965 in the particles and fields area was built to a large extent on discoveries made during the first 6 years of the space age. A summary of this work was given in reference 1 (see also ref. 2) and a comprehensive bibliography in reference 3. On the basis of this work a new picture had emerged of the Earth's immediate environment and more generally of processes in the solar system and the galaxy. Plasma, both thermal and superthermal, was considered to play a dominant role in our present understanding. The major efforts in the discipline have been the study of the properties and behavior of a collisionless, magnetized plasma and its interaction with energetic charged particles. Plasma properties appear to be responsible for a large range of important processes which occur in the outer parts of stars such as the solar corona, in interplanetary space, and in galactic space. Both solar and galactic cosmic rays are

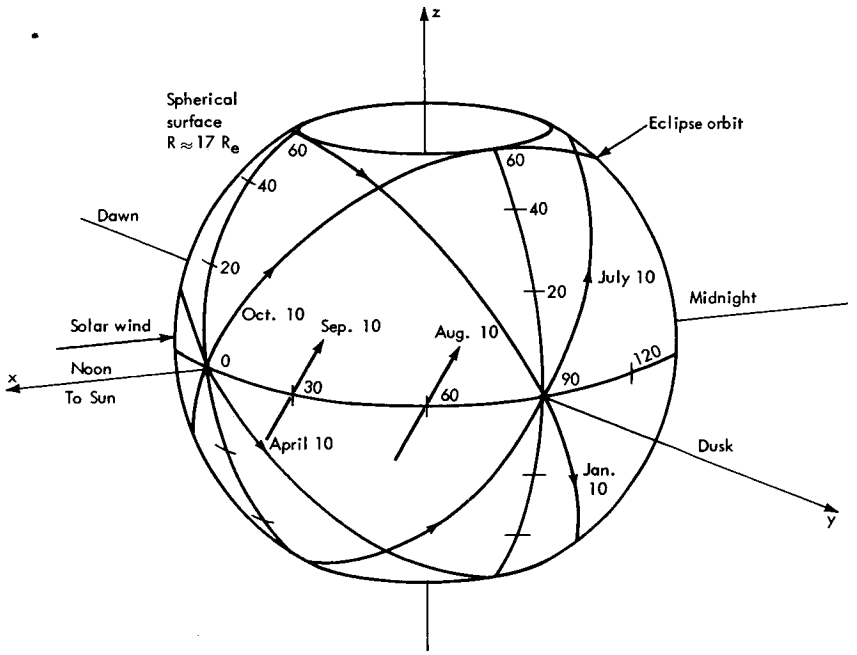

Figure 2.—**The points in space sampled by the Vela II satellite. The orbits repeat themselves once a year and over a year's time each satellite samples twice, points on a truncated spherical shell of about 17 R_e. (See ref. 53.)**

one manifestation of this; nonthermal celestial radio sources are another. At this time it appears that even the Van Allen radiation belts are controlled to a large extent by plasma processes. These general correlations are not directly obvious when one considers any one of the individual investigations which was conducted, but emerge primarily as the result of our attempts to find the physical processes by which these observations can be explained.

In contrast to earlier years of the space age, 1964 and 1965 fell during solar minimum, and many of the discoveries are particularly pertinent to this period. The solar wind with its embedded magnetic field was regular with characteristics which persisted for many solar rotations. Wilcox and Ness (ref. 4) identified a quasi-co-rotating magnetic field structure in the interplanetary medium which is closely related to the well-known "M regions." Streams of solar protons and alpha particles were discovered (refs. 5 and 6), with energies up to a few MeV, which recur regularly every 27 days and therefore appear to co-rotate with the Sun.

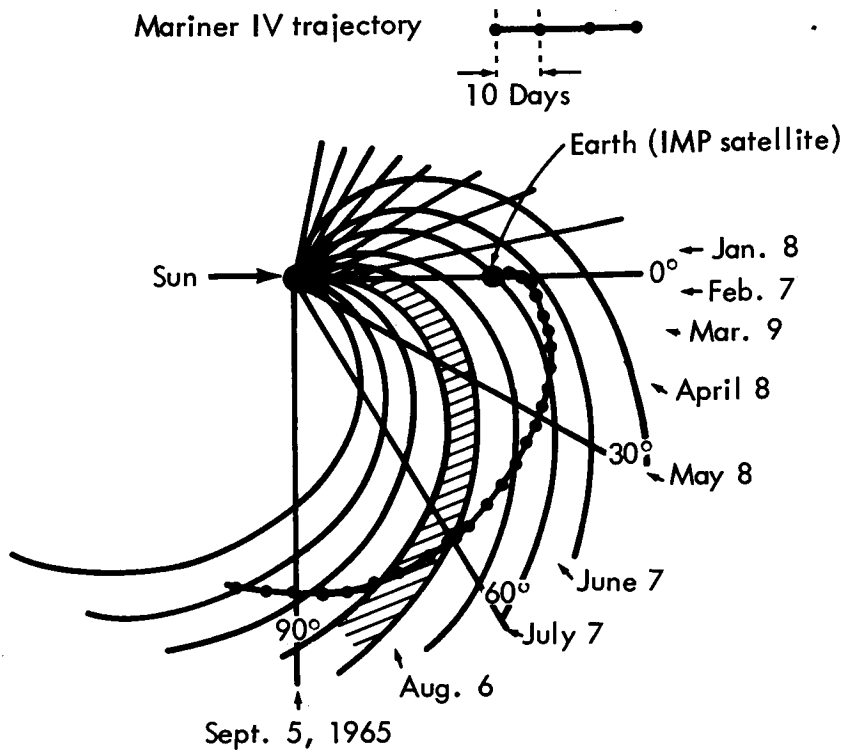

Figure 3.—**The Mariner IV trajectory with respect to the Earth-Sun system. The spiral lines, representing the idealized interplanetary magnetic-field configuration, are separated by an amount equivalent to 1 day of solar rotation. (See ref. 7.)**

The solar minimum also offered the opportunity to study the propagation of energetic solar protons through the undisturbed interplanetary magnetic field. Correlation between observations on Mariner IV and Earth satellites permitted O'Gallagher and Simpson (ref. 7) to demonstrate the anisotropic propagation characteristics of these events. Similarly, McCracken and Ness (ref. 8) have shown directly from angular-distribution measurements on Pioneer VI that magnetic field lines guide the propagation of these solar particles. On the basis of his Mariner IV measurements, Van Allen (ref. 9) discovered that electrons with energies between 40 and 160 keV are associated with some solar flares.

The penetration of galactic cosmic rays into the solar system was studied by many investigators. Periodic observations of galactic cosmic rays are now available from the last solar maximum to this minimum and their intensity modulation has been determined (ref.

10). The energy spectra and fluxes of galactic protons and alpha particles near solar minimum have been determined between 10 MeV and several GeV. Considerable progress has been made in identifying the mechanism by which galactic cosmic rays are modulated as they penetrate into the solar system (e.g., ref. 11). A modulation proportional to the product of particle rigidity and velocity has been derived from magnetic field parameters (ref. 12) which can explain many of these observations.

Further exploration of the magnetosphere has also been most fruitful. On the basis of his magnetic field measurements, Ness (ref. 13) demonstrated the existence of a neutral sheet in the geomagnetic tail. Observations with OGO I permitted the identification of several low-frequency waves in the magnetosphere. The significance of this discovery is not yet fully appreciated but it is expected that these or similar waves are intimately related to particle-acceleration, -trapping, and -dumping mechanisms. During the year a great deal of information was obtained about the fluxes, energy spectra, and the spatial and temporal variations of trapped particles. For instance, Frank (ref. 14) demonstrated the existence of diurnal variations in the outer raditation belt and in the same region Williams and Ness (ref. 15) found a 27-day periodicity in the electron population. Theories have been developed which explain particle dumping from the belts in terms of plasma instabilities (e.g., refs. 16, 17, and 18). No overall picture has emerged, as yet, which permits us to correlate a substantial fraction of these observations. It has, therefore, been decided to omit a discussion of this field; recent progress in this area is covered in reference 19.

Considerable work was also performed in the area of planetary magnetism. An upper limit was set on the magnetic dipole moment of Mars and a survey was performed with OGO II of the geomagnetic field. As yet only preliminary interpretations of these data are available and it has been decided to postpone a discussion of the implications of these results until a later date.

THE INTERPLANETARY MEDIUM

Co-rotating Sector Structures

In his original theory, Parker (ref. 20) discussed the supersonic expansion of the solar corona. This model describes a uniform radial flow of protons away from the Sun; embedded in this plasma are magnetic field lines which are directed along the so-called "garden hose" angle. Measurements with IMP I (Explorer XVIII) demonstrated (ref. 21) that the magnetic field varied considerably in both magnitude and direction, but that the average direction of the magnetic field falls

along the predicted direction. Further analysis of these data (refs. 22 and 23) revealed a correlation between the direction of the average solar photospheric magnetic field within 15° of the solar equator and observations near the Earth about 4½ days after meridional passage of a given region on the Sun. This delay corresponds to an average solar-wind velocity of 385 km/sec which falls into the range of velocities actually observed during quiescent periods.

The pattern of interplanetary magnetic field polarity is cyclic with a dominant period of 27 days, or the length of a solar rotation. Magnetic-field patterns on the surface of the Sun persist in their gross features for many solar rotations as might be expected from the persistence of sunspots. For each solar rotation, similar magnetic field configurations are then observed near the Earth with a delay of about 4½ days from the meridional passage of the region.

The autocorrelation of the magnetic polarity pattern shown in figure 4 (after Wilcox and Ness, ref. 4) indicates significant correlations for shorter time delays. These periods may be associated with a regular sector structure of solar field polarity. The sector structure observed in 1963 to 1964 with IMP I (Explorer XVIII) is shown in figure 5. It may be seen that this structure persisted with little change for at least three solar rotations. The co-rotation of the magnetic field pattern with the Sun may be demonstrated also with simultaneous observations performed on Pioneer VI and IMP III (Explorer XXVIII). The magnetic field vectors observed by Ness (ref. 24) at the two locations are shown in figure 6. The observations match almost point by point if account is taken of the time required for the pattern to rotate from the position of Pioneer to that of IMP.

The sector structure and recurrent properties are observed also in the plasma properties of the solar wind. Changes in proton density and velocity tend to coincide with sector boundaries (ref. 25). Detailed correlations between plasma and magnetic-field measurements on IMP I are in progress but have not yet been published because the analysis of the Faraday-cup data has been difficult (Bridge, private communication). The results from the Mariner II plasma measurements by Neugebauer and Snyder (ref. 26), shown in figure 7, demonstrate the existence of 27-day recurrent plasma events in 1962; recurrent increases in plasma velocity were generally preceded by peaks in plasma density. The occurrence of periodic peaks in plasma velocity is probably the immediate cause of the 27-day-recurrent geomagnetic storms which have been observed for years. As shown by Wilcox and Ness (ref. 4) these so-called "M region" storms coincide with the passage of certain of the sector boundaries of figure 5.

Protons and alpha particles with an energy of several MeV are emitted continuously from certain regions of the Sun. Since their

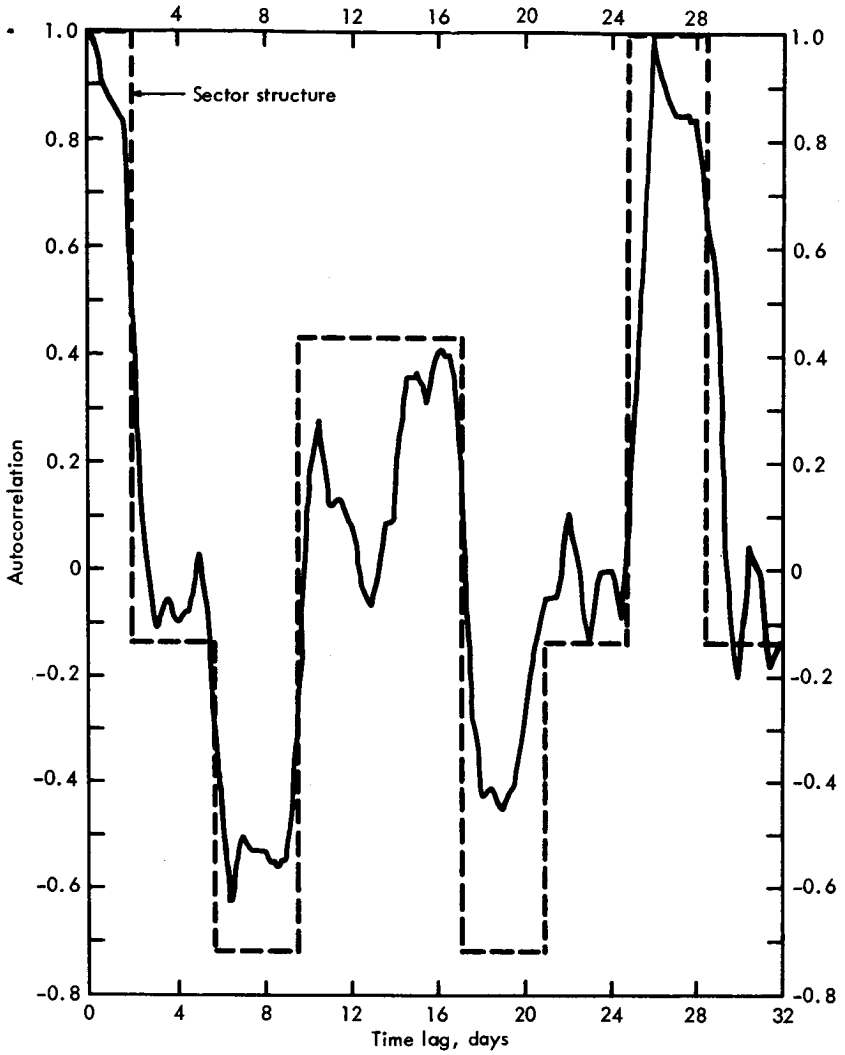

Figure 4.—Autocorrelation of the observed direction of the average interplanetary magnetic field (averaged over 3-hour periods). Data taken with IMP I from December 1963 to February 1964 were used. (See ref. 4.)

trajectories are guided by the magnetic field, these particles can be observed near Earth only once per revolution of the Sun. Observations of recurrent proton events by Bryant et al. (ref. 5) are shown in figure 8, and typical energy spectra of protons and of alpha particles are given in figure 9 (ref. 6). Conditions during solar minimum are

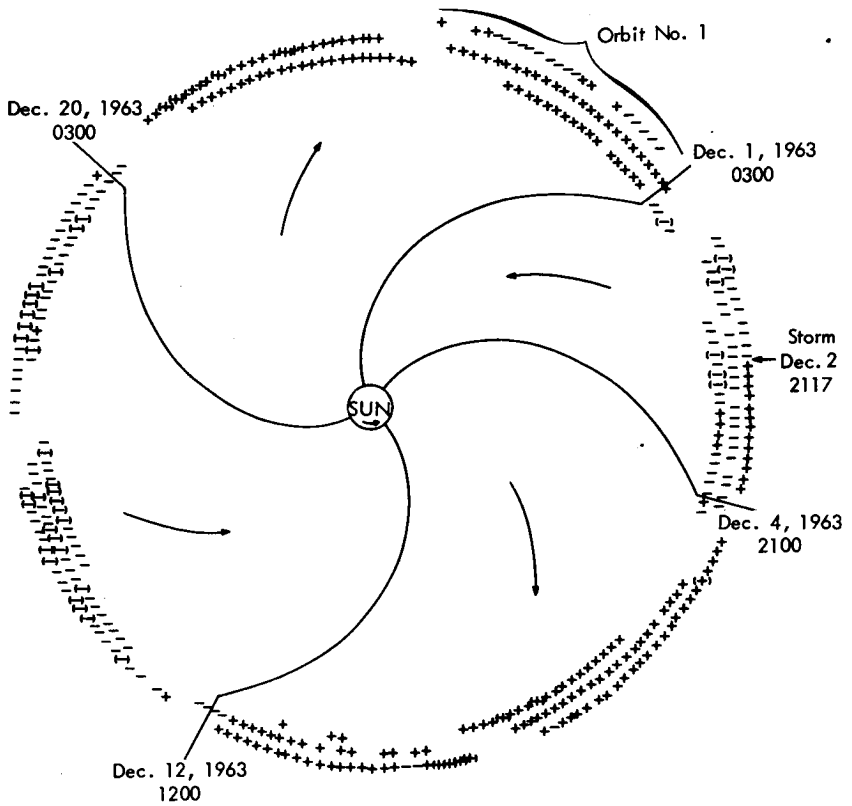

Figure 5.—Sector structure of the solar magnetic field, December 1963 to February 1964. The direction of the average experimental interplanetary magnetic field during 3-hour intervals is denoted by plus signs (away from the Sun) and minus signs (toward the Sun). Parentheses around a plus or minus sign indicate that the field direction fluctuated significantly. The solid lines represent magnetic field lines at sector boundaries. (See ref. 4.)

particularly favorable for discovering these phenomena because solar-flare-associated disturbances are relatively rare. It was possible to demonstrate directly the co-rotations of these energetic particle streams by correlating measurements performed on Mariner IV with those made near the Earth. Observations of this type were performed by O'Gallagher and Simpson (ref. 7) during August and September 1965 when Mariner IV was at the positions shown in figure 3. The event observed on August 27 at Mariner IV was seen 4.7 ± 0.3 days later at

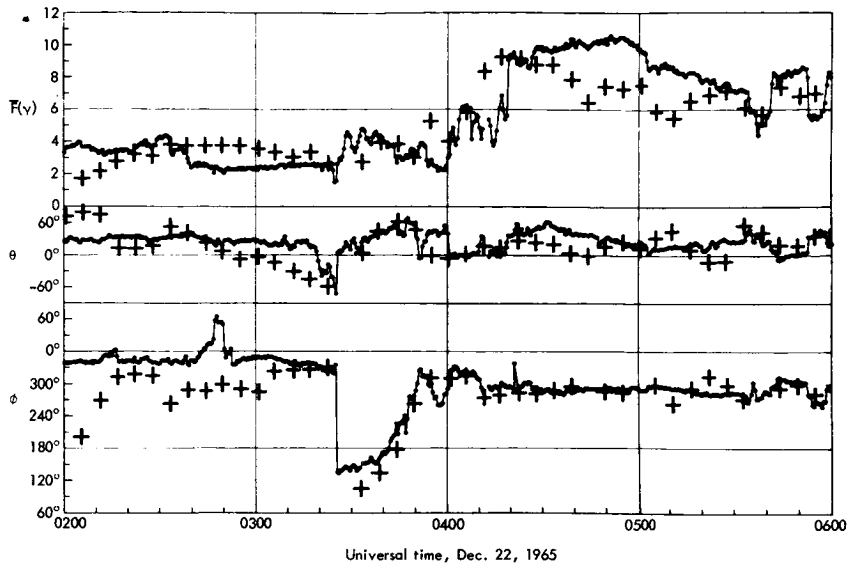

***Figure 6.*—Simultaneous measurements of the interplanetary magnetic field vector by Pioneer VI and IMP III in solar ecliptic coordinates. Each point for IMP III represents a 5.46-minute average. The IMP III points have been advanced by 57.5 minutes as compared with the predicted co-rotation time of 53 minutes. At the time these data were taken the satellites were separated by 1.3×10^6 kilometers and on opposite sides of the Earth. (See ref. 24.)**

Earth; the expected delay based on an average solar-wind velocity of 400 km/sec was 4.0 days. This region was observed again one solar rotation later on September 22, 1965, at Mariner IV and 5.5 ± 0.4 days after that at Earth; the predicted delay was 5.2 days.

Slowly evolving regions which persist for many solar rotations have been known to exist on the Sun from optical observations. A similar persistence has now been demonstrated for regions which modulate the average properties of the solar wind, its embedded magnetic field, and the emission of proton and alpha-particle streams. As yet, no one-to-one correspondence has been found between these regions and areas on the solar disk distinguishable on the basis of unique optical properties. It is to be expected, however, that future work in this area will not only lead to an understanding of the physics of the interplanetary medium but also provide a key to our understanding of the solar processes responsible for these phenomena.

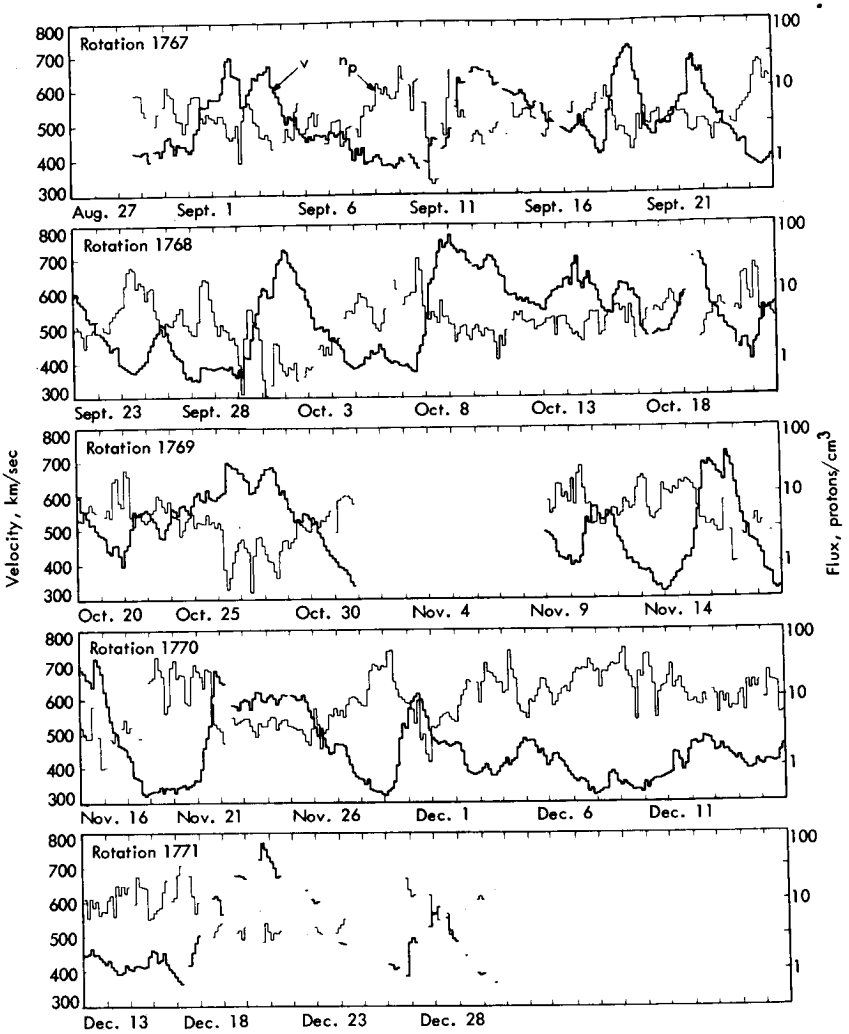

Figure 7.—Three-hour average values of plasma velocity and proton density (logarithmic scale) versus time. Density calculations were made on the basis of assumed radial solar-wind velocity with a correction for the aberration attributable to the spacecraft's motion. The time base is chosen to show the 27-day-recurrence features associated with solar rotation. (See ref. 26.)

Plasma Properties of the Solar Wind

The above findings have furnished us with a description of the average structure of the interplanetary magnetic field and the bulk flow of the solar-wind protons. On the other hand our knowledge of

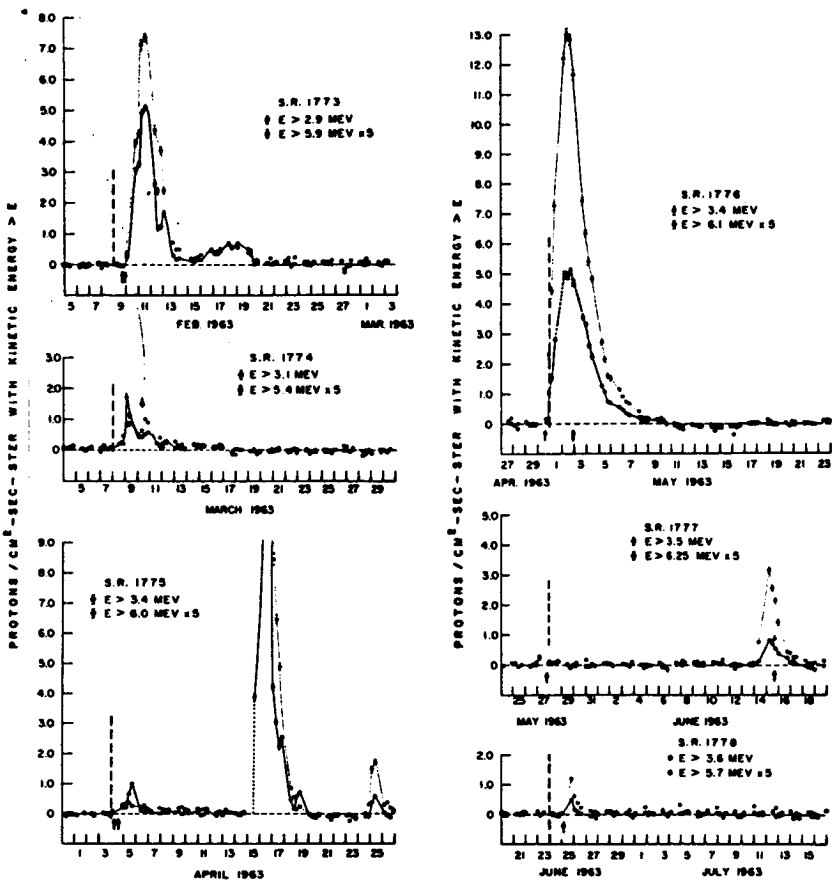

Figure 8.—**Integral proton intensities averaged over 6 hour periods are given for solar rotations Nos. 1773 to 1778. The arrows indicate sudden commencements followed by magnetic storms, the dashed line is a 27-day fiducial marker. Three flare-associated events occur in April and mid-June. (See ref. 5.)**

the instantaneous behavior and of the plasma properties of this medium is still very fragmentary. Although many observations of the solar-wind plasma have been performed, their interpretation has been most difficult. A complete description would require simultaneous measurements of the energies of the various particulate components of the solar wind as a function of their direction of motion as well as a knowledge of all time-varying electric and magnetic fields. In the absence of such a complete description, any one measurement has to be interpreted on the basis of assumptions which may not be entirely valid.

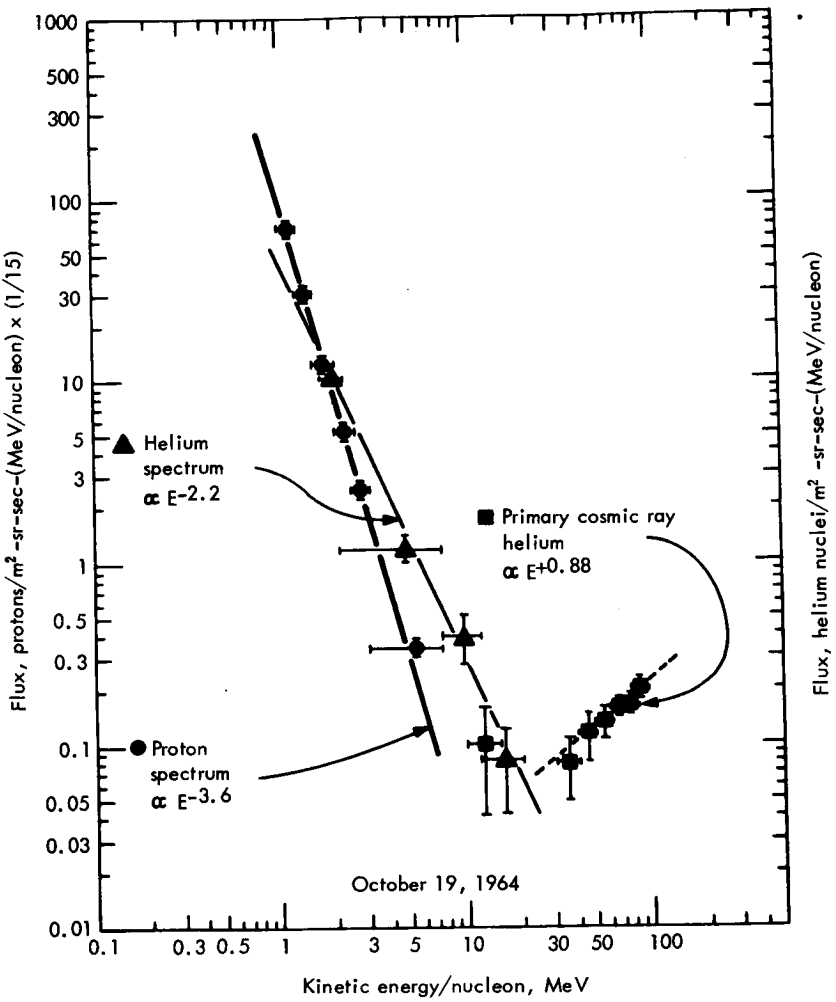

Figure 9.—**Differential proton and helium spectra observed as a 27-day co-rotating region passed OGO I. (See ref. 6.)**

Recent measurements on the Vela III and Pioneer VI spacecraft have permitted for the first time the reconstruction of detailed energy spectra as a function of arrival direction relative to the Earth-Sun line. Although instrumental effects have not yet been corrected for, it is clear from data shown in figure 10 (ref. 27) that the angular distributions are a function of proton energy. If these observations are interpreted in terms of a "plasma temperature" in the frame of reference moving with the solar wind, one has to conclude that the temperature measured parallel to the direction of motion is different from

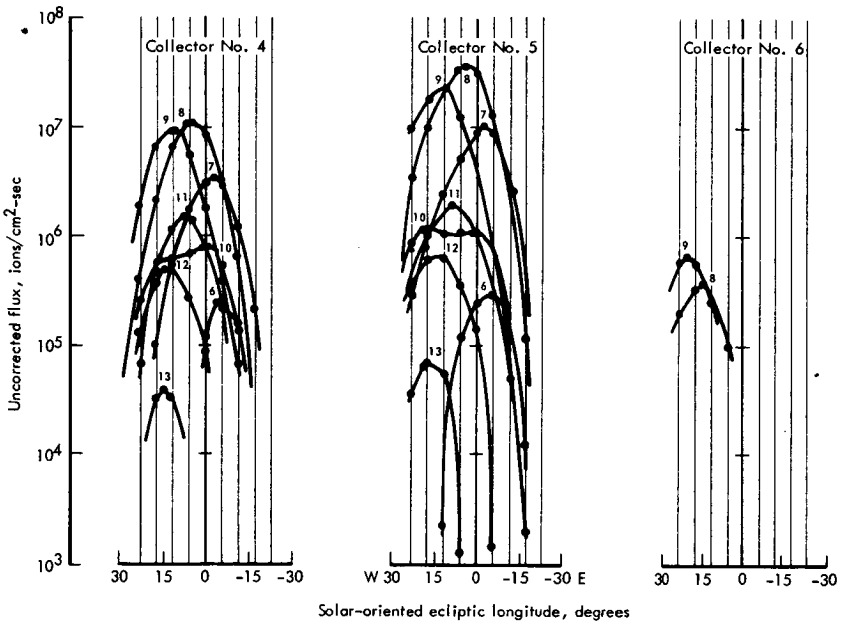

Figure 10.—**Pioneer VI Ames plasma probe angular distributions in ecliptic longitude observed on December 26, 1965, at approximately 2235 UT. Collectors 4 and 5 view 0° to 15° south and north ecliptic latitudes, respectively, and collector 6 views 15° to 30° north. Energy channels 6 to 13 are spaced logarithmically and cover the range from 0.5 to 4.5 keV. (See ref. 27.)**

that perpendicular to it. The data obtained with the electrostatic analyzer on Vela III lead to the same conclusion (ref. 28). With the instrument on Pioneer VI, it was also possible to show that the direction of bulk motion is not necessarily in the plane of the ecliptic. The data of figure 10 indicate a flow direction of 4° south ecliptic latitude. Considerable analysis has yet to be performed to correlate the out-of-the-ecliptic component of the plasma velocity with simultaneous magnetic field directions and to explain the nonradial flow of the plasma.

Although a large temperature anisotropy can exist at times, an average temperature value does provide a useful description. The large range of possible solar-wind temperatures is illustrated in figure 11 (ref. 29). The range, from 10^4 to $\sim 6 \times 10^5$ °K, is typical also of the Mariner II observations in 1962 which show a similar association of higher temperatures with larger bulk velocities.

The solar wind is clearly not in statistical equilibrium and one would therefore expect that various plasma instabilities can lead to the growth of waves. This problem has been studied extensively, for

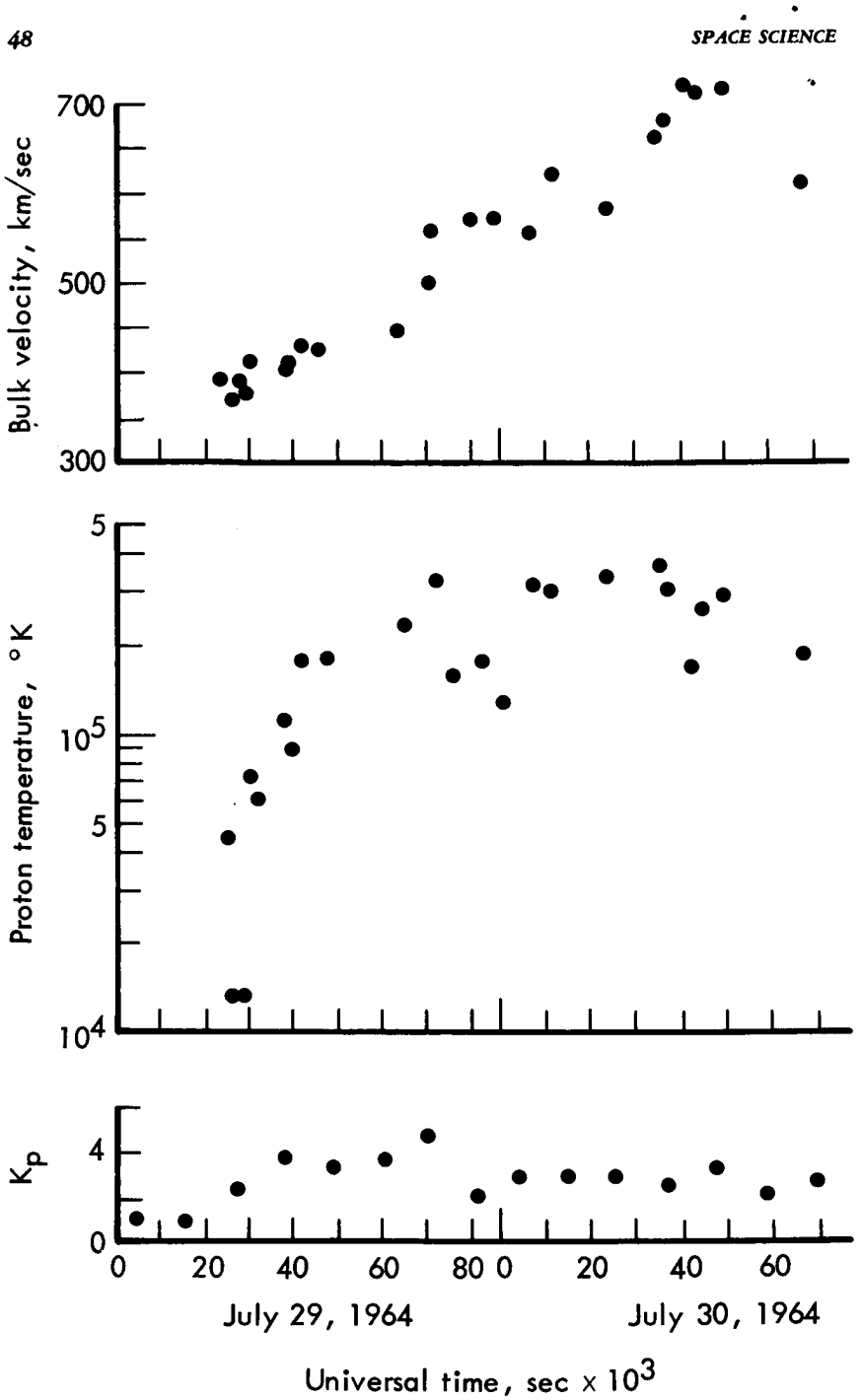

Figure 11.—Solar wind bulk velocity, proton temperature, and K_p index for July 29 and 30, 1964 (ref. 29).

instance Parker (refs. 30 and 31); Scarf (ref. 32); Scarf, Wolfe, and Silva (ref. 33); Dessler (ref. 34); and Lerche (ref. 35). In view of numerous possible wave modes, it has not yet been possible to identify the physically important processes. Coleman (ref. 36) has analyzed the low-frequency fluctuations of the Mariner II field measurements, and preliminary results from OGO I search coil measurements (see fig. 15) have been published by Holzer, McLeod, and Smith (ref. 37). Neither of these results is based on accurate measurements because the fluctuations were in both cases near the noise threshold of the instruments. Figure 12 shows typical results. The $\bar{B}$ power spectra of Coleman (ref. 38) have been multiplied by ω^2 to present them on the same basis as the search-coil data. Even though the measurements were not taken at the same time they are suggestive of a peak near the proton cyclotron frequency.

The velocity of the solar wind fluctuates between 300 and 700 km/sec; consequently, there are times when the faster moving plasma overtakes the slower. The embedded magnetic field preserves a sharp boundary between the two regions. If the relative speed is "subsonic," one would expect dissipation of the energy via plasma oscillation; on the other hand, at relative velocities above 100 km/sec a "supersonic" interaction occurs and a magnetohydrodynamic (MHD) shock forms

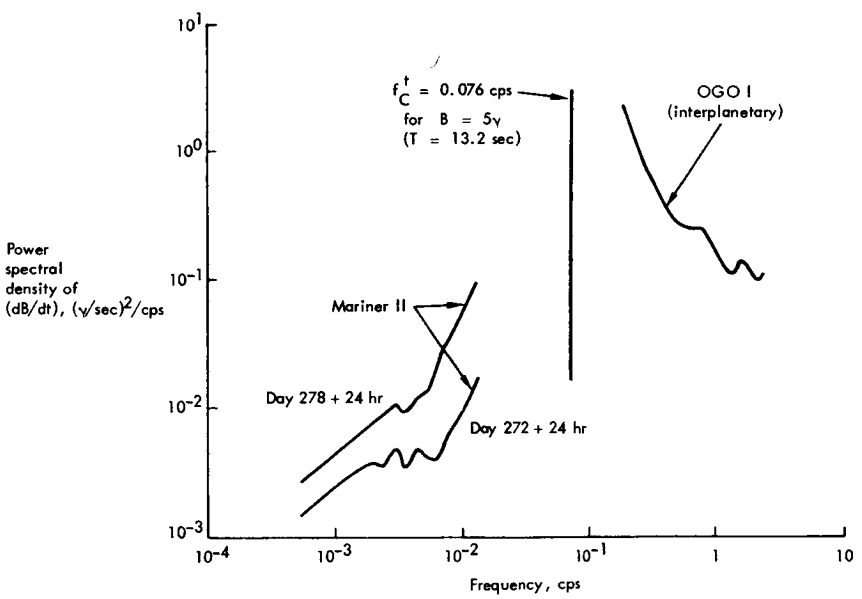

Figure 12.—Power spectra of the interplanetary magnetic field. The Mariner II results (ref. 36) have been converted to an equivalent search-coil spectral density. (See ref. 32.)

at the boundary. Colburn and Sonett (ref. 39) have analyzed Mariner II magnetic field data taken in 1962 when the Sun was more active. Even though the available data do not permit a complete description of all plasma parameters, they find strong evidence for the existence of MHD shocks. The interaction of such a shock with the magnetosphere has also been studied (refs. 40 and 41). During the coming solar maximum, around 1968, detailed investigations of this process will again become possible.

THE MAGNETOSPHERE

The Magnetosheath

The interaction of the Earth's magnetic field with the solar plasma has been a subject of scientific interest for several decades. Early satellite investigations confirmed many general features of the theoretical predictions of Chapman and Ferraro (refs. 42, 43, and 44). The magnetosphere has by now been established as a permanent feature of the Earth (fig. 13). The boundary occurs at approximately 10 Earth radii in the subsolar direction and is preceded by the magnetosheath or transition region and a detached bow shock. The fine structure of the solar wind is not well known, and consequently the interaction of the solar plasma with the unsymmetrical geomagnetic dipole presents a continuously changing dynamic situation whose exploration remains one of the prime objectives of the particles and fields discipline.

A significant departure from the Chapman-Ferraro model is, however, the collective behavior of the solar wind particles. Simultaneous observations of the undisturbed solar wind and of the transition-region plasma are shown in figure 14 (ref. 45). The solar wind consisted at that time of hydrogen, and presumably some doubly charged helium, with a bulk velocity of 720 km/sec and an approximate temperature of 2×10^5 °K. On the other hand, the OGO I spectrum, taken in the magnetosheath at a Sun-Earth-probe angle of 110°, represents a lower bulk velocity (434 km/sec) and a considerable spread in the velocity distribution (10^6 °K) with a substantial non-Maxwellian tail above 3000 eV which contains about 25 percent of the particles. Similar results were also obtained with the Vela satellites (ref. 46).

Direct particle-particle interactions cannot play a role in the redistribution of the energy because the plasma is collisionless. Therefore, it has been assumed that interactions occur via the embedded magnetic field. A search for such magnetic field oscillations has been made with OGO I. Since this spacecraft rotated about the Z axis with a period of 12 seconds, both the search-coil (fig. 15) and the flux-gate mag-

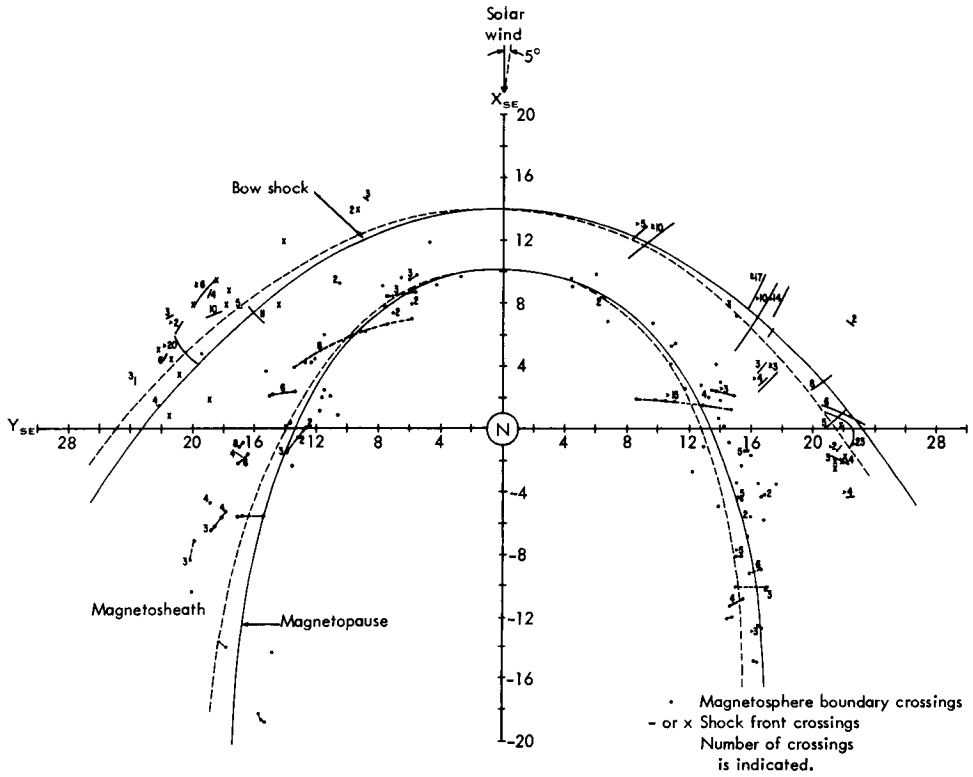

Figure 13.—Magnetospheric boundary and shock-front crossings in solar ecliptic coordinates as observed by Heppner (private communication) with OGO I. The solid and dashed boundaries were computed by Spreiter and Jones (ref. 102).

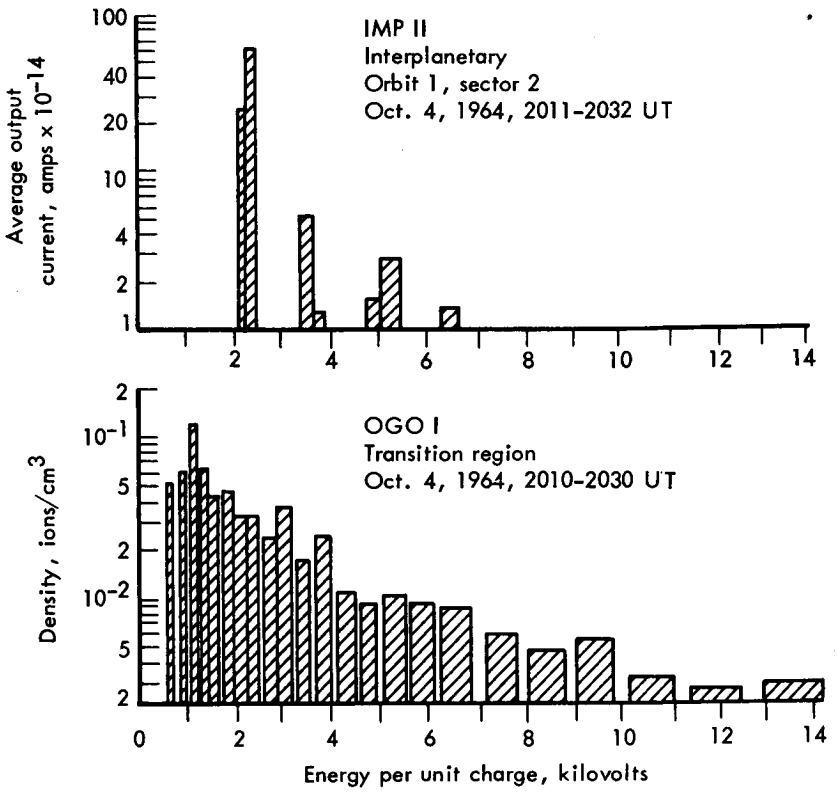

Figure 14.—**Simultaneous observation of the interplanetary solar wind with IMP II, and the plasma in the evening side of the magnetosheath with OGO I. The primary peak at 2300 to 3800 volts in the IMP II spectrum is attributed to protons and the secondary peak at 4950 to 6400 volts to doubly-charged helium nuclei. (See ref. 45.)**

netometer (fig. 16) measurements were modulated with that period. Both records also contain substantial components at higher and lower frequencies. The dominant frequency shown in figure 16 is 1 cps and was at a maximum just after the spacecraft entered the transition region at $00^h02^m10^s$. It should be noted that the oscillations do not cease abruptly at the shock front but decay gradually into interplanetary space. The interpretation of these results is still in a very preliminary state. Both particle and wave characteristics vary greatly between different times and different places in the magnetosheath. Thus, it cannot be expected that a coherent theoretical picture will emerge until after much more is known about this region.

The frequent occurrence of fluxes of energetic electrons is more evidence for particle-field interactions in the magnetosheath (refs. 47

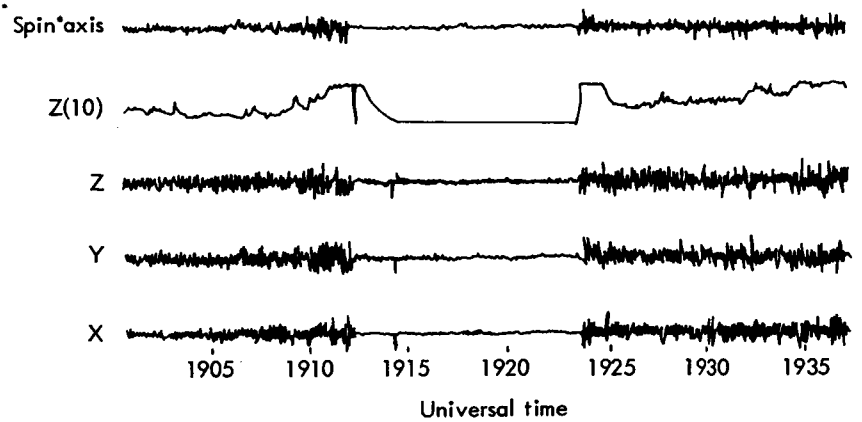

Figure 15.—**OGO I search-coil-magnetometer data from orbit 36, December 7, 1964. Multiple shock-boundary crossings on the outbound leg of the orbit at 1912 and 1924 UT and 14 R_e. The lowest three channels are the waveforms of each axis and are spin modulated. The linear combination of the three channels, shown in the top trace, should be independent of rotation. The *Z* (10) channel gives the response of one sensor, filtered with a low-pass filter of 10 Hz. (See ref. 37.)**

and 48). Locations at which they were found with IMP I are shown in figure 17. Their spectrum appears to be quite soft, with most of the electrons having energies below 40 keV. It would appear that these electrons were accelerated at or near the bow shock by an as-yet-undetermined mechanism. Fredricks, Scarf, and Bernstein (ref. 49) suggested acceleration by interactions with an ion-acoustic wave and Jokipii (ref. 50) suggested a Fermi mechanism.

The structure and stability of the bow shock and magnetospheric boundary are questions of considerable theoretical interest (refs. 35 and 51). Experimentally, it has been observed that the average boundary position is fairly stable, but there are considerable fluctuations of these boundaries between successive satellite passes. Observed boundary crossings with OGO I by Heppner (ref. 52) are shown in figure 13. The position of the bow shock, especially at large Sun-Earth-probe angles, appears to fluctuate considerably, and as many as 20 crossings, characteristic of a transition from bow shock to interplanetary medium, have been observed in one pass. The data shown in figure 15 are typical of these conditions; observations of characteristic magnetosheath conditions were interrupted for 11 minutes by interplanetary fields. Similar variations in the position of the bow shock were observed at different parts of the magnetosphere with the Vela II satellite (ref. 53).

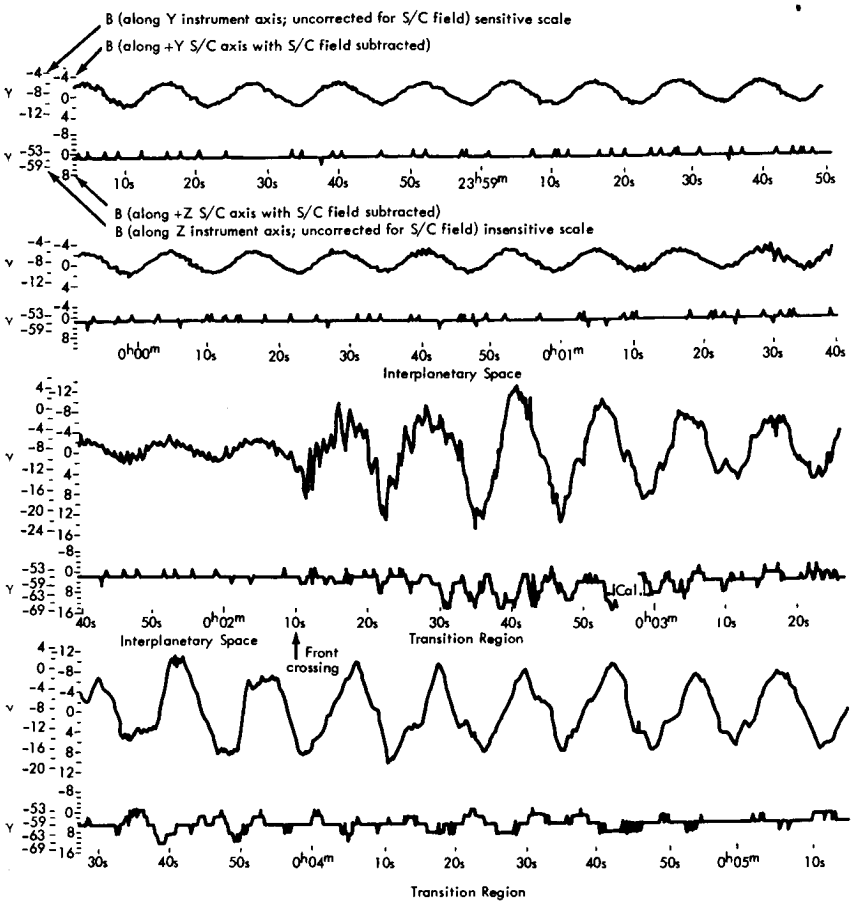

Figure 16.—**Magnetic field measurements during a bow shock front crossing with OGO I. The top trace gives the field perpendicular to the spin axis and the lower trace (Z axis) the field along the spin axis. (See ref. 52.)**

The interpretations of the apparent motion of the boundaries is difficult. Single satellite observations are inadequate to resolve different interpretations such as bulk boundary motion, hydromagnetic waves propagating locally along the boundary, or separate spatial regions with different characteristics. One case of a magnetospheric boundary motion was observed by Konradi and Kaufmann (ref. 54). They observed energetic trapped protons, which disappeared in a distance shorter than their cyclotron radius.

The Magnetospheric Tail

Theories of the magnetospheric tail were initially based on a few

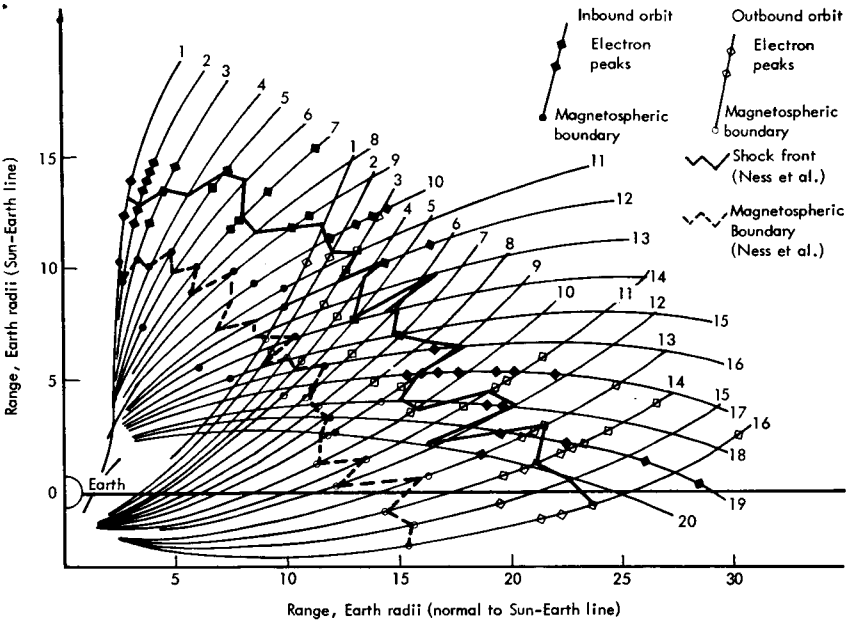

Figure 17.—**The trajectories of the first 20 orbits of the IMP I satellite are projected on the R–L_{sep} plane. The positions of the magnetospheric boundary are joined with a dotted curve and those of the bow shock are joined with a broken curve. The circular points show the boundary of the outer radiation belt and the diamond-shaped points show the positions of electron spikes in the vicinity of the bow shock. (See ref. 48.)**

isolated measurements (ref. 1). A much more complete mapping of the average field in this region has since then been performed with the IMP satellites and OGO I. Figure 18 shows the field directions and magitudes observed in the Southern Hemisphere by Ness (ref. 13). The region in which the tail field joins the dipole field was investigated by Cahill (ref. 55) and is shown in figure 19. These measurements have confirmed the general features of the theoretical models of the tail (refs. 56 and 31). In these theories, the existence of a neutral sheet had to be assumed to separate oppositely directed lines of forces near the magnetic equator. Direct evidence for the existence of this region has been obtained by Ness (ref. 13). A sample of his data is shown in figure 20. Starting from apogee at 31.4 R_e in the Southern Hemisphere until 16 R_e, the magnetic field is nearly steady and points most of the time in an antisolar direction ($\phi=180°$). At 16 R_e, however, within a distance of about 600 kilometers the field direction reverses ($\phi\sim0°$). The field strength goes almost to zero during this reversal.

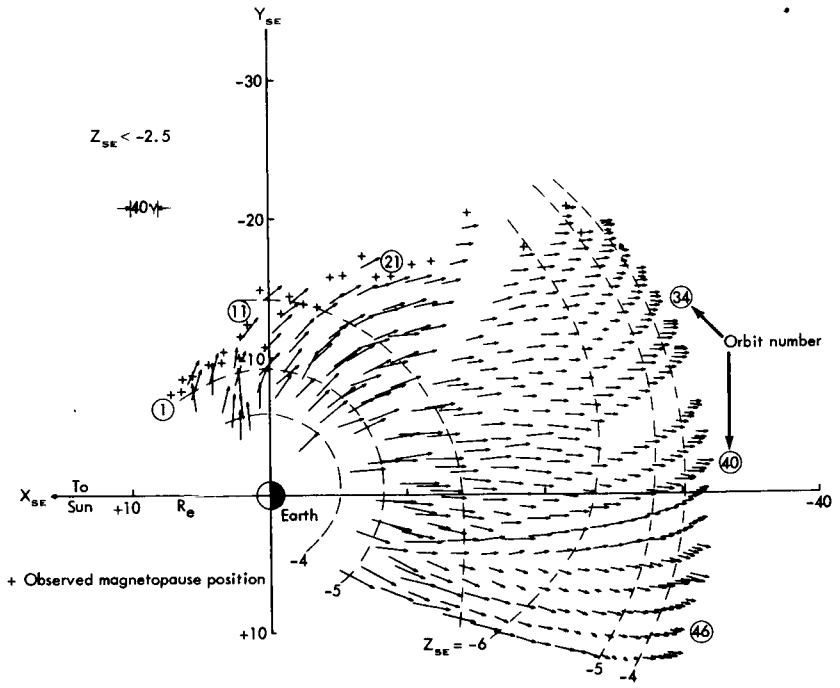

Figure 18.—**Summary of the distortion of the geomagnetic field in the Southern Hemisphere tail region from IMP I. Dashed lines give distances below the ecliptic plane in Earth radii (Z_{se} coordinates). Vectors are from hourly average components X_{se} and Y_{se} in solar ecliptic coordinates. (See ref. 13.)**

These field reversals have been observed consistently and may be considered an established feature of the magnetospheric tail.

A direct observation of the plasma making up the neutral sheet has been more difficult. Bame and coworkers (ref. 57) find omnidirectional fluxes of 10^8 to 10^9 electrons/cm^2/sec in an energy interval from 0.35 to 20 keV (fig. 21). These appear in the general location of the neutral sheet but extend over a thickness of 6 R_e or more at the 17 R_e geocentric distance observed with the Vela II satellites. The energy distribution is quasi-thermal with an energy density which is comparable to that of the expected magnetic field (ref. 58).

Shown in figure 21 is also the periodic appearance of more energetic electrons above 45 keV. Similiar "islands" of electrons above 40 keV have been observed by Anderson (ref. 59). The occurrence of these electron islands is not confined to the location of the neutral sheet. Figure 22 shows the distribution of locations where these fluxes were observed, and they fall as likely as not outside the region occupied by

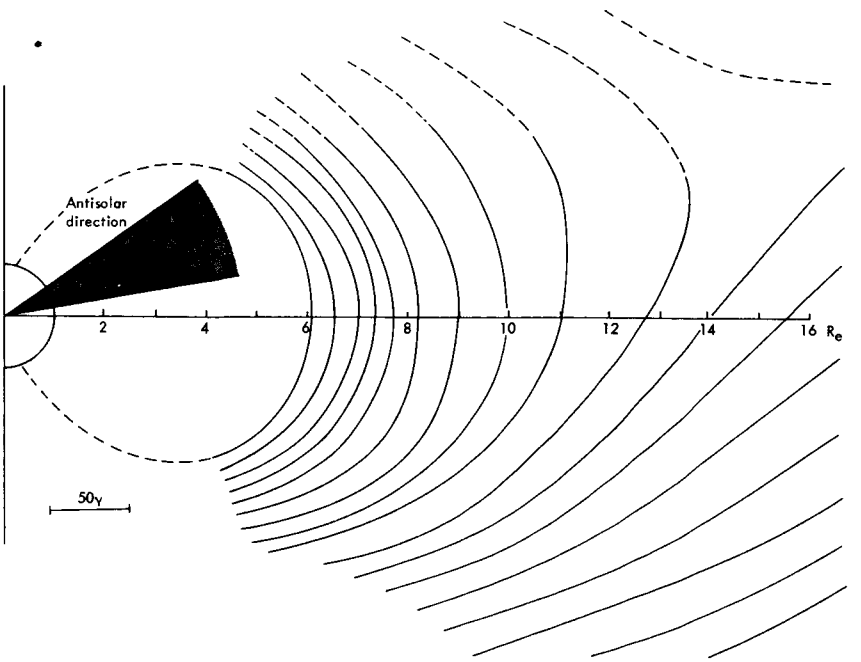

Figure 19.—**Schematic representation of magnetic lines of force in a meridional plane derived from vector field measurements performed with Explorer XIV, January 27 to February 20, 1963. (See ref. 55.)**

the neutral sheet. Coon (ref. 46) found some evidence that these fluxes occur preferentially on the dawn side of the magnetosphere, and Anderson (ref. 59) finds a frequency of occurrence which decreases with increasing distance from the Earth.

A detailed correlation has been performed between the appearance of electrons above 40 keV and changes in the magnetic field (ref. 58). The appearance of these electrons is invariably associated with a strong diamagnetic effect. The contribution of the >40 keV electrons to this effect is, however, only a few percent. Therefore, it may be presumed that these electrons are the high-energy component of a hot plasma of the type found by Bame and coworkers (ref. 57). The observations are consistent with local acceleration of the particles. The rapid onset is suggestive of plasma instabilities, but as yet no experimental observations have been made of plasma waves which should be generated in the process.

Relatively little is known about the geomagnetic tail beyond 30 to 40 R_e. Dessler (ref. 60) reasons that the geomagnetic field, plasma, and hydromagnetic radiations inside the magnetospheric tail are adequate to oppose the transverse solar wind pressure and prevent the

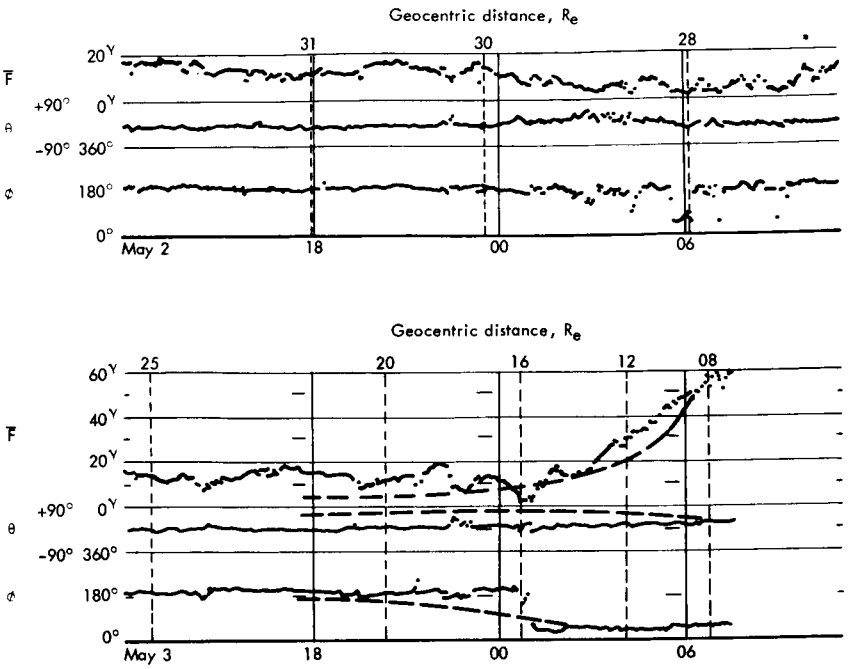

***Figure 20.*—Magnetic field data from inbound orbit 41 of IMP I, May 2 through May 4, 1964. Throughout most of this time interval the magnetic field is antisolar, although at a geocentric distance of 16 R_e the magnetic field abruptly reverses direction at the same time that it becomes very weak or zero. This spatially limited region is identified as a neutral sheet in the Earth's magnetic tail. (See ref. 13.)**

closing of the magnetospheric tail before the charge-exchange termination of the solar wind. This represents a tail length of 20 to 50 AU (10^6 R_e). On the basis of magnetic field line tying and the resultant motion of an interplanetary magnetic field line, Dungey (ref. 61) argues that the length of the tail approximates the distance traveled by the solar plasma in the time during which an individual line is attached. This corresponds to a length of approximately 10^3 R_e. The trajectory of the Mariner IV spacecraft passed through the presumed region of the magnetospheric tail at a distance of 3300 R_e in early 1965. Thin-window Geiger-Mueller tubes flown by the University of Iowa (ref. 62) recorded the presence of energetic ($E>40$ keV) electrons out to 23 R_e in the morning fringe of the magnetosphere. During the seven days which Mariner IV spent between 1° and 5° of the presumed center line of the magnetospheric tail, the Geiger-Mueller tubes failed to detect statistically significant electron fluxes which could be attrib-

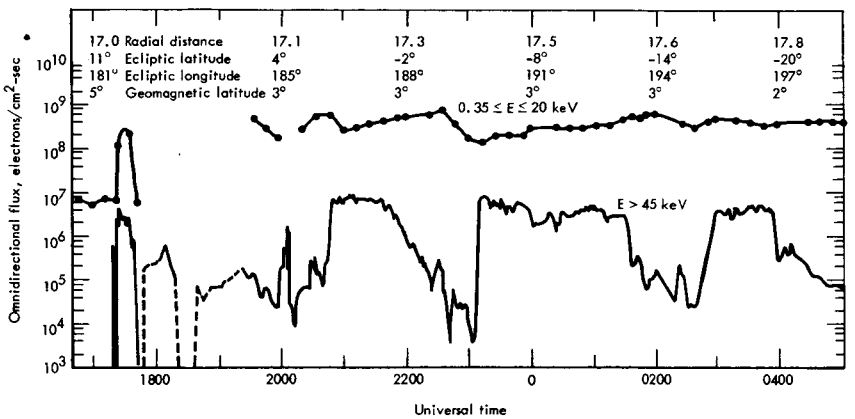

Figure 21.—**Time history of omnidirectional fluxes of electrons for a portion of a pass through the tail of the magnetosphere with the Vela II satellite. Electron flux with $0.35 \leq E \leq 20$ keV is measured with an electrostatic analyzer; flux with $E > 45$ keV is measured with a thin-window Geiger counter. Radial distance, ecliptic latitude and longitude, and geomagnetic latitude of the spacecraft are given at the top of the graph. Analyzer data are not available for those times without points. (See ref. 57.)**

uted to the magnetospheric tail. E. J. Smith (private communication, February 24, 1965) also reported no significant magnetic effects from the Mariner IV magnetometer during this period which could be related to the magnetospheric tail. Unfortunately, these results are not quite conclusive because the solar wind can have a velocity component out of the plane of the ecliptic (ref. 27). The Mariner IV spacecraft may, therefore, have passed either above or below an extended tail (see also ref. 63).

SOLAR ENERGETIC PARTICLES

We know that energetic protons are produced in certain flares and then propagate through the interplanetary medium to beyond the orbit of Earth. The determination of the acceleration mechanism and the propagation paths continues to be an active area of research. During this solar minimum it has been possible to study isolated solar flares and the subsequent propagation of the energetic protons through the undisturbed interplanetary medium. In their original analysis, McDonald and coworkers (ref. 64) showed that the time history of the proton flux from the September 28, 1961, flare can be fitted by a three-dimensional diffusion equation. On the other hand, the average magnetic field in the interplanetary medium is oriented along an Archimedes spiral and must clearly influence the propagation of

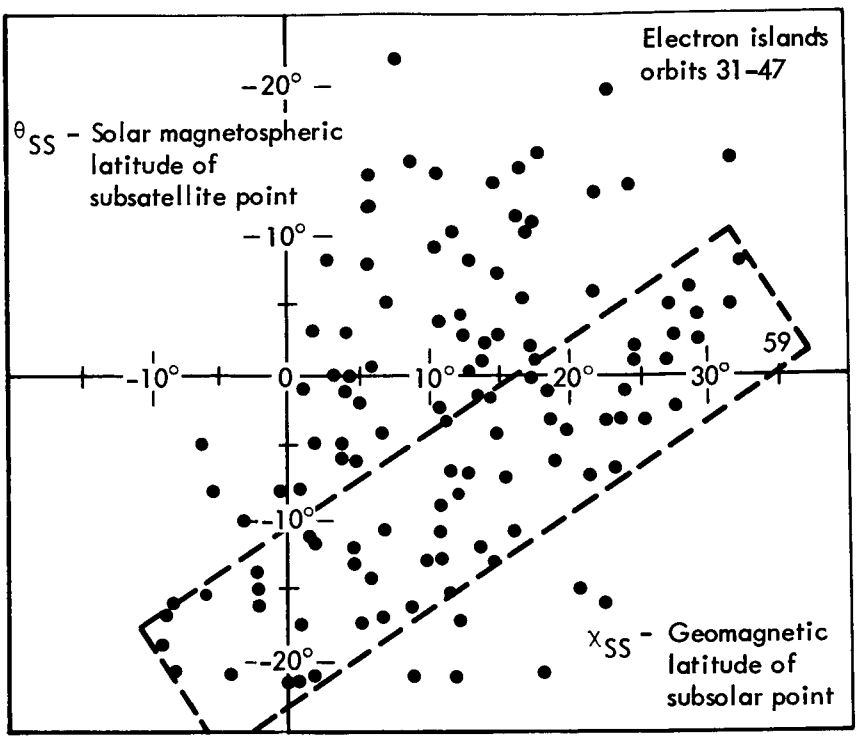

Figure 22.—**Distribution of islands of electrons with energies above 40 keV observed with the IMP I satellite in the magnetospheric tail. Had the particle fluxes preferred the neutral sheet, the points would have been grouped about the X_{ss} axis. (See ref. 59.)**

charged particles. Various attempts have therefore been made to arrive at a more realistic model (refs. 11, 65, and 66). Each of these theories appears to fit some observations better than others, and in spite of the substantial advances made last year a completely consistent picture has not yet emerged.

Parker (refs. 11 and 67) has studied the paths and energy losses of particles as they propagate through the interplanetary medium. He used a synthetic magnetic-field line constructed from IMP I measurements (see fig. 32). He found that the decay rate of solar-proton fluxes near the Earth should be the same as for isotropic diffusion but changes from $t^{-3/2}$ to $t^{-3/4}$ at larger distances from the Sun. A modification of the original energy spectrum is predicted because of adiabatic deceleration in interactions with the moving magnetic field of the solar wind.

A more empirical approach has been adopted by Fibich and Abra-

. ham (ref. 66). They use the results of Bryant et al. (ref. 68) which can be interpreted as showing that the propagation of solar protons is completely rigidity-independent. Figure 23 shows the time history of solar protons of various energies as a function of the distance they

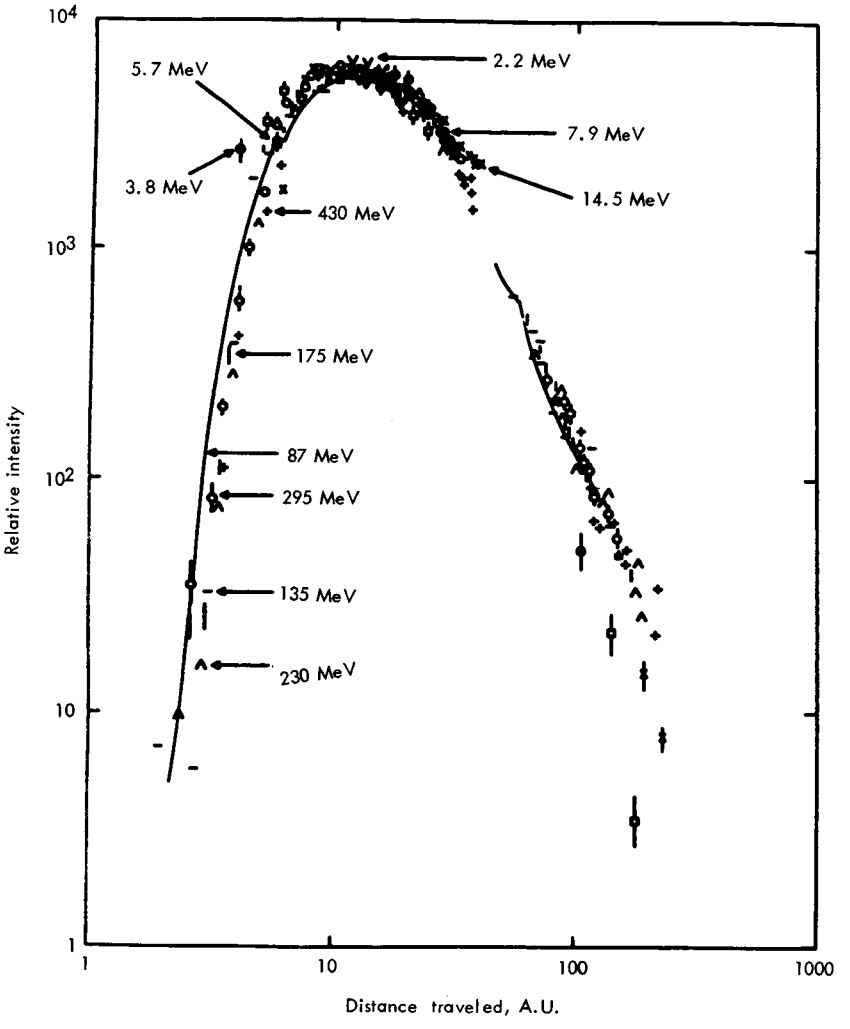

Figure 23.—Relative intensity of solar protons from the September 28, 1961, event versus distance traveled. The distance is computed for each energy component by taking the product of the corresponding particle velocity and the time from event to observation. The intensities are scaled to give the best fit to a common curve. This fit occurs over a dynamic range in energy of a few hundred, a velocity range of 14, and over a time duration of several days. (See ref. 68.)

traveled before arriving at the Earth (the assumption has been made that all protons are produced nearly simultaneously at the time of the solar flare). In this event, protons appear to travel on the average the same distance regardless of their energy: 2.2 MeV to 430 MeV. Other events (fig. 24) have similar propagation characteristics. These

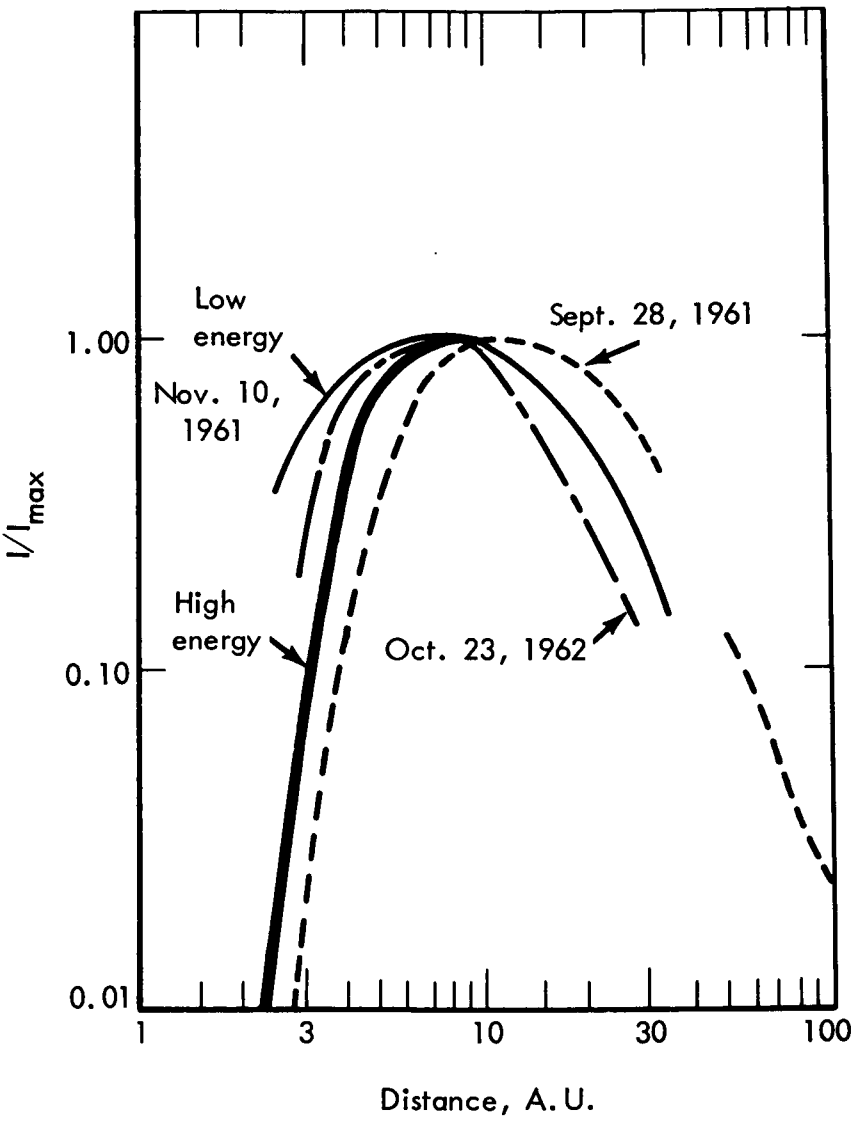

Figure 24.—Propagation curves, like those of figure 23, for three events. These curves show the distributions in the distances traveled by solar protons in reaching the Earth. (See ref. 68.)

results are particularly surprising since it is to be expected that the interplanetary medium changes significantly between the arrival of the highest energy particles and the time the lower energy group arrives. Another basic assumption in the analysis of Fibich and Abraham is that there are enough small-scale irregularities in the magnetic field to act as scattering centers. A diffusion-model analysis based on these propositions leads to the conclusion that the short-time behavior is of the one-dimensional diffusion type followed by a transition to isotropic diffusion.

Experimental observations of the anisotropy of the solar proton flux near Earth can provide another key to the propagation mechanism. No such measurements are available for the 1961 events, but they have now been performed with Pioneer VI on the small solar-proton event of December 30, 1965 (refs. 69 and 70). The observed anisotropy of 13 MeV protons, shown in figure 25, persisted more or less throughout the event. The correlation (ref. 8) between the direction of the magnetic field and the solar-particle anisotropy shown in

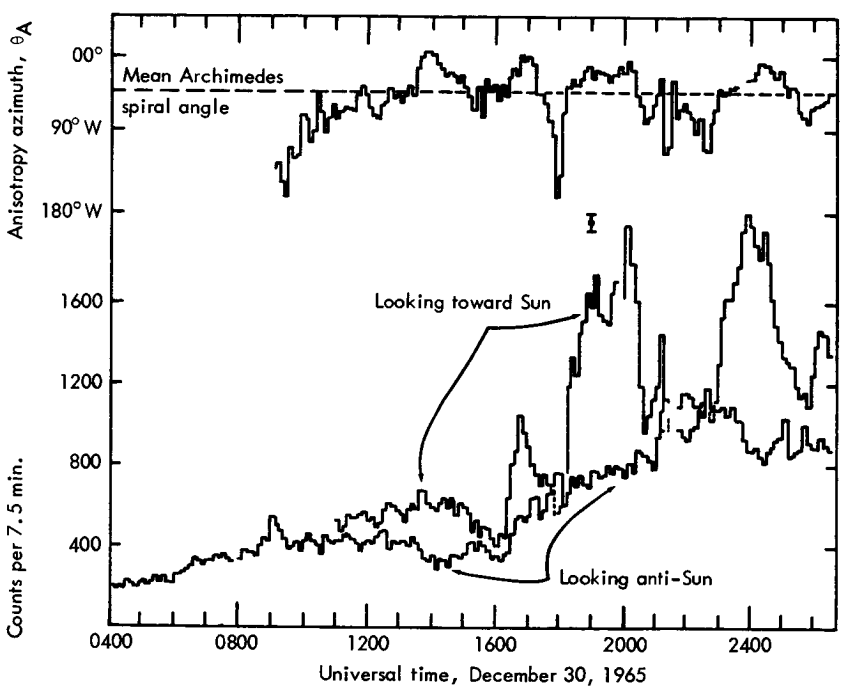

Figure 25.—Counting rates of 13 MeV solar protons coming from solar and antisolar directions and the azimuth of the solar cosmic-ray anisotropy (θ_A) during initial stages of the flare effect that commenced on December 30, 1965. (See ref. 69.)

figure 26 demonstrates clearly that the preferred propagation direction is along the field line. These observations can be interpreted readily in terms of Axford's model (ref. 65). He postulates nearly isotropic diffusion near the Sun and then almost free streaming along the field lines to the point of observation.

Simultaneous observations at several locations spaced around the Sun will be most helpful in providing a firmer basis for understanding the nature of the particle-diffusion process. Initial observations of this type were performed with Mariner IV and near-Earth satellites

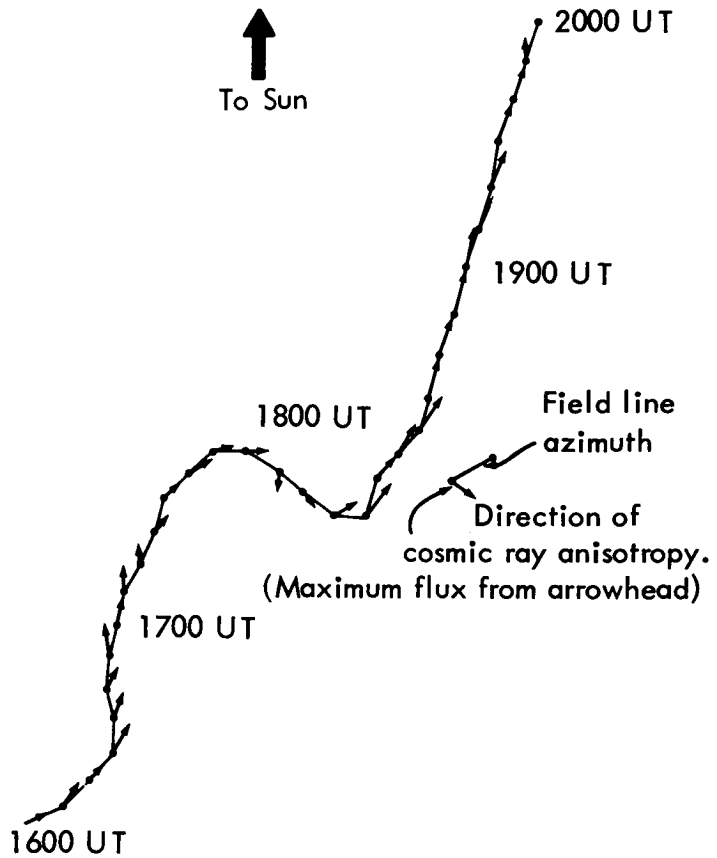

Figure 26.—The magnetic field and cosmic-ray azimuths during the interval 1600 to 2000 UT, December 30, 1965 (Pioneer VI). Note the very close correspondence of the two azimuths during the abrupt change in direction around 1800 UT. Magnetic field and cosmic-ray anisotropy directions projected into ecliptic (viewed from north ecliptic pole). (See ref. 8.)

(refs. 7 and 71). O'Gallagher found certain events which were observed at only one of the two locations. For instance, protons from the west limb flare on August 16, 1965, were observed near Earth, but not at Mariner which was on a different magnetic field line as shown in figure 2. In two cases, flare-associated protons were observed first at the location of Mariner IV and later near the Earth; however, the delay was shorter than the time required for the co-rotation of field line to the Earth. In one case it was 0.7 ± 0.2 day versus a 1.9-day co-rotation time. Since the 27-day-recurrent proton streams showed the proper delay for co-rotation (see "The Interplanetary Medium," p. 42), it would appear that cross-field line diffusion is a significant process in the propagation of solar-flare protons.

Although no unique picture has yet emerged to explain all observations, a number of conclusions which apply to small solar proton events near solar minimum can be reached. Near the Earth, low-energy protons are guided by magnetic field lines, and diffusion through interplanetary space is therefore anisotropic. Protons following solar flares diffuse across field lines to a greater extent than protons from 27-day-recurrent regions, and the propagation conditions for solar protons appear to be remarkably constant for an extended period of time. Although all of these conclusions will not apply to the more disturbed interplanetary conditions near solar maximum, they are important in providing an initial understanding of the propagation of energetic charged particles through the magnetized plasma between the Sun and the Earth.

Several other properties of solar cosmic rays have been investigated. One of these is intensity modulations of the order of 20 percent, with periods around 1 hour; these modulations affect all particle energies simultaneously (ref. 68). The lack of energy dispersion requires that the modulation occur near the point of observation. The regularity of the modulation period is suggestive of wave-particle interactions.

In addition to the proton component of solar flare events, other particles have been studied. A survey of data on the medium and heavy components of solar cosmic rays by Biswas and Fichtel (ref. 72) has established that the ratio of helium to medium nuclei does not vary between flares. On the other hand, the relative intensity of protons and alpha particles is not fixed. An upper limit has been placed on the flux of solar neutrons during solar minimum (ref. 73). The average flux is less than 0.01 neutron/cm^2/sec and no flare-associated neutron bursts were found between October 17, 1963, and mid-1965. In general, an upper limit of 1.5×10^3 neutrons/cm^2 can be placed on the integrated flux from any event which occurred during this period except

for the February 5, 1965, flare. In that case neutrons would have been masked by the early arrival of solar protons.

Observations of solar radio and X-ray bursts have furnished substantial evidence for the acceleration of electrons during solar flares, but their observation near the Earth has been conclusive in only one case (ref. 74). In that event, electrons with an energy of 100 to 1000 MeV were observed after a succession of three class 3 and 3+ flares on July 18, 20, and 21, 1961. Low-energy electrons around 40 keV which appeared to be of solar origin had been observed at various times with Earth satellites but in no case was it possible to demonstrate conclusively that these electrons could not have been generated in the magnetosphere. Observations from Mariner IV permitted the unique identification of several events in which electrons with energies of about 40 keV are associated with solar flares (ref. 9). The response of various detectors to the June 5, 1965, flare is shown in figure 27. The flux increase is largely a result of electrons with energies between 40 and 150 keV. This and similar events have subsequently been identified also from data taken near the Earth with the IMP I, IMP III, and OGO I satellites (ref. 75). For the 12 events investigated, Anderson finds a delay time of 23 to 55 minutes between the X-ray emission and electron arrival at Earth; the flares are relatively small, 1− to 1+, and in at least two cases the electron flux was anisotropic. Although it has been established that these events are associated with solar flares, the electron acceleration mechanism has not been identified. According to Parker (ref. 76), particles can be accelerated to these energies at shock boundaries between different plasma regions. It is therefore quite possible that the low-energy electrons have their origin at some distance from the site of the actual flare. The short time delay before onset, however, would not permit the plasma disturbance to travel a large distance before the initial electrons are accelerated.

GALACTIC COSMIC RAYS

Galactic cosmic rays have been studied for several decades but we are only now beginning to obtain the detailed data which should eventually permit a quantitative understanding of cosmic-ray sources and of modifications of their atomic composition and energy spectra during their propagation through space. An attempt to treat this overall problem and deduce the observed rigidity spectra has been made by Kaplon and Skadron (ref. 77). In arriving at the observed spectra, however, a number of assumptions had to be made; their study is most informative, but it is unlikely that the model is correct in all details. More directly accessible to theoretical study and experimental verification is the penetration of galactic cosmic rays into the solar system.

Under the assumption that the flux in the galaxy remains constant over periods long compared with a decade, it is possible to study directly solar modulation and explain it in terms of changes in the interplanetary medium.

Total-flux measurements with ion chambers are now available for a complete solar cycle and are shown in figure 28. These observations by Winckler and coworkers (refs. 10 and 78) reflect primarily changes in the flux of 1.7 to 2.7 GeV protons. The inverse correlation between sunspot numbers and cosmic-ray flux should be noticed as well as the delayed response of the cosmic-ray flux to

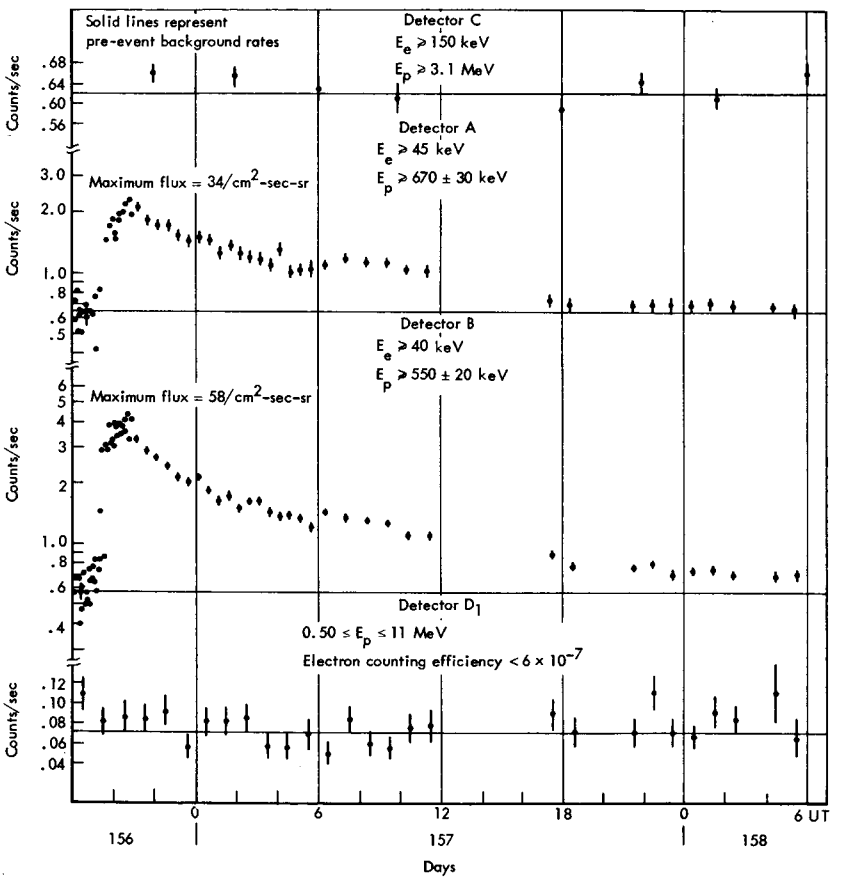

Figure 27.—Data from several detectors for the June 5 to 7, 1965, solar electron event. Counters sensitive to electron energies above 150 keV or protons above 0.50 MeV show no effect. Both counters sensitive to 40 to 150 keV electrons register the event. (See ref. 9.)

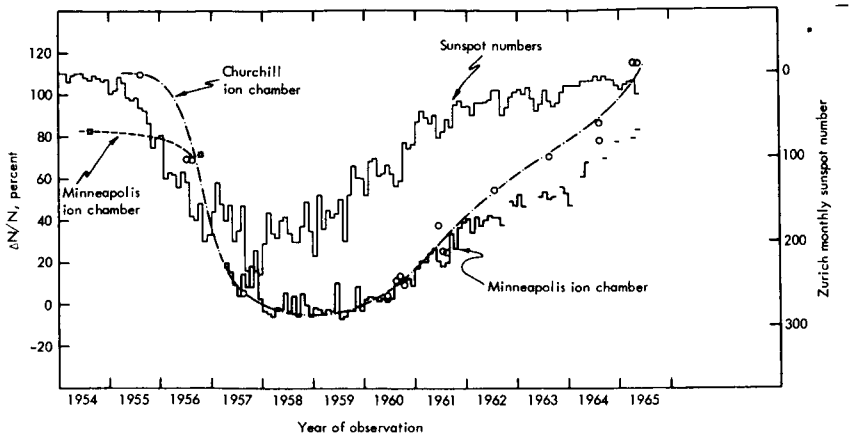

***Figure 28.*—Variation of the balloon ion-chamber rates and the sunspot numbers during the last solar cycle (1954 to 1965). Ion chamber measurements prior to 1955 are due to Neher. (See ref. 78.)**

changes in solar activity. An explanation of this modulation has been developed in terms of diffusion theory (e.g., refs. 11, 67, and 79). The various theories differ in the predicted dependence of the attenuation on particle energy and rigidity. It may be postulated that the galactic spectrum of protons differs from that of doubly-charged helium nuclei only by a normalization factor. A direct comparison of the spectra of these two types of particles as observed near the Earth would then provide a direct measure of the change. Energy spectra have been obtained for low-energy protons and alpha particles from 1963 to 1965 with the IMP satellites (Explorers XVIII, XXI, and XXVIII), and typical alpha spectra are shown in figure 29. The source of flux of particles below the minimum in the curve at about 15 MeV per nucleon has not been definitely identified. In this energy region are seen increased helium fluxes from solar flares and "M regions" and it may be assumed (ref. 80) than a small flux of solar origin remains even during periods of no solar activity.

A direct comparison can be made between the energy spectra of protons and of alpha particles for observations conducted at the same solar modulation. It may be seen from figure 30 that the two spectra are almost identical below several hundred MeV if they are plotted on a kinetic-energy-per-nucleon basis and the flux levels are normalized by a factor of 5.7. If the spectral shape of the proton flux in the galaxy is the same as for alpha particles, then the identical

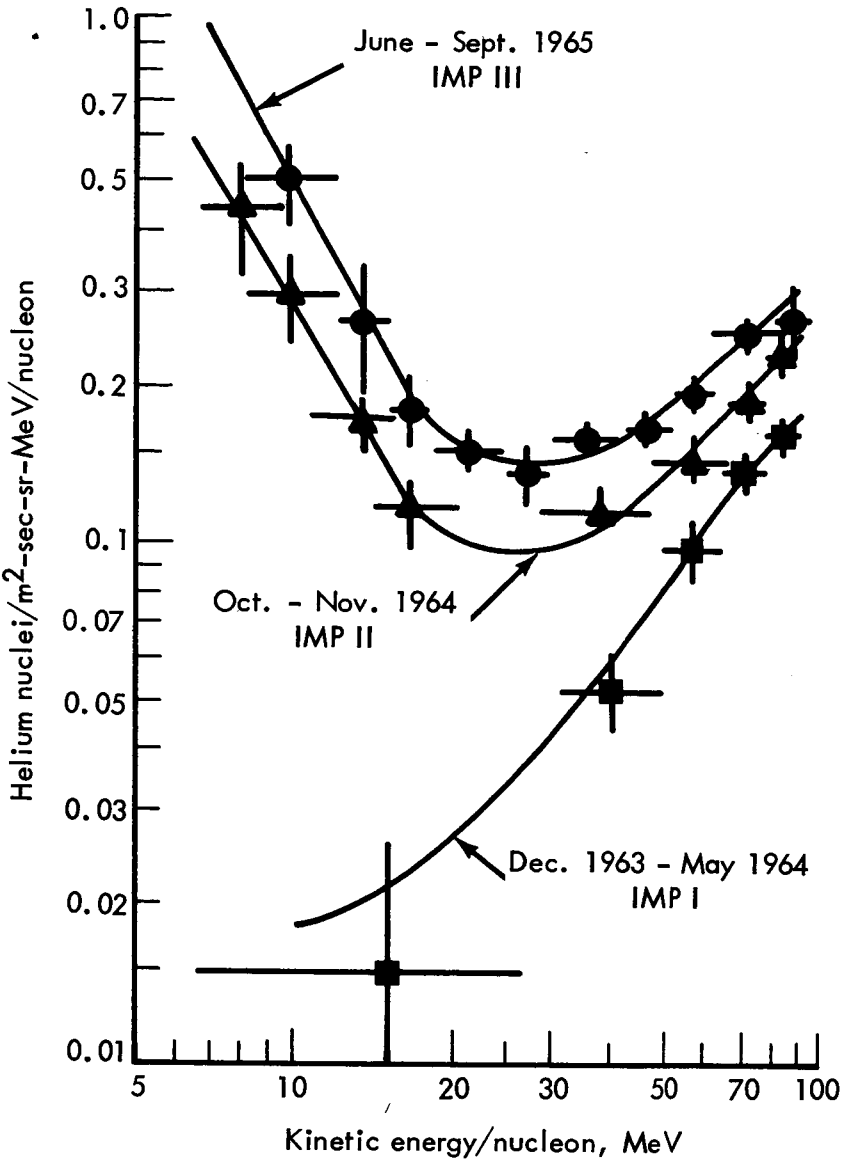

Figure 29.—Differential energy spectra for helium nuclei during three time intervals near solar minimum (1963 to 1965). These satellite measurements were made in interplanetary space and do not include periods when solar-associated particle events were present. (See ref. 12.)

energy cutoff shown in figure 30 can be explained in terms of a velocity-dependent modulation of the flux as it penetrates the solar system.

The apparently velocity-dependent modulation found at low energies does not apply for energies in the GeV region. Ormes and Webber (ref. 81) have studied this energy region with several bal-

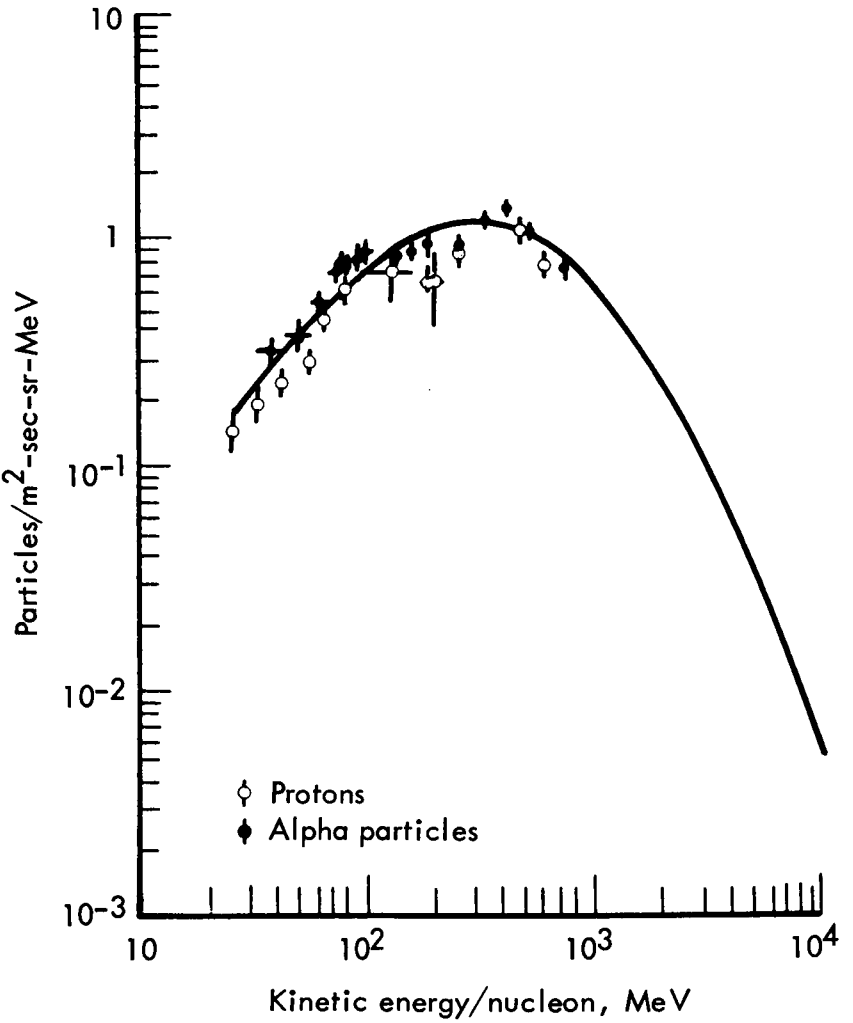

Figure 30.—Differential proton and alpha-particle spectra plotted in kinetic-energy-per-nucleon representation. The alpha-particle data have been multiplied by 5.7. The solid line represents the formula $dJ/dE = 10^8 E^{1.5} (E+500)^{-4}$. (See ref. 82.)

loon flights from 1963 to 1965 and figure 31 shows a typical proton spectrum from their work. They found that the modulation of protons from 1963 to 1965 is at least twice that for helium nuclei. Below about 400 MeV/nucleon their results are consistent with those of Balasubrahmanyan et al. (ref. 82). At relativistic energies, however, they found a flux ratio independent of energy only if the differential spectrum is expressed in terms of unit rigidity intervals rather than energy intervals. It may thus be concluded that the solar modulation effects are primarily rigidity-dependent in the region from 2 to 16 GV.

Much theoretical work has been performed to refine Parker's early models of the solar wind to obtain a quantitative understanding of the

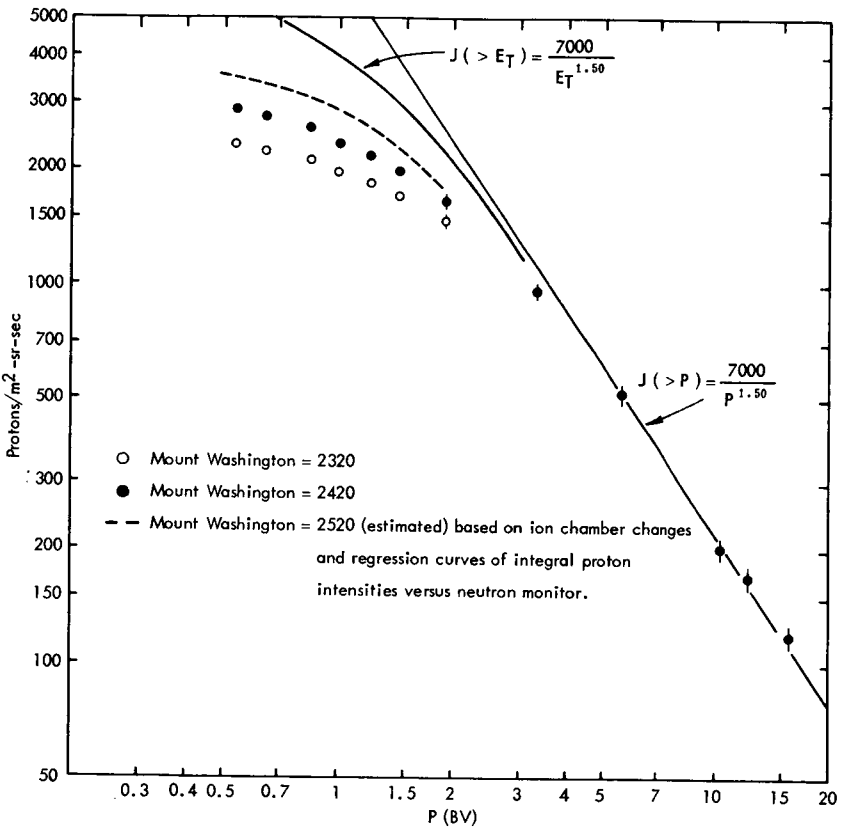

Figure 31.—Integral spectra of primary protons in a rigidity presentation. Data were taken in 1963, 1964, and 1965 on balloons under 4 to 6 g/cm² of atmosphere. Small corrections have been applied to correct observations to one of two Mount Washington monitor rates. (See ref. 81.)

solar modulation and to derive the cosmic ray flux outside the galaxy. The picture generally adopted is one in which cosmic rays are scattered by magnetic-field inhomogeneities. Therefore, the anisotropic-diffusion theory is applicable (e.g., refs. 11 and 79). The details of the various theories are not identical, but basically the problem is to derive the diffusion coefficient from the properties of the interplanetary field and then determine the particle fluxes and any changes of their energy resulting from interactions with the solar wind (ref. 67).

Parker (ref. 11) has constructed a quasi-magnetic field line for quiet solar conditions (fig. 32). Shown on the same figure are also the gyroradii of protons of various energies. Particles will be scattered most effectively if the scale size of the field fluctuations are comparable to the gyroradius. As can be seen from figure 32, the actual magnetic-field fluctuations cover a large range of gyroradii; on the other hand their character changes significantly even between different so-called "quiet" days. Thus cosmic rays diffusing into the solar system would sample a large range of conditions. Jokipii (ref. 83) has derived a diffusion coefficient for diffusion along magnetic field lines, on the basis of a power spectrum analysis of the field fluctuations observed with Mariner II (fig. 12) and Mariner IV (Coleman, ref. 36). Jokipii finds that the diffusion coefficient depends on the product of particle rigidity and velocity. Gloeckler and Jokipii (ref. 12) show that this dependence agrees with data obtained by the University of

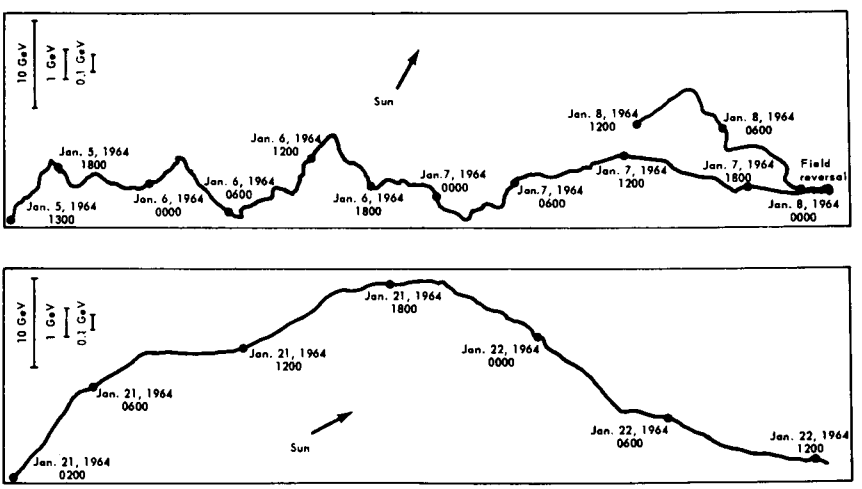

Figure 32.—The direction of the interplanetary magnetic field in the plane of the ecliptic as observed by IMP I. The direction to the Sun is indicated by the arrow and remains fixed throughout each plot. (See ref. 11.)

Chicago experiments on IMP I, IMP II, and IMP III. This form of the diffusion coefficient reduces to a rigidity dependence at relativistic energies as found by Ormes and Webber (ref. 81) and to velocity dependence at nonrelativistic energies as found by Balasubrahmanyan (ref. 82). In addition, it accounts for Webber's observation that from 1963 to 1965 the proton flux was modulated twice as much as the alpha-particle flux.

The theories should be able to account for the relative modulation not only of hydrogen and helium but also of the other elements in the cosmic-ray flux. Data are becoming available on the energy spectra of various elements (refs. 84, 85, and 86). Substantial advances in detector technology have made it possible to determine the He^3 content of the total helium flux as shown in figure 33 (refs. 87 and 88). In con-

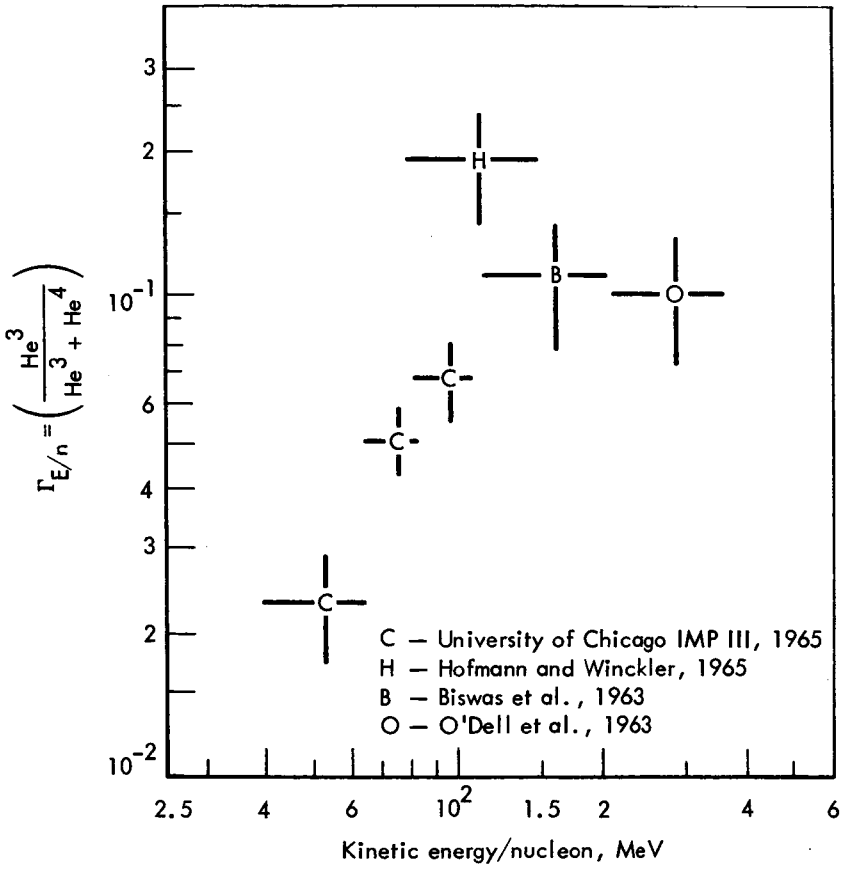

Figure 33.—The ratio of the He^3 to total galactic helium flux was obtained after an estimated solar He^4 component has been subtracted. (See ref 88.)

245-015 O—67——6

trast to the constant hydrogen-to-helium ratio in this energy region, this ratio is a function of energy per nucleon. A plausible explanation may be made on the basis that the galactic He^3 and He^4 spectra have a different energy dependence. The interpretation of these data is just beginning.

Proton I and II, launched by the U.S.S.R. in 1965, were designed for the investigation of the high-energy part of the cosmic-ray spectrum, heavy particles up to 10^{14} eV, electrons up to 10^{10} eV, and gamma rays up to 3×10^9 eV. Final evaluations of the data from Proton I have not yet been published. A preliminary reduction of the heavy-particle and proton spectrum by Grigorov and coworkers is shown in figure 34. It may be noticed that this measurement requires a much lower proton flux than had been deduced from air-shower measurements. In view of this discrepancy, it will be most interesting to see a definitive evaluation of these data. Hopefully, one would then be in a position to resolve the differences in the results.

The nonthermal radio noise from the galaxy is in general ascribed to synchrotron radiation from energetic electrons. Observation of electrons as a component of cosmic rays, however, has been relatively difficult because they constitute less than 1 percent of the proton flux. Figure 35 shows a summary of recent measurements (refs. 89, 90, 91, and 93) of the combined electron and positron flux. In addition Daniel and Stephens (ref. 92) determined that the integral flux above 16 GeV is 0.68 ± 0.20 per m^2/sec/sr. With the exception of the measurements of Cline et al. (ref. 93), all observations were performed from balloons and had to be corrected for secondary electrons. These corrections constitute a major fraction of the observed flux below about 300 MeV, and the flux shown in that energy range (fig. 35) may be in error. Hartman and Meyer (ref. 94) have investigated the positron-to-electron ratio in the energy interval from 50 MeV to 3 GeV. This experiment demonstrates clearly a substantial excess of primary electrons over positrons.

The theoretical interpretation of these results suffers from the uncertainty introduced in the extrapolation of observations from the inner solar system to fluxes in the galaxy. Still the following general conclusions may be drawn (ref. 95): (1) secondary production by collisions of protons with interstellar matter is inadequate to explain the observed positron-to-electron ratio, and a direct source of electrons has to be present; and (2) the observed fluxes are within an order of magnitude of those required to explain the observed synchrotron radiation.

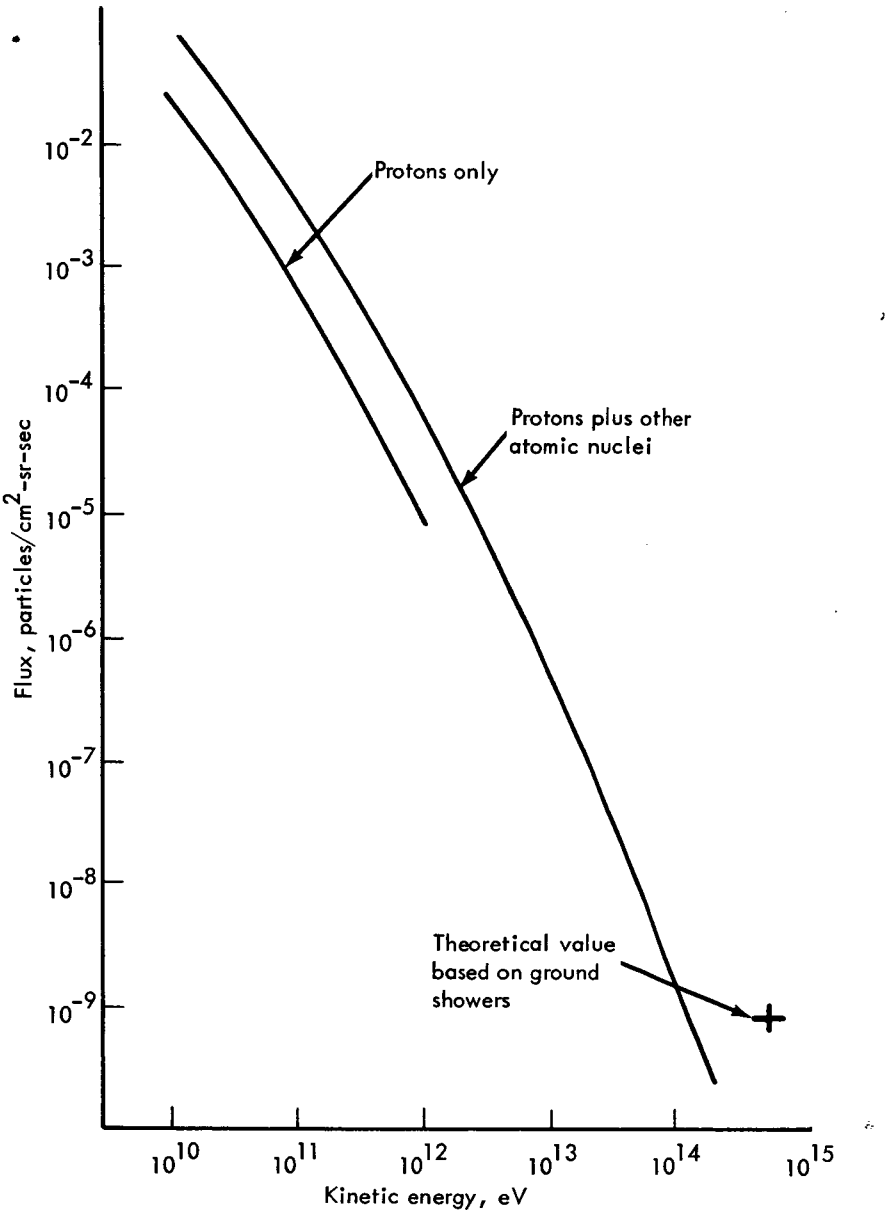

Figure 34.—Energy spectrum of cosmic-ray primaries as observed with Proton I. (Grigorov, N.; Sovenko, L.; and Skuridin, G.: Pravda release and COSPAR report, 1966.)

PLANETARY FIELDS

The Mars flyby of Mariner IV on July 14, 1965, permitted the first direct observations of the magnetic field and energetic-particle environment of Mars. As yet, only preliminary results of the encounter have been published (refs. 96, 97, and 98). In summary, the presence of Mars could not be detected on any of the records. The magnetometer and plasma measurements are entirely consistent with the prop-

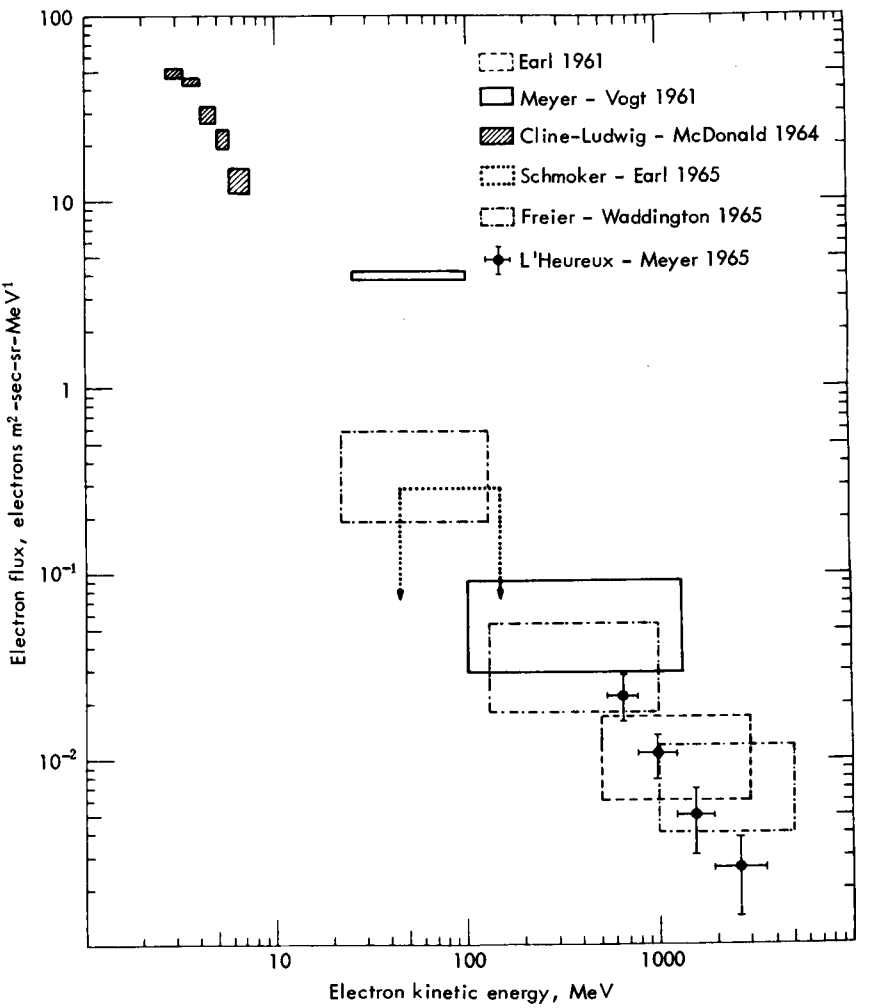

Figure 35.—Summary of experimental data on the energy spectrum of primary cosmic-ray electrons. (See ref. 95.)

erties of the undisturbed interplanetary medium even though the distance of closest encounter was only 9846.6 kilometers. The energetic particle measurements indicated the onset of a small solar-proton event shortly after the encounter (ref. 96). The interpretation of the magnetic-field observations is that any magnetic dipole moment of Mars is less than 0.03 percent of that of Earth.

The solar-wind interaction with Mars is therefore quite different from that with the Earth or the Moon and further investigations, preferably from low-orbiting spacecraft, would be most interesting. If Mars should have no permanent dipole moment, then the solar wind would interact directly with the upper atmosphere and ionosphere. The solar-wind protons would lose energy by ionization, and the magnetic field moving with the solar wind would interact with the Martian ionosphere. This could be another mechanism of gas loss from the Martian atmosphere in addition to gravitational escape.

The Mariner II magnetometer and plasma measurements have been reinterpreted (refs. 99 and 100) in the light of our present understanding of the solar wind-magnetosphere interaction. The investigators were unable to detect any effects caused by Venus. An upper limit can be derived for the magnetic moment of Venus by scaling the size of the Earth's magnetosphere and magnetosheath down to the point where Mariner II would just have missed the bow-shock region. On this basis it was concluded that the dipole moment of Venus is less than 10 percent of that of the Earth. (If the dipole axis is assumed to be perpendicular to the ecliptic plane the corresponding figure would be 5 percent.)

The present theories of geomagnetism are consistent with no permanent magnetic moment for Mars and a moment for Venus that is considerably smaller than that of the Earth. A recent review of planetary magnetic fields was made by Hide (ref. 101) who concludes that large fields are present primarily on Earth and Jupiter.

CONCLUSIONS

During 1965 steady progress was made in particles and fields research. The work performed during this period went a long way toward describing all aspects of the conditions prevailing during periods of minimal solar activity. The conclusions based on this research are important not only to the extent that they describe the Earth's environment, but also because all cosmological observations have to be reduced sooner or later to physical processes which can be studied directly. Thus the active exploration of the inner solar system may be expected to form also the basis for understanding processes occurring in other parts of the universe.

By now we have accumulated a reasonably complete description of the average magnetic fields and of the energy spectra and fluxes of the various particles. In contrast there is as yet relatively little information available about the collective behavior of the particles and their instantaneous interactions with both electric and magnetic fields. In some respects, the most exciting progress during the year came from the initial attempts at correlating these phenomena. For instance, attempts to explain the propagation of both solar and galactic cosmic rays in terms of known properties of the solar wind are beginning to bear fruit. A diffusion equation describing this phenomenon has been derived and over certain regions of space the diffusion coefficient can be derived from measured quantities or so-called "quiet" conditions. As another example, the diamagnetic effect of energetic electrons in the geomagnetic tail and neutral sheet has been directly demonstrated.

Until now, correlations between fields and the collective behavior of particles have been only qualitative but they show the way in which future progress is likely to be made. The most important question in this area relates to the mechanisms which permit transfer of energy between particles and fields. The extensive theoretical work in this area should permit the design of specific experiments to investigate various processes. Prime requirements for these experiments will be a good time resolution and many simultaneous observations at different locations. Only in that way will it be possible to separate temporal from spatial variations.

The outlook for future work in the discipline is encouraging. A substantial amount of data was obtained during the year, the analysis of which will further increase our understanding of conditions near solar minimum. During 1966 and 1967 it should be possible to extend greatly the type of simultaneous observation made with Mariner IV and Earth satellites. The introduction in 1966 of a 210-foot dish into the Deep Space Network has made it possible to track Pioneer VI and Mariner IV for distances in excess of one astronomical unit. If they and Pioneer VII work over an extended period, then it will be possible to describe in some detail the spatial extent of disturbances in the interplanetary medium and their effect on the propagation of cosmic rays.

During 1967 the activity of the Sun is expected to increase substantially. From then until about 1971, it will again be possible to investigate solar-maximum conditions. It may be worth remembering that the original satellites were designed to be launched during the IGY solar maximum (1957 to 1958), but those satellites were not sophisticated enough for detailed investigations.

Reasons for direct observations closer to the Sun and beyond the orbit of Mars continue to accumulate. As our theories about the propagation of cosmic rays throughout the solar system become more sophisticated, we will be in a better position to utilize the results from direct measurements over a greater region of space. The determination of the flux of cosmic rays in the galaxy remains an outstanding problem of great importance to cosmology. The exploration of the particle-and-field environment of Jupiter has taken on additional importance since it appears to be the nearest planet with a large magnetic field like the Earth and with an even more intense radiation belt.

APPENDIX A—SCIENTIFIC APPARATUS ON SATELLITES AND SPACE PROBES

Vela II and III (1964—40 A+B, 1965—58 A+B; Department of Defense Nuclear Test Detection Satellite)

Electrons and Positive Ions: 0.1 to 20 keV
- Electrostatic Analyzer

Electrons: 45 to 430 keV
- Gold surface barrier solid state detector
- Geiger-Mueller tubes
- Scintillation detectors

Protons: 180 to 500 keV and >800 keV
- Gold surface barrier solid state detectors
- Scintillation detectors

OGO I (1964—54A; Orbiting Geophysical Observatory)

Cosmic Rays and Solar Protons: 30 keV to 90 MeV
- Scintillation detectors
- Solid-state detector telescopes

Positrons: 0 to 3 MeV
- Gamma ray spectrometer

Protons: thermal to 4.5 MeV
- Planar ion and electron trap
- Spherical retarding-potential analyzer
- Electrostatic analyzer
- Faraday cup
- Charged-particle telescope

Electrons: thermal to 4 MeV
- Planar ion and electron trap
- Spherical retarding-potential analyzer
- Geiger-Mueller tubes
- Magnetic spectrometer

Magnetic Fields: $\pm 500\gamma$
- Flux-gate magnetometer

Micropulsations: 0.01 to 1000 Hz
- Search-coil magnetometer

Very-low-frequency electromagnetic radiation: 0.2 to 100 kHz
- Step frequency receivers, 9.5-foot diameter, toroidal antenna

IMP II and IMP III (Explorer XXI, 1964—60A and Explorer XXVIII, 1965—42A; Interplanetary Monitoring Platform)

Cosmic Rays and Solar Protons: 5 to 200 MeV
- Solid-state telescopes
- Scintillation detectors
- Geiger-Mueller tubes
- Ionization chamber

Electrons: thermal to 210 eV and >40 keV
- Planar ion and electron trap
- Faraday cup (inoperative on IMP III)
- Geiger-Mueller tubes

Protons: thermal to 8 keV
- Planar ion and electron trap
  Faraday cup (inoperative on IMP III)
  Electrostatic analyzer (inoperative on IMP III)

Magnetic Fields:
  Flux-gate magnetometer: ±40γ
  Rubidium vapor: 3 to 500γ

ERS 17 (1965—58C; Environmental Research Satellite, USAF launched)

Electrons: >40 keV, >100 keV, >400 keV
  Geiger-Mueller tubes
  Scintillator
  Solid-state detector

Protons: 2 to 20 MeV
  Scintillator
  Solid-state detector

1963—38C (U.S. Navy Launched Energetic Particle Satellite)

Protons: 1.2–100 MeV
  Solid-state detectors

Electrons: 200 keV–>3.6 MeV
  Solid-state detectors

Relay II (1964—3A; NASA Communications Satellite)

Protons: 1 to 60 MeV
  Solid-state detector
  Silicon *p–n* junction detectors
  Scintillation counter

Electrons: 0.2 to 2 MeV
  Solid-state detectors
  Scintillation counters

Injun IV (1964—76B; University of Iowa)

Protons: 0 to 40 MeV
  Solid-state detectors
  Scintillation detectors
  Silicon *p–n* detectors
  Geiger-Mueller tubes
  Spherical retarding-potential analyzer

Electrons: 0 to 2.2 MeV
  Solid-state detectors
  Scintillation detectors
  Geiger-Mueller tubes
  Spherical retarding-potential analyzer

Alpha Particles: >0.5 and >1.5 MeV
  Silicon *p–n* junction detectors

EPE IV (1964—86A; Energetic Particle Explorer)

Protons: 30 keV to 110 MeV
  Scintillation detectors
  Silicon *p–n* junction detectors

Electrons: 10 keV to >5 MeV
Scintillation detectors
Silicon p–n junction detectors
Magnetic Fields ±4000 γ
Flux-gate magnetometer

Proton I and Proton II (1965—54A, 1965—87A; U.S.S.R. High Energy Cosmic Ray Satellite)

Cosmic-ray protons and heavy nuclei up to 10^{14} eV
Cosmic-ray electrons: 3×10^{8} to 10^{10} eV
Cosmic-ray gamma rays: 10^{8} to 3×10^{9} eV
Instruments:
Detector SEZ–14: Ionization calorimeter
Interaction detector
Polyethylene and graphite filters
Proportional counters
Scintillation counters
Detector SEZ–12: Shower detector (electron energy)
Cerenkov counter
Scintillation counters
Detector SEZ–1 and GG–1:
Cerenkov counter
Scintillation counters

OV I–2 (1965—78A; USAF Orbital Pod)

Protons: 5 to 150 MeV
Solid-state detector
Electrons: 0.3 to 16 MeV

OGO II (1965—81A; Orbiting Geophysical Observatory)

Cosmic Rays and Solar Protons: 0.5 MeV to 1 GeV
Scintillation detectors
Cerenkov counter
Ionization chamber
Protons: 100 keV to 4.5 MeV
Scintillation detectors
Electrons: 10 to 100 keV and >120 keV
Scintillation detectors
Geiger-Mueller tubes
Magnetic Fields: 10 000 to 65 000 γ
Rubidium-vapor magnetometer
Magnetic Micropulsations: 0.01 to 1000 Hz
Triaxial search coil
Very-Low-Frequency Electromagnetic Radiation: 0.2 to 100 kHz
Broadband receivers, 10-foot dipole antenna
Step frequency receivers, 9½-foot diameter toroidal antenna
Tunable narrow-band receivers, 9½-foot diameter toroidal antenna

Mariner IV (1964—77A; Mars Probe)

Protons: 30 eV to 10 keV
Faraday cup

Protons: 500 keV to 320 MeV
Solid-state detectors and telescope
Geiger-Mueller tubes
Ionization chamber
Electrons: 70 keV to >320 MeV
Solid-state detectors and telescope
Geiger-Mueller tubes
Ionization chamber
Alpha Particles: 2 to 60 MeV
Solid-state telescope
Ionization chamber
Magnetic Fields: ±360 γ
Vector helium magnetometer

Pioneer VI (1965—105A; Interplanetary Probe)

Protons: 40 eV to 15 keV
Faraday cup
Electrostatic analyzer
Protons: 0.6 MeV to 200 MeV
Solid-state detector telescope
Scintillation detector
Electrons: 3 eV to 2500 eV
Faraday cup
Electrostatic analyzer
Alpha Particles and Heavy Nuclei: 2.5 to 350 MeV
Solid-state detector telescope
Scintillation detector
Magnetic Fields: ±64 γ
Flux-gate magnetometer

REFERENCES

1. ANON.: Significant Achievements in Particles and Fields 1958–1964. NASA SP–97, 1966. (Hess, W. N.; Mead, G. D.; and Nakada, M. P.: Advances in Particles and Field Research in the Satellite Era. Rev. Geophys., vol. 3, 1965, p. 521.)
2. HESS, W. N., ED.: Introduction to Space Science. Gordon & Breach Science Publishers, 1965.
3. ANON.: Particles and Fields Research. Bibliography with author index, compiled by W. N. Hess and G. D. Mead. NASA SP–7026, June 1966.
4. WILCOX, J. M.; AND NESS, N. F.: Quasi Stationary Co-Rotating Structure in the Interplanetary Medium. J. Geophys. Res., vol. 70, 1965, pp. 5793–5805.
5. BRYANT, D. A.; CLINE, T. L.; DESAI, U. D.; AND MCDONALD, F. B.: Continued Acceleration of Solar Protons in the MeV Range. Phys. Rev. Letters, vol. 14, 1965, pp. 481–484.
6. FAN, C. Y.; GLOECKLER, G.; AND SIMPSON, J. A.: Protons and Helium Nuclei Within Interplanetary Magnetic Regions Which Co-Rotate With the Sun. Proceedings of the International Conference on Cosmic Rays (London), 1965.
7. O'GALLAGHER, J. J.; AND SIMPSON, J. A.: Anisotropic Propagation of Solar Protons Deduced From Simultaneous Observations by Earth Satellites and the Mariner IV Space Probe. Phys. Rev. Letters, vol. 16, 1966, pp. 1212–1217.

8. McCracken, K. G.; and Ness, N. F.: The Collimation of Cosmic Rays by the Interplanetary Magnetic Field. J. Geophys. Res., vol. 71, no. 13, July 1, 1966, pp. 3315–3318.
9. Van Allen, J. A.; and Krimigis, S. M.: Impulsive Emission of ~40 keV Electrons From the Sun. J. Geophys. Res., vol. 70, 1965, pp. 5737–5751.
10. Callender, R. H.; Manzano, J. R.; and Winckler, J. R.: The Response of High-Altitude Ionization Chambers During the 1954–1965 Solar Cycles. J. Geophys. Res., vol. 70, 1965, pp. 3189–3201.
11. Parker, E. N.: The Passage of Energetic Particles Through Interplanetary Space. Planetary Space Sci., vol. 13, 1965, pp. 9–49.
12. Gloeckler, G.; and Jokipii, J. R.: Low-Energy Cosmic-Ray Modulation Related to Observed Interplanetary Magnetic-Field Irregularities. Phys. Rev. Letters, vol. 17, 1966, pp. 203–207.
13. Ness, N. F.: The Earth's Magnetic Tail. J. Geophys. Res., vol. 70, no. 13, July 1, 1965, pp. 2989–3005.
14. Frank, L. A.: A Survey of Electrons E>40 keV Beyond 5 Earth Radii With Explorer XIV. J. Geophys. Res., vol. 70, no. 7, Apr. 1, 1965, pp. 1593–1626.
15. Williams, D. J.; and Ness, N. F.: Simultaneous Trapped Electron and Magnetic Field Observations. NASA X-611-66-264, June 1966.
16. Kennel, C. F.; and Petschek, H. E.: Limit on Stably-Trapped Particle Fluxes. J. Geophys. Res., vol. 71, 1966, pp. 1–28.
17. Chang, D. B.; and Pearlstein, L. D.: On the Effect of Resonant Magnetic Moment Violation on Trapped Particles. J. Geophys. Res., vol. 70, 1965, pp. 3075–3083.
18. Chang, D. B.; Pearlstein, L. D.; and Rosenbluth, N. M.: On the Interchange Stability of the Van Allen Belt. J. Geophys. Res., vol. 70, 1965, pp. 3085–3097.
19. McCormac, B. M., ed.: Radiation Trapped in the Earth's Magnetic Field. D. Reidel Publishing Co., 1966.
20. Parker, E. N.: Interplanetary Dynamical Processes. Interscience (New York), 1963.
21. Ness, N. F.; Scearce, C. S.; and Seek, J. B.: Initial Results of the IMP-I Magnetic Field Experiment. J. Geophys. Res., vol. 69, 1964, pp. 3531–3569.
22. Ness, N. F.; and Wilcox, J. M.: Solar Origin of the Interplanetary Magnetic Field. Phys. Rev. Letters, vol. 13, 1964, pp. 461–464.
23. Ness, N. F.; and Wilcox, J. M.: Extension of Photospheric Magnetic Field Into Interplanetary Space. Astrophys. J., vol. 143, 1966, pp. 23–31.
24. Ness, N. F.: Simultaneous Measurements of the Interplanetary Magnetic Field. J. Geophys. Res., vol. 71, 1966, pp. 3319–3324.
25. Lyon, E.; Bridge, H.; Egidi, A.; and Rossi, B.: IMP-I Plasma Summary Data. Trans. Am. Geophys. Union, vol. 45, 1964, p. 605.
26. Neugebauer, M.; and Snyder, C. W.: Mariner IV Observations of the Solar Wind, 1, Average Properties. J. Geophys. Res., vol. 71, 1966, pp. 4469–4484.
27. Wolfe, J. H.; Silva, R. W.; McKibbin, D. D.; and Mason, R. H.: The Compositional Anisotropic and Non-Radial Flow Characteristics of the Solar Wind. J. Geophys. Res., vol. 71, 1966, pp. 3329–3335.
28. Hundhausen, A. J.; Asbridge, J. R.; Bame, S. J.; Gilbert, H. E.; and Strong, I. B.: Vela III Satellite Observations of Solar Wind Ions: A Preliminary Report. Los Alamos Report LA-DC-8118.

29. STRONG, I. B.; ASBRIDGE, J. R.; BAME, S. J.; HECKMAN, H. H.; AND HUNDHAUSEN, A. J.: Measurements of Proton Temperatures in the Solar Wind. Phys. Rev. Letters, vol. 16, 1966, pp. 631–633.

30. PARKER, E. N.: Dynamical Theory of the Solar Wind. Space Sci. Rev., vol. 4, 1965, pp. 666–708.

31. PARKER, E. N.: Dynamical Properties of Stellar Coronas and Stellar Winds. V. Stability and Wave Propagation. Astrophys. J., vol. 143, 1966, pp. 32–37.

32. SCARF, F. L.: Wave-Particle Interactions in the Solar Wind. Raumfahrtforschung, vol. 3, 1966.

33. SCARF, F. L.; WOLFE, J. H.; AND SILVA, R. W.: Plasma Instability in the Solar Wind. Paper presented at the Inter-Union Symposium on Solar Terrestrial Physics (Belgrade), 1966.

34. DESSLER, A. J.: Solar Wind and Interplanetary Magnetic Field. Rev. of Geophys., in publication.

35. LERCHE, I.: Validity of the Hydromagnetic Approach in Discussing Instability of the Magnetospheric Boundary. J. Geophys. Res., vol. 71, 1966, p. 2365–2371.

36. COLEMAN, P. J., JR.: Variations in the Interplanetary Magnetic Field: Mariner 4. Publication no. 501, Institute of Geophysics and Planetary Physics, University of California (Los Angeles), 1966.

37. HOLZER, R. E.; MCLEOD, M. G.; AND SMITH, E. J.: Preliminary Results From the OGO–I Search Coil Magnetometer: Boundary Positions and Magnetic Noise Spectra. J. Geophys. Res., vol. 71, 1966, pp. 1481–1486.

38. COLEMAN, P. J., JR.: Hydromagnetic Waves in the Interplanetary Plasma. Phys. Rev. Letters, vol. 17, 1966, pp. 207–211.

39. COLBURN, D. S.; AND SONETT, C. P.: Discontinuities in the Solar Wind. Space Sci. Rev., vol. 5, 1966, pp. 439–506.

40. RAZDAN, H.; COLBURN, D. S.; AND SONETT, C. P.: Recurrent SI^{+}-SI^{-} Impulse Pairs and Shock Structure in M-Region Beams. Planetary Space Sci., vol. 13, 1965, pp. 1111–1123.

41. SONETT, C. P.; AND COLBURN, D. S.: The SI^{+}-SI^{-} Pair and Interplanetary Forward-Reverse Shock Ensembles. Planetary Space Sci., vol. 13, 1965, pp. 675–692.

42. CHAPMAN, S.; AND FERRARO, V. C. A.: A New Theory of Magnetic Storms. Terrest. Magnetism Atmospheric Elec., vol. 36, 1931, pp. 77–97, 171–186.

43. CHAPMAN, S.; AND FERRARO, V. C. A.: A New Theory of Magnetic Storms. Terrest. Magnetism Atmospheric Elec., vol. 37, 1932, pp. 147–156, 421–429.

44. CHAPMAN, S.; AND FERRARO, V. C. A.: A New Theory of Magnetic Storms. Terrest. Magnetism Atmospheric Elec., vol. 38, 1933, pp. 79–96.

45. WOLFE, J. H.; SILVA, R. W.; AND MYERS, M. A.: Preliminary Results From the Ames Research Center Plasma Probe Observations of the Solar Wind-Geomagnetic Field Interaction Region on IMP–II and OGO–I. Ames Research Center preprint, July 21, 1965.

46. COON, J. H.: Vela Satellite Measurements of Particles in the Solar Wind and the Distant Geomagnetosphere. Report of the Advanced Study Institute on Radiation Trapped in the Earth's Magnetic Field (Bergen, Norway), 1965.

47. ANDERSON, K. A.; HARRIS, H. K.; AND PAOLI, R. J.: Energetic Electron Fluxes in and Beyond the Earth's Outer Magnetosphere. J. Geophys. Res., vol. 70, 1965, pp. 1039–1050.

48. FAN, C. Y.; GLOECKLER, G.; AND SIMPSON, J. A.: Acceleration of Electrons Near the Earth's Bow Shock and Beyond. J. Geophys. Res., vol. 71, 1966, pp. 1837–1856.
49. FREDERICKS, R. W.; SCARF, F. L.; AND BERNSTEIN, W.: Numerical Estimates of Superthermal Electron Production by Ion-Acoustic Waves in the Transition Region. J. Geophys. Res., vol. 70, 1965, pp. 21–28.
50. JOKIPII, J. R.: A Model of Fermi Acceleration at Shock Fronts With an Application to the Earth's Bow Shock. Astrophys. J., vol. 143, 1966.
51. SEN, A. K.: Stability of the Magnetospheric Boundary. Planetary Space Sci., vol. 13, 1965, pp. 131–141.
52. HEPPNER, J. P.: Recent Measurement of the Magnetic Field in the Outer Magnetosphere and Boundary Regions. NASA X-612-65-490, Nov. 1965.
53. GOSLING, J. T.; ASBRIDGE, J. R.; BAME, S. J.; AND STRONG, I. B.: Vela 2 Measurements of the Magnetopause and Bow Shock Positions. Los Alamos Scientific Laboratory. Report LA-DC-8000, 1965.
54. KONRADI, A.; AND KAUFMANN, R. L.: Evidence for Rapid Motion of the Outer Boundary of the Magnetosphere. J. Geophys. Res., vol. 70, 1965, pp. 1627–1637.
55. CAHILL, L. J., JR.: Inflations of the Magnetosphere Near 8 Earth Radii in the Dark Hemisphere. In: Space Research VI, North-Holland Pub. Co. (Amsterdam), 1966.
56. AXFORD, W. I.; PETSCHEK, H. E.; AND SISCOE, G. L.: Tail of the Magnetosphere. J. Geophys. Res., vol. 70, no. 5, Mar. 1, 1965, pp. 1231–1236.
57. BAME, S. J.; ASBRIDGE, J. R.; FELTHOUSER, H. E.; ALSON, R. A.; AND STRONG, I. B.: Electrons in the Plasma Sheet of the Earth's Magnetic Tail. Phys. Rev. Letters, vol. 16, no. 4, Jan. 24, 1966, pp. 138–142.
58. ANDERSON, K. A.; AND NESS, N. F.: Correlation of Magnetic Fields and Energetic Electrons on the IMP-I Satellite. J. Geophys. Res., vol. 71, no. 15, Aug. 1, 1966, pp. 3705–3727.
59. ANDERSON, K. A.: Energetic Electron Fluxes in the Tail of the Geomagnetic Field. J. Geophys. Res., vol. 70, no. 19, Oct. 1, 1965, pp. 4741–4763.
60. DESSLER, A. J.: Length of Magnetospheric Tail. J. Geophys. Res., vol. 69, no. 19, Oct. 1, 1964, pp. 3913–3918.
61. DUNGEY, J. W.: The Length of the Magnetospheric Tail. J. Geophys. Res., vol. 70, no. 7, Apr. 1, 1965, p. 1753.
62. VAN ALLEN, J. A.: Absence of 40 keV in the Earth's Magnetospheric Tail at 3300 Earth Radii. J. Geophys. Res., vol. 70, no. 19, Oct. 1, 1965, pp. 4731–4739.
63. DESSLER, A. J.: Discussion of Letter by J. A. Van Allen "Further Remarks on the Absence of a Very Extended Magnetospheric Tail." J. Geophys. Res., vol. 71, no. 9, May 1, 1966, pp. 2408–2410.
64. BRYANT, D. A.; CLINE, T. L.; DESAI, V. D.; AND MCDONALD, F. B.: Explorer XII Observations of Solar Cosmic Rays and Energetic Storm Particles After the Solar Flare of September 28, 1961. J. Geophys. Res., vol. 67, 1962, pp. 4983–5000.
65. AXFORD, W. I.: Anisotropic Diffusion of Solar Cosmic Rays. Planetary Space Sci., vol. 13, 1965, pp. 1301–1309.
66. FIBICH, M.; AND ABRAHAM, P. B.: On the Propagation and Diffusion of Solar Protons. J. Geophys. Res., vol. 70, 1965, pp. 2475–2484.
67. PARKER, E. N.: The Effect of Adiabatic Deceleration on the Cosmic Ray Spectrum in the Solar System. Planetary Space Sci., vol. 14, 1966, pp. 371–380.

68. BRYANT, D. A.; CLINE, T. L.; DESAI, U. D.; AND MCDONALD, F. B.: Studies of Solar Protons With Explorer 12 and 14. Astrophys. J., vol. 141, 1965, pp. 478–499.

69. BARTLEY, W. C.; BUKATA, R. P.; MCCRACKEN, K. G.; AND RAO, U. R.: Anisotropic Cosmic Radiation Fluxes of Solar Origin. J. Geophys. Res., vol. 71, 1966, pp. 3297–3304.

70. FAN, C. Y.; LAMPORT, J. E.; SIMPSON, J. A.; AND SMITH, D. R.: Anisotropy and Fluctuations of Solar Proton Fluxes of Energies 0.6–100 MeV Measured With the Pioneer VI Space Probe. J. Geophys. Res., vol. 71, 1966, pp. 3289–3296.

71. KRIMIGIS, S. M.; AND VAN ALLEN, J. A.: Observation of 500-keV Protons in Interplanetary Space With Mariner IV. Phys. Rev. Letters, vol. 16, 1966, pp. 419–423.

72. BISWAS, S.; AND FICHTEL, C. E.: Composition of Solar Cosmic Rays. Space Sci. Rev., vol. 4, 1965, pp. 709–736.

73. BAME, S. J.; AND ASBRIDGE, J. R.: A Search for Solar Neutrons Near Solar Minimum. Los Alamos Scientific Laboratory Report LA–DC–7973, 1965.

74. MEYER. P.; AND VOGT, R.: High-Energy Electrons of Solar Origin. Phys. Rev. Letters, vol. 8, 1962, pp. 387–389.

75. ANDERSON, K. A.; AND LIN, R. P.: Observations on the Propagation of Solar-Flare Electrons in Interplanetary Space. Phys. Rev. Letters, vol. 16, 1966, pp. 1121–1124.

76. PARKER, E. N.: Interplanetary Origin of Energetic Particles. Phys. Rev. Letters, vol. 14, 1965, pp. 55–57.

77. KAPLON, M. F.; AND SKADRON, G.: Model for the Origin and Properties of the Cosmic-Ray Rigidity Spectrum. Rev. Geophys., vol. 4, 1966, pp. 177–221.

78. KANE, S. R.; WINCKLER, J. R.; AND ARNOLDY, R. L.: Studies of Primary Cosmic Rays With Ionization Chambers. Proceedings of the Ninth International Conference on Cosmic Rays (London), 1965.

79. AXFORD, W. I.: The Modulation of Galactic Cosmic Rays in the Interplanetary Medium. Planetary Space Sci., vol. 13, 1965, pp. 115–130.

80. FAN, C. Y.; GLOECKLER, G.; AND SIMPSON, J. A.: Solar Modulations of the Galactic Helium Spectrum Above 30 MeV per Nucleon. Proceedings of the Ninth International Conference on Cosmic Rays (London), 1965.

81. ORMES, J. F.; AND WEBBER, W. R.: Measurements of Primary Proton and Helium Spectra and Their Modulations Using Balloon-Borne Cerenkov-Scintillation Counter. Proceedings of the Ninth International Conference on Cosmic Rays (London), 1965.

82. BALASUBRAHMANYAN, V. K.; BOLDT, E.; AND PALMEIRA, R. A. R.: Low-Energy Spectrum of Cosmic Rays as an Indication of Primary Source Characteristics and Interstellar Propagation. Phys. Rev., vol. 140, 1965, pp. 1157–1161.

83. JOKIPII, J. R.: Cosmic-Ray Propagations. I. Charged Particles in a Random Magnetic Field. Astrophys. J., vol. 146, 1966, pp. 480–487.

84. BALASUBRAHMANYAN, V. K.; AND MCDONALD, F. B.: Solar-Modulation Effects on the Primary Cosmic Radiation Near Solar Minimum. J. Geophys. Res., vol. 69, 1964, pp. 3289–3292.

85. BALASUBRAHMANYAN, V. K.; HAGGE, D. E.; LUDWIG, G. H.; AND MCDONALD, F. B.: The Multiply-Charged Primary Cosmic Radiation at Solar Minimum, 1965. J. Geophys. Res., vol. 71, 1966, pp. 1771–1780.

86. COMSTOCK, G. M.; FAN, C. Y.; AND SIMPSON, J. A.: Abundances and Energy Spectra for Nuclei of Galactic Origin Above 20 MeV per Nucleon. Proceedings of the Ninth International Conference on Cosmic Rays (London), 1965.

87. HOFMANN, D. J.; AND WINCKLER, J. R.: Isotopic Composition of Low-Energy Helium Nuclei in the Primary Cosmic Radiation at Solar Minimum. Phys. Rev. Letters, vol. 16, 1966, pp. 109–111.

88. FAN, C. Y.; GLOECKLER, G.; HSIEH, K. C.; AND SIMPSON, J. A.: Isotopic Abundances and Energy Spectra of He^3 and He^4 above 40 MeV per Nucleon From the Galaxy. Phys. Rev. Letters, vol. 16, 1966, pp. 813–817.

89. L'HEUREUX, J.; AND MEYER, P.: Flux and Energy Spectrum of Primary Cosmic Ray Electrons. Phys. Rev. Letters, vol. 15, 1965, pp. 93–96.

90. SCHMOKER, J. W.; AND EARL, J. A.: Magnetic Cloud Chamber Observations of Low-Energy Cosmic Ray Electrons. Phys. Rev., vol. 138, 1965, pp. 300–302.

91. FRIER, P. S.; AND WADDINGTON, C. J.: Electrons, Hydrogen Nuclei, and Helium Nuclei Observed in the Primary Cosmic Radiation During 1963. J. Geophys. Res., vol. 70, 1965, pp. 5753–5768.

92. DANIEL, R. R.; AND STEPHENS, S. A.: Electron Component of the Primary Cosmic Radiation at Energies $\geq$15 GeV. Phys. Rev. Letters, vol. 15, 1965, pp. 769–772.

93. CLINE, T. L.; LUDWIG, G. H.; AND MCDONALD, F. B.: Detection of Interplanetary 3 to 12 MeV Electrons. Phys. Rev. Letters, vol. 13, 1964, pp. 786–789.

94. HARTMAN, R. C.; MEYER, PETER; AND HILDEBRAND, R. H.: Observation of the Cosmic Ray Electron-Positron Ratio From 100 MeV to BeV in 1964 J. Geophys. Res., vol. 70, 1965, pp. 2713–2715.

95. MEYER, PETER: Primary Electrons and Positrons in the Cosmic Radiation. Proceedings of the Ninth International Conference on Cosmic Rays (London), 1965.

96. VAN ALLEN, J. A.; FRANK, L. A.; KRIMIGIS, S. M.; AND HILLS, H. K.: Absence of Martian Radiation Belts and Implications Thereof. Science, vol. 149, 1965, pp. 1228–1233.

97. O'GALLAGHER, J. J.; AND SIMPSON, J. A.: Search for Trapped Electrons and a Magnetic Moment at Mars by Mariner IV. Science, vol. 149, 1965, pp. 1233–1239.

98. SMITH, E. J.; DAVIS, L., JR.; COLEMAN, P. J., JR.; AND JONES, D. E.: Magnetic Field Measurements Near Mars. Science, vol. 149, 1965, pp. 1241–1242.

99. SMITH, E. J.; DAVIS, L., JR.; COLEMAN, P. J., JR.; AND SONETT, C. P.: Magnetic Measurements Near Venus. J. Geophys. Res., vol. 70, 1965, pp. 1571–1586.

100. NEUGEBAUER, M.; AND SNYDER, C. W.: Solar Wind Measurements Near Venus. J. Geophys. Res., vol. 70, 1965, pp. 1587–1591.

101. HIDE, R.: Planetary Magnetic Fields. Planetary Space Sci., vol. 14, 1966, pp. 579–586.

102. SPREITER, J. R.; AND JONES, W. P.: On the Effect of a Weak Interplanetary Magnetic Field. J. Geophys. Res., vol. 68, 1963, p. 3555.

PLANETARY ATMOSPHERES

RICHARD HOROWITZ, ROBERT F. FELLOWS,
AND HAROLD HIPSHER
Lunar and Planetary Programs
Office of Space Science and Applications, NASA

245-015 O—67——7

Planetary Atmospheres

HIGHLIGHTS

RECENT MEASUREMENTS reveal that the current description of the diurnal density bulge in the Earth's atmosphere may need to be modified, at least for altitudes above 500 kilometers. It now appears that the bulge is significantly elongated in the north-south direction. The latitude of the center is not at the subsolar point, but remains near the Equator. During quiet-Sun conditions, the atmosphere is more responsive to changes in geomagnetic activity than had previously been expected. Furthermore, the atmosphere appears to react on a world-wide basis at the same time. Significant variations in atmospheric density have been measured at altitudes near 120 kilometers. Since this is the region frequently taken as the reference altitude for atmospheric models, these density variations are significant and imply a need for reexamination of the models. From Explorer XVII data it is known that variations in atmospheric composition occurred at all altitudes covered by the orbit. The first direct in situ measurement of neutral helium at satellite altitude was also obtained. The average quiet daytime value of the neutral helium concentration at ~260 kilometers was $\sim 1.4 \times 10^6/cm^3$, and the average quiet nighttime value at 400 kilometers was $\sim 6 \times 10^5/cm^3$. Rocket measurements indicate that ions of mass-to-charge ratio greater than 48 constitute a large percent of the D-region ionization. Electron temperatures in the F-region and above exceed the neutral-particle temperatures both during the daytime and nighttime, and especially in the early-morning hours. Neutral-temperature measurements, obtained from scale-height values taken from measured N_2 density profiles, do not generally agree with the appropriate model values. Wavelike structure has been detected in some neutral temperature profiles, possibly revealing the presence of gravity waves. Simultaneous measurements of midlatitude night airglow and particle precipitation indicate that the midlatitude 5577 Å night airglow is not excited by charged particle bombardment as it is in auroras.

Recent ground-based, rocket, and Mariner IV data have greatly increased our knowledge of the Martian atmosphere. Spectroscopic measurements made during the recent Mars opposition yield values between 7 and 13 millibars for the surface pressure. The partial pres-

sure of CO_2 at the surface was found to lie between 4 and 7 millibars, an indication that CO_2 is the principal constituent of the Martian atmosphere. The ground-based results also indicate that the amount of precipitable water on Mars is approximately 15 μ when detected. The occultation measurements obtained on the sunlit side yielded a neutral scale height value of 9 ± 1 kilometers and a surface pressure of 4.9 ± 0.8 millibars. An ionosphere was observed having a maximum electron density of $9.0\pm1.0\times10^4$ electrons/cm^3 at an altitude of 123 ± 3 kilometers. The electron scale height above the maximum was 22 ± 3 kilometers. From these data, several different models of the Martian atmosphere have been generated.

Radio measurements of Venus indicate a surface temperature of approximately 600° K and a surface pressure ranging from ~10 to ~200 Earth atmospheres. The carbon dioxide abundance is a critical parameter for determining the surface pressure from radio measurements, and it is unknown although generally believed to comprise less than 5 percent of the atmosphere. The major constituent could be nitrogen. The amount of water vapor above the Venus clouds remains a debatable item. Strong and others report values near 100 μ, while Spinrad places an upper limit of 10 μ.

RESULTS OF RESEARCH

The wealth of satellite-tracking data permits a continuing examination and refinement of the general description of the response of the Earth's upper atmosphere to changes in time, season, sunspot cycle, solar activity, location, aurora, geomagnetic activity, and other geophysical phenomena. Recent analysis shows (refs. 1 and 2) that the concept of a diurnal density bulge, as previously described (ref. 3), may need to be modified, at least for altitudes above 500 kilometers. Previously, it was accepted that while an east-west asymmetry existed, i.e., an atmospheric bulge with a peak 30° east of the subsolar point, the latitude of the peak followed the latitude of the subsolar point. It now appears that the diurnal density bulge is significantly elongated in the north-south direction, and its center remains near the Equator. Furthermore, these orbit data reveal a greater sensitivity of the atmosphere to changes in geomagnetic activity as measured, for example, by the A_p or K_p index. Since there does not appear to be any dependence of delay time, i.e., time interval between a change in A_p and a corresponding change in the density, on the local time of perigee (ref. 4), one may conclude that the reaction of the atmosphere to geomagnetic disturbances appears to occur worldwide at the same time. The mean delay time is frequently given as 6 ± 3 hours (ref. 4). However, DeVries et al. (ref. 5) have recently reported variations in

delay time ranging from a near-instantaneous response when the perigee occurred near 70° latitude, to about 22 hours' delay for perigee positions near 20° latitude. These results were obtained while the A_p value varied between 12 and 154. These data suggested that the timelag might increase with increasing altitude.

Direct in situ measurements of atmospheric density obtained from sensors on board Explorer XVII were reported recently (ref. 6). Over midnorthern latitudes, instantaneously measured densities were obtained from April to June 1963. Figure 1 shows density profiles measured for satellite passes over the tracking stations. No selection of the data was made for local time, or geomagnetic or solar activity. Because of orbit characteristics, the local times of the data for altitudes above 400 kilometers are usually between 0 and 0600 hours. The data below 400 kilometers are more generally distributed throughout the day. A number of conclusions regarding atmospheric variations can be made from figure 1. First, however, it should be noted that internal consistency checks performed indicate that for altitudes less than 500 kilometers, variations greater than approximately ± 20 percent reflect actual changes in atmospheric density. The Harris-Priester (ref. 7) model densities for $S=90$ at 1400 and 0400 hours are shown for comparison purposes as dashed lines. During the 3-month interval, the density varied by a factor of 4 at 270 kilometers and by a factor of 10 at 450 kilometers. Some of the changes correlate with changes in the 10.7-centimeter solar flux and with geomagnetic activity. Some variations do not appear to correlate with changes in either of the above. The gage measurements reveal a more dynamic atmosphere than that inferred from models based on drag data. Furthermore, it should be noted that during solar minimum, the diurnal change in density at 200 kilometers, as determined from drag measurements, is approximately 1.9, somewhat larger than the value of about 1.3 given by current models. In fact, comparatively large changes in density have recently been reported at the 120-kilometer altitude by Spencer et al. (ref. 8) and Champion (ref. 9). The implications of sizable changes at the commonly-referred-to boundary level for model atmospheres will be discussed later both in connection with composition measurements and atmospheric motions.

Composition

The neutral composition experiments aboard the Explorer XVII satellite represent an important first step toward measuring, on a global scale, the composition of the neutral atmosphere and its temporal variations. The ultimate objective is to define large-scale systems, and to understand the processes occurring in the thermosphere. Shown in table I is a small part of the published neutral concentrations (ref.

Table I.—*Number Densities of the Neutral Atmospheric Constituents* [a]

Date	Local time, hr	Altitude, km	Geographic		α, deg	A_p	$F_{10.7}$	Number density, number/cm^3		
			Longitude, deg	Latitude, deg				He	N_2	O
3 April 1963	3.2	400	−10.1	54.6	56.8	4	74	6.91×10^5	9.27×10^6	8.36×10^6
	3.9	431	−.6	51.5	63.3				6.65×10^6	5.97×10^6
3 April 1963	4.5	472	−63.8	46.7	67.9	4	74	5.04×10^5		2.46×10^6
	5.0	506	−57.4	42.4	74.3				2.20×10^6	1.55×10^6
3 April 1963	5.3	538	−101.0	38.0	78.7	4	74	2.79×10^5	4.49×10^6	1.21×10^6
	5.7	575	−96.2	33.1	85.1				2.87×10^6	8.01×10^5
3 April 1963	5.2	528	−126.8	39.2	77.4	4	74	3.20×10^5	4.18×10^6	1.29×10^6
	5.6	565	−121.8	34.3	83.9				3.00×10^6	9.07×10^5
4 April 1963	18.9	395	−81.4	−5.3	60.3	19	70	7.39×10^5	3.95×10^6	1.23×10^7
	19.1	364	−78.1	.7	53.4				4.44×10^6	1.84×10^7
4 April 1963	20.9	260	−78.7	35.7	13.6	19	70	1.47×10^6	3.05×10^8	2.69×10^8
	21.3	259	−73.0	40.9	7.2				2.73×10^8	2.30×10^8
4 April 1963	3.4	417	−8.8	52.2	51.3	19	70	6.21×10^5	2.78×10^6	4.88×10^6
	4.0	450	−.3	48.6	57.9				1.36×10^6	2.55×10^6
4 April 1963	3.5	420	−56.3	51.8	52.0	19	70	5.68×10^5	2.65×10^6	5.16×10^6
	4.1	453	−48.1	48.0	58.6				1.34×10^6	2.85×10^6

4 April 1963	4.0	451	−73.0	48.2	57.4	19	70	4.58×10^{5}	1.77×10^{6}	2.59×10^{6}
	4.5	485	−65.9	43.9	64.1				8.90×10^{5}	1.27×10^{6}
4 April 1963	4.9	524	−83.9	38.8	70.1	19	70		2.06×10^{6}	1.18×10^{6}
	5.3	560	−79.0	34.0	76.6				1.31×10^{6}	6.77×10^{5}
4 April 1963	4.6	495	−112.9	42.6	64.6	19	70	3.62×10^{5}	1.80×10^{6}	1.63×10^{6}
	5.0	530	−107.3	37.9	71.1				1.08×10^{6}	9.30×10^{5}
5 April 1963	4.1	471	−73.4	44.7	54.6	32	72	3.55×10^{5}	1.64×10^{6}	3.11×10^{6}
	4.5	505	−67.3	40.2	61.1				6.52×10^{5}	1.61×10^{6}
5 April 1963	4.7	523	−88.9	37.7	64.4	32	72	4.23×10^{5}	1.19×10^{6}	1.68×10^{6}
	5.1	559	−84.2	32.7	70.8				7.26×10^{5}	9.77×10^{5}
5 April 1963	4.4	495	−117.7	41.4	59.2	32	72	2.86×10^{5}	1.16×10^{6}	2.02×10^{6}
	4.8	531	−112.3	36.6	65.7				6.27×10^{5}	9.87×10^{5}
6 April 1963	2.5	389	−1.3	53.7	33.8	19	78	3.86×10^{5}	7.67×10^{6}	9.66×10^{6}
	3.2	420	7.9	50.3	40.4				3.12×10^{6}	5.18×10^{6}
6 April 1963	3.5	440	−60.0	47.6	42.7	19	78	6.13×10^{5}	1.86×10^{6}	5.66×10^{6}
	4.0	474	−53.1	43.2	49.3				7.34×10^{5}	2.85×10^{6}
6 April 1963	3.9	472	−77.9	43.5	47.8	19	78	4.61×10^{5}	1.62×10^{5}	2.65×10^{6}
	4.3	507	−72.1	38.8	54.3					1.04×10^{6}
6 April 1963	4.7	544	−91.2	33.5	61.0	19	78	4.39×10^{5}	2.35×10^{5}	6.93×10^{5}
	5.0	581	−86.9	28.4	67.5				2.06×10^{5}	3.41×10^{5}

[a] From ref. 10.

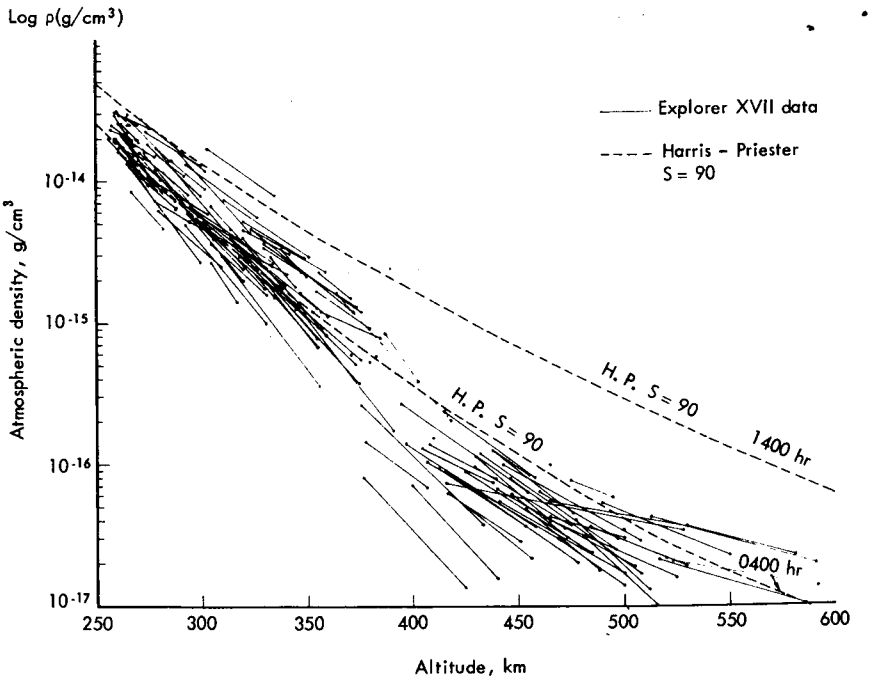

***Figure 1.*—Density profiles from Explorer XVII satellite and the Harris-Priester model for $S=90$. (From ref. 6.)**

10) conveniently arranged in tabular form. It should be noted that the number densities shown are measured values and not values computed from a particular model. Most of the column headings are self-explanatory, so that, e.g., A_p and $F_{10.7}$ are measures of the geomagnetic activity and the solar decimeter flux, respectively. The column marked "α" shows what is essentially the angle between the axis of the spectrometer and velocity vector. The absolute accuracy of the number-density data, state the experimenters, is ± 40 percent. The relative accuracy for a given component varies between ~ 5 and 20 percent and depends upon the angle α. In addition to providing a wealth of new composition data, this experiment provided the first direct measurement of neutral atmospheric helium at satellite altitudes. At any given altitude in orbit, sizable variations in number density were measured.

As reported in reference 10, the average quiet daytime conditions near a 260-kilometer altitude were observed to be: $N(\mathrm{N_2}) = 1.5 \pm 0.5 \times 10^8$ cm^{-3}; $N(\mathrm{O}) = 2.4 \pm 0.4 \times 10^8$ cm^{-3}; and $N(\mathrm{He}) = 1.4 \pm 0.3 \times 10^6$ cm^{-3}.

The average quiet nighttime conditions at 400 kilometers were: $N(N_2) = 2.0 \pm 1.0 \times 10^6$ cm^{-3}; $N(O) = 1.0 \pm 0.4 \times 10^7$ cm^{-3}; and $N(He) = 6.0 \pm 2.0 \times 10^5$ cm^{-3}.

The data show that at about 600 kilometers, helium and atomic oxygen have comparable abundances. In the region from 300 to 600 kilometers, atomic oxygen is the principal constituent, whereas between 250 and 300 kilometers, molecular nitrogen and atomic oxygen, on the average, have comparable number densities. These data also point out the importance of "proper" satellite orbit and lifetime to identify uniquely the effects of such variables as time, location, and altitude on the measurements.

The need for vertical soundings through the atmosphere to obtain neutral atmosphere composition measurements is well recognized. Not only is there a scarcity of data, but also the available data are frequently not accurate enough to permit unique determinations of temperature and temperature gradients in the thermosphere. For a number of reasons this deficiency in the data is particularly serious in the region from 90 to 130 kilometers. Computed high-altitude model atmospheres which are widely used in atmospheric studies are generated from some reference region within this interval. Therefore, uncertainties in the base values and their variations are reflected in the model values at all higher altitudes. However, significant progress has been made recently toward remedying this situation.

Spencer et al. (ref. 8) recently reported day and night firings of thermosphere probes designed to measure the molecular nitrogen concentration and neutral atmospheric temperature. They observed that at 200 kilometers the measured diurnal variation in N_2 density was a factor of 2.8 during the January minimum, and 1.8 during the spring maximum. They state that the absolute accuracy of the concentration measurements is 25 percent or better; the relative accuracy between profiles is 10 percent or better. The temperature results and their implications are discussed later. These values for the daytime-to-nighttime density ratio are significantly larger than the variations predicted from model atmospheres. The thermosphere probe data at 250 kilometers show average N_2 densities lower by approximately a factor of 2 than those of the models. Lower total-density values were also reported by Newton et al. (ref. 6) based on their Explorer XVII density data.

Figure 2 (ref. 11) is a comparison of measured number densities of N_2, O_2, O, and Ar as a function of altitude with predictions (solid curves) based on hydrostatic equilibrium and the ideal gas law. The computed curves were normalized at 150 kilometers. The close agreement between measured and computed values provides confirmation of

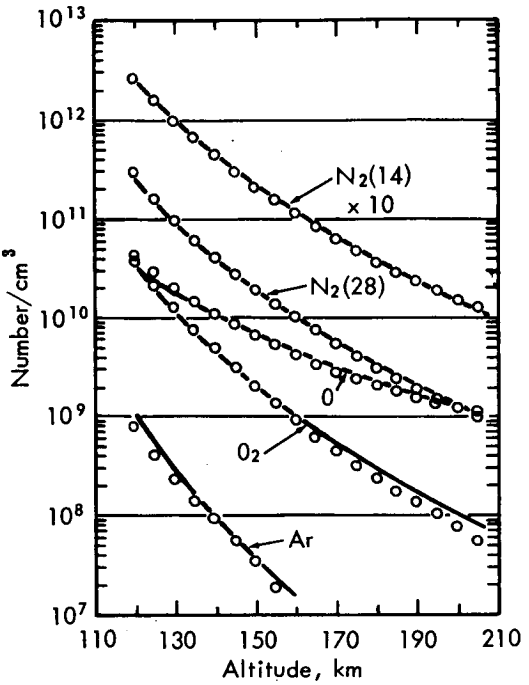

Figure 2.—Number densities of the neutral atmospheric constituents as a function of altitude. (From ref. 11.)

the frequently used assumption that the major atmospheric species are in diffusive equilibrium in this height range.

Nier, (ref. 12) in summarizing results of several rocket firings, notes that on all flights—1963 and 1965—the $N(N_2)/N(Ar)$ ratio indicates a lower altitude for the existence of diffusive equilibrium than that frequently used in model atmospheres (ref. 13). He further reported that his 1965 data showed the number density of atomic oxygen to be less by a factor of about 2 at 200 kilometers than the value he obtained in 1963, while the new measurements of molecular nitrogen and oxygen at this height were approximately twofold higher than those from the earlier flight. His measured helium concentrations provide an approximate value for atmospheric helium abundance which appears to be lower than expected from current model atmospheres, but is in reasonable agreement with extrapolations of the helium data obtained from Explorer XVII (ref. 10). This observed decrease in O and increase in O_2 resulting in an approximately fourfold change in the $N(O)/N(O_2)$ ratio appears to be confirmed by E. J. Schaefer and his coworkers at the University of Michigan. However, based on a firing in December 1965 at 0400 local time, Mauersberger et al. (ref. 14) noted a high content of O described by $N(O)/N(O_2) \approx 1$ at 118 kilometers and ≈ 6 at 150 kilometers. They also show a lower altitude (≈ 107 kilometers)

for diffusive equilibrium. Perhaps their most surprising result is the measurement of an irregularity in the density profiles near 135 kilometers; that is, density is observed to decrease, then increase, and decrease again as the altitude steadily increases. This curious result is discussed further later, both in terms of temperature and gravity-wave manifestations.

Accurate measurements of the neutral concentrations of both major and minor constituents are needed even in the altitude range below the thermosphere; i.e., in the mesosphere itself. Not only are the measurements here important in establishing large-scale motions, escape rates, and so on, but they would materially contribute to an understanding of the physics and chemistry of the processes taking place in this complex environment, particularly since pertinent dissociation and recombination rates are poorly known. It was noted earlier that Barth (ref. 15), using a rocket-borne UV spectrometer, measured the gamma bands of nitric oxide at 2150 Å. The NO profile obtained between 80 and 130 kilometers was quite unexpected. In fact, on the basis of these measurements, it appears that mechanisms other than those recently proposed are needed for explaining the formation of the D-region of the ionosphere. The higher NO density measured might even affect the theories of the nighttime E-region.

As new data are obtained, the understanding of the D-region becomes even more difficult because of the unexpected results obtained. For example, Donahue et al. (ref. 16), analyzing data from their sodium dayglow rocket experiment, detected a narrow layer of neutral sodium at 93.5 kilometers. The maximum density measured was 5×10^4 atoms/cm^3 and the profile conformed closely to that of the 23^+ ion peak reported recently by Narcisi and Bailey (ref. 17). The neutral profile did not contain a second peak as was observed in the ion measurements. Donahue (ref. 16) notes that the narrowness of the ledges, the marked density gradients, and the coincidence of the two curves appear to require a common narrow source at about 93.5 kilometers. On the basis of his in situ rocket measurements of ion distributions in this region, Narcisi (ref. 18) observed that ions of mass-to-charge ratio greater than 48 constitute a large percent of the D-region ionization. They may be, in fact, ions of metals and metal oxides.

Clearly, more data are needed to permit a good understanding of the processes occurring in this region.

Temperature

It was noted earlier (ref. 19) that—

> the temperature distribution of the upper atmosphere becomes isothermal above about 200–300 kilometers. The temperature in this isothermal region

has been found to be variable, ranging between extreme limits of about 600° and 1800° K, but occasionally higher. There is a diurnal variation with the maximum daytime temperature about 1.33 times the minimum nighttime temperature. There are variations from day to day that correlate well with solar activity and geomagnetic variation. There are annual and semiannual variations, the causes of which are not well understood. The longest-term and largest-amplitude variation is associated with the sunspot cycle. There is also a latitudinal variation.

The temperature at the mesopause is variable, generally having its maximum value at high latitudes in winter and its minimum value in summer. At high latitude in summer, the temperature is especially low, near 140° K; these very low temperatures are associated with the presence of noctilucent clouds.

The electron temperature was found to exceed the neutral-particle temperature in the ionospheric E- and F-region and above. The difference is especially pronounced in the early morning hours, and varies inversely as the electron density.

While total-density data alone do not provide a unique measurement of atmospheric temperature, they do provide significant information about increased heating in the upper atmosphere due to, e.g., changes in A_p, the daily geomagnetic index. Explorer XVII density measurements revealed that a greater degree of heating of the atmosphere occurred for small variations in the planetary magnetic index than was previously expected (ref. 6). For example, an increase of 70° K would result from a variation of A_p from 2 to 8; this change correlates with a solar-wind speed change from 350 to 430 km/sec. Thus, instead of the previously determined relationship that the increase of atmospheric temperature is proportional to the geomagnetic index A_p, i.e., $\triangle T \propto A_p$, it is now apparent that for comparatively low values of A_p, a logarithmic approximation is a better representation; i.e., $\triangle T \propto \log A_p$. Satellite drag data taken during quiet geomagnetic conditions also reveal this logarithmic dependence (ref. 20).

From what has been presented, it should be clear that while numerous graphs, charts, and tables appear in the open literature containing numerical values for atmospheric temperature, these values are approximate and in many cases the result of theoretical calculations of what the temperature should be, based on the given assumptions. Similarly, discussions regarding thermal equilibrium in the upper atmosphere must be viewed with the knowledge that in most instances the neutral atmospheric temperature used comes from some appropriate table or model, and does not, in fact, reflect simultaneous measurements of all the parameters being considered. Therefore, the two graphs shown in figures 3 and 4 (ref. 8) are particularly significant and reflect progress toward an accurate description of the thermal structure of the upper atmosphere.

Figure 3 summarizes some of the thermosphere probe temperature measurements based on the scale height of the molecular-nitrogen

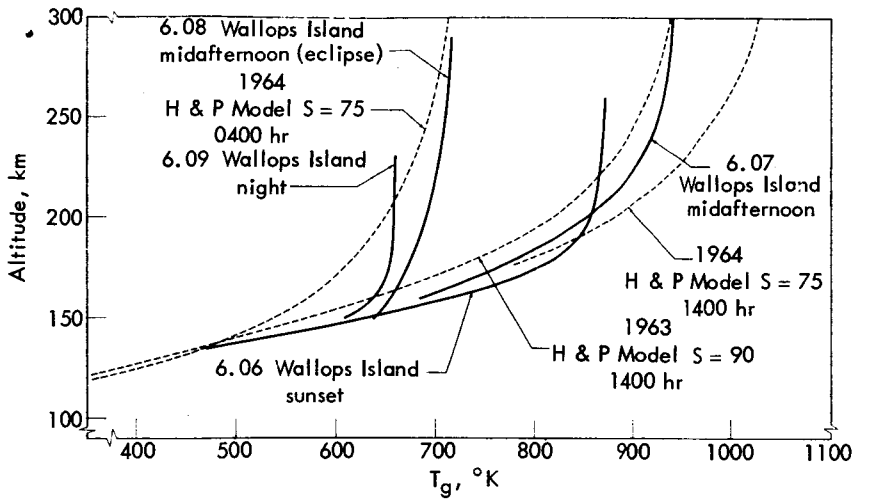

Figure 3.—**Neutral-gas temperature profiles from thermosphere probe measurements and various theoretical model atmospheres.**

density, obtained under different atmospheric conditions. Dashed curves represent appropriate model-atmosphere temperature profiles. These data are discussed in detail in the original text and are shown here to emphasize again the caution which should be exercised in applying model-atmosphere values to physically real problems. Figure 4 displays the diurnal temperature variation (maximum and minimum) obtained from the measured values of N_2 concentration; i.e., data were obtained within a 13-hour interval, under quiet-Sun conditions. Appropriate model-atmosphere temperature profiles are shown for comparison. Particularly noteworthy, in addition to the geophysical data contained here, are the indicated error flags, based not only on the uncertainty in the N_2 density values but also on recognition that "not all possible curves that could be drawn within the density error flags are acceptable. . . ." The point to be noted here is that by obtaining precise data, such as those presented here and eventually even more accurate than those shown, one will be able to discuss unambiguously the temperature gradients in the thermosphere, both to improve our understanding of processes occurring there and to obtain better models. Furthermore, these measurements would also answer the question, "To what extent do internal gravity waves disturb the temperature profile?"

Motions

It has been observed, primarily from sodium release during rocket flights, that strong shear zones exist at altitudes from 70 to 120 kilometers. These shear zones are frequently associated with reversals in the

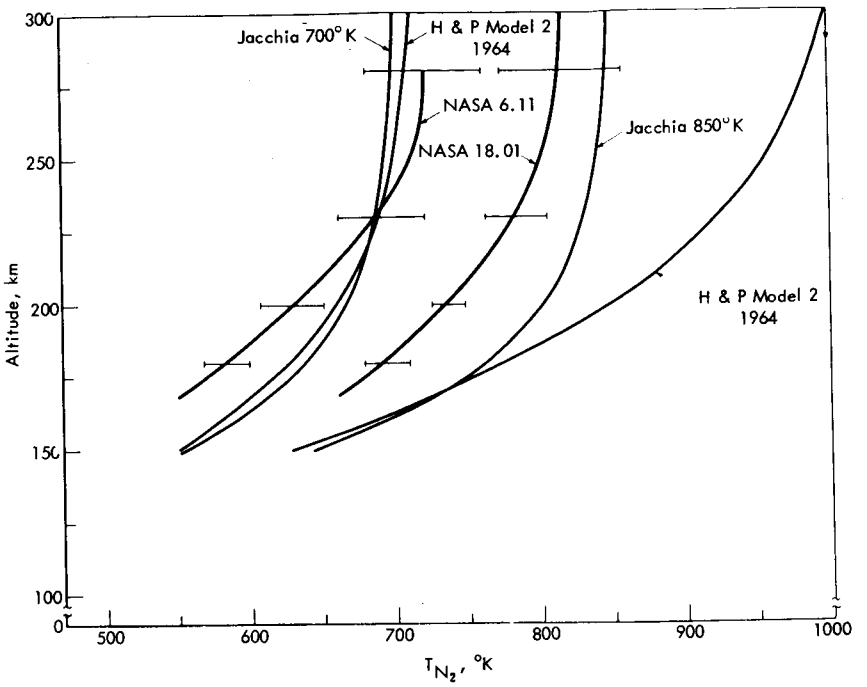

***Figure 4.*—Diurnal temperature variation obtained from measured neutral nitrogen concentration.**

wind which tend to recur with a spacing of a few kilometers. Internal gravity waves were postulated to explain this wind behavior. Recent releases of trimethyl aluminum (TMA) have permitted, on a few occasions, an identification of tidal oscillations. Webb (ref. 21), reporting on data obtained from the Meteorological Rocket Network, notes that a diurnal heat wave and tidal circulation effectively stir the mesopause and provide vertical motions required to support noctilucent-cloud particles. He cites the "strong diurnal temperature variation and resultant tidal circulation generated by the Earth's rotation and ozone absorption of solar ultraviolet in a thin stratopause layer." Current theories (ref. 22) depict this tidal energy as exciting various modes of oscillation, principally with periods of 12 and 24 hours. These modes are not transmitted equally through the ionosphere. The oscillations increase in amplitude until they reach heights from 100 to 120 kilometers, where their energy is dissipated. A number of mechanisms exist for generating smaller scale gravity waves. For example: "The viscous drag [i.e., frictional heating] between successive layers moving in different directions . . . represents a major source of energy transfer from organized wind motions directly into thermal energy content" (ref. 23).

Johnson (ref. 24) notes that—

> Eddy mixing in the lower thermosphere, in conjunction with other well-known physical processes, exerts an important influence on the atmosphere at higher levels. It tends to keep the atmosphere well mixed, and in so doing, it must compete with the effects of molecular diffusion. . . . Changes in the rates of eddy mixing therefore change the altitude above which molecular diffusion predominates. . . . Eddy mixing also produces a heat transport that is generally larger than the molecular conductive heat transport below the turbopause and greater than radiative transfer above about 65 kilometers. This eddy heat transport constitutes an important heat loss from the thermosphere. . . .

While theoretical considerations of the generation and probable effects of tidal and gravity waves have developed to an advanced stage, direct experimental data bearing on these theories are only recently becoming available. Thus, it was noted previously (ref. 19) that ion-temperature measurements (ref. 25) showed a wavelike pattern. It is only recently (refs. 14 and 26) that "unexplained" reversals in the neutral temperature profiles have been observed.

Airglow

The existence of a hydrogen geocorona around the Earth was revealed by hydrogen Lyman-alpha observations made from rockets. The hydrogen emissions (H-alpha and Lyman-alpha) in the upper atmosphere result from fluorescence, or scattering of solar radiation; in addition, an extraterrestrial component of the Lyman-alpha radiation has been identified. Donahue (ref. 27) reports that these "Lyman-alpha and H-alpha airglow observations indicate that there is a diurnal and solar-cycle variation in the hydrogen abundance." They suggest the following values for the hydrogen content:

Table II.—*Estimated Hydrogen Content per Centimeter² Column Above 120 Kilometers*

Period	Day	Night
1957–1959	5×10^{12}	18×10^{12}
1963	12×10^{12}	30×10^{12}
1964	30×10^{12}	50×10^{12}

". . . Generally the agreement with models is best if the density at 100 kilometers is between 2 and 3×10^{7} per cm³" (ref. 27). The numerous theoretical studies describing the proper equilibrium distribution, effects of lateral flow, and other factors, attest to the fact that adequate measurements of the atomic-hydrogen distribution around the Earth are not presently available.

By way of review, it should be noted that Fastie et al. (ref. 28) obtained intensity-altitude profiles for resonance scattering by atomic hydrogen at 1216 Å, atomic oxygen at 1304 and 1356 Å, and atomic nitrogen at 1200 Å, by using a rocket-borne spectrophotometer. Zipf and Fastie (ref. 29) observed the emission-altitude profile for N_2^+ at 3914 Å, and the resonance scattering of nitric oxide in the gamma bands at 2155 Å was observed by Barth (ref. 15).

In a recent Javelin rocket experiment (ref. 30), the nighttime O I emission at 6300 Å was measured.

> The data indicated that the OH and continuum radiation were below the rocket at 120 kilometers as expected, and the red line emission lay in a band stretching from about 150 kilometers to slightly less than 300 kilometers with maximum intensity between 200 and 250 kilometers. The top of this layer appeared to lie at the approximate altitude of F^2 maximum, where an ion mass spectrometer also aboard the rocket measured a sharp maximum in oxygen-ion density. No red radiation above the photometer threshold of about 10 Rayleighs was detected above 300 kilometers.

Reed et al. (ref. 31) reported large variations in the intensity of the 6000-Å line as measured from the OGO II satellite. Nighttime values ranged from 1 to 25 photons/cm^3 sec, and daytime values were approximately an order of magnitude higher.

O'Brien et al. (ref. 32) measured simultaneously the midlatitude night airglow and particle precipitation. From the flight data, it was concluded that the "midlatitude 5577 Å night airglow is not excited by charged-particle bombardment as it is in auroras . . . less than 3 percent of the midlatitude 5577 Å night airglow can be termed permanent aurora . . . . The experiment places an upper limit of 5 R on the brightness of N_2^+ at 3914 Å, and thereby implies that the total midlatitude nighttime ionizing radiation deposits less than 2×10^{-2} erg/cm^2 sec^1 at altitudes above 85 kilometers."

Mars

Before the use of infrared-spectroscopic techniques for studying the Martian atmosphere in 1963, the value given for the Martian surface pressure was of the order of 85 millibars. The first results using the infrared techniques indicated lower values ranging near 25 millibars (ref. 33). This technique is based on the measurement of the strong bands of CO_2 at 1.6 and 2 μ which are pressure broadened (ref. 34) and give a value for the product (CO_2 Abundance) $\times$ (Total pressure). Since the CO_2 abundance can be measured from the weak bands at 8689 and 10 500 Å, a value for the surface pressure is obtained. Spectroscopic measurements made during the recent Mars opposition yield values between 7 and 13 millibars for the surface pressure. The partial pressure of CO_2 at the surface was found to be between 4 and

7 millibars, an indication that CO_2 is the principal constituent of the Martian atmosphere.

Ground-based measurements also indicate that the amount of precipitable water on Mars (ref. 35) is approximately 15 μ when detected. The weak lines appear first over the subliming north polar cap and migrate south over the planet. Owen (ref. 36), based on his measurements for NO_2 absorption and N_2^+ emission, sets an upper limit of 8 micron-atmospheres for the abundance of NO_2 in the Martian atmosphere. The two molecular species N_2 and A are used frequently to account for the difference between the partial pressure of CO_2 and the estimated total surface pressure.

Evans (ref. 37) obtained ultraviolet (2400 to 3500 Å) spectrograms of Mars from an Aerobee-rocket-borne spectrograph launched March 19, 1965. From the data obtained, and from considerations of the atmospheric scattering properties and surface reflectivity, he concluded that the likely upper limit range of the Martian surface pressure is between 10 and 20 millibars. Furthermore, supplying realistic estimates for the value of the reflectivity of the surface and the "blue haze," he obtains a lower limit range of from 5 to 15 millibars.

The Mariner IV occultation experiment also provided new data about the Martian atmosphere (ref. 38).

> Changes in frequency, phase, and amplitude of the Mariner IV radio signal, caused by the passage through the atmosphere and ionosphere of Mars, were observed immediately before and after occultation by the planet. Preliminary analysis yields estimates of the refractivity and density of the atmosphere near the surface, the scale height in the atmosphere, and the electron-density profile of the Martian ionosphere. . . .
>
> Approximately 1 hour after its closest approach to Mars on July 15, 1965, the Mariner IV spacecraft disappeared beyond the limb of the planet, as seen from Earth, and remained in occultation for approximately 54 minutes. Immediately prior to the beginning and immediately after the end of occultation, the spacecraft's S band (2300 megacycles) radio signal passed through the atmosphere and ionosphere of Mars, both on its way up to the spacecraft and on its way to Earth after being coherently retransmitted. When the signal reached the Earth approximately 12 minutes later, it marked the first time that a coherent radio transmission has been used to probe the atmosphere and ionosphere of another planet.

The phase change caused by the atmosphere was 30 wavelengths and that due to the ionosphere was 10 wavelengths. In order to achieve the required measurement accuracy, it was necessary to know the total phase change due to all causes other than the atmosphere and ionosphere of Mars with an accuracy of better than 1 part in 10^{11}. The experimeters stated that they demonstrated this accuracy by their ability to predict the range rate of the probe based on the analysis of tracking data taken before and after planetary encounter to an accuracy of better than 0.0015 meter/second.

245-015 O—67——8

On entry into occultation on the sunlit side (ref. 39), the scale height was estimated to be 9 ± 1 kilometers, and it was concluded that the primary constituent of the lower atmosphere was CO_2 at $\approx180°\pm20°$ K, and at a surface pressure of 4.9 ± 0.8 millibars. An ionosphere was observed, having a maximum electron density of $9.0\pm1.0\times10^4$ electrons/cm^3 at an altitude of 123 ± 3 kilometers. The electron scale height above maximum was 22 ± 3 kilometers. Exit from occultation occurred over a dark region. The scale-height value obtained was 12 ± 1 kilometers. The estimated temperature was $240°\pm20°$ K and the surface pressure was 8.4 ± 1.3 millibars. No ionospheric effect was detected, indicating an upper electron-density limit for a possible layer of $\sim4\times10^3$ electrons/cm^3.

Thus, from ground-based, rocket, and Mariner IV data, a generally consistent picture is obtained of a low Martian surface pressure ranging between about 5 and 10 millibars, the principal atmospheric constituent being CO_2. However, starting with these data and an assumed surface temperature of $\sim200°$ K, one can evolve different models of the Martian atmosphere all of which are consistent with available measurements. This situation results because there are competing physical processes occurring in the Martian atmosphere, and their relative importance cannot be uniquely determined at this time. Some of the models which have been developed are summarized briefly in the following paragraphs.

Johnson (ref. 40) interpreted the ionospheric data to indicate that the electron peak is analogous to the ionospheric F_2 peak on Earth. Since spectroscopic data imply that the atomic oxygen formed by the photodissociation of CO_2 is not swept away by the solar wind, "it must be a principal constituent of the Martian upper atmosphere and its ions must produce the principal band of ionization observed by Mariner IV." Starting with a predominantly CO_2 atmosphere at a surface temperature of 210° K, his model contains a tropopause which occurs at an altitude of 14 kilometers and has a temperature of 140° K. Above this height, the temperature profile shows a decrease with altitude at the rate of 0.64° C per kilometer, following the solid carbon dioxide vapor pressure curve up to 100 kilometers where the temperature is 85° K. At higher altitudes the atmosphere is isothermal. Thus, there is no thermosphere. Several objections have been raised on physical grounds (refs. 41 and 42) to the proposed low exospheric temperature and to the absence of a thermosphere in which temperature increases with altitude.

The model generated by Gross, McGovern, and Rasool (ref. 41) leads to an exospheric temperature of $550°\pm150°$ K. They start with a surface temperature of 200° K and a CO_2 atmosphere that is in radiative equilibrium up to 80 kilometers, at which altitude CO_2 dissocia-

tion by solar ultraviolet radiation becomes effective. Furthermore, it is postulated that above 80 kilometers the dissociation products of CO_2, viz, CO and O, are in diffusive equilibrium. Noting that at an exospheric temperature of 550° K, both H_2 and He will be lost rapidly but that atomic oxygen will not escape, they speculate that the present atmosphere of Mars may be a remnant of a heavier primitive atmosphere similar in composition to that observed on Jupiter today.

> . . . If the total amount of CO_2 in the Martian atmosphere is 5 millibars, then from the cosmic abundance table, it follows that there must be at least 2 millibars of Ne and 1 millibar of N_2 in the atmosphere. Both these gases are difficult to observe from Earth and their identification on Mars must therefore await in situ exploration.

Chamberlain and McElroy (ref. 42)—

> have computed a model atmosphere with 44 percent CO_2 and 56 percent N_2 that will fit the observations, provided that CO_2 is not strongly dissociated. The major ionization is in an E-region produced by solar X-rays; the dominant ion is probably NO^+ or O_2^+. A discussion of the radiative losses by CO_2 shows that a normal thermosphere develops and that the exospheric temperature (at top of thermosphere) is at least 400° K. . . . If the mean molecular weight is considerably larger than that assumed in this model, the observed ionospheric peak might be an F_1 region produced by solar ultraviolet radiation. . . .

Leighton and Murray (ref. 43), based on their study of the heat balance of the planet, conclude that frozen CO_2 is probably the dominant substance comprising the Martian polar caps. Among other observations, they note that—

> . . . The partial pressure of CO_2 in Mars' atmosphere may be regulated by the north polar cap; . . . the total pressure of the Martian atmosphere may change semiannually by a significant amount because of the freezing out of much of the atmospheric CO_2 at either pole. . . .

In reviewing current observations, Rea (ref. 44) notes the essentially permanent presence of particles in the Martian atmosphere. "The most likely prospects for the aerosols are ice or carbon dioxide crystals, or dust particles, with diameters in the submicron region." The yellow clouds are almost certainly due to dust storms. It appears that the white and blue clouds are related and are clouds of crystalline H_2O or CO_2.

Venus

Radio-emission measurements at wavelengths from 3 millimeters to 40 centimeters indicate a Venus average surface temperature of about 600° K. Clark et al. (ref. 45), describing their 10.6-centimeter measurements, report that the surface temperature at the center of the disk lies between 615° and 630° K; at the poles it ranges from 425° to 460° K. The temperature of the subsolar point was $630° \pm 70°$ K. It should be noted here that the interpretation of radio-emission data in

terms of temperature must be regarded as tentative, because of the possibility that the emissions come, at least in part, from nonthermal sources. The surface-pressure value determined from the emission data depends strongly on the assumed composition of the atmosphere. Thus, the surface-pressure estimates vary from about 10 Earth atmospheres to greater than 200 atmospheres. An atmosphere composed of 5 percent CO_2 and 95 percent N_2 would lead to a surface pressure of 100 atmospheres. The CO_2 abundance is a critical factor here and is unknown, although it is generally believed to be less than 5 percent of the atmosphere. The major constituent could be nitrogen.

Infrared measurements indicate that the Venus cloud temperature is about 250° K. The pressure at the cloud level is poorly known and is estimated to lie between 90 and 600 millibars. It is generally accepted that the clouds of Venus are composed of ice crystals. Strong's data (ref. 46), obtained with a balloon-launched 30-centimeter telescope, was corrected for water vapor above the clouds and compared with the reflection spectrum of a laboratory ice cloud at −39° C. The agreement was good, suggesting that there is about 100 μ of water vapor above the Venus ice-crystal clouds. This water-vapor abundance is consistent with results reported by Dollfus (ref. 47). However, there are conflicting data concerning the quantity of water vapor in the atmosphere of Venus. As discussed in reference 48, Spinrad, working at 8200 Å, has been unable to detect any water vapor and has set an upper limit of approximately 10 μ of precipitable water. Each of these investigators applied different techniques to different water-vapor bands. Perhaps these different results reflect a large variation in the opacity of the atmosphere of Venus in the near infrared. Deirmendjian (ref. 49) compared Strong's cloud spectrum with spectra of dense cirrus ice clouds on Earth obtained from instruments aboard a high-flying airplane, and also obtained good agreement. Strong (ref. 46) notes that the presence of water vapor and ice clouds can explain why the shady side of the planet is approximately the same temperature as the sunlit side. He suggests that the heat source is the latent heat of water vapor, liberated as the vapor condenses to form clouds. Sagan et al. (ref. 50) estimates that the cloud particles have a mean radius ranging between 7.5 and 10 μ, and thus permit up to about 50 percent of the incident sunlight to penetrate to the planet's surface. However, since these clouds are opaque to the thermal radiation from the planet, an efficient "greenhouse effect" is operative.

REFERENCES

1. JACCHIA, L. G.; AND SLOWEY, J.: The Shape and Location of the Diurnal Bulge. Smithsonian Institution Astrophysical Observatory, Special Report no. 207, 1966.
2. KEATING, G. M.; AND PRIOR, E. J.: Latitudinal and Seasonal Variations in Atmospheric Densities Obtained During Low Solar Activity by Means of the Inflatable Air Density Satellites. Paper presented at the Seventh International Space Science Symposium (COSPAR) (Vienna, Austria), 1966.
3. JACCHIA, L. G.: Density Variations in the Heterosphere. Ann. Geophys., vol. 22, no. 1, 1966, pp. 75–85.
4. PRIESTER, W.: On the Variations of the Thermospheric Structure. NASA TN D–3167, 1965.
5. DE VRIES, L. L.; FRIDAY, E. W.; AND JONES, L. C.: Analysis of Density Data Deduced From Low-Altitude High Resolution Satellite Tracking Data. Paper presented at the Seventh International Space Science Symposium (COSPAR), (Vienna, Austria), 1966.
6. NEWTON, G. P.; HOROWITZ, R.; AND PRIESTER, W.: Atmospheric Density and Temperature Variations From the Explorer XVII Satellite and a Further Comparison With Satellite Drag. Planetary Space Sci., vol. 13, 1965, pp. 599–616.
7. HARRIS, ISADOR; AND PRIESTER, WOLFGANG: Theoretical Models for the Solar-Cycle Variation of the Upper Atmosphere. NASA TN D–1444, p. 261.
8. SPENCER, N. W.; TAEUSCH, D. R.; AND CARIGNAN, G. R.: N_2 Temperature and Density Data for the 150 to 300 km Region and Their Implications. Ann. Geophys., vol. 22, no. 2, 1965, pp. 151–160.
9. FAIRE, A. C.; AND CHAMPION, K. S. W.: Paper presented at the Sixth International Space Science Symposium (COSPAR), (Mar del Plata, Argentina), 1965.
10. REBER, C. A.; AND NICOLET, M.: Investigation of the Major Constituents of the April–May 1963 Heterosphere by the Explorer XVII Satellite. Planetary Space Sci., vol. 13, 1965, pp. 617–646.
11. HEDIN, A. E.; AND NIER, A. O.: Diffusive Separation in the Upper Atmosphere. J. Geophys. Res., vol. 70, no. 5, 1965, pp. 1273–1274.
12. NIER, A. O.; AND HEDIN, A. E.: The Neutral Composition of the Lower Thermosphere. Paper presented at the Seventh International Space Science Symposium (COSPAR), (Vienna, Austria), 1966.
13. Working Group IV of COSPAR, 1965: CIRA 1965. COSPAR International Reference Atmosphere, second ed., North-Holland Pub. Co. (Amsterdam), 1965.
14. MAUERSBERGER, K.; MÜLLER, D.; OFFERMANN, D.; AND VON ZAHN, U.: Neutral Constituents of the Upper Atmosphere in the Altitude Range of 110 to 160 km Above Sardinia. Paper presented at the Seventh International Space Science Symposium (COSPAR), (Vienna, Austria), 1966.
15. BARTH, C. A.: Rocket Measurement of the Nitric Oxide Dayglow. J. Geophys. Res., vol. 69, 1964, pp. 3301–3303.
16. DONAHUE, T. M.: The Problem of Sodium Distribution. Paper presented at the Seventh International Space Science Symposium (COSPAR), (Vienna, Austria), 1966.
17. NARCISI, R. S.; AND BAILEY, A. D.: Mass Spectrometric Measurements of Positive Ions at Altitudes From 64 to 112 Kilometers. J. Geophys. Res., vol. 70, no. 15, 1965, pp. 3687–3700.

18. NARCISI, R. S.: Ion Composition of the Mesosphere. Paper presented at the Seventh International Space Science Symposium (COSPAR), (Vienna, Austria), 1966.
19. ANON.: Significant Achievements in Planetary Atmospheres: 1958–1964, NASA SP-98, 1966.
20. JACCHIA, L. G.; AND SLOWEY, J.: Temperature Variations in the Upper Atmosphere During Geomagnetically Quiet Intervals. J. Geophys. Res., vol. 69, no. 19, 1964, pp. 4145–4148.
21. WEBB, W. L.: Circulation of the Middle and Upper Atmosphere. Paper presented at the Seventh International Space Science Symposium (COSPAR), (Vienna, Austria), 1966.
22. HINES, C. O.: Tides, Gravity Waves and Shear Waves. Paper presented at the Seventh International Space Science Symposium (COSPAR), (Vienna, Austria), 1966.
23. ROSENBERG, N. W.: Chemical Releases at High Altitudes. Science, vol. 152, no. 3725, 1966, pp. 1017–1027.
24. JOHNSON, F. S.: Turbopause Processes and Effects. Paper presented at the Seventh International Space Science Symposium (COSPAR), (Vienna, Austria), 1966.
25. KNUDSEN, W. C.; AND SHARP, G. W.: Evidence for Temperature Stratification in the E Region. J. Geophys. Res., vol. 70, 1965, pp. 143–160.
26. FAIRE, A. C.; AND CHAMPION, K. S. W.: Falling Sphere Measurements of Atmospheric Density, Temperature, and Pressure at Fort Churchill, Canada, and Eglin, Florida. Paper presented at the Seventh International Space Science Symposium (COSPAR), (Vienna, Austria), 1966.
27. DONAHUE, T.: The Problem of Atomic Hydrogen. Aeronomy Symposium of the International Association of Geomagnetism and Aeronomy (Cambridge, Mass.), Aug. 16–20, 1965. (Abstract, IAGA News, vol. 4, Nov. 1965, p. 52.)
28. FASTIE, W. G.; CROSSWHITE, H. M.; AND HEATH, D. F.: Rocket Spectrophotometer Airglow Measurements in the Far Ultraviolet. J. Geophys. Res., vol. 69, 1964, pp. 4129–4140.
29. ZIPF, E. C.; AND FASTIE, W. G.: An Observation of the (0,0) Negative Band of N_2^+ in the Dayglow. J. Geophys. Res., vol. 69, 1964, pp. 2357–2368.
30. GULLEDGE, I. S.; AND PACKER, D. M.: Altitude Distribution of the Nighttime OI Emission at 6300 Å. (Abstract, Trans. A.G.U., vol. 46, no. 1, 1965, pp. 61–62.)
31. REED, E. I.; AND BLAMONT, J. E.: Some Results Concerning the Principal Airglow Lines as Measured From the OGO II Satellite. Paper presented at the Seventh International Space Science Symposium (COSPAR), (Vienna, Austria), 1966.
32. O'BRIEN, B. J.; ALLUM, F. R.; AND GOLDWIRE, H. C.: Rocket Measurement of Midlatitude Airglow and Particle Precipitation. J. Geophys. Res., vol. 70, no. 1, 1965, pp. 161–174.
33. KAPLAN, L. D.; MÜNCH, G.; AND SPINRAD, H.: An Analysis of the Spectrum of Mars. Astrophys. J., vol. 139, 1964, pp. 1–15.
34. HUNTEN, D. M.: CO_2 Bands and the Martian Surface Pressure. Paper presented at the Cal Tech-JPL Lunar and Planetary Conference, Sept. 13–18, 1965, JPL Tech. Memo no. 33–266, 1965, pp. 240–244.
35. SPINRAD, H.: Spectroscopic Observations of Mars, 1964–65. Paper presented at the Cal Tech-JPL Lunar and Planetary Conference, Sept. 13–18, 1965, JPL Tech. Memo no. 33–266, 1965, pp. 245–246.

36. OWEN, T.: Recent Observations of the Photographic Spectrum of Mars—A Preliminary Report. Paper presented at the Cal Tech-JPL Lunar and Planetary Conference, Sept. 13–18, 1965, JPL Tech. Memo no. 33–266, 1965, pp. 247–251.
37. EVANS, D. C.: Ultraviolet Reflectivity of Mars. Science, vol. 149, no. 3687, 1965, pp. 969–972.
38. KLIORE, A.; ET AL.: Occultation Experiment: Results of the First Direct Measurement of Mars' Atmosphere and Ionosphere. Science, vol. 149, 1965, pp. 1243–1248.
39. KLIORE, A.; CAIN, D. L.; AND LEVY, G. S.: Radio Occultation Measurement of the Martian Atmosphere Over Two Regions by the Mariner IV Space Probe. Paper presented at the Seventh International Space Science Symposium (COSPAR), (Vienna, Austria), 1966.
40. JOHNSON, F. S.: Atmosphere of Mars. Science, vol. 150, 1965, pp. 1445–1448.
41. GROSS, S. H.; MCGOVERN, W. E.; AND RASOOL, S. I.: Mars: Upper Atmosphere. Science, vol. 151, 1966, pp. 1220–1221.
42. CHAMBERLAIN, J. W.; AND MCELROY, M. B.: Martian Atmosphere: The Mariner Occultation Experiment. Science, vol. 152, 1966, pp. 21–25.
43. LEIGHTON, R. B.; AND MURRAY, B. C.: Behavior of Carbon Dioxide and Other Volatiles on Mars. Science, vol. 153, 1966, pp. 136–144.
44. REA, D. G.: The Atmosphere and Surface of Mars—A Selective Review. Paper presented at the Cal Tech-JPL Lunar and Planetary Conference, Sept. 13–18, 1965, JPL Tech. Memo No. 33–266, 1965, pp. 209–238.
45. CLARK, B. G.; AND KUZMIN, A. D.: Observations of 10.6 cm Radiation From Planet Venus. Physics Today, vol. 18, Sept. 1965.
46. STRONG, J.: Balloon Telescope Studies of Venus. Paper presented at the Cal Tech-JPL Lunar and Planetary Conference, Sept. 13–18, 1965, JPL Tech. Memo no. 33–266, 1965, pp. 147–149.
47. DOLLFUS, A.: Contribution au Colloque. Paper presented at the Cal Tech-JPL Lunar and Planetary Conference, Sept. 13–18, 1965, JPL Tech. Memo no. 33–266, 1965, pp. 187–202.
48. MUHLEMAN, D. O.: Summary Remarks on Venus. Paper presented at the Cal Tech-JPL Lunar and Planetary Conference, Sept. 13–18, 1965, JPL Tech. Memo no. 33–266, 1965, pp. 203–205.
49. DEIRMENDJIAN, D.: Comments on the Detection of Water and Ice Clouds on Venus. Paper presented at the Cal Tech-JPL Lunar and Planetary Conference, Sept. 13–18, 1965, JPL Tech. Memo no. 33–266, 1965, pp. 150–154.
50. SAGAN, C.; AND POLLACK, J. B.: Properties of the Clouds of Venus. Paper presented at the Cal Tech-JPL Lunar and Planetary Conference, Sept. 13–18, 1965, JPL Tech. Memo no. 33–266, 1965, pp. 155–163.

PLANETOLOGY

M. W. Molloy and Urner Liddel
Lunar and Planetary Programs
Office of Space Science and Applications, NASA

Planetology

SUMMARY

THE MOST FRUITFUL, and spectacular, achievements in planetology during 1965 were made by space probes. Mariner IV revealed the scientifically startling fact that large craters cover at least a part of the Martian surface. The Ranger VIII and IX missions extended our detailed knowledge of the lunar mare and crater floors, while the Soviet Zond III recorded new images of the hidden face of the Moon. Gemini missions IV to VII returned synoptic terrain photographs of the Earth's surface, in color from orbit, providing an indication of the data quality anticipated from manned lunar missions. The U.S.S.R. spacecraft Venera II passed within 14 900 miles of Venus on February 27, 1966; Venera III impacted the planet on March 1, 1966, but did not return data on the descent to the surface because of communications failure.

Significant progress continued in Earth-based observations of the Moon. Hundreds of hot spots on the lunar surface, which correspond to sharp hemispherical craters, were revealed by infrared mapping. High-resolution radar is providing additional reflectivity data on these and other lunar features. Cartographic and photogeologic mapping of the Moon at 1:1 000 000 scale is approaching completion, while mapping of the lunar equatorial belt (Apollo landing zone) at 1:500 000 scale is well underway. Ten potential lunar landing sites for Surveyor and Apollo have been designated for Lunar Orbiter photographic coverage, and the scientific community has been invited to concentrate investigation on these sites.

Optical, radio, and radar astronomy continued to probe the nature of other planets. The presence of major mountain chains on Venus is indicated by radar investigations, while Jupiter appears to be behaving like a star, as well as a planet, by releasing more heat than is probably manufactured in its own interior by ordinary radioactivity.

Meteorite research achieved significant advances, the result, to a large extent, of electron microprobe studies; tektite investigations concentrated on the supposed sources of tektites by means of structural and microchemical investigations.

Terrestrial analogs of lunar and planetary surface features were studied in the field and in the laboratory by regional mapping of major geologic structures of volcanic and possible meteorite impact origin, by hypervelocity impact investigations, and by detailed mineralogic studies of shock effects.

Two major planning sessions were held, one by the Space Science Board of the National Academy of Sciences (ref. 1) and the other by NASA (ref. 2), which resulted in the recommendation of scientific objectives and priorities for the exploration of the Moon and the planets over the next two decades.

INTRODUCTION

This report summarizes achievements in the discipline of planetology during 1965, the seventh year since the formation of the National Aeronautics and Space Administration (NASA). These accomplishments encompass space-flight investigations, ground-based observations and experiments, and theoretical studies.

For the most part, this is a continuation of the 1958 to 1964 report, with additional detail in the areas of Earth-based investigations and meteorite studies. As an introduction, the scope of planetology and the techniques of investigation are summarized from the 1958 to 1964 report (Beckerley, ref. 3).

It should be noted that this report includes information only to January 31, 1965—not modified by later observations and conclusions.

SCOPE OF PLANETOLOGY

Planetology is the study of the condensed material of the solar system: the planets (including Earth), satellites, asteroids, comets, meteorites, and related objects. These solid objects can be studied with respect to their isotopic, elemental, and chemical compositions; the combination, arrangement, and evolution of the mineral phases and rock units present; the textural, topographic, and geomorphic properties of the surface; the internal structure and body properties of the solid objects as entities; and the origin, history, and potential development of these objects.

The evolution of ancient life forms and large-scale climatic features are of interest to planetology; in these respects this discipline verges on biosciences and planetary atmospheres. The interaction of the interplanetary medium with the condensed material of the solar system may result in the modification of surface material and the creation of

internal fields; in these respects, the disciplines of solar physics and particles and fields relate to planetology. With the exception of meteorite analyses and spacecraft measurements, primary data on these solid objects have been assembled by means of terrestrial observations at many points on the electromagnetic spectrum; in this respect, planetology has depended and continues to depend on astronomy.

The objective of planetology studies is the understanding of the objects in the solar system, excluding the Sun. The techniques employed encompass many of the methods developed to investigate the Earth. Measurements of other planets have initiated a comprehensive program of correlating planetary properties. Comparative planetology will provide an appreciation of the equation of state of condensed material throughout the solar system. In turn, this understanding will result in significant advances in the study of the origin, development, and future of the Earth as a planet.

TECHNIQUES OF INVESTIGATION

The tools employed by planetologists are numerous and diverse. Space-flight investigations acquire remotely sensed and analytical measurements of lunar and planetary bodies from flyby, orbiting, impacting, and landing spacecraft. In the future, samples returned and observations by scientist-astronauts are expected to complement and enhance these measurements.

The most comprehensive techniques to date have been the methods of classical and modern astronomy: the optical telescope with imaging, photometric, polarimetric, radiometric, and spectroscopic auxiliaries; and radar pulse and radio-emission investigations.

A blend of astronomical and space-probe techniques is about to reach fruition in the Orbiting Astronomical Observatory (OAO). OAO missions in the future could provide measurements of the Moon and planets as well as of stellar and galactic objects. At present, balloon-borne and rocket-borne instrumentation, raised above the veil of the Earth's atmosphere, seek answers to these celestial problems.

Photogeologic techniques, which involve the systematic analysis of photographic images supplemented by telescopic observations, have been successful in determining the gross structure and stratigraphy of the lunar surface. Topographic base maps for this research have been prepared by photogrammetric techniques using photographs taken in varying lunar librations. Both the photogeologic and photogrammetric methods are being used on the imagery acquired by the Ranger and Mariner spacecraft.

Laboratory methods include the comprehensive investigation of meteorite, tektite, and cosmic dust specimens; simulation studies of lunar, and now Martian features; and hypervelocity impact, shock, and ultra-high-pressure studies. Field investigations emphasize the analogies between terrestrial, lunar, and planetary counterpart features, at all scales.

Finally, theoretical analyses extend from inductive synthesis of planetary interior models to deductive construction of lunar surface fine structure. Encompassed within these extremes are hypotheses concerning the nature and origin of lunar and planetary bodies, their similarity to the Earth, and the future development of the solar system.

OBSERVATIONS FROM SPACECRAFT

The year 1965 was one of outstanding lunar, planetary, and Earth-orbital spaceflight success. (See figs. 1 and 2.)

Ranger VIII, launched February 17, 1965, achieved the second successful lunar photographic impact mission, obtaining 7137 pictures from the southwestern portion of the Moon to the Sea of Tranquility.

Ranger IX impacted in the floor of the crater Alphonsus on March 24, 1965, completing the Ranger series of launches, and obtaining 5814 pictures some of which were viewed live from the Moon over the nationwide television networks.

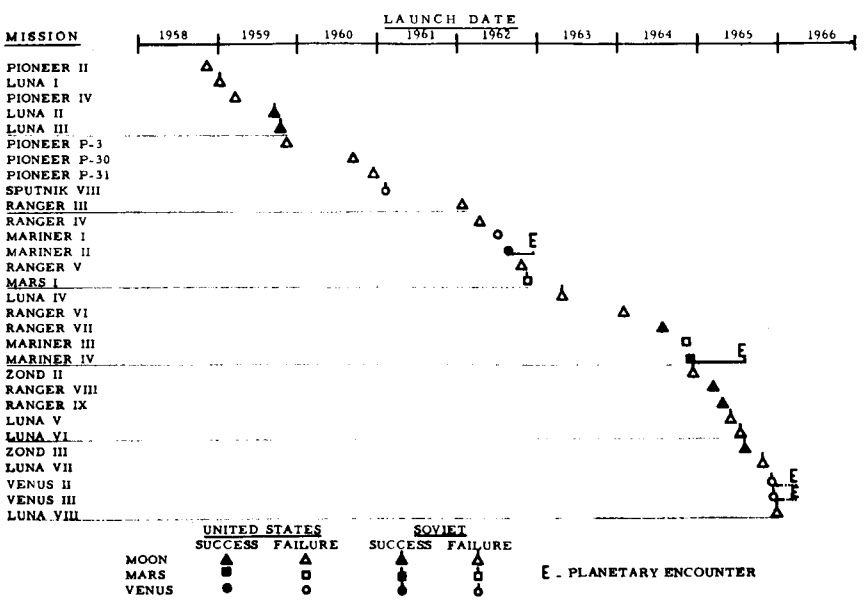

Figure 1.—**Lunar and planetary flight record.**

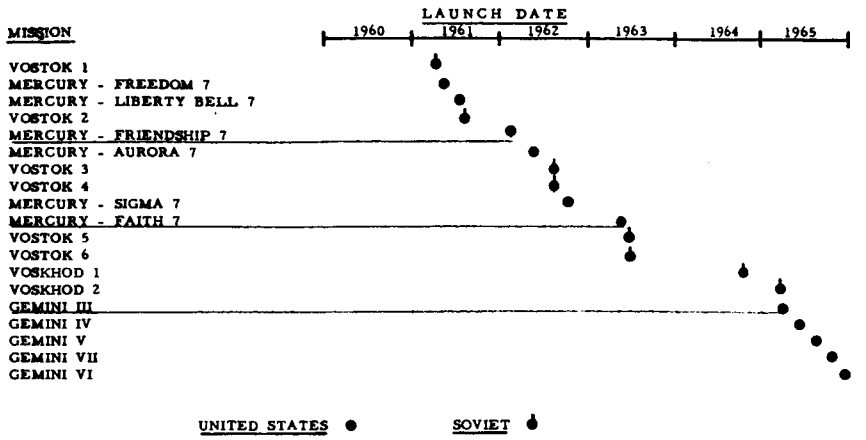

Figure 2.—**Manned Earth-orbital flight record.**

Mariner IV completed a successful flyby of the planet Mars on July, 14, 1965, acquiring 22 television images of the Martian surface, occultation measurements of the Martian atmosphere, and particles and fields measurements of the planetary environment.

Zond III photographed the far side of the Moon on July 20, 1965, obtaining images of a heretofore unknown part of the lunar surface. Certain photographs overlap with the visible side of the Moon; others adjoin the 1959 Luna III photographs of the concealed side.

Luna V, VI, VII, and VIII impacted the Moon between May and December 1965, after unsuccessful attempts to achieve soft landings on the lunar surface.

Venera II and III were launched by the Soviets on November 12 and 16, 1965, on trajectories toward the planet Venus. The December 21, 1965, report from the U.S.S.R. indicated that both the spacecraft and scientific instrumentation were functioning normally.

The manned Gemini series of Earth-orbital flights began with Gemini III on March 23, 1965; followed by Gemini IV on June 3–7, 1965; Gemini V on August 21–29, 1965; Gemini VII on December 4–18, 1965; and Gemini VI on December 15–16, 1965. Synoptic terrain photography was the primary planetology experiment on these flights. The Gemini photographs are similar to the imagery expected from manned lunar orbital missions, providing a detailed, regional picture of geologic structure, stratigraphy, and geomorphology for selected portions of the terrestrial surface.

Ranger Missions VII, VIII, and IX

Since the summer of 1964, three Ranger spacecraft have been launched on successful lunar photographic missions. Ranger VII,

launched July 31, 1964, took 4316 high-quality photographs of the Moon's surface (refs. 2, 4, 5, 6, and 7), before impacting at lunar coordinates 10.7° S, 20.7° W, in the northwestern portion of Mare Nubium. The impact area is traversed by outlying rays from the craters Copernicus and Tycho, with the landing point itself at the trailing end of a fan-shaped ray of Tycho. The region in which the Ranger VII photographic mission terminated was subsequently named "Mare Cognitum" by the 12th General Assembly of the International Astronomical Union.

Ranger VIII was launched on February 17, 1965, and impacted the Moon on February 20, 1965, at 2.7° N, 24.8° E, in Mare Tranquillitatis, after taking 7137 photographs of excellent quality. Unlike Rangers VII and IX, which plunged nearly vertically into the Moon, Ranger VIII approached at an angle that permitted its cameras to sweep across a large segment of the lunar surface. It was possible, therefore, to obtain pictures of a wide variety of lunar features, including the first closeups of lunar highlands, a relatively low-level view of the border area of Mare Tranquillitatis clearly showing lunar rills, and irregular or linked depressions.

Ranger IX was launched on March 21, 1965, and impacted on March 24 at 12.9° S, and 2.4° W, in the northeastern sector of the interior of the crater Alphonsus, after taking 5814 photographs comparable in quality to those taken by Rangers VII and VIII. These were the first pictures taken inside a lunar crater at close range and were transmitted over public television during the last minutes of the flight.

The scientific accomplishments of the Ranger missions may be summarized in terms of—

(A) Gain in resolution.

(B) Detailed structure of the mare floor.

(C) Structure of the crater Alphonsus and surroundings.

Some of the outstanding observations which have resulted from the major gain in resolution provided by the Ranger imagery include: the predominance of craters in the lunar topography, down to the smallest areas; the absence of rubble on the surface; the smoothed and "windblown" appearance of the countless shallow depressions which dominate the topography below a scale of 300 meters; the striking similarity of mare and crater floors; and the complex nature of the crater Alphonsus, which evidences both internal and external forces in shaping its features.

The following summary of scientific interpretations by the Ranger Experimenter Team (R. L. Heacock, G. P. Kuiper, E. M. Shoemaker, H. C. Urey, and E. A. Whitaker) is excerpted from the Ranger VII

report (Heacock et al., ref. 8) and the Ranger VIII–IX report (Heacock et al., ref. 9).

Target Selection

The results and conclusions from the Ranger flights may be better appreciated if the basis for the lunar target selection is understood. The lunar maria have been categorized on the basis of the slight shift in their reflected solar spectra toward red or blue (fig. 3).

Figure 3.—Red and blue lunar mare. (Courtesy of the Lunar and Planetary Laboratory, University of Arizona.)

245-015 O—67——9

Figure 3 shows a photograph of the Mare Imbrium region of the lunar surface; the darker tones should be interpreted as the redder sections. This photograph was printed from a sandwich consisting of an original negative ultraviolet plate and a positive copy of an original negative infrared plate, both taken at the 82-inch telescope of the McDonald Observatory of the University of Texas on May 29, 1964.

Ranger VII impacted a "red" mare area now called Mare Cognitum. Since further classification of lunar maria was scientifically significant and important to the manned landing program, Ranger VIII was targeted to sample a representative blue mare in the Apollo landing zone. The landing sites on the Moon for each Ranger mission are indicated in figure 4.

The prime alternatives for Ranger IX were highland terrain and targets of specific scientific interest. Since Ranger VII had viewed

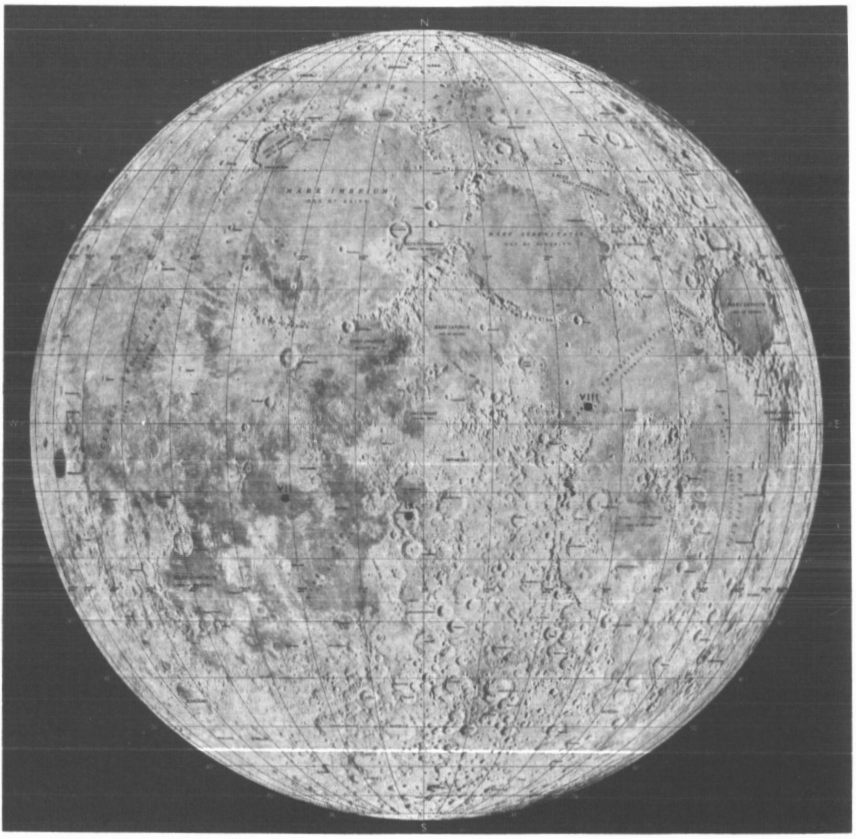

Figure 4.—Ranger VII, VIII, and IX lunar landing sites.

highland terrain in its impact in Mare Tranquillitatis, it appeared opportune to direct Ranger IX to one of several large lunar craters. The crater Alphonsus, on the northeastern edge of the Mare Nubium, is distinguished by a central peak which is suspected of having emitted gases (Kozyrev, ref. 10). Eight prominent dark-halo craters mark the floor of Alphonsus; all are associated with peripheral rills on the crater floor. Ranger IX, therefore, was aimed to, and successfully impacted on, the floor of the crater Alphonsus between the central peak and a group of prominent dark-halo craters.

Figure 5 shows the eastern edge of the Alphonsus floor with part of the surrounding wall in the right-hand portion of the picture. The crater floor is cut by prominent rills which are lined with dark-halo-type craters that have covered part of the rills. The crater walls have soft contours and are almost featureless.

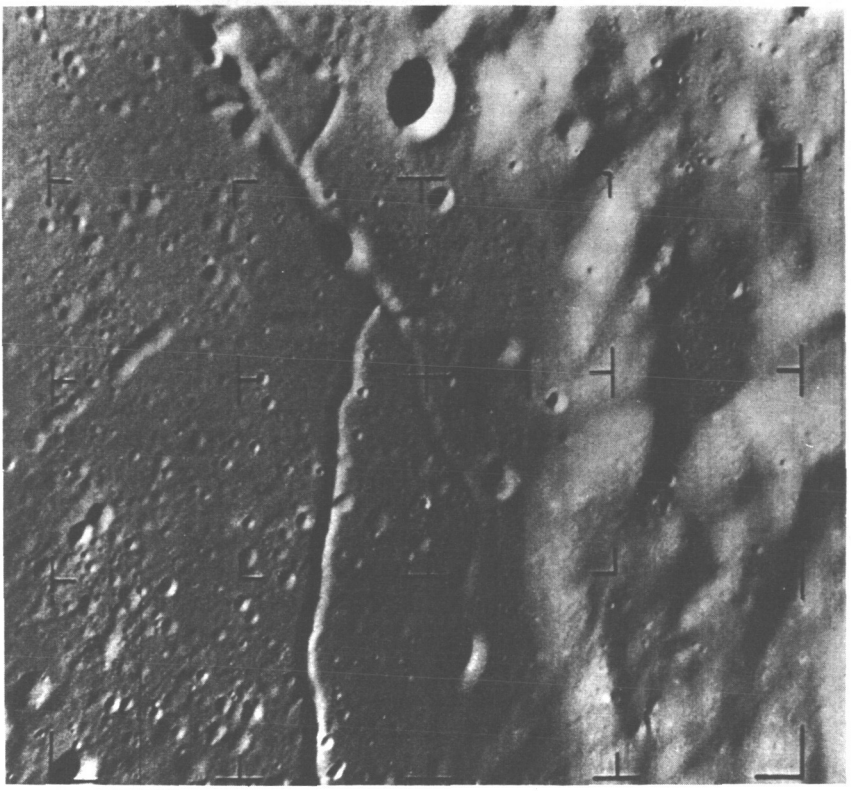

Last full B-camera frame, Ranger IX. Time: 1 minute and 17 seconds before impact. Spacecraft altitude: 115 miles above Moon. North is at the top.

Figure 5.—Dark-halo craters on the floor of the crater Alphonsus.

The interest of the Ranger program in mare-type terrain reflects the conviction that the maria are less precipitous than the uplands, have a shorter and less complex history, and are likely to be more interpretable. The absence in the maria of large mountain systems and a dense overlapping distribution of craters favored their selection for soft landings of Surveyor and Apollo spacecraft.

In retrospect, these estimates appear to have been valid, although some reservation must be made on the simplicity of the mare surface because of the discovery of numerous collapse depressions, first found by Ranger VII and confirmed on the Ranger VIII and IX records.

Resolution Gain

The progressive increase in resolution in successive photographs, taken as the spacecraft approaches the Moon, provides a transition from features known from Earth-based observations to new features never seen before. The Ranger imagery of the lunar surface represents a gain in resolution of 1000 times beyond the existing Earth-based capability. This increase represents a marked advance in the state of knowledge of detailed and large-scale lunar features, which is comparable to the invention of the microscope in medical science. The best resolution ever achieved in ground-based lunar photography is 270 meters obtained in a series of records by G. Herbig in 1963 with the Lick Observatory 120-inch telescope. The performance of a successful terminal attitude maneuver on the Ranger IX mission resulted in a resolution of approximately 0.3 meter in the final images. Ranger VII achieved 0.5 meter final resolution; Ranger VIII obtained a resolution of approximately 1.5 meters. The quality of the Ranger record from all three flights is uniformly good to excellent.

Detailed Structure of the Mare Floor

Cratered Topography

One of the most apparent new facts is that craters are the dominant topographic features of the lunar surface at all scales down to the smallest features observed (less than 1 meter across). (See fig. 6.) The number of craters continues to increase rapidly with decreasing crater size in accordance with the trends established from Earth-based observations.

Figure 6 shows craters down to 40 feet in size. Several large shallow depressions with "tree-bark" texture in their walls can be seen, in addition to many dimple craters near the top and lower left margins.

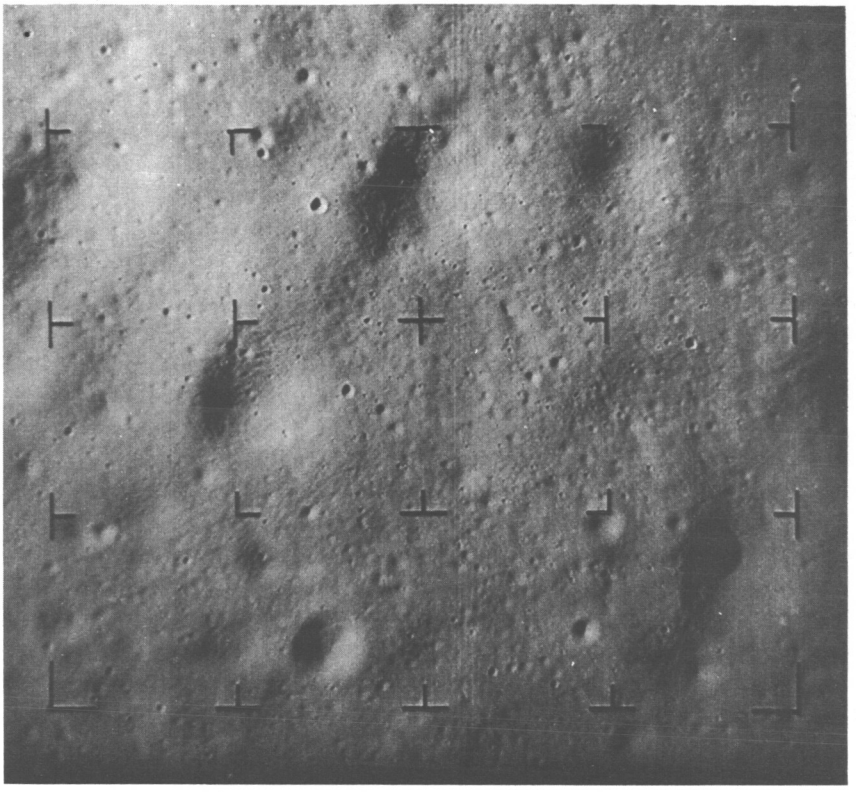

Time: 2.97 seconds before impact. Spacecraft altitude: 4.5 miles above Moon. Dimensions: 2.1 by 2.0 miles.

Figure 6.—**Last complete A-camera frame exposed by Ranger IX, showing "tree-bark" texture.**

Absence of Protuberances

A major fact revealed by the Ranger photographs is the scarcity of small positive-relief features, including small surface bumps or isolated protuberances. The absence of rocks strewn all over the lunar surface is a striking aspect of the Ranger photographs. Except for crater rims and wrinkle ridges on the mare surface, which have been known from Earth-based telescope observation, protuberances are so rare in the high-resolution photographs as to require very careful search to be discovered.

"Windblown" Surface

Most of the craters smaller than 250 or 300 meters in diameter have smoothly rounded rims. In this respect they differ strikingly from

most of the larger craters on the lunar maria observed through a telescope. This is one of the most significant new facts established by the Ranger VII photographs.

Craters less than 300 meters across have a large variation in depth-to-diameter ratio. The majority are proportionately shallower and have more gentle interior slopes than larger craters. These differences give a "smoothed" or "windblown" appearance to the highest resolution photographs. It seems certain that considerable smoothing of the smaller craters has occurred, which seems to have very nearly obliterated craters as large as 300 to 400 meters in some cases. This interpretation indicates that the fragmented material on the inside of these craters may be some 30 to 40 meters deep.

Fine Structure of the Mare Floor

One of the most significant discoveries achieved by the Ranger photographs was the observation of the fine structure of the mare floor. Figure 7 (ref. 8) is a photomosaic composed of the last highest resolution photograph from the Ranger VII F-A-camera, with the last five partial-scan camera photographs superimposed. This mosaic shows the fine structure of the Moon's surface as revealed by Ranger VII, and illustrates the increasing detail captured as the Ranger approached the lunar surface. The darker areas running as continuing bands between shallow craters are resolved into much structural detail, similar in appearance to tree bark or glacial moraines. Dr. Kuiper notes the similarity of these continuous flow bands to patterns observed in terrestrial lava flows on Mauna Loa, Hawaii, and to glacial moraines, both of which are two-layered structures with similar mechanisms of motion and deposition.

Collapse Features

There is considerable evidence for collapse features in the open crevasses, in the shallow, elongated, rimless valleys, and possibly in the dimple craters. Some of the dimple craters, which have conical walls steepening toward the center, look as though slumping has occurred into a crevasse below. Some of the dimples have small objects at the bottom. This may indicate that there are rocky or metallic objects lying near the surface in a layer of soft, porous material. The depth of such material would be at least equal to the depth of the dimples; that is, up to some 20 meters.

Secondary Craters

Secondary craters, resulting from the throwout of material from a primary impact site, are abundantly represented in the Ranger VII and VIII photographs. Figure 8 is a Ranger VII photograph show-

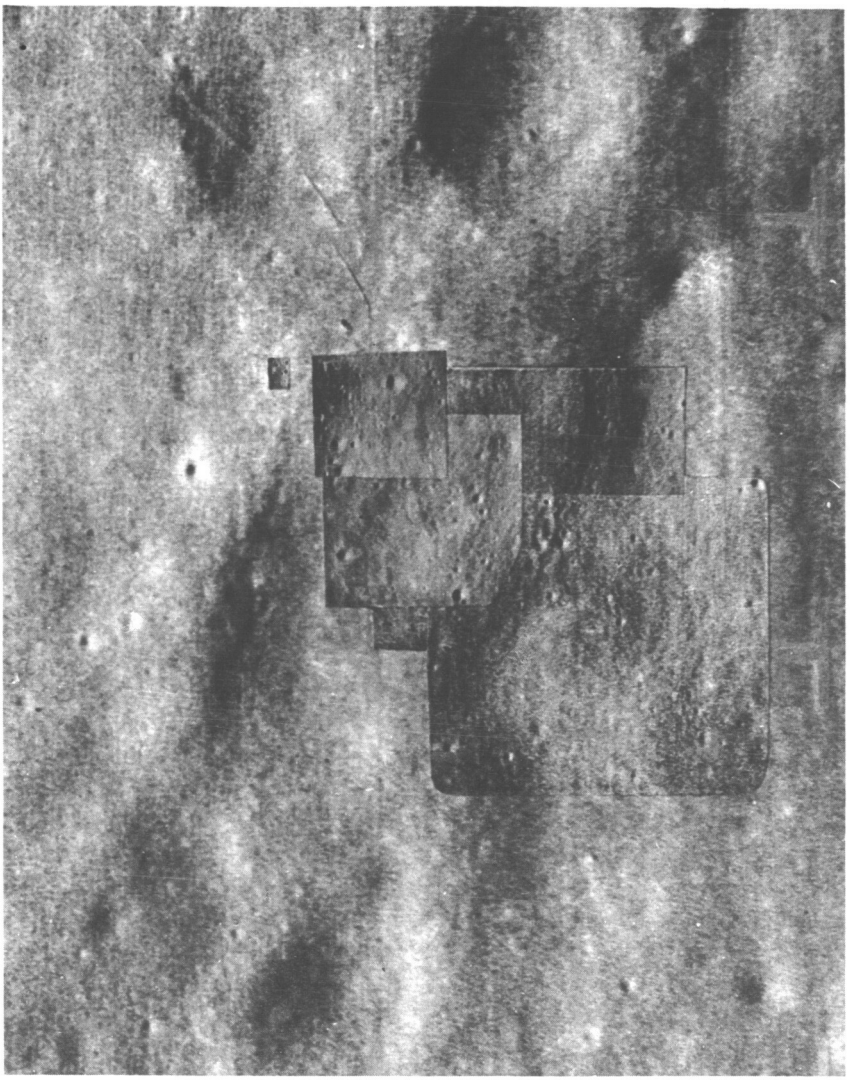

Figure 7.—**Ranger VII photomosaic. The large photograph is 1⅔ miles wide. The smallest photograph is approximately 100 feet on its longest side.**

ing the approximate boundaries of a ray and the distribution of secondary craters within the ray. In Mare Cognitum, a majority of the secondary craters may be identified with three major secondary crater swarms. Two of these correspond with major ray systems from Copernicus and Tycho. A third major swarm is associated with the primary crater Bullialdus. The secondary craters, like those identified with

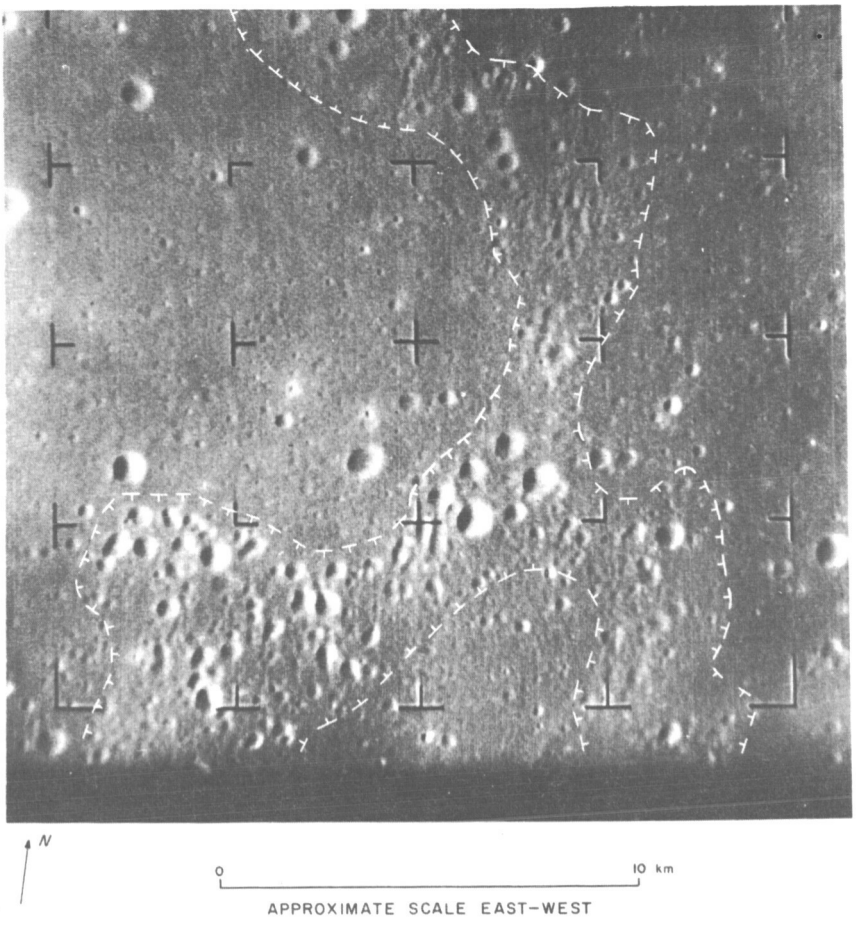

Figure 8.—**Secondary crater swarms in a lunar ray. (From E. M. Shoemaker, in Heacock et al., ref. 8)**

Earth-based telescopes, are typically shallow, elongated, have low irregular rims, or no rims at all, and are frequently composite, consisting of several overlapping or adjoining smaller craters.

Structure of the Crater Alphonsus and Surroundings

The area photographed by Ranger IX contains the large craters which are nearly at the center of the lunar disk: Ptolemaeus, Alphonsus (fig. 9), Arzachel, Albategnius, and Hipparchus.

In figure 9, Alphonsus fills the right half of the photograph. Alpetragius is near the lower left with a broad central mountain, and Davy-A is in the top left corner. Eight craters with dark patches are seen near the crater wall. The floor of Alphonsus has a higher crater

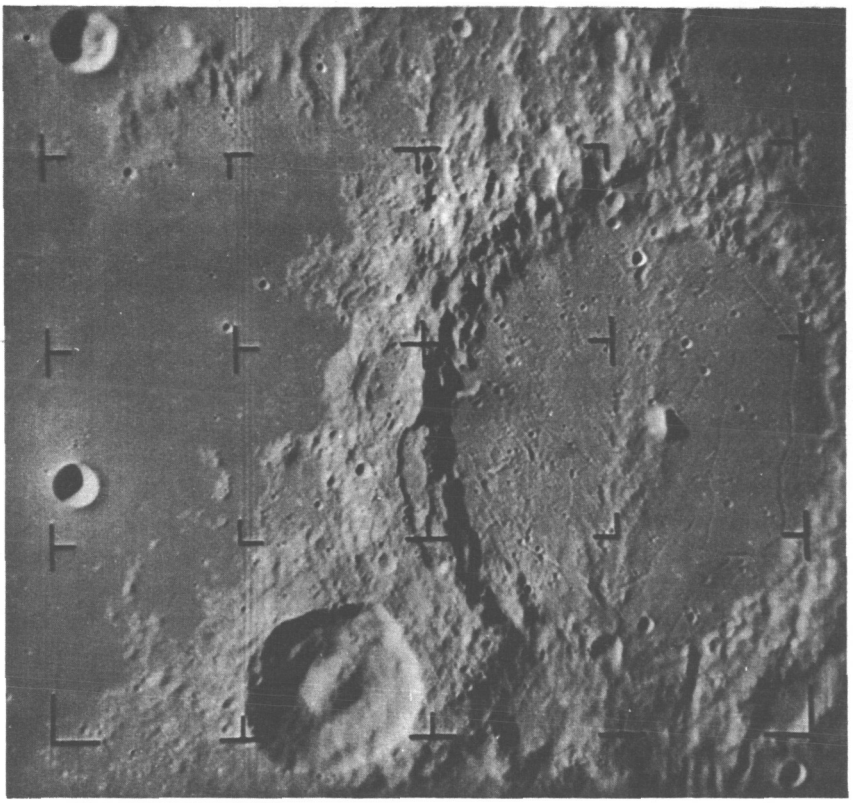

Frame number 35. Camera A. Time: 2 minutes and 50 seconds before impact. Spacecraft altitude: 258 miles above Moon. Dimensions: 121 by 109 miles.

Figure 9.—**Lunar craters in the vicinity of Alphonsus.**

density than the adjacent Mare Nibrium on the left. The following observations have been advanced by members of the Ranger Experimenter Team (Heacock et al., ref. 9).

The Central Peak of Alphonsus

The region of the central peak of the crater Alphonsus, with a rill running through its shadow, is shown in figure 10.

The central peak is a "white" mountain on which may have been an "eruption." By comparison with the surrounding terrain, the central mountain is nearly featureless, as if covered with snow, which may reflect the effects of volcanic fumarole activity. The reflectivity of the peak is more than twice that of the surroundings. The dense cover of depressions and the structural detail seen on the crater floor are absent from the mountain down to its base.

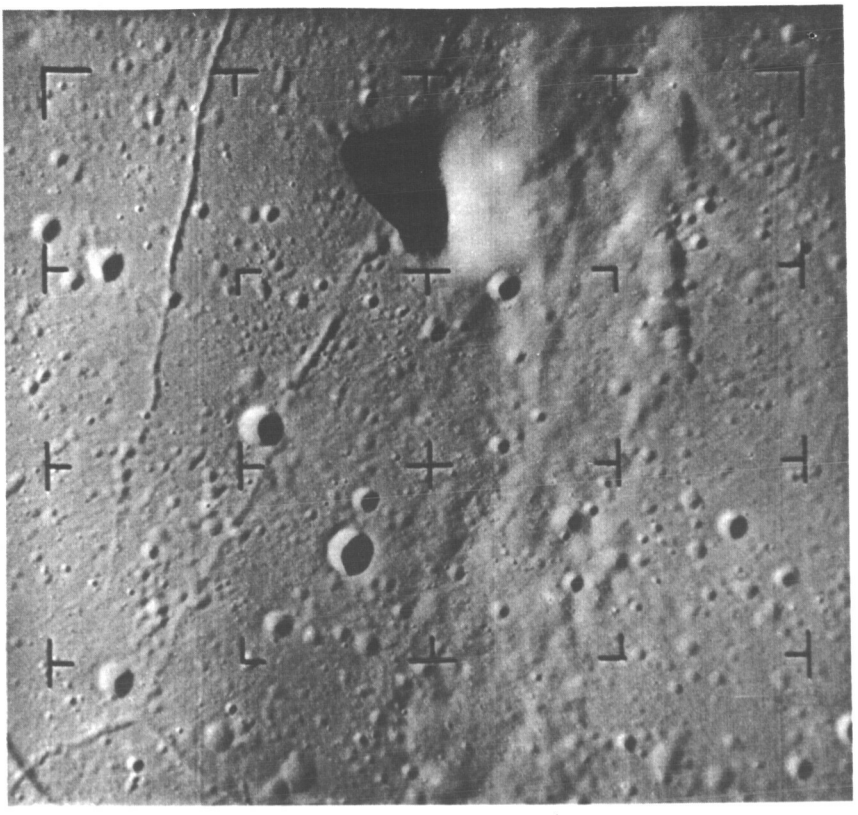

Eighth from last Ranger IX A-frame. Time: 38.8 seconds before impact. Spacecraft altitude: 58 miles above Moon. Dimensions: 28 by 26 miles.

Figure 10.—Central peak in the crater Alphonsus.

The major axes of the central peak and central spine, the two most prominent structures on the floor of Alphonsus, correspond with the direction of the Imbrian fracture system, and probably formed along subcrustal fractures associated with the Imbrian system. It should be noted that the fine structure of the spine forms part of the global lineament systems. This is also true of the fine structure of the mare ridges.

Dark-Halo Craters

All eight dark-halo craters (fig. 5) on the floor of the crater Alphonsus occur squarely on rills and must therefore be associated with them rather than be due to impact.

Thin blankets of dark material surround the craters, and have partly filled the rills. The dark deposits have no sharp boundaries

and terracing can be seen, an indication that the deposits are debris or ash (pyroclastics), rather than laval flows. The occurrence of clusters of small craters and scars indicate that substantial blocks were ejected from the craters. Stereoscopic observation indicates that the blankets are very rough, with single masses scattered to greater distances.

Rill System

The Alphonsus rills appear to be V- or U-shaped channels, 0.6 to 1.0 kilometer wide, mostly without raised rims, and with inner slopes of approximately 10° to 20°. Some rills are quite shallow and tend to break into a chain of shallow depressions.

Depressions on the adjacent crater floor extend right up to the border of the rills and even onto the rill slope, as if the rills did not exist. Fractures may run parallel to the rill and there is evidence that at several points the rill has developed a local explosion center similar to, but much smaller than, the dark-halo craters.

Crater Walls

The walls of Alphonsus reach a maximum of about 2 kilometers above the floor. The mountains forming the crater wall are remarkably smooth and rounded. In addition, there is evidence for subsidence and local melting. A major graben runs from a high-level "lava lake" to the crater floor; and furrows follow the base of the several mountains facing the floor.

Numerous small white projections, several with craters on top, are observed in the walls, possibly reflecting volcanic fumarole activity similar to that proposed for the central peak. The shallow, circular depressions, so abundant on the crater floors, are absent from the walls, although large conical depressions do occur. Although the crater walls appear much brighter than the floor, examination of full Moon photography demonstrates that the tonal differences are due to slope differences.

Crater Floor

A striking feature of the floor of the crater Alphonsus is the resemblance, in almost every respect, to mare-type terrain. Shallow circular depressions are prevalent. Major depressions show an intricately woven pattern similar to the "tree-bark" structure seen in the Ranger VII photographs. Dimple craters abound and a few sharp craters are noted, although soft craters outnumber sharp ones by factors up to nearly 100 times at a crater diameter of 100 meters. Domes occur on the crater floor, occasionally showing summit dimple craters.

Lineaments

Lineaments observed on the Ranger photographs of Alphonsus include ridges, linear depressions, breaks in slopes, and straight crater walls. Remarkably narrow lineaments also occur on the crater floor, both as positive and negative structures. Their widths go to the limit of resolution of 0.2 meter.

The directions of the small-scale lineaments coincide with the directions of large-scale lineaments in the terra areas adjacent to Mare Tranquillitatis and Alphonsus. Similar relationships are seen in the Ranger VII and VIII photographs. Four sets of lineaments can be distinguished on the basis of azimuthal frequency; three belong to the lunar grid system of lineaments (Strom, ref. 11); the fourth set is radial to the center of Mare Imbrium.

In nearly all cases, the observed lineaments are undeflected as they cross topographic features. The lineaments are apparently caused by planar structures intersecting the surface with dips close to vertical. The lack of observable shallow dips may not indicate that these structures are completely absent, however, as shallow dipping structures are difficult to recognize on aerial photographs. The only recognized exceptions to the generally steep dips are seen on the last complete B-camera photograph (Ranger IX, photograph B–608) in which many of the lineaments are deflected as they cross shallow craters. The observed apparent shallow dips here may reflect true dips of the underlying structures, or the deflections of the lineaments may result from downslope creep in the top few meters of the lunar surface.

Sharp-Rimmed Craters

A few sharp-rimmed steep-walled craters may be observed in most of the Ranger photographs. They range in size from craters known from telescopic observations down to craters a few meters in diameter. Some of these craters are surrounded by bright halos and small systems of rays; others are not. These steep-walled craters are remarkable for their uniformity of shape over a very large range of sizes from a few meters up to several kilometers in diameter.

Distribution of Craters

In the Ranger VII photographs, a large number of craters are found to be clustered within a ray-covered area identified with the large crater Tycho (fig. 8). The largest craters of the clusters occur near the ends of each ray nearest Tycho. Some of the small craters clustered in the Tycho rays are shallow and elongated, like known secondaries; others are relatively deep and circular.

Small-Scale Lineaments

Faint linear structures consisting of crater chains, elongated craters, shallow linear depressions, and ridges are visible on the last photographs taken before impact. Larger lineaments have been mapped from Earth-based photography in previous studies. A comparison of the azimuth-frequency diagrams for Ranger VII photographs (Heacock et al., ref. 8, pp. 67–69) demonstrates that the directions of small-scale positive and negative mare lineaments coincide with the azimuths of large-scale lineaments in adjacent terra areas. Similar analyses of small-scale mare lineaments in Ranger VIII photographs indicate that they are practically identical with neighboring large-scale lineaments. This suggests that the small-scale relief is structurally controlled and is related to global lunar fracture systems.

Slope Roughness

Measurement of slopes in the last Ranger VII photographs reveals that slopes over 90 percent of the area are less than 15° (measured over 1-meter-slope length); over 50 percent are less than 5°; and about 10 percent are less than 1°. The roughness of a surface of this type does not appear to present an unreasonable risk to landing Surveyor or Apollo spacecraft.

Crater and Surface Characteristics

Most of the craters seen in the Ranger VII photographs were interpreted as produced by secondary impact. The number of craters less than approximately 100 meters in diameter is less than the number predicted, an indication that many craters have been destroyed by ballistic erosion and the formation of later craters. The frequency of craters in this size range is the same on all three sets of Ranger photography, an indication that the surfaces have reached a steady-state crater density (Shoemaker, in Heacock et al., ref. 8, p. 75).

Comparison of the smallest craters photographed by Ranger IX with craters on Earth of the same size, produced by explosives and missile impacts, suggests that the lunar surface layer is weakly cohesive to noncohesive.

Cartographic and Geologic Mapping

A contour map has been prepared by photogrammetric techniques for the next-to-last and third-from-last A-frames of Ranger VIII. The area in Mare Tranquillitatis was found to be nearly level, with local slopes near 7°.

Five geologic units on the floor of Alphonsus have been discriminated on Ranger IX photographs. Many of the craters are alined

and are apparently of internal origin. A series of geologic maps with a variety of scales has been constructed from Ranger VIII and IX photography. These have been used to refine telescopic mapping, to discriminate new stratigraphic units, and to plan astronaut traverses (Heacock et al., ref. 9).

Measurements of the polarization of light from specific regions on the Moon have been found useful in the discrimination of geologic units. In general, maximum polarization and albedo are inversely related, but anomalous relationships have been found among mare units.

A map showing the albedo variations of the lunar equatorial belt has been prepared from a full Moon plate which has been printed on high contrast film at controlled levels of exposure.

Gravitational Constant and Mass

Analysis of the tracking data from the Ranger flights has provided new results for the quantities GM (Gravitational constant × Mass) of the Earth and Moon. Ranger VII data give for the Earth: $GM = 398\,601.3 \pm 1.5$ km^3/sec^2. The chief significance of this result lies in the increased reliability; for the Earth, the accuracy is increased from about 7¼ parts per million, attained from previous Earth-based studies, to 2 or 3 parts per million, a factor of about 3. The value for the GM of the Moon has been similarly increased by a factor of about 10.

Mariner IV (Mars 1964)

The scientific results of the Mariner IV Mars mission, of interest to planetology, were acquired during planetary encounter by the television, magnetometer, radiation, micrometeorite, and occultation experiments.

Television Experiment

On July 14, 1965, the Mariner IV spacecraft successfully acquired 22 pictures of the planet Mars, taken from distances of 17 000 to 12 000 kilometers during the flyby encounter. During the following week the images were transmitted to Earth from magnetic tape storage onboard the spacecraft. The complete set of pictures was released to the scientific community and the public on July 29, 1965.

Further reduction by computer processing techniques was applied to the Mariner IV photographs in order to remove noise, to enhance contrast, and to fill in data bits which were omitted in the initial processing of Mariner telemetry. An analysis of the surface features by the principal investigator, R. B. Leighton, and his associates at the California Institute of Technology, B. C. Murray and R. P. Sharp,

and at the Jet Propulsion Laboratory, J. D. Allen and R. K. Sloan, will provide the detailed study. The following comments are taken from a preliminary summary of the more prominent surface features present in the pictures, and the physical and geological inferences drawn by the investigators for the television experiment (Leighton et al., ref. 12).

"The Mariner IV photographs have provided the first closeup look at Mars, revealing the scientifically startling fact that large craters cover at least part of the surface. This is a profound revelation which leads to far-reaching fundamental inferences concerning the evolutionary history of Mars, and the uniqueness of Earth within the solar system." The investigators go on to state that "frame number 11 of the Mariner sequence must surely rank as one of the most remarkable scientific photographs of this age." This photograph is shown in figure 11, in which the crater distribution and the morphology of the Martian surface in the vicinity of Atlantis between Mare Sirenum and Mare Cimmerium can be seen. The largest crater is about 185 kilometers in diameter. The partial obliteration implies internal tectonic forces and erosional processes.

Although only about 1 percent of the Martian surface was sampled (fig. 12), at least 70 craters are clearly distinguishable on Mariner IV photographs 5 to 15. These range in diameter from 4 to 120 miles and it seems likely that larger and smaller craters exist on the surface. The observed craters have rims rising a few hundred feet above the surrounding surface, with a depth of a few thousand feet below the rims. Crater walls appear to slope at angles up to 10°.

Figure 12 shows the areas photographed by Mariner IV. The longest line, curved at the top and trailing off straight to the lower right, represents the edge of Mars as viewed from the spacecraft during the 25 minutes that photographs were taken. Areas to the right of the lower curved line were in the Sun's shadow. Picture No. 1, at the top, showed the edge of Mars and the blackness of space beyond, and picture No. 2 overlapped the lower right portion of No. 1. Picture No. 19 entered the shadow line near Aonius Sinus. The circled dot near Amazonis is the point where the Sun was directly overhead, or vertical to the surface of the planet.

The number of large craters present per unit area on the Martian surface, and the size distribution of those craters, is closely comparable to the densely cratered lunar uplands, as illustrated in figure 13.

Loomis (ref. 13) notes that a proportion of the craters less than 30 kilometers in diameter evidently has been obliterated by erosion of material from their rims and deposition on their floors. The proportion of obliterated craters rises with decreasing diameter. Assuming

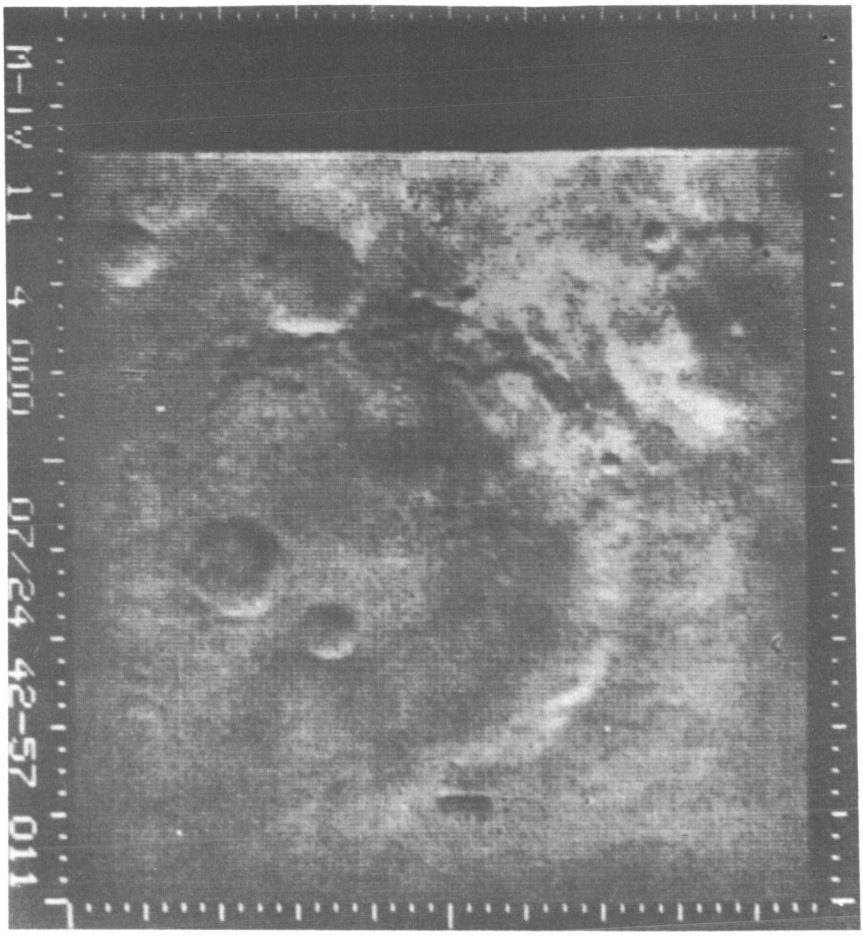

North is at the top. The Sun, 47° from the zenith, illuminates the surface from the top of the photograph. Taken with a green filter on July 14, 1965, at a slant range of 7800 miles. Dimensions: 170 by 150 miles (north-south). Location: 31° south latitude, 197° east longitude.

Figure 11.—Large craters on the Martian surface.

that craters with original diameters of 30 kilometers had an original depth of about 3 kilometers, Loomis concludes that on Mars the lateral redistribution of material by wind apparently has been much more rapid than lateral redistribution on the Moon.

Several additional features of the Martian surface are discussed by Loomis. Slightly less than half of the largest crater (185 kilometers in diameter) observed in the Mariner IV photographs (fig. 11 for example) has been obliterated; this implies that the crater has been

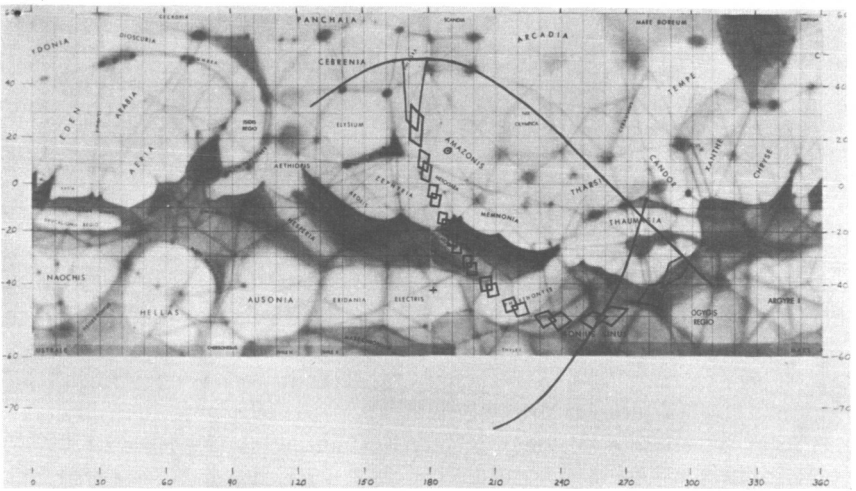

Figure 12.—Martian surface area photographed by Mariner IV.

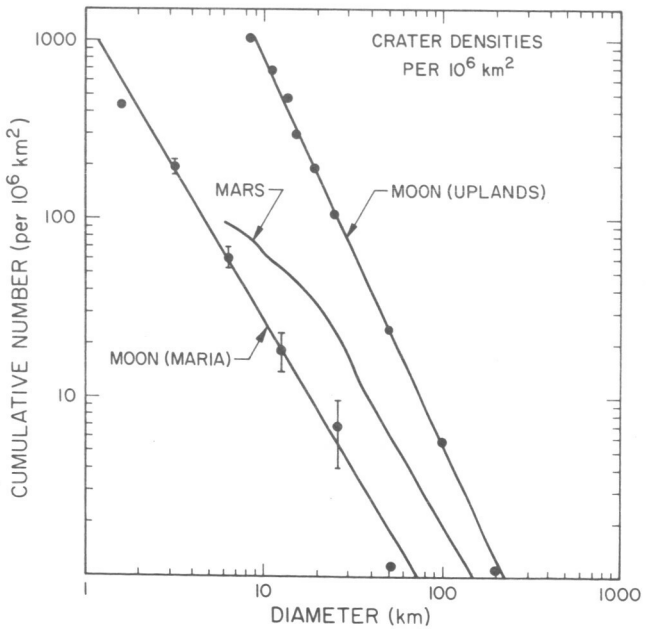

Figure 13.—Size distribution of lunar and Martian craters. (Courtesy of R. B. Leighton.)

245-015 O—67——10

faulted, or that the surface on which it was formed was tilted before or after its formation. No evidence of severe deformation is seen, such as distortion of craters, or faults which would indicate horizontal compression. Finally, several pictures contain areas of striking reflectivity differences, some of which may be caused by frost, particularly on slopes at low angle to the incident sunlight, but others of which are unexplained.

In appearance, the Martian craters closely resemble impact craters on Earth, both artificial and natural, and the craters of the Moon. Craters of widely different degrees of preservation and, presumably, age are distinguishable. A few elongated markings of diffuse nature are present in the Mariner photographs. One such feature looks like a part of the edge of a very large crater and, perhaps significantly, lies near the border of a Martian dark area. In the southern subpolar latitudes, where the season was late midwinter at the time of flyby, some craters appear to be rimmed with frost. Burgess (ref. 14) has noted that picture No. 11 does contain a lineament coincident with the location of a "canal." No earthlike features, such as mountain chains, great valleys, ocean basins, or continental masses, were recognized. The flight path did not cross either polar cap.

The existence of a lunar-type cratered surface, even in only a 1-percent sample, has profound implications about the origin and evolution of Mars and further enhances the uniqueness of Earth within the solar system. By analogy with the Moon, much of the heavily cratered surface of Mars must be very ancient, perhaps 2 to 5×10^9 years old (Shoemaker et al., ref. 15). The remarkable state of preservation of such ancient surface leads to the inference that no atmosphere significantly denser than the present very thin one has characterized the planet since the time that surface was formed. Similarly, it is difficult to believe that free water, in quantities sufficient to form streams or to fill oceans, could have existed anywhere on Mars since that time. The presence of such amounts of water (and consequent atmosphere) would have caused severe erosion over the entire surface.

The principal topographic features of Mars, in the areas photographed by Mariner IV, appear to have been produced by stress and deformation originating within the planet, in contrast to the case of Earth. Earth is internally dynamic, giving rise to mountains, continents, and other such features, whereas Mars evidently has been inactive for a long time. Lack of internal activity is also consistent with the absence of a significant magnetic field on Mars, as determined by the Mariner IV magnetometer experiment.

As anticipated, the Mariner IV photographs neither demonstrate nor preclude the possible existence of life on Mars. Terrestrial geological experience would suggest that the search for a fossil record

appears less promising if Martian oceans never existed. On the other hand, if the Martian surface is truly "near pristine," that surface may prove to be the best and perhaps the only place in the solar system still preserving clues to primitive organic development, traces of which have long since disappeared from Earth.

Magnetometer, Radiation, and Micrometeorite Experiments

The Mariner IV magnetometer, radiation, and micrometeorite measurements, during the period of closest approach to Mars, were essentially unchanged from their interplanetary values.

No magnetic field effects definitely attributable to the presence of the planet were observed. It is assumed that the interaction of the solar wind with a significant Martian dipole moment would have produced effects geometrically similar to those observed near the Earth, but with a scale determined by the magnitude of the dipole moment. This assumption has been used to establish an upper limit for the Martian dipole moment. Since the bow shock is the feature of a planet's interaction with the solar wind that occurs farthest from the planet (except possibly for the magnetic tail, which the instrument was never in a position to detect because of the nature of the trajectory), the ability to detect such a shock front forms the basis for the analysis.

The data indicated that the upper limit to the magnetic moment of Mars lies between 3×10^{-4} and 10^{-4} that of Earth. Some of the consequences of the small upper limit for the Mars magnetic field are immediately apparent. Any field-producing dynamo must be nearly inactive.

Since the rotation rates of Mars and the Earth are nearly the same, absence of a strong magnetic field may indicate that Mars has not differentiated sufficiently to form a conductive fluid core. The Martian interior now appears definitely to be more like the interior of the Moon than that of Earth. A magnetic moment of 3×10^{-4} that of Earth implies a surface field at the magnetic equator of only 100 gammas. It also means that the flux of cosmic rays everywhere above the atmosphere will be comparable to what is observed at Earth over the polar regions. The elevation of the magnetopause in the subpolar region is, at most, 5000 kilometers, or 1.5 times the radius of Mars. The very weak fields and low inductance value for the magnetopause imply that any belts of trapped radiation on Mars must be very small and weak. If the dipole moment is zero, radiation will not be trapped.

Lack of an entrapping magnetosphere apparently explains the absence of trapped radiation belts around the planet. The significance of this feature to planetology arises from the lack of shielding which the surface has from bombardment by the solar wind. Degradation and possibly erosion of surface materials by radiation disintegration

and sputtering may have extensively modified the nature of the Martian surface.

The implications of the absence of an encircling dust cloud are more tenuous. This may reflect the extremely low atmospheric density and a resulting decrease in fragmentation of incoming meteorites; or perhaps the action of the planet in sweeping out a path in the interplanetary debris (Alexander et al., ref. 16) may have reduced the particle flux below the level required to maintain a cloud in an equilibrium condition. These processes may in turn be reflected in the number of particles which have struck the surface of Mars through time (Anders and Arnold, ref. 17; Witting, Narin, and Stone, ref. 18; and Baldwin, ref. 19).

Occultation Experiment

Occultation of the Mariner IV spacecraft by the planet Mars, and the accompanying interruption and modification of the transmitter signal, have provided measurements of the density and scale height of the Martian atmosphere. These data will also provide a new figure for the radius of the planet.

After the spacecraft passed its closest approach point, it went behind the planet as viewed from Earth. As the telemetry signal disappeared, its amplitude and frequency changed because of diffraction and refraction from the planet and its atmosphere. Preliminary results of the occultation experiment are as follows:

Atmospheric scale height, km	8–9
Surface refractivity	3.7–4.2
Maximum ionospheric density, electrons/cc at 120 km	10^5

The atmospheric pressure at the Martian surface, reported by Kliore et al. (ref. 20), is less than 10 millibars. Such a low total pressure raises problems about the atmospheric composition and the rates of escape of various constituents such as Ar^{40}, which should have been produced by radioactive decay of K^{40} (Loomis, ref. 13). This in turn reflects on the composition of the surface material and on the problems of planetary differentiation, internal thermal regime, and possible mechanisms for the formation of surface features.

The minimal amounts of oxygen and moisture which appear to be present lessen the role of oxidation and hydration as active forces in decomposing exposed minerals to soil, in eroding topographically high surface features, and in transporting the material to points of sedimentary deposition.

Russian Photography of Far Side of Moon

The Russian space station Zond III was placed in Earth parking orbit on July 18, 1965, and successfully injected on a lunar flyby tra-

jectory. About 25 photographs of the far side of the Moon were obtained on July 20, 1965, when the probe was within 11 570 kilometers of the Moon. According to Pravda (Lipsky, ref. 21), the spacecraft was also designed to investigate the physics of remote interplanetary space, and to test various onboard installations. The following description of the mission and interpretation of the scientific results is excerpted from the preliminary reports by Y. N. Lipsky (refs. 21 and 22).

The flyby trajectory and distance were designed to optimize aerial coverage on the far side, resolution of surface features, and lighting conditions. The probe approached the Moon from the western edge, moving toward the morning terminator, which virtually coincided with the edge of the region photographed in 1959 by Luna III. While the photographs were being taken, the Sun was directly above the north rim of the crater Riccioli, obliquely illuminating and revealing the topographic features of the unknown surface with long shadows.

The new photographs cover practically all the previously unrecorded surface of the Moon. They also show a substantial portion of the visible hemisphere, permitting the reliable location of new features on the standard selenographic coordinate system. The photographs confirm the earlier conclusion that there is a major dissimilarity between the visible and hidden hemispheres of the Moon. The far side has fewer maria and is in general lighter and more mountainous. Only two small maria, separated by a ridge, are added to existing knowledge of the lunar surface. The northern part of the far side of the Moon consists of one gigantic continent which is substantially larger than the antipodal southern continent on the near side. In contrast, the northern side on the near face is largely covered by maria.

From the 1959 photographs, it was concluded that the far side is more densely pockmarked with craters than the visible face. This concentration has been fully confirmed; a preliminary catalog of newly discovered formations already contains more than 100 entries. On a single photograph over 600 craters between 5 and 20 kilometers in diameter, about 200 between 20 and 50 kilometers, about 40 between 50 and 100 kilometers, and perhaps a dozen craters larger than 100 kilometers are shown. The smallest craters which can be distinguished are 3 kilometers across.

On the whole, craters on the far side have the usual characteristics. Some have central peaks, others ray systems, and large overlapping craters are frequent. Of great interest are extended chains of craters 10 to 30 kilometers in diameter. Like certain bright rays on the visible side, they originate in a bright continental region north of Mare Orientale.

Ranger VII photographs resolved bright rays, which cross maria, into multitudes of small craters; a similar relation between the newly discovered crater chains and the rays is possible. There are also crater chains on the near side of the Moon, such as one south of Archimedes, and a somewhat larger one west of Copernicus. But the crater chains on the far side are different and much longer—in some cases extending more than 1500 kilometers. No such features are found on the near side.

Another interesting feature on the Moon's far side are the numerous ring-shaped concavities called "thalassoids." These are large depressions with diameters up to more than 500 kilometers. In size and shape they are comparable to maria, but differ in having conspicuously crater-scattered floors and in lacking the characteristic dark color of maria. An example is the thalassoid that is centered on longitude −125°, latitude +3°. Its maximum diameter is 430 kilometers. Although the edge stands out rather clearly, there is no conspicuous raised rim; that is, the formation is a depression rather than a ring of mountains. The floor is covered by many irregularities of various sorts, including a fault running through its central part. The thalassoid is crisscrossed by two crater chains, in the northwest and south, and by bright rays.

The largest crater on the floor of this thalassoid has a diameter of about 50 kilometers, gently sloping inner sides, and a 10-kilometer crater on its western wall. Of two contiguous 30-kilometer craters in the southern part of the thalassoid, the southern one has a raised rim whereas the northern one does not. Several light patches stand out clearly.

On the near side of the Moon there are no large thalassoids as conspicuous as this, although the craters Janssen and Clavius, as well as the continental region southeast of Janssen, are somewhat similar to thalassoids.

The Soviet selenologist A. V. Khabakov noted a curious depression which is partly occupied by Mare Nectaris. In the past, this depression may have constituted a gigantic thalassoid more than 1000 kilometers in diameter, bordered by Pyrenees and Altai Scarp. Part of it may have been filled subsequently, becoming Mare Nectaris. This implies that the maria and thalassoids are of similar origin. There are also thalassoidlike formations on Mars. Frames 10 and 11 of the Mariner IV photographs show these features, in addition to lunar-type craters.

Gemini IV, V, VI, and VII Manned Earth-Orbital Missions

Six Gemini missions were flown during 1965 (table I). The Gemini IV to VII flights carried the synoptic terrain photography experi-

Table I.—*1965 Gemini Missions*

Mission	Astronauts	Orbits	Launch	Recovery	Scientific experiments	Mission accomplishment
Gemini II	Unmanned	(a)	Jan. 19, 1965	Jan. 19, 1965		Reentry test.
Gemini III	V. I. Grissom and J. W. Young.	3	Mar. 23, 1965	Mar. 23, 1965	3	Orbital maneuvering system, control of reentry trajectory.
Gemini IV	J. A. McDivitt and E. H. White.	62	June 3, 1965	June 7, 1965	11	Extravehicular activity, long-duration flight.
Gemini V	L. G. Cooper, Jr., and C. Conrad, Jr.	120	Aug. 21, 1965	Aug. 29, 1965	16	Extended physiological studies, fuel cell use.
Gemini VII	F. Borman and J. Lovell		Dec. 4, 1965	Dec. 18, 1965		Extended physiological studies, target vehicle for Gemini VI.
Gemini VI	W. Schirra and T. Stafford.		Dec. 15, 1965	Dec. 16, 1965		Orbital rendezvous with Gemini VII.

[a] Suborbital.

ment. A brief summary of the Gemini IV results has been published (Lowman, ref. 23); the following synopsis is taken from that report.

Approximately 100 frames of 70-millimeter color film, usable for terrain studies, were obtained during the Gemini IV mission. Most are of excellent quality with respect to exposure, resolution, and spacecraft orientation. The exposure locations and times of all the 70-millimeter pictures have been published and are available from the Photographic Technology Laboratory of the Manned Spacecraft Center.

Priority was given to photography of East Africa, the Arabian Peninsula, Mexico, and the southwestern United States. A continuous series of pictures was also obtained covering the flight path on the 32d revolution from the Pacific coast of Mexico to central Texas. The first picture of this series (fig. 14(a)) shows an area about 75 miles on a side in Baja California (fig. 14(b)); Bahia de Todos Santos, on the Pacific coast of Mexico, is visible at the lower left.

A large amount of geologic detail is evident in the picture. The line of contact between Quaternary alluvium (light-colored material at upper and center right) and bedrock may be easily drawn. A number of different igneous rock types can be distinguished on the basis of color, although they could not be identified on the basis of this picture alone. Perhaps the most striking geologic feature is the long linear valley at the lower left, parallel to the edge of the spacecraft window. This valley, identified as a fault on the basis of preliminary examination of the picture, in fact follows the Agua Blanca fault zone, one of the major tectonic features of Baja California. A number of linear valleys are apparent, either parallel to the Agua Blanca fault zone, or intersecting it; they presumably represent subsidiary faults.

The potential value of hyperaltitude photography for regional studies is illustrated strikingly by the fact that this fault, so obvious from space, was not discovered until 1965 (Allen and Silver, ref. 24) and then, interestingly enough, from aerial reconnaissance. The most recent prior authoritative publication on the geology of Baja California (Beal, ref. 25) gives no hint of the existence of the fault, nor does it show more than one rock type. However, figure 14 shows no evidence of what was mapped by Beal as a probable major fault (the San Pedro Martir fault) bounding the east side of the Sierra de Juarez. It is likely that figure 14 will be of value in studying the tectonic structure of Baja California, since it is possible to delineate other faults outside the area mapped and reported by Allen and Silver.

Figure 15 shows the third photograph taken in the 32d revolution series. It shows the mouth of the Colorado River entering the Gulf

of California; the distance shown is about 70 miles across at the bottom of the picture. Considerable geologic detail is shown, such as the various rock types near the eastern shore of the Gulf and the fault just east of the Colorado River (the southward-trending linear feature outlined in white on the eastern side of the river). Sand dunes in the desert (right) are also visible.

Of particular interest, however, is the amount of detail evident in the Gulf of California. The sinuous patterns off the river mouth resemble those near the Ganges River, which were photographed on the Mercury-Atlas 9 flight and identified as turbidity currents (Lowman, ref. 26). However, R. F. Gettys of the U.S. Naval Oceanographic Office has demonstrated that this pattern is actually the bottom topography of the Gulf of California which is only a few feet deep at this point. Although Gettys finds figure 15 unsuitable for actual

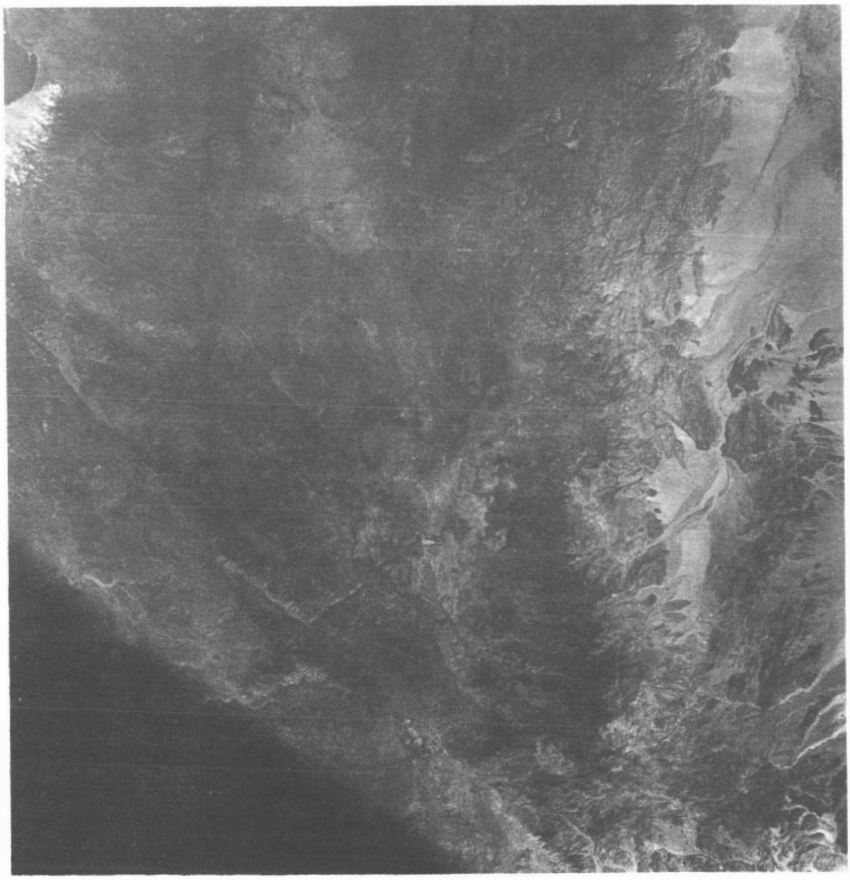

(a) Photograph taken from Gemini IV.

Figure 14.—Baja California.

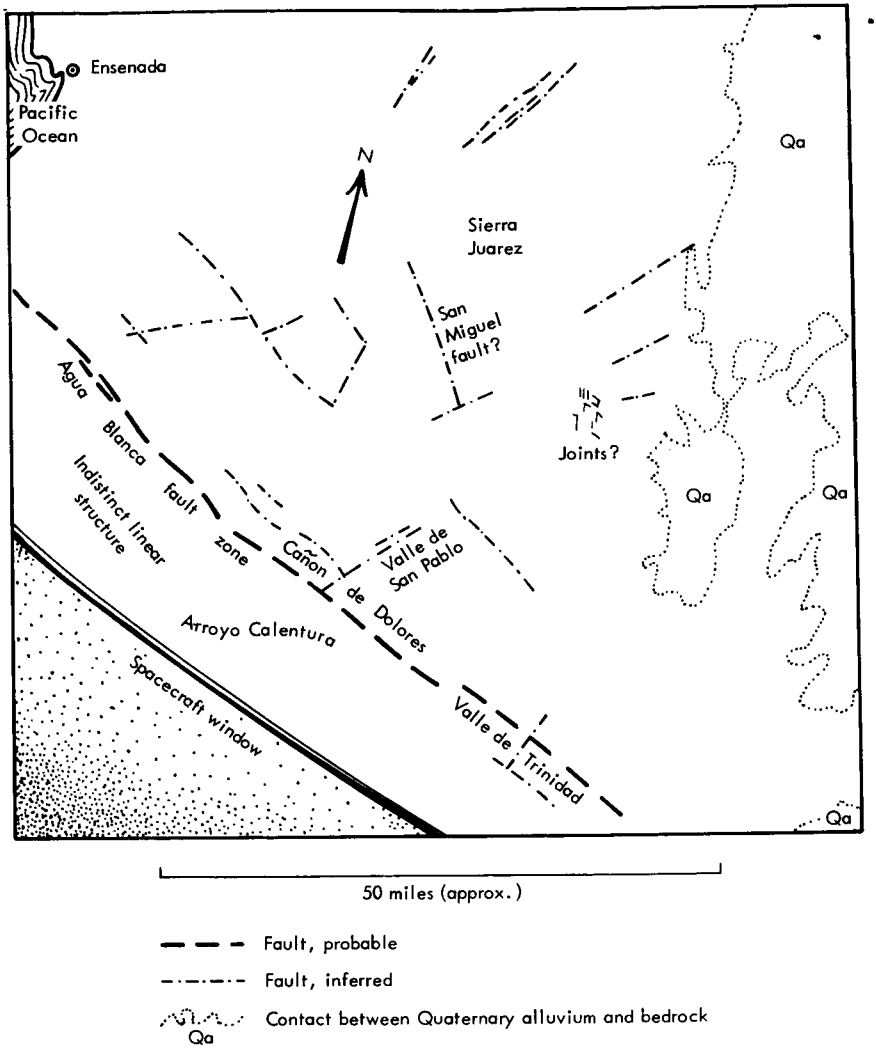

(b) Structural sketch map by Paul D. Lowman, Jr., NASA Goddard Space Flight Center, principal investigator of the Gemini synoptic terrain photography experiment.

Figure 14.—**Concluded.**

depth mapping, he points out that the synoptic view of sediment distribution provided by the spacecraft altitude is of great interest to oceanographers.

Fifth in the 32d revolution series, figure 16 shows part of the Gulf of California (left), the Sierra del Pinacate volcanic field in Sonora, Mexico (center), and part of Yuma County, Ariz. (upper right).

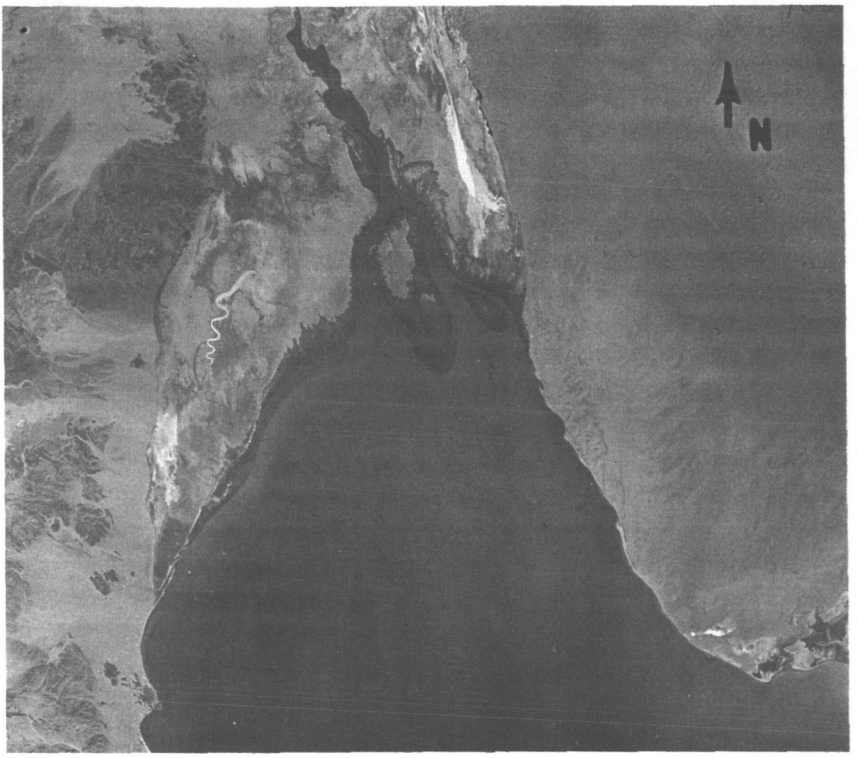

Figure 15.—**Mouth of the Colorado River entering the Gulf of California.**

The photograph is of geologic value in several respects. In addition to the submarine topography in the Gulf of California previously mentioned, many major structural and lithologic features are apparent. The most striking of these features is the Pinacate volcanic field. The Pinacate field has been known for hundreds of years; however, it is not delineated on the latest (1960) geologic map of Mexico, which has a scale about equal to that of the Gemini IV photograph. Figure 16 could also be used to revise the alluvium-bedrock contacts on the geologic map. Of greater interest, however, is that many bedrock lithologic units can also be differentiated and identified with the aid of available geologic maps. In Yuma County, for example, the contacts between Mesozoic granite (light) and Mesozoic schists and gneisses can be traced and, in many places, extrapolated across the Mexican border. The apparent similarity and continuity of granites in the various northwest-trending ranges tend to support the inference (Eardley, ref. 27) that the entire area is underlaid by one or more batholiths.

Figure 16.—**Pinacate volcanic field, Mexico. Scale: about 80 miles on a side.**

Another potential use of space photography is suggested by figures 17(a) and 17(b). These figures show by photograph and sketch an area in which two major tectonic provinces merge. Figure 17(a) is a Gemini IV photograph showing portions of southern New Mexico, Chihuahua, and Sonora, Mexico. The linear mountains at the left are the continuation of the Sierra Madre Oriental, characterized by folds similar to those in the Appalachians. The mountains at the lower right, however, are chiefly block-faulted mountains, typical of the Basin and Range Province, and are placed in the Basin and Range class by Eardley. It can be seen that these two types of mountain structure merge without marked change of direction, a relation which could be realized only by extensive field mapping in Mexico and the United States.

Similar topographic and geologic detail is present in Gemini photographs of other areas of the world. The application of this informa-

tion is particularly significant in the geologic reconnaissance of remote areas and in the economics of the world.

If we can increase our knowledge of the Earth's geology, it follows that we can use this knowledge in the search for new sources of water or mineral products which are so important to man's well-being. Furthermore, the techniques for photogeologic reconnaissance of terrestrial surfaces have application to the investigation of lunar and planetary surfaces as well.

The Gemini photographs are of considerable meteorological and oceanographical interest as well as a source of geological information. All three types of data may be represented in a single photograph, a reminder of the interrelationship of phenomena in nature and the increasing interrelationship of scientific investigations.

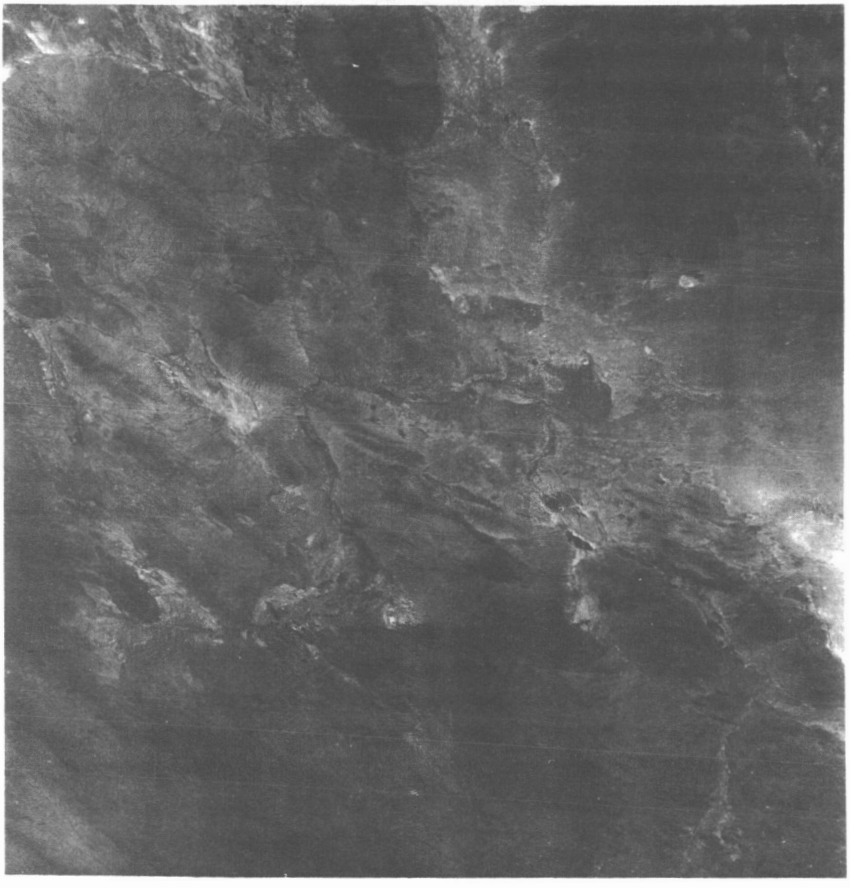

(a) Photograph taken from Gemini IV.

Figure 17.—Transition between block-faulted and folded mountains.

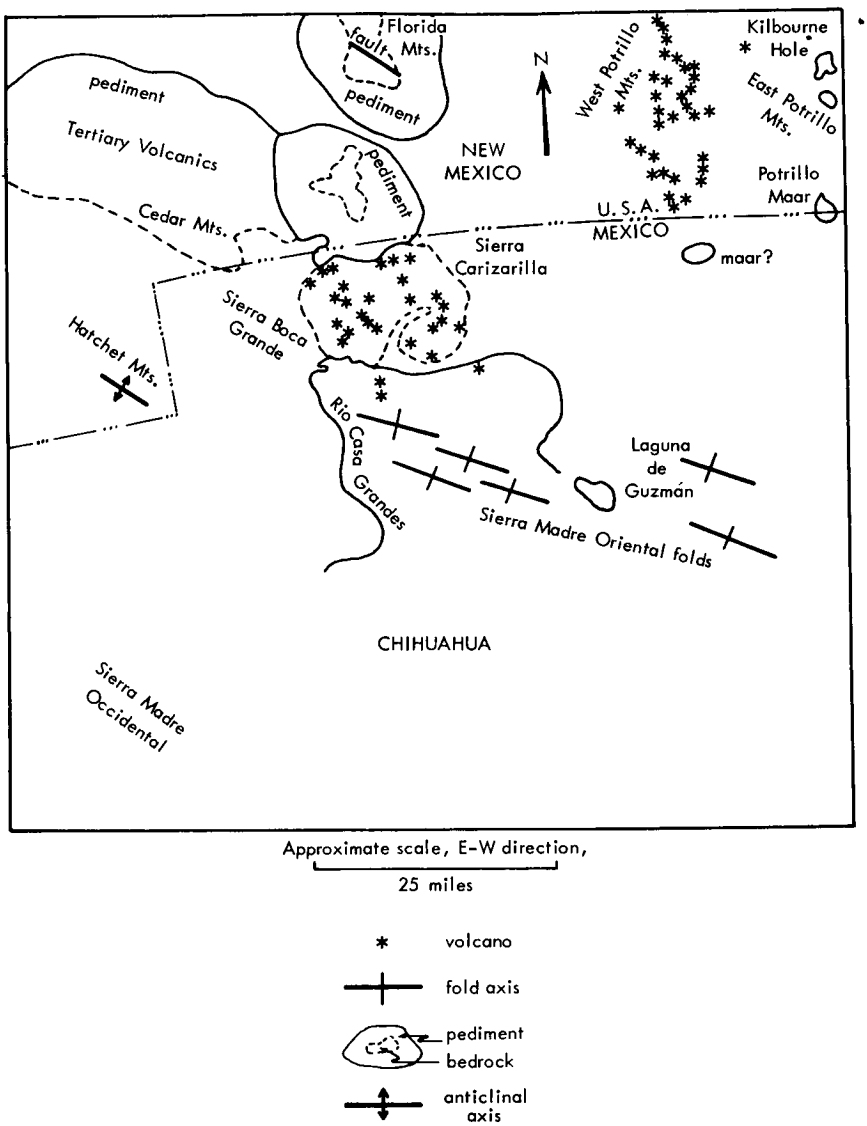

(b) Structure and physiography of northwestern Chihuahua, Mexico, and southern New Mexico. Sketch map by Paul D. Lowman, Jr.

Figure 17.—Concluded.

Venera II and III

On November 12 and 16, 1965, two Russian spacecraft were successfully ejected from Earth orbit on trajectories toward the planet Venus. Russia has not missed a Venus or Mars opportunity since the Sputnik VIII Venus probe, launched February 12, 1961.

An official announcement distributed by Tass on December 21, 1965, stated that the course of Venera II had been corrected in flight "in order to bring it closer to Venus," and that the probe will now pass "at the prescribed distance" from the planet (*The Evening Star*, ref. 28). The distance at encounter was not given. The announcement stated that regular radio contact was being maintained with both probes, which were then at a distance of 9.6 million miles (Venera II) and 8.9 million miles (Venera III) from Earth. Temperature and pressure conditions aboard the probes were reported normal, and the scientific instrumentation was functioning normally.

Luna Missions V, VI, VII, and VIII

During 1965, four Soviet spacecraft were launched in attempts to land "automatic stations" equipped "with various measuring apparatus for conducting scientific research" (source: Tass) with the intent of achieving a soft landing on the surface of the Moon (table II).

Table II.—*Luna V to VIII Launch Record*

Mission	*Launch date*
Luna V	May 9, 1965
Luna VI	June 8, 1965
Luna VII	Oct. 4, 1965
Luna VIII	Dec. 3, 1965

This series of launches apparently continues a lunar soft-landing program begun on April 2, 1963, by Luna IV, which missed the Moon by 4600 nautical miles after Jodrell Bank reported midflight maneuvers. On the Luna V to VIII flights, signals ceased abruptly, possibly indicating crash landings at lunar impact.

Shortly after the Luna V impacted the surface of the Moon in Mare Nubium, a dust cloud was reportedly observed (unsigned article, *Izvestiya*, May 16, 1965, p. 5) by the astronomical observatory at Rodewitsch, East Germany. This cloud was described as having been visible for about 10 minutes after impact. At the time of best visibility (5.5 minutes after impact) the size was estimated as 230 kilometers long and 80 kilometers wide. Dust clouds or unusual phenomena have not been confirmed for this or other lunar impacts, although attempts have been made to observe them.

EARTH-BASED LUNAR OBSERVATIONS

Surface Measurements

In August 1965 a review of the present state of knowledge of the lunar surface was held by the Tycho Study Group as part of the Manned Space Science activities. The following summary draws upon the report prepared by that Group (ref. 29).

The gross and intermediate features of the lunar surface have been established by means of the optical telescope. Photographic atlases (Kopal et al., ref. 30; Kuiper, ref. 31), including rectified imagery (Kuiper et al., ref. 32, Whitaker et al., ref. 33), have been prepared for the visible surface of the Moon. The Ranger spacecraft have provided high-resolution imagery near their impact sites on the lunar surface (ref. 2; Heacock et al., refs. 8 and 9). Luna III and Zond III (Lipsky, refs. 21 and 22) have photographed the greater portion of the Moon's far side.

Measurements of the intensity and polarization of sunlight scattered by the lunar surface, as a function of incident and observing angle, are interpretable in terms of the particle size and density of the surface material. The conclusion reached is that finely divided, opaque, and highly porous material covers the lunar surface to optical depths (1 mm). Whether the material is particulate (dust) or vesicular (froth) (Halajian, ref. 34) is not yet resolved, although a "fairy castle structure" of arborescent granular growths has been suggested on theoretical and empirical grounds (Hapke, refs. 35 and 36; Hapke and Van Horn, ref. 37) as the most likely explanation of the lunar backscattering phenomena (fig. 18). Erosional processes, including micrometeorite bombardment, which have progressively softened the observable features of the Moon, provide a source for lunar dust (Gold, refs. 39 to 41). Volcanic processes, and the sputtering effects of the solar wind, could produce vesicular materials.

Kuiper and Whitaker (Heacock et al., ref. 8) have emphasized that local color differences are observable when color exaggeration techniques are applied to lunar photography (fig. 3). These color differences may reflect either rock (lava) material of varying composition with slight dust cover or large surface flows (dust) from different source areas. While spectral data should reflect chemical and mineralogical composition of the local lunar rock units, the interaction of the solar plasma with the lunar surface may alter the material so that reliable conclusions are no longer possible.

Infrared measurements indicate that the sharp, hemispherical, ray craters on the lunar surface gain and lose heat more slowly than the surrounding terrain. This evidence indicates that these areas are somewhat more dense, or more tightly bonded, than the typical lunar material, or both. A material consisting of approximately 70 percent voids, with the bonding of crushed basalt, would be consistent with the thermal data. The depth of infrared investigations is comparable to that of visual observations.

Microwave emission measurements yield lunar temperatures, with an effective depth of several centimeters, which are in consonance with the infrared data.

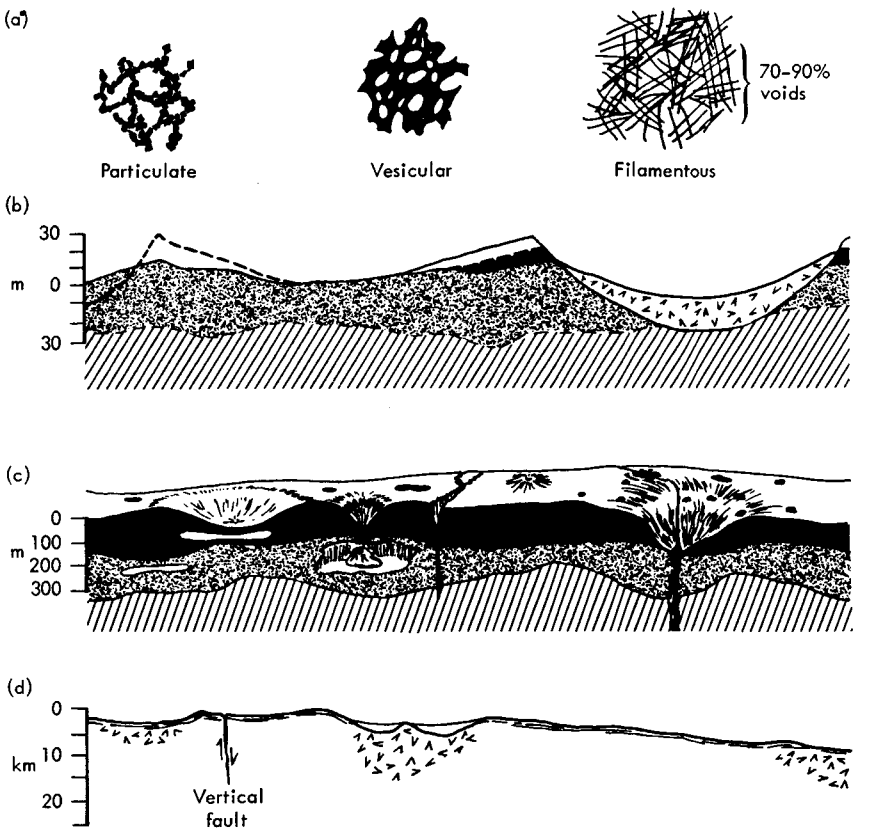

(a) Highly porous surface material composed of fairy castle, slag, or filament structures.

(b) Gardened layer on lunar plains, composed of buried craters, impact craters, throwout ejecta blankets, and brecciated crater floors overlying in the bedrock surface. (Shoemaker sketch, ref. 2).

(c) Lava flow model of lunar mare and crater floors showing collapse depressions, dimple craters draining into open cavities, fissure systems related to the global lunar grid pattern, chain craters, and dark-halo craters located on fissures and surrounded by rough ejecta blankets.

(d) Generalized cross section of the Moon after U.S. Geological Survey "Geologic Map of the Aristarchus Region of the Moon," by H. J. Moore (ref. 38).

Figure 18.—Current lunar surface models.

Radar reflection measurements have improved in resolution so that the radar brightness of individual large features on the lunar surface may now be mapped. The strength of the return signal is a measure of both density and surface roughness. The radar wavelengths penetrate beyond the optical layer and provide information on the upper half meter, or so, of lunar material. The dielectric constant, measured

from the overall radar return at a range of wavelengths, is consistent with a material comprised of 70 percent voids (fig. 18). A distribution of slopes has been obtained, but whether this roughness is on the surface or indicates the presence of inhomogeneities below the surface cannot be ascertained. The bright radar reflectivity of sharp-featured and ray craters indicates either increased surface roughness or density, or both. In conjunction with the high thermal inertia of the same features, it is probable that the "dust" layer at these points is thin, exposing the underlying rock and permitting its different characteristics to be observed.

The presence of dust on the lunar surface is supported by reasoning based on the finely divided nature of the surface inferred from photometric data; the thermal inertia ($K\rho c$) of the lunar surface measured by infrared methods; the exceedingly low dielectric constant measured by radar, microwave, and polarization techniques; the probable rate of meteorite infall through time and the resulting fragmentation of surface material; and the erosion of lunar features, which is apparent in the progression from sharp to faint structures.

Estimates of the thickness of the dust layer vary from millimeter amounts to several kilometers. The conclusion that the lower slopes in the maria basins reflect greather dust thicknesses than the rougher highlands appears reasonable on conservation-of-energy grounds alone.

Cartographic Mapping and Terrain Analysis

Two separate series of lunar topographic charts of the visible surface of the Moon are being developed by Department of Defense agencies, with NASA support. These charts are compiled from a careful combination of Earth-based photography and visual observations. The 1:1 000 000 series (fig. 19) presently supports the photogeological mapping program and all mission planning for manned and unmanned lunar exploration programs. The 1:500 000 maps (fig. 20) are a supplemental series which cover the Apollo zone of interest.

Associated with the topographic mapping effort are several studies utilizing Ranger photographs as experimental data for photogrammetric and photometric analysis. Mosaics of Ranger VIII and IX photographs have been constructed at scales from 1:1 000 000 to 1:5000. Stereographic compilation measurements were investigated to develop optimum methods and equipment for the production of lunar topographic maps. Ranger VIII and IX lunar charts and topographic maps have also been completed (figs. 21 to 25). This work is providing procedures and operating skills which are required for the analysis of Lunar Orbiter imagery.

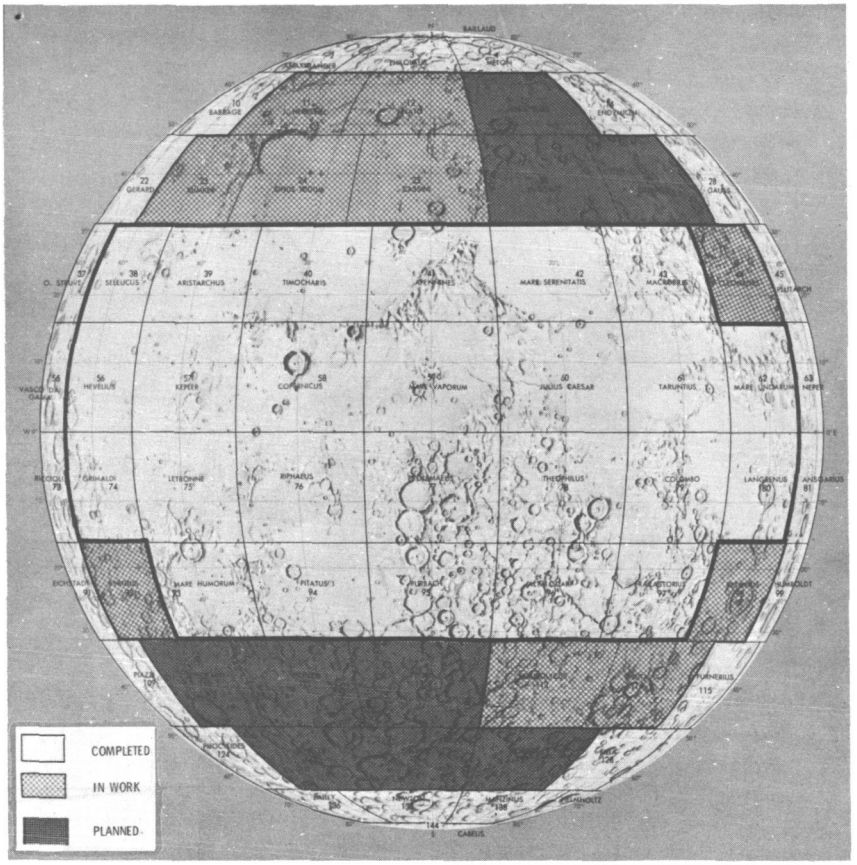

Figure 19.—The 1:1 000 000 series of lunar charts.

Earth-based telescopic photography will soon provide for a fundamental selenodetic control system consisting of precise 3-coordinate locations for 525 lunar surface features. The features form a relative geometric network which permits conversion of coordinates to physical distances on the Moon. Error analysis of the network and additional ties to the points in the lunar limb regions are still in progress.

The U.S. Air Force, Aeronautical Chart and Information Center (ACIC), has used the Ranger photographs to refine the Lunar Aeronautical Chart (LAC) series of shaded relief maps of the Moon. LAC–76 was the largest scale map (1:1 000 000) previously available for the Ranger VII impact area. ACIC has now published a new series of maps based upon Ranger VII photographs, at 1:1 000 000, 1:500 000, 1:100 000, 1:10 000, and 1:1000 scales (ACIC Ranger VII Lunar Charts, RLC 1–5). Figures 21 to 25 show the preliminary

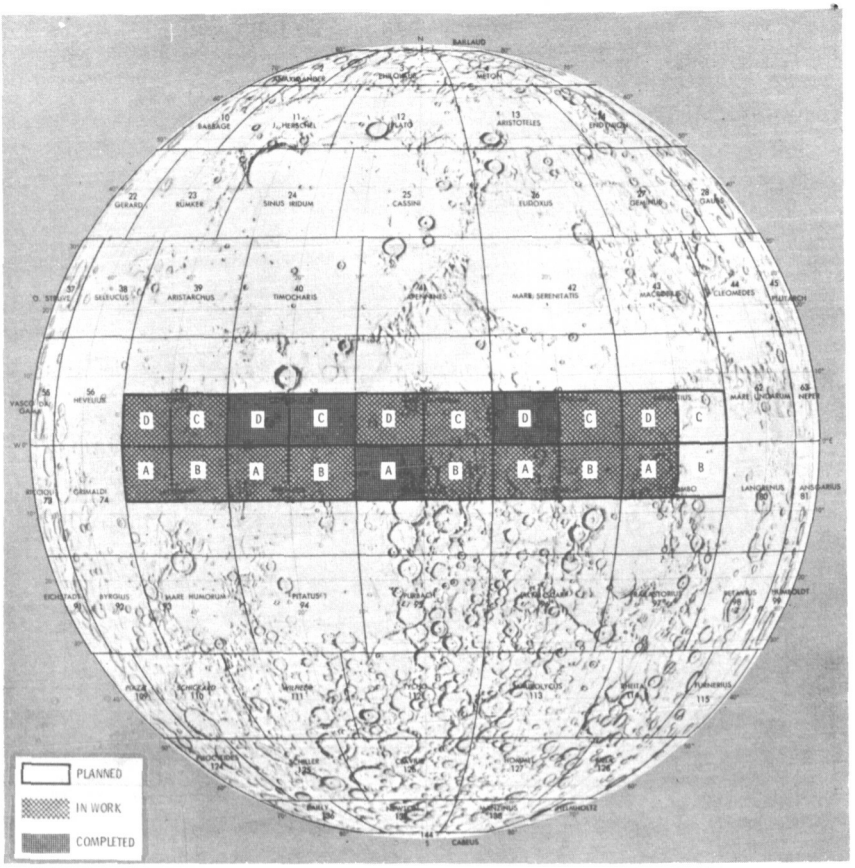

Figure 20.—**The 1:500 000 series of lunar charts.**

mosaics for the crater Alphonsus, the Ranger IX impact area, at scales from 1:1 000 000 to 1:2000. These charts provide in a condensed, qualitative form much of the new lunar topographic data acquired by the Ranger missions.

A photometric method of lunar-slope analysis, suggested first by van Diggelen in 1951, has been refined and enlarged by J. F. McCauley and his colleagues at the U.S. Geological Survey. The modified technique, conveniently termed "photoclinometry," is based on the observation that the brightness of an element of the lunar surface is a function of the normal albedo, the slope of the surface, and the Sun's angle of elevation. The surface slope can be determined from a knowledge of the other three quantities. In practice, a high resolution lunar photograph is scanned with a recording microdensitometer; the resulting brightness values are corrected for lateral variations in normal albedo

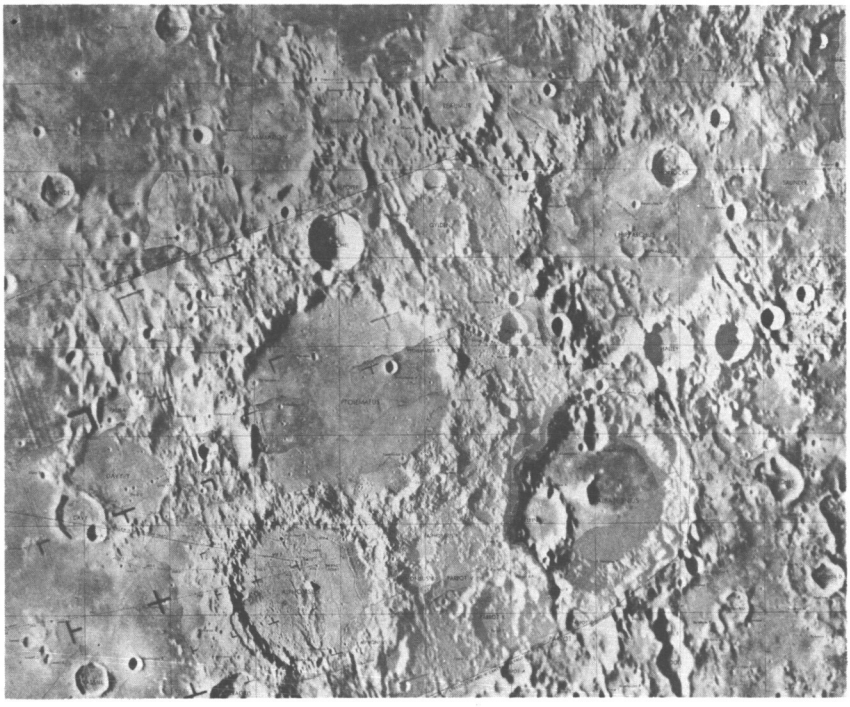

Figure 21.—**Ranger IX photomosaic of the crater Alphonsus and surrounding area; 1:1 000 000 scale.**

and then compared with the brightness values of level terrain under the same Sun angle. The method can be readily programed for computers and large numbers of slope values generated. The slopes thus measured represent the east-west component of the true slope of the surface.

A statistical analysis of slope components generated in this fashion was used in a terrain analysis of the lunar equatorial belt (10° N to 10° S, 60° W to 15° E). Relative roughness of the lunar surface was mapped on the basis of the distribution of six terrain units defined on the basis of these statistics. If it is assumed that the normal albedo of the surface does not change with increasing resolution, the method can be extended to high resolution imagery from unmanned space probes.

A technique has been established for photometric calibration of lunar plates by comparison of density readings of selected spots on the plates and photoelectric measurements of the same spots through the telescope. The lunar observations are made when the Moon nearly duplicates the phase and libration corresponding to the epoch of the

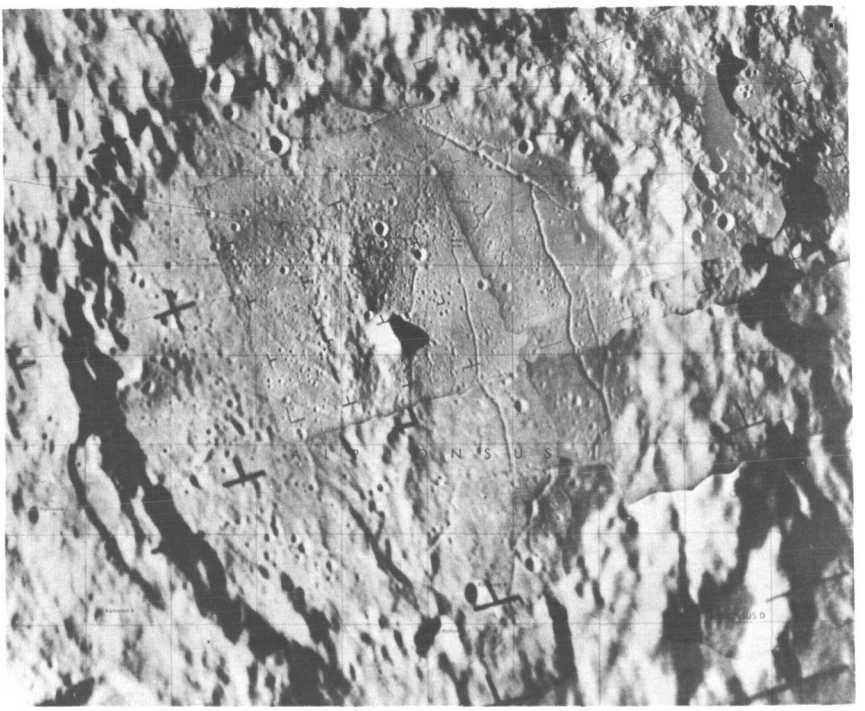

Figure 22.—**Ranger IX photomosaic of the crater Alphonsus; 1:250 000 scale.**

plates. This will greatly add to the stock of plates useful for photometric studies.

Geologic Mapping

A total of 28 lunar quadrangles, covering the lunar equatorial belt from 70° W to 70° E and 32° N to 32° S, have been mapped by the Branch of Astrogeology, U.S. Geological Survey, at a scale of 1:1 000 000 (fig. 26). Preliminary editions of these geological maps are available as open-file reports. Of these, several are available in colored final editions (Moore, ref. 38; Carr, ref. 42; Eggleton, ref. 43; Hackman, ref. 44; Marshall, ref. 45).

Scientific observations accomplished during the course of this mapping include delineation of probable ejecta blankets from both the Mare Orientale and Mare Humorum Basins in the Byrgius quadrangle; an early generation of mare material on a bench at the margin of the Mare Serenitatis Basin, analogous to the Apennine Bench at the margin of the Mare Imbrium Basin; subdivisions of the Fra Mauro Formation, believed to be ejecta from the Mare Imbrium

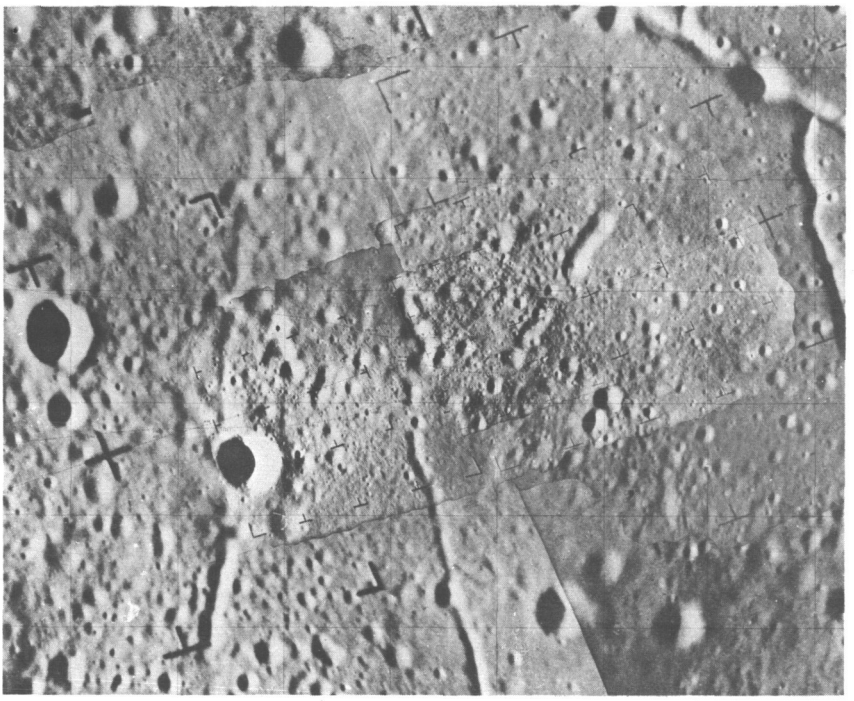

Figure 23.—**Ranger IX photomosaic of the crater Alphonsus; 1:50 000 scale.**

Basin, into several subunits with a radially symmetrical distribution; several probable volcanic units, most of which are associated with rills in the north-central part of the Moon; the youth and volcanic nature of two types of domes in the Marius Hills in the western Oceanus Procellarum; and a suggested common pattern of rim crest collapse in the crater Petavius and Mare Crisium, which indicates that collapse along faults of the lunar grid may be significant in the deformation of many larger lunar craters and mare basins.

The geologic mapping in the equatorial belt has been compiled at a scale of 1 : 5 000 000 to furnish an overall view of lunar stratigraphic relations; this is available in preliminary form as an open-file report. A tentative sequence of basin formation has been established from oldest to youngest: Fecunditatis, Serenitatis, Nectaris, Crisium, Imbrium, Orientale.

Infrared Measurements

Use of modern infrared methods and detection systems in lunar infrared observations (8–14 μ) has proved to be a fruitful venture. Probably the most outstanding discovery of recent years in this field

Figure 24.—**Ranger IX photomosaic of the crater Alphonsus; 1:10 000 scale.**

is the anomalous cooling behavior of the eclipsed Moon, reported by Shorthill and Saari (ref. 46). Their observations, made between 10–12 μ, disclosed almost 400 lunar areas which remain hotter than their surroundings during eclipses. The index map of figure 28 (from ref. 47) shows the location of hot spots and extended areas of thermal enhancement on the lunar surface during a total eclipse on December 19, 1964. Most of these areas were associated with bright craters, but whole mare are thermally enhanced as well. The magnitudes of certain anomalies (that of the crater Mösting C, for example) are such that the areas involved behave thermally like bare rock.

Several significant observations have been made (ref. 46) concerning the observed lunar thermal features. Although the hot spots are associated with bright features, there are bright features which are not thermally anomalous; thus there does not appear to be a direct relationship between visual brightness and thermal response. A comparison of radar reflectivity contours with the infrared eclipse data shows there is no simple correlation between the measurements. For instance, some areas of enhanced radar return do not show anom-

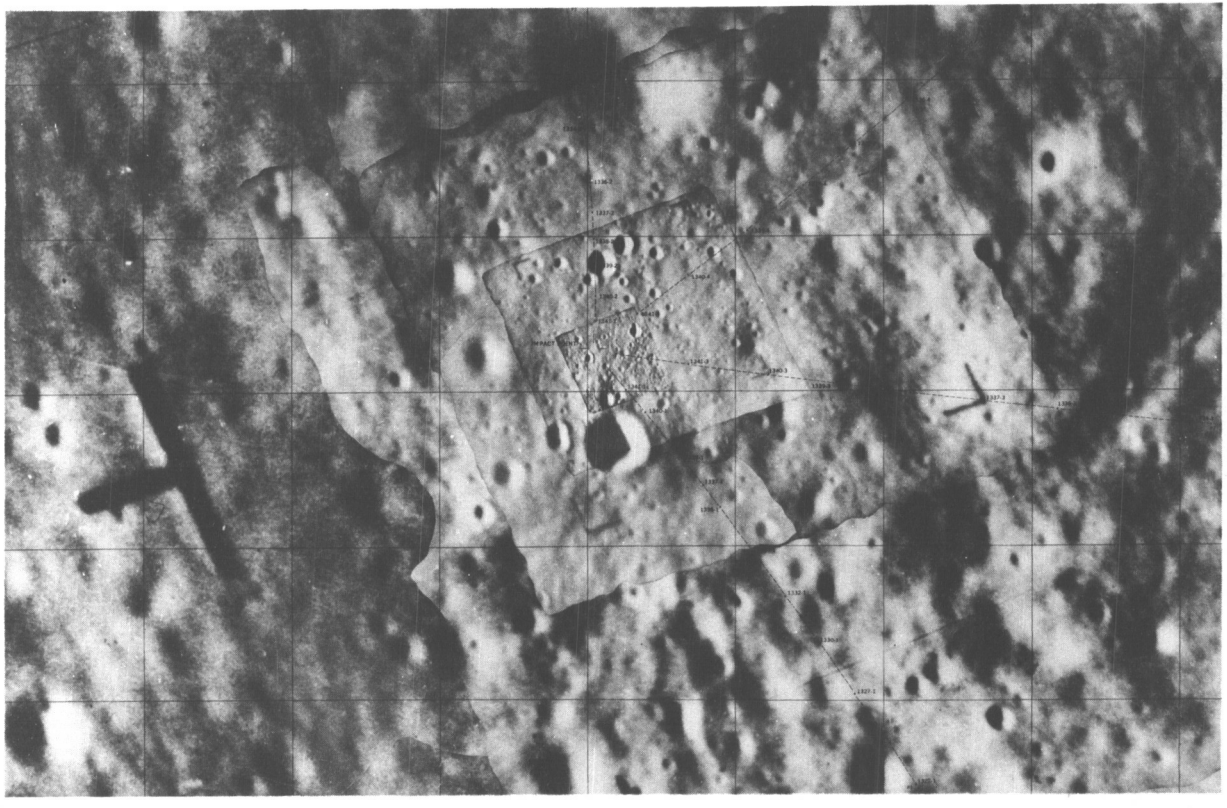

Figure 25.—Ranger IX photomosaic of the crater Alphonsus; 1:2000 scale.

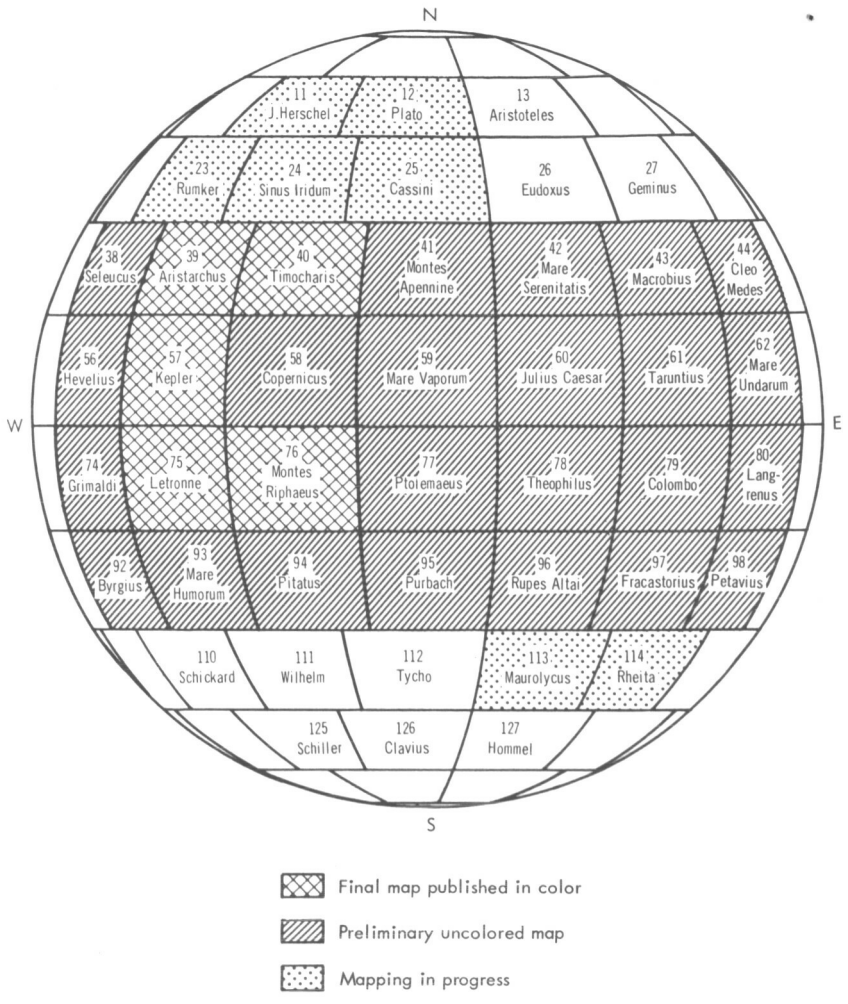

Figure 26.—**Status of lunar geologic mapping at 1:1 000 000 scale.**

alous eclipse cooling; the radar contours of the ray craters Copernicus and Tycho are decidedly different from their isotherms during totality. The concentration of hot spots in Mare Tranquillitatis can be understood either in terms of random impact origin, if the properties of the original surface have enhanced and prolonged the anomalous thermal behavior, or in terms of nonrandom internal processes.

Luminescence

Observations of transient color phenomena on the Moon's surface (Kozyrev, ref. 10; Greenacre, refs. 48 and 49; Kopal and Rackham,

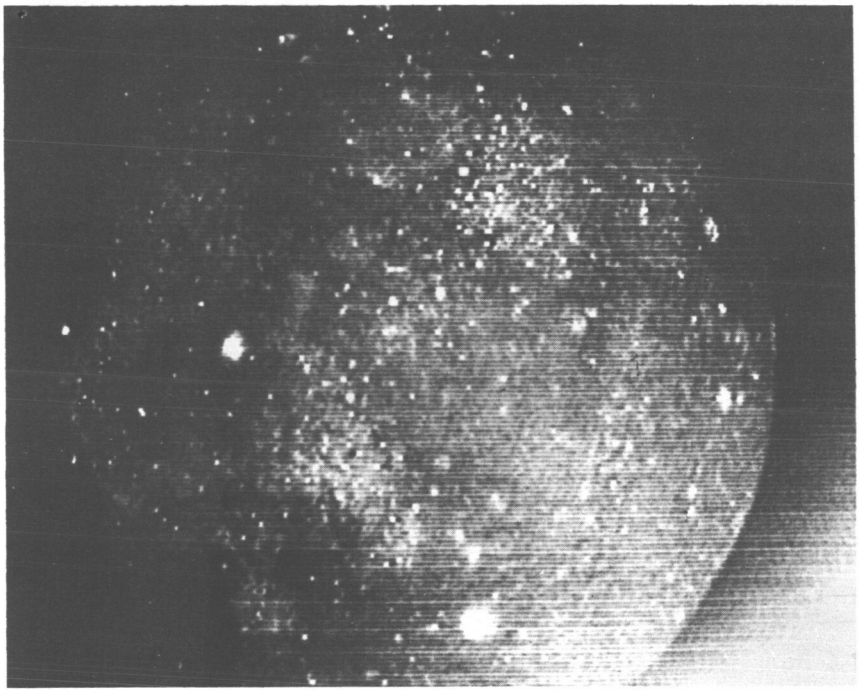

Figure 27.—**Lunar thermal anomalies during solar eclipse. (Photograph courtesy of The Boeing Co.)**

ref. 50) and the general correlation between lunar brightness and solar activity over the past few decades (Gehrels et al., ref. 51; Bell and Wolbach, ref. 52) have led to the hypothesis that lunar surface rocks luminesce under bombardment by solar particle radiation (Kopal and Rackham, ref. 53; Kopal, ref. 54). Transient reddening has been observed visually, spectroscopically, and photographically in the vicinity of Alphonsus, Aristarchus, and Kepler. These areas have thus become prime targets of increased observational study by many observatories (Kopal, ref. 54; Young, ref. 55; Gilheany, ref. 56). Such continuous monitoring of known "active" areas is expected to be fruitful during the next 5 years, as solar activity increases to its maximum.

Laboratory experiments have been conducted recently to provide fundamental information on the luminescence characteristics of possible lunar rocks and minerals when excited by particle bombardment (Durham et al., ref. 57; Greenman et al., ref. 58; Nash, ref. 59) and electromagnetic radiation (Greenman et al., ref. 58). It has been shown qualitatively that luminescence, excited by proton bombardment

Figure 28.—**Lunar thermal anomalies, index map. (From ref. 47.)**

(simulating the action of the solar wind) of silicate rocks and minerals, reproduces many of the color and brightening effects observed recently on the Moon (Nash, ref. 59). However, quantitative measurements of proton and electron excitation efficiencies and considerations of the energy content of known solar particle flux do not account for the intensity of the observed lunar color phenomena (Nash, ref. 59; Flam and Lingenfelter, ref. 60). In general, it has been found that the observed light energy from these phenomena is too great to have been luminescence stimulated by the known incident solar ion flux, especially in view of the very low excitation efficiencies of probable lunar surface rocks. These findings have led to several uncertainties as to the real cause of the phenomena and/or the actual source of energy which produced them (Nash, ref. 59; Flam and Lingenfelter, ref. 60; Cameron, ref. 61.

Continued observations and experimental work are being conducted in an attempt to determine the extent and significance of solar-ion-excited luminescence on the Moon.

ANALYSIS OF EXTRATERRESTRIAL MATERIAL

A meteorite can be considered as a natural space probe that formed somewhere in the solar system during the past 5 billion years and returned a specimen from outer space without human aid. Meteorite research provides part of the background which is essential for the interpretation of the scientific data obtained by space probes, as well as the study of environmental conditions which are encountered in space.

The composition and structure of meteorites differs from that of terrestrial rocks; meteorites contain minerals unknown in the crust of the Earth; their time of original crystallization was either coincident with or preceded the formation of the planets in the solar system. Analysis of cosmogenic isotopes in meteorites has revealed complex histories of irradiation, breakup, and space erosion. Conclusions concerning the cosmic abundances of the elements are largely based on interpretation of meteorite analysis.

The recent expansion of meteorite investigations follows a long period of comparative neglect. The number of minerals recognized in meteorites has doubled since 1960, and some of these are compounds previously unknown either in terrestrial rocks or as laboratory products.

A special importance of meteorite research for the space program lies in the direct application of the laboratory techniques developed for meteorite analysis to the investigation of returned lunar samples. Whatever may be the nature of the lunar surface, the material of which it is composed and the environment to which it has been subjected are more likely to resemble meteorites than any terrestrial rocks.

Tektites consist of a silica-rich glass, generally in small, rounded masses, which resembles, yet is distinct from, any terrestrial volcanic obsidian (Mason, ref. 62). They have an unusual chemical composition, which resembles a few granites and rhyolite, and are found in a few strewn fields in areas that preclude a volcanic origin. Unlike other meteorite types, tektites have not been observed to fall, and their identification as extraterrestrial objects is still disputed.

Meteorite Research

An overall picture of meteorite research activities includes programs in areas of nuclear physics, biology, and astronomy, as well as in the fields of mineralogy and petrology, chemical composition, and age dating which are summarized here. Some research projects extend

over more than one field, but are discussed under the heading that seems most appropriate.

Mineralogy and Petrology

Great advances have been made in mineralogical studies of meteorites during the past year, the result, to a large extent, of the application of the electron microprobe to the investigation of small grains of accessory minerals. The following new minerals have been described which are valuable as indicators of the conditions under which these rocks form:

Ureyite, $NaCrSi_2O_6$	(Frondel and Klein, ref. 63).
Merrihveite, $(K, Na)_2Fe_5Si_{12}O_{30}$	(Dodd et al., ref. 64).
Roedderite, $(K, Na)_2Mg_5Si_{12}O_{30}$	(Fuchs and Frondel).
Perryite, Ni_5Si	(Fredriksson and Henderson, ref. 65).
Sinoite, Si_2N_2O	(Keil and Andersen, ref. 66).

In addition, two phosphates, graftonite and sarcopside, previously known from terrestrial rocks, have been identified in a meteorite (Olsen and Fredriksson, ref. 67).

Other mineralogical studies based on microprobe work include those of Keil and Andersen (ref. 68) on the Jajh deh Kot Lalu enstatite chondrite; Duke and Brett on copper in stones; and Fredriksson and Reid (ref. 69) on glass in the Chainpur chondrite.

Measurements of nickel-iron gradients across the Widmanstätten structure of iron meteorites and application of diffusion theory to these data indicate that iron meteorites cooled at a rate of 1° to 10° C per million years (Wood, ref. 70; Goldstein and Ogilvie, ref. 71; Short and Andersen, ref. 72).

The study of diamonds in the Canyon Diablo meteorite continues to stir controversy. Anders (ref. 73) and Lipschutz dispute the findings of Carter and Kennedy and claim that the diamonds have been formed by shock on impact, not by equilibrium growth. The significance of cohenite as a possible high-pressure phase in meteorites is also the subject of controversy between Lipschutz and Anders on the one hand and Ringwood (ref. 74) on the other.

Shock effects in meteorites have been the subject of increased interest, in view of their significance in deducing the physical conditions on extraterrestrial bodies. Brecciation and veining, especially on stony meteorites, have been studied extensively in the past. Recently the shock effects on individual minerals, indicated by strain, recrystallization, and distortion or destruction of the crystal structure, have been carefully investigated in the meteorites themselves, in impactites from meteorite craters, and in laboratory-shocked material (Lipschutz, Milton, Fredriksson).

Some interesting X-ray diffraction work on the structural condition of meteorite pyroxenes has been reported by Pollack (ref. 75), and Mason (ref. 76) has briefly considered the origin of plagioclase in chondrite meteorites.

The electron microprobe, combined with petrographic study with the microscope, has enabled Dodd and Van Schmus (ref. 77) to define a group of unequilibrated ordinary chondrites. Apparently mild thermal metamorphism has erased the nonequilibrium features (variable mineral composition, presence of glass, and so forth) from most of the ordinary chondrites. These authors show that the chondrites with olivines and pyroxenes of variable composition (disequilibrium chondrites) are also remarkably unrecrystallized; i.e., they have very pronounced chondritic texture and they contain primary glass. Their findings put certain limitations on existing cosmological models, in particular, on the hypothesis of Wood (ref. 78), which states that chondrites are formed by condensation from unfractionated solar gas.

Study of individual chondrules (e.g., Fredriksson and Reid, ref. 69) indicates that chondrules are formed by quenching of liquid droplets. Dodd has also made petrofabric analyses of a number of chondrites, and found preferred orientation of the chondrules, suggesting a relict sedimentary fabric. This may indicate an origin for these meteorites similar to a terrestrial volcanic tuff.

Detailed mineralogical and petrographical descriptions with chemical analyses were published of the Forest City, Tennasilm, Geidam, and Weston meteorites (Mason and Wiik, ref. 79). Buseck and Moore have described a new iron meteorite, the Bloody Basin octahedrite from Arizona. McCall (ref. 80) has described the unique Mount Egerton meteorite from Western Australia. A comprehensive account of the hexadrite group of iron meteorites has been published by Henderson (ref. 81), and a similar account of the enstatite chondrites has been prepared by Mason (ref. 82).

Chemical Composition

Major Elements

It is unfortunately true that careful measurements of minor and trace elements, of rare gases, and of isotopes have been made on meteorites which have not yet been adequately characterized mineralogically and petrographically, nor have they been chemically analyzed for the major elements. This has been due largely to the difficult and time-consuming task of meteorite analysis, and the very few competent analysts in this field. Dr. Wiik from the Geological Survey of Finland is at present a visiting professor at Arizona State University, continuing his program of meteorite analysis and training students in

this field. The Division of Meteorites at the Smithsonian Institution has added another chemist to its staff and has initiated a planned program of meteorite analyses.

An interesting development is the use of activation analysis for determining major elements in meteorites. Wing (Argonne National Laboratory) pioneered the determination of O and Si in stony meteorites by this technique and it has been further developed by Vogt and Ehmann (refs. 83 and 84). While the standard analytical method for determining SiO_2 in meteorites is satisfactory and reliable, the possibility of direct determination of O is an important development, especially for meteorites like the carbonaceous chondrites. Neutron activation analysis for major elements is particularly appropriate for very small samples, such as individual chondrules and mineral separates; this work is being actively pursued by Schmitt and Goles.

Minor and Trace Elements

The investigation of minor and trace elements in meteorites continues to be a field of very active research. The versatility of neutron activation analysis has made it the favored method, as can be seen from the list of investigators and determinations during 1965 shown in table III.

The data of Cobb and Moran (ref. 85) Baedecker and Ehmann (ref. 86), Vogt and Ehmann (refs. 83 and 84), and R. A. Schmitt of Astronautics in San Diego indicate that some meteorite classes (e.g., ordinary chondrites) are depleted in certain elements in comparison with carbonaceous and enstatite chondrites. It is unlikely that one simple event alone in the history of meteorites can account for their differences.

Much work in compositional analysis has also been carried out by other methods. Nichiporuk and Brown (ref. 87) have reported spectrographic determinations of Ru, Rh, Pd, Ir, and Pt in irons and the metal phase of chondrites. Nishimura (Hokkaido University) has continued his work on the colorimetric determination of Zn in meteorites. Moore and Lewis (ref. 88) have determined C in many stony meteorites by using a combustion method. Fleischer, Price, and Walker (ref. 89) have used their fission track technique for the determination of U at very low concentrations and for the identification of extinct Pu.

This field of work will continue to be a very active one. The distribution of minor and trace elements in the individual phases of a meteorite will provide a better understanding of the processes by which these elements were incorporated in the meteorites.

Table III.—*Neutron Activation Analysis of Meteorites*

Ehmann and coworkers	University of Kentucky	Au, Ir, Pt, Ta.
Schmitt	General Atomic	Rare earths, Se, Cr, Mn, Co, Cu.
Goles and Greenland	University of California, San Diego.	In, Cu, Zn, Ga, Se, Te, Ag, Pd, Cd.
Reed	Argonne National Laboratory.	Ba, Bi, U, Ag, Pd.
Wasson	University of California, Los Angeles.	Ga, Ge.
Fisher	Cornell University	Al, F, Sc, Mn, Na, Co.
Lovering and coworkers	Australian National University.	U, Th, Re, Os.
Smales and coworkers	Atomic Energy Research Agency, England.	Trace elements in irons.
Esson, Stevens, and Vincent.	University of Manchester, England.	As, Sb.
Von Gunten and coworkers.	Institut für Reaktorforschung, Switzerland.	Cl, Br.

Rare Gases

During the past few years, intensive research on the rare gases in meteorites has been carried out in many institutions, both here and abroad. Measurements of rare gases have been emphasized because they possess a combination of significant properties, as follows:

(*a*) Rare gas isotopes are produced in a number of different nuclear transformations and reactions (short- and long-lived radioactive decay, spallation reactions, fission), and their measurement provides much information on the origin and subsequent history of the meteorites.

(*b*) The initial abundance of the rare gases included in the material at the time of its formation is generally very low; therefore, even the contribution from processes with very low production rates can be measured.

(*c*) The rare gases cover a very large mass range in the periodic table, and many or even all of their 23 stable isotopes can be measured in a single small sample.

(*d*) The experimental methods for the determination of rare gas concentrations and their isotopic compositions are extremely sensitive, and the necessary extraction and purification techniques for handling such small gas samples are well developed.

Particular emphasis has been given to studies of the so-called primordial rare gases, which occur in some meteorites in addition to the ordinary radiogenic and cosmogenic rare gases. It was found (e.g., Eberhardt et al., ref. 90) that the primordial rare gases are enriched

in the surface layers of individual mineral grains. Solar wind was suggested as a possible source.

The institutions which have specialized in rare gas determinations in meteorites are as follows:

University of California, Berkeley, Physics Department (Reynolds, Pepin, Merrihue)
University of Minnesota, Physics Department (Nier, Signer—now in Zurich)
University of Chicago, Fermi Institute (Anders, Heymann)
Smithsonian Astrophysical Observatory (Fireman)
University of Arkansas, Chemistry Department (Kuroda, Rowe)
Brookhaven National Laboratory (Schaeffer, Stoenner)
McMaster University, Hamilton, Ontario (Thode)
Max Planck Institut, Mainz (Hintenberger, Wanke, Voshage)
Max Planck Institut, Heidelberg (Zähringer)
University of Berne, Physics Department (Geiss, Eberhardt)

Isotope Work (Excluding Rare Gases)

Investigations of isotopic composition of elements other than the rare gases have been pursued in only a few institutions. Epstein, Taylor, and their coworkers (California Institute of Technology) have studied O^{18}/O^{16} ratios in a wide variety of meteorites and minerals separated from them. Thode and his coworkers at McMaster University have reported on variations in S^{34}/S^{32} ratios in elemental sulfur, sulfide sulfur, and sulfate sulfur extracted from the Orgueil meteorite. The O^{18}/O^{16} ratio was measured in specimens from most stony meteorite classes, both on bulk samples and on separated mineral phases (Reuter et al., ref. 91; Taylor et al., ref. 92). On the basis of these data, certain genetical relationships are apparent between individual meteorite classes. The isotopic composition of several other elements was measured in meteorites and compared with the same ratios obtained from terrestrial assemblages (e.g., Monster et al., ref. 91; DeLaeter and Jeffrey, ref. 94; Murthy and Sandoval, ref. 95). The respective ratios agree within the limits of analytical errors.

Investigations of the isotopic composition of the heavier elements in meteorites have detected no anomalies. Wetherill (University of California, Los Angeles) has reported on Mo; Murthy and Sandoval (ref. 95; University of California, San Diego), on Cr; and Dews and Newberry (University of California, Berkeley), on Ag. Dews has also reported on Li, finding no anomaly, in contrast to the earlier work of Shima and Honda.

Organic Compounds

Published work in this field has somewhat diminished during 1965. To some extent this may be due to the difficulties inherent in inves-

tigating the black intractable "soot" that comprises most of the organic matter in the carbonaceous chondrites. Work on this problem is in progress at the following institutions: University of California, San Diego (Nagy and coworkers); University of Houston (Oro and coworkers); University of Chicago (Hayatsu and Anders); Esso Research Laboratories (Meinschein); Geophysical Laboratory (Hoering); University of London (Mueller and coworkers); and Vernadsky Institute, Moscow (Vdovykin). The biological or nonbiological origin of these organic compounds remains a controversial subject. Urey (ref. 96) has recently published a comprehensive review of this topic. He concludes: "Many lines of evidence strongly suggest that biogenic material exists in these meteorites [carbonaceous chondrites] and that it probably is indigenous." In a recent paper, Studier, Hayatsu, and Anders (ref. 97) report that the pattern of organic compounds in the carbonaceous chondrites fits the pattern to be expected from near-equilibrium reactions between hot gases in a solar nebula. This important field will evidently continue to be one of intensive research.

Meteorite Ages

Numerous determinations have been made of the ages of meteorites by using a variety of methods based on different nuclear reactions. It is meaningless to talk about the age of a meteorite in a general sense. Different methods, involving various elements and assumptions, usually give different ages. Actually, each nuclear reaction gives a point on the time scale for a specific event in the history of the meteorite sample, such as nucleosynthesis, general chemical separation processes, formation of the minerals in the sample, subsequent heating, breakup of a possible parent body, and time of fall of the meteorite.

Current work on the time of crystallization of individual minerals in meteorites, as determined by U-Pb, K-Ar, and Rb-Sr methods, shows an increasing degree of agreement between the different methods. Rb-Sr ages of silicate minerals separated from nodules of the Weekeroo Station iron meteorite have been measured (Wasserburg et al., ref. 98), yielding an age of 4.7×10^9 years. Under the assumption that the silicates are cogenetic with the iron meteorite as a whole, which seems reasonable, this number can be considered to represent the age of the iron meteorite. This number agrees well with dates of stone meteorites, but disagrees strikingly with the high K-Ar ages of up to 11×10^9 years reported earlier by Stoenner and Zähringer (ref. 99) for other iron meteorites.

The results are consistent with a time of crystallization about 4.6×10^9 years ago, a time common to all meteorite types. Meteorites are thus by far the oldest objects yet found; they antedate the oldest

terrestrial rocks by at least a billion years. The results of measurement of extinct I^{129} from the Xe^{129} content of meteorites indicate that crystallization followed relatively closely after nucleosynthesis, probably within a few hundred million years.

In contrast to the high age of crystallization, the time of breakup of parent meteorite bodies, as given by the cosmic-ray exposure ages (Lipschutz et al., ref. 100; Heymann, ref. 101), was comparatively recent. Current work, carried out in the United States, in Germany, and in Switzerland, has shown that irons have exposure ages of the order of hundreds of millions of years, whereas the exposure ages for the stones are much lower. Of the common meteorites, most of the bronzite chondrites lie in a single cluster with an exposure age of about 4 million years, whereas the hypersthene chondrites cluster at 3, 7 to 13, and 16 to 31 million years. Perhaps each of these clusters represents a single breakup of a parent body. Wanke believes that the evidence strongly favors a lunar origin for the bronzite chondrites, whereas the hypersthene chondrites come from beyond the Earth's orbit, probably from Mars or the asteroids.

Tektite Investigations

During calendar year 1965, studies on tektites tended to concentrate on the supposed sources of tektites or their supposed parent materials. Barnes (ref. 102) has drawn attention to the probability that the most primitive type of tektite is one to which he gave the name of "Muong Nong." These tektites are nearly identical with others of the same strewn field, but they show much more detail in their petrographic structure, as can be seen in figure 29. Barnes pointed out that these tektites often contain angular voids, which contrast with the spherical or ellipsoidal voids seen in other specimens, and in congealed liquids in general. He concluded that Muong Nong tektites were formed by partial welding of fragmental material, the angular voids being the spaces between fragments.

Barnes' idea that they are primitive contrasts with the suggestion by O'Keefe (ref. 103) that the pumicelike Igast material is the original form.

Walter (ref. 104) found coesite in some small inclusions of pure SiO_2 in Muong Nong-type tektites. This supports the impact theory of the origin of tektites.

Another series of investigations sought the source material of tektites in terrestrial impact craters. The study of the tracks produced in glass by the natural fisson of U^{238} has given a new dating technique. This technique indicates that the age of the moldavites is close to the age of the great impact crater of the Ries Kessel (Fleischer et al., ref.

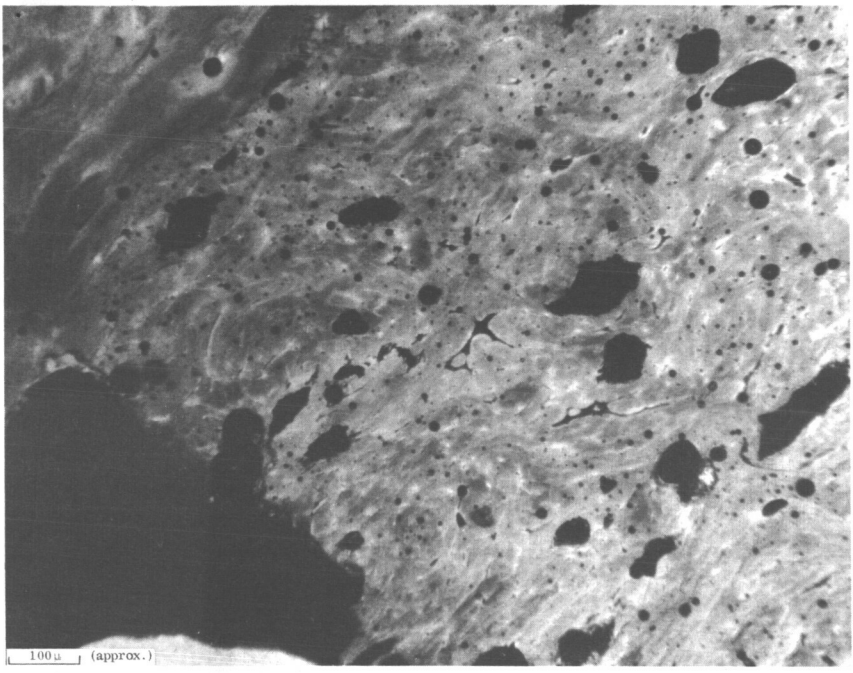

Figure 29.—**Muong Nong tektite. Thin section. Internal structures include contorted, parallel layering and angular voids.**

89), a conclusion already drawn on grounds of K-Ar dating and stratigraphy. The new dating procedures are not sufficiently precise to upset the stratigraphic evidence of a measurable difference in date, however.

The same techniques were employed to study the relation between the Bosumtwi crater and the Ivory Coast tektites. (See ref. 89.) The results showed very large scatter in age; both appear to be late Pliocene or early Pleistocene. Studies of the strontium-rubidium ratios (Schnetzler et al., ref. 105) indicate that the age of differentiation, some 2 billion years ago, is the same for Ivory Coast tektites as for the Bosumtwi glass. While this evidence supports a similar origin for the two, it does not explain the great differences in petrography between the impactites and the tektites.

SCIENTIFIC RESEARCH

Laboratory and theoretical studies provide both the empirical observations and the analytical models needed for understanding new phenomena and for planning of future investigations. Significant at-

tention has been devoted to the study of hypervelocity impact effects on different materials. Particles are accelerated by various techniques to speeds in excess of 1 kilometer per second and directed against targets of different materials. Recent construction of vertical gun facilities has permitted study of the effect of hypervelocity impact on noncohesive, highly fragmental targets.

High pressure, including the shock effects of hypervelocity impact, may induce permanent phase changes in minerals. These are studied by mineralogical and crystallographic techniques, and are important for distinguishing between impact and volcanic phenomena.

Theoretical studies cover the spectrum from the structure of planetary surfaces and interiors to the origin of matter and the evolution of the solar system. Theory attempts to organize and synthesize our observations into a coherent view which may then be used to predict additional properties or behavior.

Impact Shock Effects

The surfaces of the Moon, Mars, and perhaps Mercury have been extensively modified by repeated hypervelocity impacts of small bodies of the solar system. Each primary hypervelocity collision produced thousands of low-speed projectiles which were ejected into ballistic trajectories across the planetary surfaces. The low-speed projectiles in turn impacted the surfaces to produce secondary craters and additional ejecta. As a consequence, the terrestrial planets with little or no atmosphere have been bombarded by a large range of sizes of bodies which crossed their orbits. Because of the absence of significant atmospheric weathering agents, their surface features and surface properties have been shaped to a large degree by the effects of such impacts. Over long time periods their surfaces have been worked and reworked to produce a cratered, ejecta-littered terrain consisting of fragmental, shocked mineral assemblages.

Laboratory studies on mechanisms of hypervelocity impact crater formation and effects of shock on natural materials have continued during the past year. A significant amount of work has been done on the mechanics of cratering, with particular emphasis on penetration of the skin of spacecraft structures by micrometeoroids. (See ref. 106.) Information gained in these endeavors has been of value to planetology, for it has indicated that target strength is of decided importance in determining the dimensions of the final crater, and that the effective target strength changes with the scale of the event. These findings have an important bearing on the problem of scaling results from small laboratory craters across many orders of magnitude to interpret the effect of large impacts of planetary surfaces (Gault and

Moore, ref. 107). Until the role of target strength is firmly established, such scaling is impossible.

Additional information on the effects of gravity on crater formation is needed to compare laboratory results on Earth with results on craters formed on the Moon or Mars. Results of one study (Moruski and Teal, ref. 108), in which chemical explosive cratering techniques in cohesionless sand were used in various gravity fields, indicate that $D \propto (1/g)^{1/7}$, where D is the diameter of the crater. Further work is required before precise estimates of crater size as a function of projectile kinetic energy can be made for even small craters on planets other than the Earth.

Study of shock damage to minerals and mineral assemblages is continuing, but most of the effort in this field of study has been directed toward assessing damage to metals used in spacecraft structures. Further work on shock damage to quartz (DeCarli and Milton, ref. 109) indicates that quartz can invert during shock to a short-range order (SRO) phase with sixfold coordination. A small portion of this SRO phase may develop the long-range order of stishovite in times less than 10 microseconds. Coesite has not been formed under experimental shock conditions, but it is suspected that coesite may form from the SRO phase after the shock pressure attenuates below the stability of the SRO phase during a protracted pressure pulse.

A novel study of the chemical changes induced by shock loading of a nickel-iron target by a nickel-iron projectile in air (Schmitt et al., ref. 110) indicates that considerable chemical fractionation occurred in molten droplets ejected from the crater but that none occurred in nonmelted phases. The droplets, congealed to spherules, were depleted in nickel and chromium; the iron was oxidized to magnetite; and the silicon was segregated into patches.

Cratering studies carried out by NASA during the past year have been directed toward obtaining an understanding of the surface properties of the Moon by empirical methods. Results of laboratory and field investigations of impact cratering reported in abstract form (Gault and Quaide, ref. 111) indicate that the geometric forms of small craters of suspected secondary origin observed on Ranger film records can be reproduced in the laboratory as primary craters by using thick targets of materials with low cohesive strength.

Theoretical Model Studies

Knowledge of the history, composition, and structure of the interiors of the planets, satellites, and small bodies of the solar system is required to understand their origins. Until direct measurements are

made, models may be unrealistic and theoretical studies must be based on assumptions. Such studies are nevertheless of considerable value in summarizing the state of knowledge concerning fundamental properties of the solar system. They contribute further in delineating problem areas for investigation.

Theoretical model studies of the Earth have been carried out for many years. Conclusions regarding the internal constitution of other terrestrial planets are dependent on the assumptions as to the nature of the Earth's core. Confirmation that the mantle-core boundary does not result from a pressure-induced phase change, but instead is a compositional discontinuity, is one of the year's most significant contributions (Kovach and Anderson, ref. 112). This result was determined by using the equation of state of iron, computed from shock wave by Hugoniot, and the terrestrial density distribution, determined from free oscillations of the Earth induced by strong seismic shocks rather than previous assumptions regarding homogeneity, thermal gradients, and hydrostaticity. It has been postulated that the material of the core must represent a phase change if the terrestrial planets are all of similar composition; however, if the core material is chemically distinct, the planets must differ in overall chemical composition. Kovach and Anderson's study also demonstrates that the Earth, Venus, and Mars could have the same chemical compositions with chemically distinct iron-rich cores, provided the external radius of Mars is about 3310 kilometers. Since Mars appears to be a nearly homogeneous body, mantle and core material would necessarily be mixed and similar to an undifferentiated Earth. The Moon and Mercury must differ in composition.

A model study of Mercury (Plageman, ref. 113) suggests that the planet may have a large iron core (Radius=2112 km) and a thin mantle (334 km) if we assume that the internal structure of Mercury is similar to the Earth's, as suggested by its mean density (5.31 ± 0.27 grams/centimeter^3), and that the surface density of Mercury is 3.3 grams/centimeter^3. Values of pressure and density at the center of the planet calculated from this model by using the equation of hydrostatic equilibrium are 7.37 gm/cm^3 and 0.327×10^{12} dynes/cm^2. The extreme values of temperature distribution, calculated from this model, indicate that the highest temperature occurs on the sunward side of Mercury at the core-mantle boundary. These results suggest that neither the core nor the mantle of Mercury is molten.

A new model calculation of the thermal history of the Moon (Fricker and Reynolds, ref. 114), for which a low initial temperature and a variable concentration of radioactive heat sources is assumed, indicates that a major portion of the Moon has never been molten. If

the initial abundance of radioactive sources is less than that of the chondritic meteorites, appreciable melting or differentiation is not expected. With chondritic concentrations, partial melting could take place in the interior below a depth of 350 kilometers. Partial melting would produce differentiation and concentration of radioactive heat sources in upper levels. Such a process is required if there has been significant volcanic activity on the Moon.

Further theoretical considerations published in 1965 are concerned primarily with the Moon. Calculations using Chandrasekhar's linearized theory of motion show that effects of convection could not account for the large difference $C-A$ of the moments of inertia of the Moon about its polar and equatorial axes (Kopal, ref. 115). Nor could such a difference arise as a result of nonsymmetric deformation due to thermal expansion where the nonsymmetric expansion is driven by the difference in insolation between the equator and the poles (Kopal, ref. 116).

Calculations concerning the shape, gravity field, and strength of the Moon, made using the theory of a rotating gravity field which has a triaxial ellipsoid as an equipotential surface, indicate that the surface of the Moon cannot be equipotential and that the Moon is not in hydrostatic equilibrium (Caputo, ref. 117). Differences between observed and calculated values of the shape are assumed to result from internal strength. Under the assumption that the Moon has a rigidity similar to that of the upper mantle of the Earth, the minimum strength necessary to support the bulges has been calculated for models with various thermal histories (no core and various sizes of cores).

The change in shape of a circular crater in a highly viscous medium has been derived from the hydrodynamic equations of motion. Correspondence is good between shapes derived from the theory and shapes observed on the Moon, but the time constant suggests that the large lunar craters are much younger or that the viscosity of lunar rocks is much greater than has been thought.

TERRESTRIAL COUNTERPARTS OF LUNAR AND PLANETARY FEATURES

The problem of the origin of the lunar surface features, more properly the geomorphology of the lunar surface, has occupied scientific thought since the time of Galileo. Recently, the Mariner IV spacecraft acquired images of the Martian surface with sufficient resolution for geological analysis to be meaningfully extended to Mars, as well as to the Moon.

The dominant feature of both lunar and Martian surfaces is the presence of craters—circular depressions, with or without raised rims and radial ray patterns, and with or without central peaks or other internal structure. The primary emphasis, as a consequence, has been placed on circular geologic structures (meteorite craters, volcanic collapse, and caldera structures and cryptoexplosion craters), nuclear and conventional explosive craters, and their associated phenomena (shock deformation, throwout patterns, and high-pressure mineralogy).

A major review of terrestrial analog studies was held as part of the Conference on Geological Problems in Lunar Research, by the New York Academy of Sciences (ref. 118). The following papers from this review illustrate the progress which is being made in this complex subject:

W. E. Elston (ref. 119) reviewed volcano-tectonic depressions with dimensions comparable to those of large lunar craters. The Mogollon Plateau in New Mexico appears to be a ring-dike structure, with extensive rhyolite ash flows, which bears a striking resemblance to some of the larger craters on the Moon.

The large lunar craters are interpreted as surface calderas by G. J. H. McCall (ref. 120), which are related to terrestrial volcanic calderas. The systems of intersecting fracture lines which traverse the lunar surface, and the craters, are considered to comprise an integrated volcano-tectonic pattern. If the physical disparity between terrestrial and lunar surface conditions is taken into consideration, an analogy may be drawn between lunar volcanism and terrestrial volcanic gas emission (and associated fumarolic deposits).

Amstutz (ref. 121) concludes that the source of energy for the polygonal structures in Missouri which he has studied has been derived from crustal movements, and that these structures may result from diapiric doming and ring-dike faulting. The features are similar in size distribution to ring dikes in shield areas and volcanic structures. They show a pattern of alternating slip and deformation; of repeated faulting and uplifting; and of ring-graben formation.

A different origin for two of the Missouri structures, Crooked Creek and Decaturville, is proposed by Dietz (ref. 122). He concludes that Barringer (Meteor) Crater, Steinheim Basin, Wells Creek Basin, Serpent Mound and Kentland Structures, Sierra Madera, Vredefort Ring, and Clearwater West and Carswell are very similar, so that a single explanation must be found for all. Shock criteria, particularly shatter cones, distinguish these astroblemes or ancient meteorite impact scars from volcanic and related endogenic structures which display similar circularity and evidence of natural explosive force. Furthermore, if maria are impact basins filled with magma and overlain by

welded tuff, the Sudbury intrusive lopolith in Canada bears reasonable interpretation as an astrobleme equivalent of a small lunar mare.

On the other hand, Bucher (ref. 123) points out that the largest circular structures on three continents lie along the axes of major regional tectonic patterns, and are closely associated with deep-seated volcanic phenomena. He concludes that the presence of shatter cones, or high-pressure minerals (coesite) in structures developed by powerful, explosive forces is not sufficient evidence for impact from above.

From a theoretical point of view, Beals (ref. 124) has examined the phenomena which might reasonably be associated with a large meteorite impact in terms of impact energy, crater diameter, and impact lava volume and depth. The unresolved problem of central uplifts in lunar craters has been considered, together with the influence of features of known origin on the interpretation of a nearby crater of unknown origin. Beals suggests that a critical, quantitative examination of the fundamental physical criteria of identification is needed, in addition to a more thorough examination of ancient craters. Since it is clear that no single theory can account for all circular features on the Earth's surface, it is likely that the same situation exists on the surface of the Moon.

A further example of divided interpretations of the same circular terrestrial features is found in papers by Currie (ref. 125) and Dence (ref. 126) on a series of Canadian craters. In agreement with the conclusions of Amstutz and Bucher (refs. 121 and 123), Currie thinks that the craters occur along a great welt on the Canadian Shield which has been raised since late Paleozoic time. Local structural features, usually older faults, determine the site of the craters, which are formed by cycles of uparching and collapse. The continental distribution of the craters, together with associated hydrothermal and volcanic activity, suggests that they are associated with events in the mantle which are related to degassing of the Earth. Dence, however, concludes that it has not been considered necessary to abandon the general hypothesis of meteoritic impact, although current theory is inadequate to explain many aspects of the structures revealed by investigations to date. The model required to fit the more complex craters possesses a central uplift, a ring uplift, and an outer annular depression. Such a model reproduces the essential structural features of the Vredefort Ring and many cryptoexplosion structures. Thus, an origin by meteoritic impact for all these structures is supported by the investigations of the Canadian craters. Dence concludes that the metamorphic and structural features should be studied further in order to advance the theory of hypervelocity as the mechanism of formation for complex craters.

After a detailed examination of both the impact and the cryptoexplosion mechanism to account for the many perplexing features of the Wolf Creek Crater, McCall (ref. 127) concludes that the evidence is about evenly divided on the origin of this magnificent and mysterious crater. In summing up the case for either origin, he points out that those geologists who maintain reservations do so not simply to provoke argument, but because there are certain very real and baffling conflicts of evidence. Being schooled in the geological discipline, they are conscious that geology has provided numerous cases of the first and apparently obvious answer, which has been subsequently proved erroneous.

One of the criteria for distinguishing between meteorite and volcanic craters is examined by Elston and Lambert (ref. 128) and Manton (ref. 129) in papers on shatter cones. The former describes striated cones at a small volcanic vent near Albuquerque, N. Mex. These resemble shatter cones which are believed both to be a criterion of meteorite impact and to indicate that volcanic explosions sufficiently powerful to form shatter cones have occurred. Manton concludes that when the since-deformed strata are restored to their original positions, the orientation of shatter cone axes in the Vredefort Ring converges to a centrally located focus which apparently was close to the original land surface. If the shatter coning was due to a shock, the shock was directed downward and outward. However, since the ring of rocks was at one time nearly vertical, the force of gravity may have been the orienting factor. The origin of the shatter cones in this case would be related to other events in the geological evolution of the subcontinent rather than to an extraterrestrial event.

Another criterion for the resolution of possible origins for lunar structures is geophysical measurements. Geyer and Van Lopik (ref. 130) emphasize that in order to gain the ability to obtain and interpret lunar data correctly, we must first determine and catalog the geophysical properties of terrestrial features. They conclude that it is desirable to conduct detailed and accurate magnetic and gravity surveys of meteoritic impact, volcanic, and cryptoexplosion features in order to establish criteria and to establish a valid basis for making terrestrial-lunar comparisons.

Developing this approach, Brereton (ref. 131) and Lowman (ref. 132) review magnetic data obtained from surveys across Meteor Crater and Sierra Madera, respectively. Brereton concludes that the magnetic anomaly which appears to be associated with Meteor Crater cannot possibly be related to a buried mass of extraterrestrial material; however, its presence could lend credence to a terrestrial origin for this feature. Although the origin of Sierra Madera is far from settled, Lowman concludes that the evidence presently favors a buried igneous

intrusion as being responsible for the development of the structure. However, further geological and geophysical studies are needed to settle the problem and to clarify the origin of cryptoexplosion structures in general.

LUNAR LANDING SITE SELECTION

A lunar site selection study has been conducted by the U.S. Geological Survey in conjunction with the Lunar Orbiter and Surveyor Projects, Bellcomm, Manned Spacecraft Center, and NASA Headquarters. As a result, the lunar surface has been categorized into several terrain types, and promising targets for Lunar Orbiter photography have been selected within the Apollo and Surveyor landing areas. Figure 30 shows the 10 potential areas on the Moon that have been selected for photography by the Lunar Orbiter spacecraft. The areas include examples of all the major types of lunar terrain to permit assessment of their suitability for spacecraft landings. Nine of the sites are within the area proposed for Apollo manned lunar landings outlined by the black rectangle. Eight of the areas are potential sites for Surveyor soft-landing spacecraft. During its 8-day picture-taking trip across the target area, Lunar Orbiter will be in an orbit with an apolune of 1150 miles and a perilune as low as 29 miles with a period of 3½ hours. One target area will be photographed about every five orbits and up to four pictures radioed to Earth. Following the photography of all 10 sites, the remaining 160 pictures will be transmitted to Earth stations.

This work is based on lunar photogeologic mapping by the U.S. Geological Survey, using topographic maps prepared by the U.S. Air Force Aeronautical Chart and Information Center. Extensive telescopic observation of the Moon has been utilized by the geologists who prepared the maps. Ranger photointerpretation conclusions have influenced the terrain assessment procedure. Quantitative measurements of slope component and frequency distribution have been used extensively to evaluate lunar morphology and to provide a basis for judgment of relative surface roughness.

Lunar terrain units have been rated in terms of increasing relative roughness in the following order: dark mare, average mare, ridged mare, ray-covered mare, highland basins, floors of deformed craters, subdued uplands, crater rims, and sculptured highlands. (See ref. 133, p. 18.) Although the upland and crater units are rougher than general mare types, those areas may have significantly higher bearing strength than the mare materials.

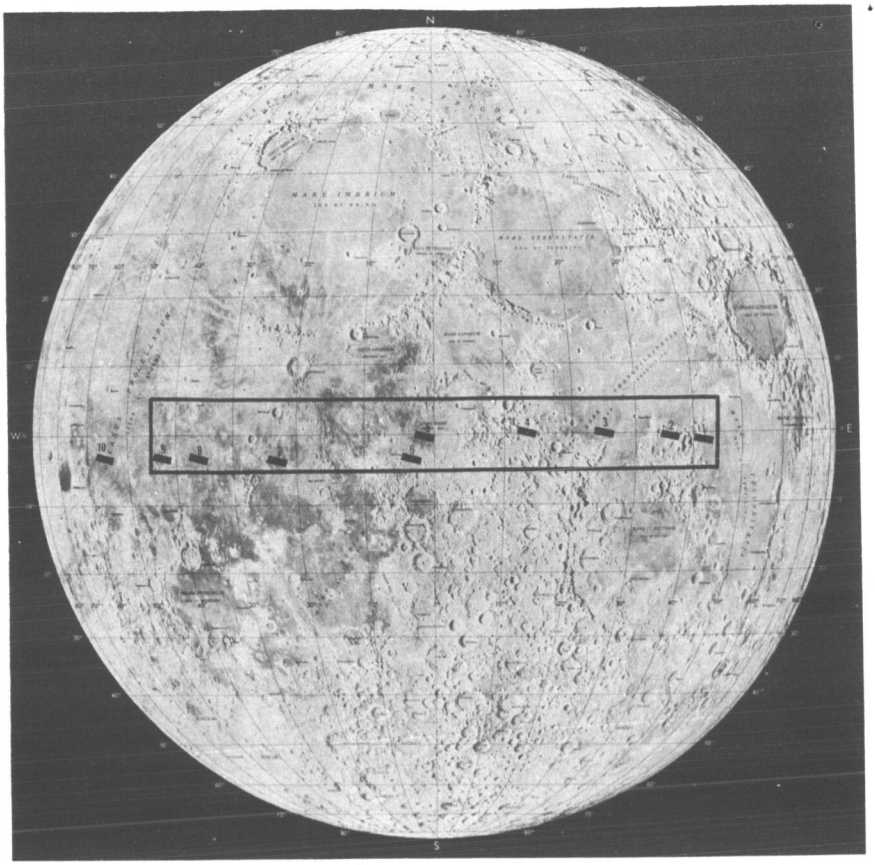

Figure 30.—Lunar Orbiter photographic target areas.

PRESENT STATE OF KNOWLEDGE

Speculation about the Moon, Mars, and Venus has been delimited as a result of spaceborne investigations. We have made major advances in our understanding of these bodies. New measurements have been made which further delineate the parameters of the solar system.

Moon

Lunar Surface

The current interpretation of the features and measurements of the lunar surface is that meteoritic and cometary impacts are the primary sources of the craters. Magmatic activity has also been present on the Moon, and the fillings of crater floors may reflect volcanic outpourings. The alinement of surface features, with the exception of crater ray

systems and secondary crater loops, indicates internal tectonic activity. Micrometeoritic bombardment results in a wearing away and softening of features, and produces a layer of rubble and dust. This dust is very finely divided and of very low density at the surface, but increases in coarseness with depth. The thickness of the surface debris is a function of the general age of the area; for old areas, the average thickness should be approximately a meter. This complex model has resulted, in large measure, from interpretations of the Ranger VII, VIII, and IX photographs. The results of the Ranger missions failed to support most hypotheses in detail; and more extensive knowledge of several concepts, including volcanic and impact processes, appears to be required to explain the fine structure of the lunar surface.

The surprising aspects of the model are those revealed by the tremendous gain ($\times 1000$) in resolution of the Ranger imagery over Earth-based observations; for instance:

(*a*) A tremendous clustering of small craters occurs which characterizes the rays associated with certain primary craters. Whitaker and Urey have proposed comets as possible sources of temporary, directed atmospheres which distribute the ray material to great distances in radial patterns.

(*b*) A remarkable similarity exists in the fine structure of mare areas and the floor of the crater Alphonsus.

(*c*) There is a predominance of shallow depressions with smoothly rounded rims and a "smoothed" or "windblown" appearance at resolutions below 300 meters. Such features may be produced by micrometeorite or solar particle erosion of secondary-impact craters, by deposition of dust over sharper craters, by collapse of cavities in a cooling flow, or by viscous adjustment of the surface toward isostatic equilibrium. The presence of fine fractures, "tree-bark structures," dimple craters, and other features have been used to refute these theories. Recent experiments by Gault and Quaide (ref. 111) indicate that similar features may be produced by primary hypervelocity impact in thick targets of materials with low cohesive strength. If many diverse mechanisms can produce similar features, it is possible that the effects of more than one process are in evidence.

(*d*) There are dimple craters with conical walls which steepen toward the center, apparently indicating slump of material into a hidden cavity.

(*e*) Protuberances strewn over the lunar surface are absent, and small positive relief features other than rounded domes and a few surface bumps are rare.

(*f*) An interesting relationship exists among the linear depressions called rills, chain craters, and dark-halo craters.

(*g*) Of interest is the detailed structure of the dark-halo craters which are placed squarely on rills and surrounded by blankets of dark material which have partly filled the rills. These rough dark deposits have no sharp boundaries or layers, indicating that they are composed of ash or debris rather than lava flows. Clusters of small craters and scars indicate that substantial blocks were ejected from the craters.

(*h*) The walls of the crater Alphonsus are remarkably smooth and rounded.

(*i*) A marked uniformity exists in the shape of the few, sharp-rimmed, steep-walled (primary) craters observed at all scales.

Far Side of the Moon

The gross nature of the hidden hemisphere of the Moon had been defined by the 1959 U.S.S.R. Luna III mission as a heavily cratered, mountainous, highland area with rare, small mare. The Soviet Zond III confirmed these findings and photographed craters with central peaks, ray systems, and large overlapping craters. Long chains of craters are considerably more developed than on the visible side, in some cases extending more than 1500 kilometers. An unusual crater form which is frequently observed on the far side of the Moon is a "thalassoid," or a large ring-shaped concavity which is comparable to mare in size and shape, but lacks the dark floor and has a cratered floor instead.

Photogeologic Mapping and Interpretation

Geologic mapping of the near side of the Moon has detailed the structure and stratigraphy of a major portion of the observable lunar surface. Preliminary versions of lunar geologic quadrangles have been used to classify and evaluate the characteristics of lunar terrain units. These studies have resulted in the choice of Surveyor and Lunar Orbiter target sites which hopefully will be verified as Apollo landing sites. Data and samples from these missions will help resolve many of the major questions which remain about the nature, origin, and history of the Moon.

Mars

The significant conclusions concerning the surface of Mars and the outstanding problems which warrant investigation during exploration of the planet have been summarized by the Mariner IV television investigators (Leighton et al., ref. 12), the National Academy of Sciences (ref. 134), and Loomis (ref. 13). On a planetary scale, optical measurements and observations of the orbit of Phobos indicate that the equatorial regions of the surface are a few tens of thousands

of feet higher than the polar areas. On a continental scale, Loomis concludes that there is no positive evidence which indicates that the dark areas are higher or lower in elevation than the light areas, which are assumed to be deserts. This assumption is based on observations of huge clouds which often sweep surfaces of these areas—much like duststorms across a desert. The existence of mountains has been inferred from bright spots observed often at a few, fixed localities (de Vaucouleurs, ref. 135); these spots are assumed to be clouds surrounding isolated mountain peaks.

The composition of the Martian surface has been interpreted as powdered silicates and/or limonite on the basis of visible and infrared spectra and polarization studies. Loomis (ref. 13), in reviewing the data and conclusions which relate to this subject, indicates that present knowledge supports the iron oxide coating (goethite and hematite) interpretation. He notes that this may not necessarily indicate that the iron has weathered from near-surface rocks since Mars is the closest planet to the asteroid belt and could have received surface iron by meteoritic impact.

The Mariner IV photographs provide a startling insight into the existence and nature of craters on Mars on a 3- to 200-kilometer scale. The distribution and morphology of the craters is much like that of the highland areas of the Moon, with the exception that there are considerably fewer craters on Mars with diameters smaller than about 30 kilometers. This implies an obliteration process, such as lateral redistribution by wind, which has eroded material from the crater rims and deposited it on their floors.

The heavy crater distribution recorded in the Mariner pictures implies that the surface of Mars is old and that rapid erosion by running water may never have taken place. Beyond this, presently available interpretations of the pictures have not resolved the detailed nature of the light and dark areas, the canals, the "wave of darkening," and many other questions which await future investigations.

In a comprehensive review of the atmosphere of Mars, Johnson (ref. 136) notes several important implications relating to the geologic history of Mars. Mars is so cold that the water vapor released into its atmosphere has mainly collected as ice at the surface (which may now be covered by dust) leaving carbon dioxide in the atmosphere. Without liquid water, carbon dioxide has accumulated to its present concentration without significant loss to geologic deposits (such as limestone). The total amount of carbon dioxide which has been released on Mars appears to be on the order of a thousand times less than that released on Earth. Since gases from the interior of the Earth have been released mainly by volcanic activity, it is reasonable to conclude

245-015 O—67——13

that the volcanic activity on Mars has been a thousand times less than that on Earth.

Venus

The continuous cloud cover of Venus has restricted knowledge of the surface and interior of the planet to a series of inferences drawn from 3.15-centimeter microwave radiation (Smith and Carr, ref. 137) and radar measurements at 12- and 68-centimeter wavelengths (Millstone Radar Observatory, ref. 138; Victor and Stevens, ref. 139, Maron et al., ref. 140; Thomson et al., ref. 141; Kotelnikov, ref. 142). These data indicate that the surface temperature of the sunlit hemisphere is about 600° K, some 145° K higher than the surface temperature of the dark hemisphere; that the echo pulse shape reflects a surface smoother, in dimensions of radar wavelength, than that of the Moon; and that the dielectric constant deduced from the radar cross section is about that of quartz, a fact which supports the conclusion that the surface is silicate rock.

The radar spectrum has also been analyzed in order to determine the period of rotation of the planet (Kotelnikov, ref. 142; Smith and Carr, ref. 137, Carpenter, ref. 143). Measurements made during the 1964 conjunction have verified the retrograde rotation (period of 249 ± 6 days; Carpenter, ref. 144) and have indicated the presence of major mountain chains stretching across the surface of the planet. While telescopic observations, balloon flights, and measurements by the Mariner II spacecraft have provided significant information on the atmosphere of Venus, knowledge of the surface and interior of the planet is at least an order of magnitude lower than that known about the planet Mars. The Venusian cloud cover will seriously impede progress in this area by photogeologic techniques. On future missions to Venus, radar methods and thermal mapping may be able to acquire imagery and surface properties from orbital altitudes, or from within the atmosphere. The high surface temperatures and extreme atmospheric environment of Venus may preclude all but the simplest drop types of missions.

Jupiter

A summary of the present state of knowledge of Jupiter has been undertaken (JPL Engineering Planning Document No. 280, Sept. 15, 1965) in order to focus attention on the significant questions which may be resolved by observations from spacecraft. Since a Jupiter probe requires approximately 2 years of travel time, the opportunity exists for extended interplanetary measurements such as those made by Mariner II and Mariner IV. Additional investigations may be

desirable for the portion of the trajectory which passes through the asteroid belt.

Jupiter is one of the great outer planets, differing radically from the small, dense, terrestrial planets. Located more than 5 astronomical units from the Sun, Jupiter is the largest object outside the Sun in the solar system, 11 times the Earth's diameter and 318 times its mass. The mean density of 1.35 gm/cm^3 suggests that Jupiter differs markedly in composition and structure from the Earth.

Great bands of clouds obscure the surface of Jupiter from visual observations. Because of the great mass of the planet, much of the primordial gaseous material may have been retained. Unique surface features and alteration may have been produced by the interaction of the Jovian atmospheric hydrogen, methane, and ammonia with the condensed material of the planet, which is probably metallic hydrogen.

Studies related to the planetology of Jupiter include investigations of the topography, morphology, and composition of the surface; the extent and history of chemical differentiation, if any, within the planet; the sources of internal energy which are released, including radioactive, gravitational, and nuclear energy; the internal structure of the planet; and the relation of the magnetic field of Jupiter to a possible fluid core which is suggested by the existence of belts of trapped radiation about the planet.

The so-called "Red Spot," a huge, elliptical, orange-pink blemish in the southern tropical zone of Jupiter, is one of the profound mysteries of the solar system. During the past 134 years, its position has shifted through at least 1080° of longitude in a coordinate system chosen to minimize this effect, showing remarkable accelerations in 1880, 1912 to 1920, 1926, and 1936. It has brightened several times, most recently in 1962. Between 1879 and 1882 it rose to an intensity never before observed in any Jovian markings. While the "Red Spot" is a phenomenon of the Jovian atmosphere, it may reflect surface features such as a mountain range or a fluid vortex resulting from enormous Coriolis forces.

The effects of the satellites Io and Ganymede on Jovian radio-emission may indicate either their tidal effects on the planet or that these satellites possess magnetic fields. They are interesting bodies in their own right, and are much more tractable to investigation than Jupiter itself.

Other Major Planets

Jupiter, Saturn, Uranus, and Neptune are the so-called major planets, characterized by large masses and small mean densities. In addition to those features mentioned previously for Jupiter, the following features are also worthy of note.

Saturn is the only planet known to possess rings. The rotation axis of Uranus is highly inclined to the plane of the ecliptic. Neptune has a large satellite, Triton, which is in a retrograde orbit. Uranus and Neptune have mean densities greater than those of Jupiter and Saturn but less than those of the terrestrial planets. Hydrogen may not be the main constituent of Uranus and Neptune.

Mercury and Pluto

Mercury and Pluto share many uncertainties and a few similarities in their orbital characteristics and body properties. They lie at the opposite extremes of the solar system. Each has an anomalously large orbital eccentricity and inclination, raising uncertainties about the past histories of these planets with respect to their neighbors.

The mass and radius of Mercury are so poorly known that the density may lie between 3.6 and 6.6. Perturbations of the orbit of Neptune suggest that the mass of Pluto is similar to that of Uranus, a much larger planet, and that the mean density is like that of the terrestrial, rather than the major planets.

The photometric (Pettit, ref. 145), polarimetric (Gehrels and Teska, ref. 146), and radar reflection (Kotelnikov, ref. 147) properties of Mercury are similar to those of the Moon. The surface temperature has been measured as 613° K by infrared techniques (Pettit, ref. 145), and as 380° K by microwave emission techniques (Howard et al., ref. 148). The difference in thermal measurements may reflect the distribution of temperature across the disk of Mercury, as well as the physical properties of the surface materials.

The rotation of Mercury has been estimated from the apparent motion of surface features (Dollfus, ref. 149) as being synchronous with the 88-day period of revolution about the Sun. Radar observations, however, indicate a period of 57 days; no satisfactory determination of the rotation axis is available (ref. 1). The only firm conclusions from the visual work is that Mercury has a system of large-scale markings whose apparent motion, with respect to the terminator, is consistent with the theoretical prediction of a significant libration.

REFERENCES

1. ANON.: Space Research—Directions for the Future. Part One: Planetary and Lunar Exploration. Space Science Board, National Academy of Sciences, National Research Council, Washington, D.C., Dec. 1965.
2. ANON.: NASA 1965 Summer Conference on Lunar Exploration and Science. NASA SP–88, 1965.
3. BECKERLEY, J. G.: Significant Achievements in Planetology 1958–1964. NASA SP–99, 1966.

4. KUIPER, G. P.: Lunar Results From Rangers 7 to 9. Sky and Telescope, Special Supplement, May 1965, pp. 293–308.
5. ANON.: Ranger VII Photographs of the Moon. Part I: Camera "A" Series. NASA SP–61, 1965.
6. ANON.: Ranger VII Photographs of the Moon. Part II: Camera "B" Series. NASA SP–62, 1965.
7. ANON.: Ranger VII Photographs of the Moon. Part III: Camera "P" Series. NASA SP–63, 1965.
8. HEACOCK, R. L.; KUIPER, G. P.; SHOEMAKER, E. M.; UREY, H. C.; AND WHITAKER, E. A.: Ranger VII. Part II: Experimenters' Analyses and Interpretations. NASA CR–62347, 1965.
9. HEACOCK, R. L.; KUIPER, G. P.; SHOEMAKER, E. M.; UREY, H. C.; AND WHITAKER, E. A.: Ranger VIII and IX. Part II: Experimenters' Analyses and Interpretations. NASA CR–74894, 1966.
10. KOZYREV, N. A.: Observations of Volcanic Process on the Moon. Sky and Telescope, vol. 18, Feb. 1959, pp. 184–186.
11. STROM, R. G.: Analysis of Lunar Lineaments, I. Tectonic Maps of the Moon. Communication of the Lunar and Planetary Laboratory, Univ. of Arizona, vol. 2, no. 39, 1964, p. 1.
12. LEIGHTON, R. B.; MURRAY, B. C.; SHARP, R. P.; ALLEN, J. D.; AND SLOAN, R. K.: Mariner IV Photography of Mars: Initial Results. Science, vol. 149, Aug. 1965, pp. 627–630.
13. LOOMIS, A. A.: Some Geologic Problems of Mars. Bull. Geological Soc. Am., vol. 76, Oct. 1965, pp. 1083–1104.
14. BURGESS, E.: There are "Canals" on Mars. Spaceflight, vol. 8, no. 2, 1966, pp. 46, 47, 74.
15. SHOEMAKER, E. M.; HACKMAN, R. J.; AND EGGLETON, R. E.: Interplanetary Correlation of Geologic Time. Advances in the Astronautical Sciences, vol. 8, Plenum Press, 1963, pp. 70–89.
16. ALEXANDER, W. M.; MCCRACKEN, C. W.; AND BOHN, J. L.: Mariner IV Micrometeorite Data. Science, vol. 149, 1965, p. 1240.
17. ANDERS, E.; AND ARNOLD, J. R.: Age of Craters on Mars. Science, vol. 149, 1965, pp. 1494–1496.
18. WITTING, J.; NARIN, F.; AND STONE, C. A.: Mars: Age of Its Craters. Science, vol. 149, 1965, pp. 1496–1498.
19. BALDWIN, R. B.: Mars: An Estimate of the Age of Its Surface. Science, vol. 149, 1965, pp. 1498–1499.
20. KLIORE, A. J.; CAIN, D. L.; LEVY, G. S.; ESHLEMAN, V. R.; FJELDBO, G. F.; AND DRAKE, F. D.: The Mariner IV Occultation Experiment. Science, vol. 149, 1965, pp. 1243–1248.
21. LIPSKY, Y. N.: Major Victory for Soviet Science; New Data on the Invisible Side of the Moon. Pravda, No. 228 (17181), Aug. 17, 1965, p. 3.
22. LIPSKY, Y. N.: Zond-3 Photographs of the Moon's Far Side. Sky and Telescope, vol, 30, no. 6, Dec. 1965, pp. 338–341.
23. LOWMAN, P. D., JR.: Experiment S–5, Synoptic Terrain Photography During Gemini IV. Proceedings of the Manned Space Flight Experiments Symposium, Gemini Missions III and IV, NASA TM–X–56861, 1965, pp. 19–28.
24. ALLEN, C. R.; AND SILVER, L. T.: Agua Blanca Fault—A Major Transverse Structure of Northern Baja California, Mexico. Bull. Geological Soc. Am., vol. 71, Apr. 1960, pp. 457–482.
25. BEAL, C. H.: Reconnaissance of the Geology and Oil Possibilities of Baja California, Mexico. Geological Soc. Am. Memoir 31, 1948.

26. LOWMAN, P. D.: A Review of Photography of the Earth From Sounding Rockets and Satellites. NASA TN D–1868, 1964.
27. EARDLEY, A. J.: Structural Geology of North America. Second ed., Harper's, New York, 1962.
28. ANON.: Venus 2 Is on Target, No. 3 Shifted, Reds Say. Associated Press Rept., The Evening Star, Washington, D.C., Dec. 31, 1965.
29. "TYCHO" Study Group, Univ. of Minnesota: Report of August 1965 "TYCHO" Meeting. NASA CR–69878, 1965.
30. KOPAL, Z.; KLEPESTA, J.; AND RACKHAM, T. W.: Photographic Atlas of the Moon. Academic Press, 1965.
31. KUIPER, G., ED.: Photographic Lunar Atlas. Univ. of Chicago Press, 1960.
32. KUIPER, G. P.; ARTHUR, D. W. G.; AND WHITAKER, E. A.: Rectified Lunar Atlas. Univ. of Arizona Press, 1962.
33. WHITAKER, E. A.; KUIPER, G. P.; HARTMANN, W. K.; AND SPRADLEY, L. H.: Rectified Lunar Atlas. Univ. of Arizona Press, 1963.
34. HALAJIAN, J. D.: The Case for a Cohesive Lunar Surface Model. Annals of the New York Academy of Sciences, vol. 123, art. 2, 1965, pp. 671–710.
35. HAPKE, B.: Effects of a Simulated Solar Wind on the Photometric Properties of Rocks and Powders. Annals of the New York Academy of Sciences, vol. 123, art. 2, 1965, pp. 711–721.
36. HAPKE, B.: Second Preliminary Report on Experiments Relating to the Lunar Surface. Rept. 127, Center for Radiophysics and Space Research, Cornell Univ., 1962.
37. HAPKE, B.; AND VAN HORN, H.: Photometric Studies of Complex Surfaces, With Applications to the Moon. J. Geophys. Res., vol. 68, 1963, pp. 4545–4570.
38. MOORE, H. J.: Geologic Map of the Aristarchus Region of the Moon. Map I–465 (LAC–39), U.S. Geological Survey, 1965.
39. GOLD, T.: The Lunar Surface. Monthly Notice 115 of the Roy. Astron. Soc., 1955, pp. 585–604.
40. GOLD, THOMAS: Dust on the Moon. Vistas in Astronautics. Vol. II, Morton Alperin and Hollingsworth F. Gregory, eds., Pergamon Press, 1959, pp. 261–266.
41. GOLD, T.: Structure of the Lunar Surface. Rept. 156, Center for Radiophysics and Space Research, Cornell Univ., 1963.
42. CARR, M. H.: Geologic Map and Section of the Timocharis Region of the Moon. Map I–462 (LAC–40), U.S. Geological Survey, 1965.
43. EGGLETON, R. E.: Geologic Map of the Riphaeus Mountains Region of the Moon. Map I–458 (LAC–76), U.S. Geological Survey, 1965.
44. HACKMAN, R. J.: Geologic Map and Sections of the Kepler Region of the Moon. Map I–355 (LAC–57), U.S. Geological Survey, 1962.
45. MARSHALL, C. H.: Geologic Map and Sections of the Letronne Region of the Moon. Map I–385 (LAC–75), U.S. Geological Survey, 1963.
46. SHORTHILL, R. W.; AND SAARI, J. M.: Nonuniform Cooling of the Eclipsed Moon: A Listing of Thirty Prominent Anomalies. Science, vol. 150, 1965, pp. 210–212.
47. SAARI, J. M.; AND SHORTHILL, R. W.: Thermal Anomalies on the Totally Eclipsed Moon of December 19, 1964. Nature, vol. 205, 1965, pp. 964–965.
48. GREENACRE, J.: A Recent Observation of Lunar Color Phenomena. Sky and Telescope, vol. 26, 1963, pp. 316–317.

49. GREENACRE, J. C.: The 1963 Aristarchus Events in Geological Problems in Lunar Research. Annals of the New York Academy of Sciences, vol. 123, art. 2, 1965, pp. 811–816.

50. KOPAL, Z.; AND RACKHAM, T. W.: Lunar Luminescence and Solar Flares. Sky and Telescope, vol. 27, 1964, pp. 140–141.

51. GEHRELS, T.; COFFEEN, T.; AND OWINGS, D.: Wavelength Dependence of Polarization III. The Lunar Surface. Astron. J., vol. 69, 1964, pp. 826–852.

52. BELL, B.; AND WOLBACH, J. G.: Lunar Eclipses and Forecasting the Solar Minima. Icarus, vol. 4, 1965, pp. 409–414.

53. KOPAL, Z.; AND RACKHAM, T. W.: Excitation of Lunar Luminescence by Solar Activity. Icarus, vol. 2, 1963, pp. 481–500.

54. KOPAL, Z.: Lunar Luminescence. Sci. Am., vol. 212, 1965, pp. 28–37.

55. YOUNG, J. W.: Aristarchus Observations—Table Mountain Observatory. JPL SPS No. 37–34, vol. IV, Pasadena, Calif., 1965, pp. 183–184.

56. GILHEANY, J. J.: Operation Moon-Blink. The Strolling Astronomer, vol. 18, 1965, pp. 183–187.

57. DURHAM, C. J.; GEAKE, J. E.; AND WALKER, G.: Luminescence of Enstatite Achondrite Meteorites. Nature, vol. 203, 1964, pp. 134–136.

58. GREENMAN, J. A.; BURKIG, V. A.; GROSS, H. G.; AND YOUNG, J. F.: Feasibility Study of the Ultraviolet Spectral Analysis of the Lunar Surface. Douglas Aircraft Rept. SM–48259, Santa Monica, Calif., Mar. 1965.

59. NASH, DOUGLAS B.: Proton-Excited Silicate Luminescence: Experimental Results and Lunar Implications. J. Geophys. Res., vol. 71, May 15, 1966, pp. 2517–2534.

60. FLAM, E. J.; AND LINGENFELTER, R. E.: Lunar Luminescence. Nature, vol. 205, 1965, pp. 1301–1303.

61. CAMERON, A. G. W.: Particle Acceleration in Cislunar Space. Nature, vol. 204, 1964, p. 785.

62. MASON, B.: Principles of Geochemistry. Second ed., John Wiley & Sons, Inc., 1958.

63. FRONDEL, C.; AND KLEIN, C., JR.: Ureyite, $NaCrSi_2O_6$: A New Meteoritic Pyroxene. Science, vol. 149, 1965, pp. 742–744.

64. DODD, R. T.; VAN SCHMUS, W. R.; AND MARVIN, U. B.: Merrihueite, A New Alkali-Ferromagnesian Silicate From the Mezo-Madaras Chondrite. Science, vol. 149, 1965, pp. 972–974.

65. FREDRIKSSON, K.; AND HENDERSON, E. P.: The Horse Creek, Baca County, Colorado, Iron Meteorite. Trans. Am. Geophys. Union, vol. 46, 1965, p. 121.

66. KEIL, K.; AND ANDERSEN, C. A.: Occurrences of Sinoite, Si_2N_2O, in Meteorites. Nature, vol. 207, 1965, p. 745.

67. OLSEN, E.; AND FREDRIKSSON, K.: Iron Phosphates in Iron Meteorites. Trans. Am. Geophys. Union, vol. 46, 1965, pp. 121–122.

68. KEIL, K.; AND ANDERSEN, C. A.: Electron Microprobe Study of the Jajh deh Kot Lalu Enstatite Chondrite. Geochim. et Cosmochim. Acta, vol. 29, 1965, pp. 621–632.

69. FREDRIKSSON, K.; AND REID, A. M.: A Chondrule in the Chainpur Meteorite. Science, vol. 149, 1965, pp. 856–860.

70. WOOD, J. A.: The Cooling Rates and Parent Planets of Several Iron Meteorites. Icarus, vol. 3, 1964, pp. 429–459.

71. GOLDSTEIN, J. I.; AND OGILVIE, R. E.: The Growth of the Widmanstätten Pattern in Metallic Meteorites. Geochim. et Cosmochim. Acta, vol. 29, 1965, pp. 893–920.

72. SHORT, J. M.; AND ANDERSEN, C. A.: Electron Microprobe Analyses of the Widmanstätten Structure of Nine Iron Meteorites. J. Geophys. Res., vol. 70, 1965, pp. 3745–3759.

73. ANDERS, E.: Diamonds in Meteorites. Sci. Am., vol. 213, no. 4, Oct. 1965, pp. 26–36.

74. RINGWOOD, A. E.: Origin of Chondrites. Nature, vol. 207, 1965, pp. 701–704.

75. POLLACK, S. S.: Disordered Enstatite in Meteorites II. Am. Mineralogist, vol. 51, 1966, p. 1722.

76. MASON, B.: Feldspar in Chondrites. Science, vol. 148, 1965, p. 943.

77. DODD, R. T.; AND VAN SCHMUS, R.: Significance of the Unequilibrated Chondrites. J. Geophys. Res., vol. 70, 1965, pp. 3801–3811.

78. WOOD, J. A.: On the Origin of Chondrules and Chondrites. Icarus, vol. 2, 1963, pp. 152–180.

79. MASON, B.; AND WIIK, H. B.: The Composition of the Forest City, Tennasilm, Weston, and Geidam Meteorites. Am. Museum of Natural History, New York, Am. Museum Novitates, no. 2220, 1965.

80. MCCALL, G. J. H.: A Meteorite of Unique Type From Western Australia: The Mount Egerton Stony-Iron. Min. Mag., vol. 35, 1965, pp. 241–249.

81. HENDERSON, E. P.: The Hexahedrites. Smithsonian Museum Bull. 148, no. 5, 1965.

82. MASON, B.: The Chemical Composition of Olivine-Bronzite and Olivini-Hypersthene Chondrites. Am. Museum of Natural History, New York, Am. Museum Novitates no. 2223, 1965.

83. VOGT, J. R.; AND EHMANN, W. D.: Oxygen in Stony Meteorites. Radiochim. Acta, vol. 4, 1965, pp. 24–28.

84. VOGT, J. R.; AND EHMANN, W. D.: Silicon Abundances in Stony Meteorites by Fast Neutron Activation Analysis. Geochim. et Cosmochim. Acta, vol. 29, 1965, pp. 373–383.

85. COBB, J. C.; AND MORAN, G.: Gallium Concentrations in the Metal Phases of Various Meteorites. J. Geophys. Res., vol. 70, 1965, pp. 5309–5311.

86. BAEDECKER, P. A.; AND EHMANN, W. D.: The Distribution of Some Noble Metals in Meteorites and Natural Materials. Geochim. et Cosmochim. Acta, vol. 29, 1965, pp. 329–342.

87. NICHIPORUK, W.; AND BROWN, H.: The Distribution of Platinum and Palladium Metals in Iron Meteorites and in the Metal Phase of Ordinary Chondrites. J. Geophys. Res., vol. 70, 1965, pp. 459–470.

88. MOORE, C. G.; AND LEWIS, C.: Carbon Abundances in Chondritic Meteorites. Science, vol. 149, 1965, pp. 317–318.

89. FLEISCHER, R. L.; PRICE, P. B.; AND WALKER, R. M.: On the Simultaneous Origin of Tektites and Other Natural Glasses. Geochim. Acta, vol. 29, 1965, pp. 161–166.

90. EBERHARDT, P.; GEISS, J.; AND GROGLER, N.: Further Evidence on the Origin of Trapped Gases in the Meteorite Khor Temiki. J. Geophys. Res., vol. 70, 1965, pp. 4375–4378.

91. REUTER, J. H.; EPSTEIN, S.; AND TAYLOR, H. P.: O^{18}/O^{16} Ratios of Some Chondritic Meteorites and Terrestrial Ultramatic Rocks. Geochim. et Cosmochim. Acta, vol. 29, 1965, pp. 481–488.

92. TAYLOR, H. P.; DUKE, M. B.; SILVER, L. T.; AND EPSTEIN, S.: Oxygen Isotope Studies of Minerals in Stony Meteorites. Geochim. et Cosmochim. Acta, vol. 29, 1965, pp. 489–512.
93. MONSTER, J.; ANDERS, E.; AND THODE, H. G.: S^{34}/S^{32} Ratios for the Different Forms of Sulphur in the Orgueil Meteorite and Their Mode of Formation. Geochim. et Cosmochim. Acta, vol. 29, 1965, pp. 773–779.
94. DELAETER, J. R.; AND JEFFREY, P. M.: The Isotopic Composition of Terrestrial and Meteoritic Tin. J. Geophys. Res., vol. 70, 1965, pp. 2895–2903.
95. MURTHY, V. R.; AND SANDOVAL, P.: Chromium Isotopes in Meteorites. J. Geophys. Res., vol. 70, 1965, pp. 4379–4382.
96. UREY, H. C.: Biological Material in Meteorites: A Review. Science, vol. 151, no. 3707, Jan. 1966, pp. 157–166.
97. STUDIER, M. H.; HAYATSU, R.; AND ANDERS, E.: Organic Compounds in Carbonaceous Chondrites. Science, vol. 149, 1965, pp. 1455–1459.
98. WASSERBURG, G. J.; BURNETT, D. S.; AND FRONDEL, C.: Strontium-Rubidium Age of an Iron Meteorite. Science, vol. 150, 1965, pp. 1814–1818.
99. STOENNER, R. W.; AND ZÄHRINGER, J.: Potassium-Argon Age of Iron Meteorites. Geochim. et Cosmochim. Acta, vol. 15, 1958, pp. 40–50.
100. LIPSCHUTZ, M. E.; SIGNER, P.; AND ANDERS, E.: Cosmic Ray Exposure Ages of Iron Meteorites by the Ne^{21}/Al^{26} Method. J. Geophys. Res., vol. 70, 1965, pp. 1473–1489.
101. HEYMANN, D.: Cosmogenic and Radiogenic Helium, Neon, and Argon in Amphoteric Chondrites. J. Geophys. Res., vol. 70, 1965, pp. 3735–3743.
102. BARNES, V. E.: Terrestrial Implications of Layering, Bubble-Shape, and Minerals Along Faults in Tektite Origin. Geochim. et Cosmochim. Acta, vol. 28, 1964, pp. 1264–1271.
103. O'KEEFE, J. A.: Origin of Tektites, in Space Research, Proceedings of the First International Space Science Symposium, Nice, Jan. 1960 (H. Kallman Bijl, ed.), Interscience, New York, 1960.
104. WALTER, L. S.: Coesite Discovered in Tektites. Science, vol. 147, 1965, pp. 1029–1032.
105. SCHNETZLER, C. C.; PINSON, W. H.; AND HURLEY, P. M.: Rubidium-Strontium Age of the Bosumtwi Crater Area, Ghana, Compared With the Age of the Ivory Coast Tektites. Science, vol. 151, 1966, pp. 817–819.
106. Proceedings of the Seventh Hypervelocity Impact Symposium, vols. I to VI, Feb. 1965.
107. GAULT, D. E.; AND MOORE, H. J., II: Scaling Relationships for Microscale to Megascale Impact Craters. Proceedings of the Seventh Hypervelocity Impact Symposium, vol. VI, Feb. 1965, pp. 341–351.
108. MORUSKI, L. K.; AND TEAL, D. J.: An Investigation of the Effects of Gravity on Crater Formation in a Cohesionless Medium. M.S. thesis, Air Force Inst. of Tech., 1965.
109. DECARLI, P. S.; AND MILTON, D. J.: Stishovite: Synthesis by Shock Wave. Science, vol. 147, 1965, pp. 144–145.
110. SCHMITT, R. A.; KEIL, K.; AND GAULT, D. E.: Electron Microprobe Study of a Crater and Ejecta Produced by Hypervelocity Impact Against a Ni-Fe Target. Proceedings of the Seventh Hypervelocity Impact Symposium, vol. V, Feb. 1965, pp. 105–121.
111. GAULT, D. E.; AND QUAIDE, W. L.: Interpretation of Ranger Photographs Based on Impact Cratering Studies. (Abstract) Trans. Am. Geophys. Union, vol. 46, no. 1, 1965, p. 138.
112. KOVACH, R. L.; AND ANDERSON, D. L.: The Interiors of the Terrestrial Planets. J. Geophys. Res., vol. 70, 1965, pp. 2875–2882.

113. PLAGEMAN, S.: A Model of the Internal Constitution and Temperature of the Planet Mercury. J. Geophys. Res., vol. 70, 1965, pp. 985–993.

114. FRICKER, P. E.; AND REYNOLDS, R. T.: Thermal History of the Moon. (Abstract) Trans. Am. Geophys. Union, vol. 46, no. 1, 1965, p. 139.

115. KOPAL, Z.: Possible Effects of Convection on Lunar Moments of Inertia. Icarus, vol. 4, 1965, pp. 173–176.

116. KOPAL, Z.: Effects of Thermal Expansion on the Moments of Inertia on the Moon. Icarus, vol. 4, 1965, pp. 166–172.

117. CAPUTO, M.: Shape, Gravity Field, and Strength of the Moon. J. Geophys. Res., vol. 70, 1965, pp. 3993–4003.

118. New York Academy of Sciences, J. Green, Chairman: Geological Problems in Lunar Research. Annals of the New York Academy of Sciences, vol. 123, art. 2, July 15, 1965, pp. 367–1257.

119. ELSTON, W. E.: Rhyolite Asho-flow Plateaus, Ring-dike Complexes, Caloeras, Lopoliths, and Moon Craters. Annals of the New York Academy of Sciences, vol. 123, art. 2, July 15, 1965, pp. 817–842.

120. MCCALL, G. J. H.: The Caldera Analogy in Selenology. Annals of the New York Academy of Sciences, vol. 123, art. 2, July 15, 1965, pp. 843–875.

121. AMSTUTZ, G. C.: Tectonic and Petrographic Observations on Polygonal Structures in Missouri. Annals of the New York Academy of Sciences, vol. 123, art. 2, July 15, 1965, pp. 876–894.

122. DIETZ, R. S.: Astroblemes, Lunar Craters, and Maria. Annals of the New York Academy of Sciences, vol. 123, art. 2, July 15, 1965, pp. 895–896.

123. BUCHER, W. H.: The Largest So-Called Meteorite Scars in Three Continents as Demonstrably Tied to Major Terrestrial Structures. Annals of the New York Academy of Sciences, vol. 123, art. 2, July 15, 1965, pp. 897–903.

124. BEALS, C. S.: The Identification of Ancient Craters. Annals of the New York Academy of Sciences, vol. 123, art. 2, July 15, 1965, pp. 904–914.

125. CURRIE, K. L.: Analogues of Lunar Craters on the Canadian Shield. Annals of the New York Academy of Sciences, vol. 123, art. 2, July 15, 1965, pp. 915–940.

126. DENCE, M. R.: The Extraterrestrial Origin of Canadian Craters. Annals of the New York Academy of Sciences, vol. 123, art. 2, July 15, 1965, pp. 941–969.

127. MCCALL, G. J. H.: Possible Meteorite Craters—Wolf Creek, Australia and Analogs. Annals of the New York Academy of Sciences, vol. 123, art. 2, July 15, 1965, pp. 970–978.

128. ELSTON, W. E.; AND LAMBERT, P. W.: Possible Shatter Cones in a Volcanic Vent Near Albuquerque, New Mexico. Annals of the New York Academy of Sciences, vol. 123, art. 2, July 15, 1965, pp. 1003–1016.

129. MANTON, W. I: The Orientation and Origin of Shatter Cones in the Vredefort Ring. Annals of the New York Academy of Sciences, vol. 123, art. 2, July 15, 1965, pp. 1017–1049.

130. GEYER, R. A.; AND VAN LOPIK, J. R.: Use of Geophysical Measurements in Lunar Surface Analysis. Annals of the New York Academy of Sciences, vol. 123, art. 2, July 15, 1965, pp. 1160–1174.

131. BREETON, R. G.: Aeromagnetic Survey of Meteor Crater, Arizona. Annals of the New York Academy of Sciences, vol. 123, art. 2, July 15, 1965, pp. 1175–1181.

132. LOWMAN, P. D., JR.: Magnetic Reconnaissance of Sierra Madre, Texas, and Nearby Igneous Intrusions. Annals of the New York Academy of Sciences, vol. 123, art. 2, July 15, 1965, pp. 1182–1197.
133. ANON.: Lunar Orbiter, Mission A Description. LOTD–102–0, Lunar Orbiter Project Office, Langley Research Center, NASA, Sept. 29, 1965.
134. ANON.: Biology and Exploration of Mars. Space Science Board, National Academy of Sciences, National Research Council, Publication 1296, 1966.
135. DE VAUCOULEURS, G.: Physics of the Planet Mars. Faber & Faber, London, 1954.
136. JOHNSON, F. S.: Atmosphere of Mars. Science, vol. 150, no. 3702, Dec. 1965, pp. 1445–1448.
137. SMITH, A. G.; AND CARR, T. D.: Radio Exploration of the Planetary System. D. Van Nostrand, Princeton, 1964, pp. 52–57.
138. Staff of Millstone Radar Observatory: The Scale of the Solar System. Nature, vol. 190, 1961, p. 592.
139. VICTOR, W. K.; AND STEVENS, R.: Exploration of Venus by Radar. Science, vol. 134, 1961, p. 46.
140. MARON, I.; LUCHAK, G.; AND BLITZSTEIN, W.: Radar Observations of Venus. Science, vol. 134, 1961, p. 1419.
141. THOMSON, J. H.; TAYLOR, G. N.; PONSONBY, J. E. B.; AND ROGER, R. S.: A New Determination of the Solar Parallax by Means of Radar Echoes From Venus. Nature, vol. 190, 1961, pp. 519–520.
142. KOTELNIKOV, V. A.: Radar Contact With Venus. Paper presented at 12th International Astronautical Congress, Washington, D.C., Oct. 1961.
143. CARPENTER, R. L.: Studies of Venus by CW Radar. Astron. J., vol. 69, 1964, p. 2.
144. CARPENTER, R. L.: Study of Venus by CW Radar—Results of the 1964 Conjunction. Astron. J., vol. 70, 1965, p. 134.
145. PETTIT, E.: Planetary Temperature Measurements. Vol. III of Planets and Satellites, ch. 10, G. P. Kuiper and B. M. Middlehurst, eds., Univ. of Chicago Press, 1961.
146. GEHRELS, T.; AND TESKA, T. M.: The Wavelength Dependence of Polarization. Appl. Opt., vol. 2, 1963, p. 67.
147. KOTELNIKOV, V. A.: In Radar Observations of Mars and Mercury. Sky and Telescope, vol. 25, 1963, p. 191.
148. HOWARD, W. E.; BARRETT, A. H.; AND HADDOCK, F. T.: Measurement of Microwave Radiation From the Planet Mercury. Astrophys. J., vol. 136, 1962, p. 995.
149. DOLLFUS, A.: Visual and Photographic Studies of Planets at the Pic du Midi. Vol. III of Planets and Satellites, ch. 15, G. P. Kuiper and B. M. Middlehurst, eds., Univ. of Chicago Press, 1961.

SOLAR PHYSICS

P. J. DICKERMAN
Illinois Institute of Technology Research Institute

H. J. SMITH
Physics and Astronomy Programs
Office of Space Science and Applications, NASA

245-015 O—67——14

Solar Physics

SUMMARY

DURING 1965, the second year of the International Quiet Sun Year (IQSY), scientists throughout the world made a concerted effort to coordinate their observations of the Sun and solar-terrestrial relationships, and to take maximum advantage of the quiet solar conditions. In 1965 there were launched an Orbiting Solar Observatory, OSO II, and Explorer XXX to monitor solar flare X-rays; in addition, several solar radiation experiments were performed on the polar-orbiting geophysical observatory, OGO II. Besides these satellites, a large number of sounding rockets were flown to study particular aspects of solar activity, and an airplane expedition observed from the stratosphere the IQSY total solar eclipse.

There were numerous observations of the shape, color, brightness, and polarization of the Sun's corona, as well as valuable additions to our knowledge of the spectrum of the corona and the chromosphere. All these data provide a very complete picture of the extent of the corona and the activity and physical conditions within it during solar minimum.

Major progress was made in the development of telescopes, spectrographs, and photometers for application to the ultraviolet, infrared, and long-wavelength-radio radiation from the Sun. There was advanced development of numerous instruments for rocket and satellite solar observations.

Important observational data were obtained for the extreme ultraviolet (EUV) spectrum of the quiet Sun (below 300 Å), providing both center-limb variations and semi-absolute photometric measurements. The interpretation of the Sun's UV spectrum was advanced by several significant theoretical calculations of atomic structures. Energy-level and cross-section calculations permitted the identification of individual emission lines in the corona, and features in the continuum originating at photospheric and chromospheric levels. Two major theoretical advances were the recognition of the very significant role of autoionization processes in the Sun's atmosphere, and the identification of CO molecules in the Sun's UV spectrum.

Further interpretation of data from satellites launched in previous years increased our understanding of the X-ray emission of flares, and provided additional measurements of the Sun's UV flux at times of

varied levels of overall solar activity. A definitive analysis of data obtained on rocket flights in earlier years provided identification of prominent emission lines found in the neighborhood of 10 Å, and demonstrated the relationship between long- and short-wavelength X-ray emission across the Sun's disk. X-ray pictures of the Sun taken with pinhole cameras revealed significant X-ray emission from regions outside the solar limb, confirming our understanding of the location and processes of radiative emission from coronal condensations.

In studies of the solar corona, progress was made in the interpretation of OSO I spectrometer data, resulting in more refined temperature assignments for quiet, inactive solar regions. A sounding rocket flight provided unique UV spectroscopic observations, in which the coronal spectrum was observed independently of the chromospheric contribution, and to a much lower threshold of absolute energy emission. Data obtained from the total eclipse of May 30, 1965, will permit later estimation of the temperature and pressure structure of the Sun's atmosphere at minimum conditions, in comparison with essentially identical observations made in more active years of the previous solar cycle. At least nine new emission lines were discovered during the eclipse. Polarization observations were made of both the 5303-Å coronal emission line and the F-corona out to great heights above the limb. Theoretical interpretation and analysis of the structure of the corona proceeded on many fronts, particularly relating to the polarization of light by the corona, and the excitation and radiation equilibria of the corona and the chromosphere.

Significant advances were made in the application of infrared detector technology to solar observation. Observations of the total eclipse of May 30, 1965, revealed new emission lines in the 1- to 3.5-μ range. At longer wavelengths, solar active regions were studied daily in the millimeter range by a large radio telescope, which disclosed close correlation between 3.2-millimeter emission regions and H-α plage incidence.

A profound and far-reaching review of the national program in space solar astronomy was conducted by the Space Science Board. The report of the study provided a strong endorsement of pursuing both unmanned satellite and rocket programs, as well as using manned spaceflight technology to create and operate larger solar telescopes in space in future decades.

INTRODUCTION

Solar astronomy has as its principal task the analysis of electromagnetic radiation emitted by the Sun. It is thus in a rather central position, and contributes to many diverse fields such as stellar astronomy, planetary atmospheres, atomic physics, terrestrial radio communication, and even the manned space-flight program.

It is clear that with the goal of learning as much as possible of the Sun's characteristic radiation, the solar spectrum must be examined at all wavelengths. This includes the extremes to which the Earth's atmosphere is opaque. Thus an important part of any sustained program of solar investigation involves carrying telescopes, spectrographs, and other instruments above the atmosphere by rockets, satellites, and probes. In this way, the vitally important UV and X-ray solar spectrum can be investigated, as well as the far-infrared region—from 20 μ up to 1 millimeter. By maintaining a close relationship between space research and the ground-based programs during the coming years, much can be learned about the many little-understood activities and features of the Sun.

This document undertakes to summarize the progress that has been made in these areas of research during 1965.

FLIGHT PROGRAMS

The solar physics program carried out during 1965 resulted in the launching of various sounding rockets as well as two satellites in the OSO series. The following section provides comments on the objectives and instrumentation used for some of these flights and, where possible, gives some idea of preliminary results. Neither the listing nor the descriptions can be considered complete at this time, however, since much of the data are still being analyzed.

Rocket Flights

Rocket flights have played a significant role in solar research conducted during 1965. Aside from their use for direct studies in solar physics, sounding rocket flights are being used more and more for development of telescopes to be flown on Orbiting Solar Observatories (OSO), Advanced Orbiting Solar Observatories (AOSO), Apollo Telescope Mounts (ATM), and eventually, Manned Orbiting Telescopes (MOT). Rockets are also needed for periodic checking and calibration correction of many long-lived orbiting experiments, and also for carrying out particular researches suggested by satellite results. Flights made during this reporting period include the following:

Nike-Apache, February 3, 1965

The instrumentation was designed to measure the neutron intensity above the Earth's atmosphere, the flux of solar X-rays and Lyman-α radiation, and to determine ionospheric electron densities. A peak altitude of 142 kilometers was reached; indications are that all instruments functioned properly and good data were obtained.

Nike-Apache, April 2, 1965

The flight was designed to provide data on the neutron intensity, solar X-ray flux, Lyman-α radiation, and ionospheric electron density at different altitudes. Performance was satisfactory and successful results were obtained.

Nike-Apache, April 9, 1965

As part of the U.S. participation in the IQSY program, this vehicle was instrumented to measure electron density, electron temperature, Lyman-α and 1450 Å solar radiation. Satisfactory data were apparently obtained.

Aerobee 150 Flights

April 12, 1965

The primary objective was to obtain a monochromatic picture of the Sun in the Mg II line at 2802.7 Å, using a birefringent filter as a spectroheliograph. Solar spectral irradiance measurements were also made using photoelectric radiometers. Performance and experimental results were good.

October 26, 1965

The primary objective was to obtain a monochromatic picture of the Sun in the Mg II line at 2802.7 Å. A secondary objective was to make absolute measurements of the solar flux in the regions of 1700 and 2800 Å. A preliminary review of the records indicated that the pointing control did not point the experiment at the Sun. However, the instrumentation otherwise performed as expected.

March 17, 1965

The objective was to obtain X-ray spectroheliograms in the 8- to 20-A and 44 to 60 Å regions. Measurements of the solar X-ray flux in the 1 to 20 Å region were also made. A peak altitude of 156 kilometers was reached. Preliminary results indicate that excellent spectroheliograms were obtained.

Skylark (April 9, 1965)

This flight was launched from Woomera, Australia, and carried two Culham Laboratory experiments. These were considered successful, giving new data on the chromospheric and coronal UV spectrum and providing new EUV spectroheliograms.

Nike-Apache (August 24, 1965)

The primary objective of this flight was the measurement of daytime ion and electron densities and solar flux in the EUV and Lyman-α

lines in the ionosphere at altitudes from 50 to 200 kilometers. Solar UV monitoring was accomplished with a planar secondary-emission detector. Performance was satisfactory and good data were obtained throughout the flight.

Aerobee 150 (October 20, 1965)

The purpose of this flight was to launch a package containing two externally occulted coronagraphs, a photometric spectroheliograph, a Cassegrain telescope with a narrow-field UV detector, and an ion chamber to observe the Ikeya-Seki comet and to measure total solar flux in Lyman-α. Primary experimental objectives of the coronagraph observations were not met because the dust cover failed to eject. Some data on the solar Lyman-α flux were obtained, however, and excellent spectroheliograms in helium light were secured.

OSO Satellites

The objectives of the Orbiting Solar Observatory program are to advance our understanding of the Sun's structure and behavior and to determine the physical processes by which the Sun influences the Earth.

OSO I, the first of this class of satellites, was launched in 1962 and proved to be one of the most successful U.S. scientific satellites, from both an engineering and a scientific standpoint. Two additional OSO spacecraft designed to further the work of OSO I were prepared for launching in 1965. A brief description of these satellites is given below.

OSO II

OSO II, launched February 3, 1965, has two main sections. The spinning base portion, called the wheel, provides gyroscopic stability and houses the telemetry, command, batteries, control electronics, and gas spin-control arms and five experiment packages. The top section, called the sail, is fan shaped and points at the Sun. The sail contains the two primary solar-pointing experiment packages and solar cells to convert solar energy into electrical power.

The instruments, controlled by ground command, scan the entire solar surface. In addition to the scanning capability, a new digital telemetry system is employed as well as a new command system capable of receiving 70 commands compared with 8 for OSO I.

The satellite was successful in many important aspects, though some important parts of its mission were not fulfilled. The spectrometer, which was to cover the 500 to 1500 Å range, did not produce any data. However, additional measurements planned for that mission produced results of great significance in our study of the Sun from

above the Earth's atmosphere. With a white-light coronagraph, the brightness distribution and polarization of the Sun's corona were studied, and observations vital to the understanding of the changes in the temperature and force of the solar wind were made. A set of UV telescopes was arranged to map the Sun in radiations of hydrogen, helium, and very highly ionized iron (at wavelengths of 1216, 304, and 388 Å), much in the way that a TV image is produced by scanning and the sequential transmission of brightness information. These spectroheliograms of the chromosphere and corona made by the Naval Research Laboratory represent the very first application of this fundamental technique of satellite solar astronomy. Yet another telescope was included in OSO II to map the sources of solar X-rays in two energy bands. These X-ray spectroheliographs were supplemented by intensity monitors to examine with very high time resolution the varying spectral distribution of solar X-rays in three bands between 2 and 60 Å. Observations with this X-ray photometer have confirmed in numerous events what was suspected from earlier rocket observations, that certain types of flares produce the very-high-energy (bremsstrahlung) radiation while others do not have a notable emission in these short wavelength regions.

Additional fundamental solar observations were made by an improved version of the gamma-ray telescope flown on OSO I in 1963 to study gamma-ray flux in the 0.15 to 0.55 MeV range. Of particular interest in this energy range is the 0.5 MeV "emission line," which would be the telltale signature of certain classes of thermonuclear reactions suspected to occur in the Sun's atmosphere. OSO II also carried onboard experiments to measure the brightness and distribution of zodiacal light, to map the sky (stars, nebulae, and Milky Way) in several UV wavelength bands, and to study the emissivity of various materials under the radiation environment present in space. With the exception of the solar spectrometer, all of the OSO II experiments have yielded valuable data, even though some of the instruments ceased functioning sooner than expected.

OSO–C

The third Orbiting Solar Observatory, OSO–C, launched in August 1965, failed to achieve orbit. The experiments on this satellite, designed to continue and extend the earlier OSO measurements, included repetitive recording of the Sun's X-ray spectrum from 1 to 400 Å and, with a second instrument, from 250 to 1300 Å. A combination of these observations would have provided the most powerful tool available to astronomers in studying both the energetic processes on the Sun and the way small changes in solar radiation produce specific reactions in

the Earth's near-space environment and upper atmosphere. These experiments are so important to our program of exploring the Sun's UV and X-ray radiations that immediate steps were taken to prepare another OSO with an identical experiment package to be launched later in 1966.

Explorer XXX

The IQSY Solar Explorer, Explorer XXX (also called NRL Solrad 8), was launched in November 1965. It was built by the Naval Research Laboratory and is part of the solar investigation program which NRL began in 1949 with sounding rockets and continued with rockets and Solrad satellites. The scientific objectives of Explorer XXX are to monitor the Sun's energetic X-ray emissions with standardized X-ray photometers and to measure the intensity and spectral quality of X-ray emission during flare development. Explorer XXX provides real-time data telemetry to all scientific groups throughout the world who choose to receive it. It also contains a data storage unit, read out daily, that records data from two of its X-ray detectors over each 24-hour period. The following data are being transmitted on standard telemetry channels. As indicated, some switching of detectors can be effected by ground command.

Channel Assignments—Explorer XXX

Channel	Range and solar monitor
3	1 to 8 Å GM detector; 0.5 to 3 Å GM detector.
4	44 to 60 Å ion chamber, or 1 to 8 Å ion chamber.
5	8 to 16 Å ion chamber, or 8 to 16 Å ion chamber.
6	1080 to 1350 Å ion chamber; 1225 to 1350 Å ion chamber.
7	1 to 20 Å ion chamber; 1 to 8 Å ion chamber.
8	Pulse width aspect detector.

The satellite is equipped with a gas-jet servo system which is currently keeping the equatorial plane within 3° of the Sun. The satellite is also fitted with a rudimentary memory system that provides full-orbit recording of the same data that are provided to channels 4 and 5. Data on the other channels appear only in real time.

The IQSY Solar Explorer (Explorer XXX) achieved the desired orbit, and acquired the proper orientation; its X-ray detectors are functioning as designed. In general, the satellite appears to be providing excellent data, except that both detectors on channel 6 are providing off-scale signals. The 1080 to 1350 Å (Lyman-α) ion chamber is only slightly saturated and usable data from unsaturated

portions of the detector response signal can probably be extracted from the records.

The measurements will be of great value in obtaining a clearer picture of rapid time variations in solar flare X-ray emission and, when correlated with ground-based optical and radio measurements, will increase our understanding of the complex relationships between polar radiation and associated geophysical phenomena.

GROUND-BASED OBSERVATIONS

The great range of wavelengths of significant solar radiation, the time variations and structural detail of this radiation and the range of brightness encountered, demand that all possible techniques be considered in attempting to solve a given problem. Often results of different types of measurement will overlap, but more important is the fact that they complement each other and permit more rapid progress to be made. It is felt that in this manner ground-based experiments will, for years to come, play an important role in the overall solar program. These measurements will be essential in planning space experiments and in providing vital information for the interpretation of space measurements.

During this reporting period, the ground-based observational program was of course highlighted by the solar eclipse measurements. Participation in the observation of this event was marked by those groups interested in the turbulent processes of the solar atmosphere and the response of the Earth's atmosphere and ionosphere to an abrupt interruption of solar radiation.

Since the eclipse was of somewhat unusual length (lasting for more than 5 minutes), the event was of particular interest. Moreover, it took place close to the minimum between solar cycles Nos. 19 and 20, and contributed to many IQSY objectives. The viewing time was extended for some experiments by the use of a number of jet aircraft, which could fly at nearly 600 mph along the path of totality, providing more than 9 minutes of total eclipse viewing time. Island-based observations were conducted by scientific teams on Manuae and Bellingshausen in the Samoa and Scilly Island groups. On Bellingshausen, work centered around coronal ultraviolet and infrared spectrophotometry and chromospheric spectral photography. On Manuae, experiments were concerned with infrared chromospheric photometry, measuring the height variations of chromospheric hydrogen lines, and spectrophotometry of hydrogen- and helium-series limits in the chromosphere.

REVIEW OF RESULTS

Instrumentation Development

Ultraviolet Instrumentation

While practically all types of appropriate instruments and systems are continually being improved, the development of EUV detectors and standard sources remains especially significant. Until recently, ionization detection techniques in the important region from about 60 to 1000 Å were apparently not really "absolute" (Hinteregger, 1965, ref. 1). Thermoelectric detection was, on the other hand, quite difficult below 500 Å. Improved techniques were therefore needed, particularly for the wavelength range from about 60 to 500 Å. Substantial progress in this direction is now being achieved (Ederer and Tomboulian, 1964, ref. 2; Samson and Kelly, 1964, ref. 3), due largely to experimental studies of rare gases and advanced theoretical work.

In the search for a satisfactory absolute EUV source, it has been determined that the electron synchrotron is perhaps the only theoretically acceptable device which can deliver the necessary radiant power. Experimental work with this sort of equipment has been resumed recently using the 180-MeV synchrotron at the National Bureau of Standards. This has led to significant contributions (Codling and Madden, 1964, ref. 4), even though the work was not oriented toward absolute intensity calibration.

An instrumentation development which is also worthy of mention here is the EUV spectroheliograph designed for AOSO by Neupert, Underwood, and Lindsay (1965, ref. 5). It is intended that this instrument, viewing in the region 170 to 400 Å, will provide the spatial resolution required to yield valuable information on the solar corona. The advantages of EUV observations are that active regions could be observed on the disk as well as on the limb, information on the properties of the transition layer could be obtained, and the system would not be affected by scattered photosphere radiation.

X-Ray Instrumentation

No new basic instruments have been developed recently for the soft X-ray region, but existing instruments have been modified and improved. In particular, a spectroheliograph consisting of a telescope and crystal spectrograph is being developed for AOSO, and measurements using a crystal spectrometer on a rocket have been reported. Also, further measurements have been made of solar X-ray fluxes using ionization counters, and soft X-ray solar images have been obtained using pinhole cameras on rocket flights.

Spatially resolving instrumentation include X-ray pinhole cameras used by Russell (1965, ref. 6; 1965, ref. 7), the Kitt Peak National Observatory (see monthly report for July and August 1965), and Blake et al. (1965, ref. 8). The Aerobee rocket used by Kitt Peak Observatory used a pointing control with 1-arc-minute pitch stability and ±1.5-arc-minute roll stability. Russell used a Skylark rocket with ±4-arc-minute pitch stability and ±2.5° roll stability.

A spectroheliograph designed for use on AOSO is described by Muney et al. (1965, ref. 9). This instrument is significant in that it will combine spatial and spectral resolution in one instrument and will be used in conjunction with the high pointing accuracy of AOSO. A grazing-incidence mirror will give a maximum angular resolution of 5 arc-seconds and a bent-crystal spectrograph will select the desired wavelength. An X-ray collimator telescope with a 13° half angle, a spectral range from 7 to 200 keV, and a proportional counter was described by Hicks and Reid (1965, ref. 10). Blake et al. (1965, ref. 8) describe measurements made with a resolution of approximately 1 arc-minute over two wavelength bands.

Spectrally resolving instrumentation and detector development has been marked by improvements in ionization counters. The construction of a photoionization chamber for the 0.1 to 8 Å region is described by Young and Stober (1965, ref. 11); various types of counters and thin windows are described by Van Allen et al. (1965, ref. 12) and Blake et al. (1965, ref. 8) for the wavelength range from 1 to 60 Å.

Blake et al. (1965, ref. 8) describe a Bragg crystal spectrometer flown on a pointed rocket and covering the spectral range 2 to 90 Å. The wavelength range was actually covered by three coupled spectrographs with separate crystals. For the long wavelengths, crystals with large lattice spacing were used, octadecyl hydrogen succinate and magnesium lignocerate, the latter actually being used in the form of a multilayer film. The spectrometer was used without entrance or exit collimators. The ½° angular width of the solar disk determined the width of spectral lines observed, though narrower lines were observed from sources smaller than the solar disk.

Solar UV Spectrum

Solar EUV spectroscopy began in 1946 with the flight of a V–2 rocket over White Sands in New Mexico. It was not until after 1958, however, that satisfactory data were obtained at short wavelengths (say below 1000 Å). The work has been carried on at an increasing pace since that time and the overall progress is generally considered satisfactory.

The emphasis has by now changed somewhat from rocketry to Orbiting Solar Observatory development. There are, however, several

recent rocket flights which should be mentioned here. One of these (Hall et al., 1965, ref. 13) covered the solar spectrum from 312 to 55 Å with a telemetering grating monochromator similar to many AFCRL instruments of the past. This flight noted an apparently real reduction of approximately 50 percent in the intensity of the Fe XV 284 Å line as compared with previous data. This was attributed to a long-term solar variation; a more systematic satellite survey will have to be obtained, however, before a meaningful quantitative description can be given.

Another recent rocket flight (Burton and Wilson, 1965, ref. 14) employed a simple EUV spectroheliograph and attitude-control system to obtain information about the intensity distribution of line emissions on the solar disk. He II 304 Å shows slight limb brightening and the Fe IX 171 Å image suggests a rather strong equatorial limb brightening. Emission from active centers is less obvious than in soft X-ray images obtained on the same flight. Initial considerations also indicate that the limb brightening of emission between 60 and 150 Å is real.

In addition to the experimental work mentioned above, several theoretical contributions have been made in recent months based principally on rocket-flight data obtained during the past few years. Such a study was that of the Ar I and K I isoelectronic sequences by Feldman, Fraenkel, and Hoory (1965, ref. 15), which resulted in the identification of certain solar UV lines, particularly those of Fe VIII, Fe IX, Ni X, and Ni XI. Energy level classifications were proposed for these lines and the interaction between the configurations $3p^e\ 3d^{R-1}$ np, nf and $3p^5 3d^{R-1}$ were investigated. In another instance, a number of intense lines which have been observed in the 165 to 200 Å region of the solar spectrum were identified by Cowan and Peacock (1965, ref. 16). By comparing solar spectra with those of theta pinches and intense sparks and by making use of theoretical energy-level calculations, a number of the observed lines were attributed to specific transitions in Fe VIII to Fe X. Classification of lines at longer wavelengths becomes increasingly difficult due to overlapping of spectra from an increasing number of ionization stages. However, the fourth positive bands in the CO molecule between 1600 and 2000 Å were recently demonstrated to be present in the solar spectrum (Goldberg, Parkinson, and Reeves, 1965, ref. 17) and are probably the main contributors to the continuum jump at 1700 Å. Further work by Hesser and Dressler (1965, ref. 18) provided absolute transition probabilities for these bands. Theoretical cross sections calculated by the same group for transitions in the silicon continuum have also

245-015 O—67——15

provided an identification of the discontinuity beyond 1550 Å (Rich, private communication).

Another interesting contribution is the explanation offered by Kodaira (1965, ref. 19) for the intensity jump in the solar spectrum at 2085 Å. As is well known, there is a sharp decrease in the intensity of the continuum and a sudden weakening of the Fraunhofer lines below this wavelength. This has been attributed to the ionization edge of Al I $3p^2P^o$ at 2074 Å and corroboration is offered by deriving the effective number of Al I $3p^2P^o$ on the ionization edge from the curve of growth of the Al I lines. This interpretation is subject to further confirmation, however.

Results of past rocket observations of the solar spectrum curve were also used in developing a model for the H II region (Williams, 1965, ref. 20). This information, along with density data furnished by Mariner II, was used to compute curves showing the degree of ionization of the gas as a function of distance from the Sun for a wide range of densities. For each density, the ionization equilibrium was determined for two electron temperatures, 8000° and 20 000° K. It appears from this work that the ionization structure is rather insensitive to the electron temperature and that virtually none of the gas surrounding the Sun is in a fully ionized state.

Additional ultraviolet work is discussed below in the section on coronal emission.

Soft X-Ray Emission

Satellite Measurements

Further data reduced from the U.S./U.K. Satellite Ariel I have been reported by Pounds (1965, ref. 21) and show the considerable enhancement of 4 to 14 Å radiation during solar flares in the 1962 flight. These data correlate with flare-associated radio bursts, particularly in the microwave region near 3000 Mcs/sec confirming that both thermal and nonthermal processes are involved in the X-ray emission. Microwave bursts occurred simultaneously with a number of X-ray enhancements, and when absent the X-ray enhancement was small. More high-resolution spectral and spatial X-ray data are required to provide a definitive explanation of the flare X-ray emission. The contribution of characteristic X-radiation in solar flares is discussed by Acton (1965, ref. 22) and shows the importance of obtaining high-resolution spectral data.

Measurements made in the 1- to 14-Å range by the Injun I satellite have been reported by Van Allen et al. (1965, ref. 12). This satellite was attached to and made measurements concurrently with the NRL

Solar Radiation III satellite whose results were reported previously. Measurements made by Injun I during the second half of 1961 indicated that the "quiet day" solar flux was approximately 5×10^{-4} ergs/cm^2/sec which is relatively independent of the assumed blackbody temperature of the Sun. During flares the flux was considerably enhanced; as high as 7×10^{-2} ergs/cm^2/sec during an H-α flare of importance 3.

Spectrally Resolved Rocket Measurements

Bragg-type crystal spectrometers were flown on two Aerobee rockets launched by NRL in 1963 and described by Blake et al. (1965), ref. 8). A series of prominent emission lines were found between 13 and 25 Å and the stronger lines have been identified as emissions from O VII, O VIII, N VII, and Fe XVII. Measurement of the widths of the spectral lines, which were related to the angular width of the solar source, indicate that the O VIII and Fe XVII emissions came from a small active plage region, while the O VII and N VII emissions were from the whole solar disk. By comparison with an independent measurement which used an 8 to 20 Å ion chamber, it was shown that 75 percent of the radiation in this wavelength range was due to the O VIII and Fe XVII emissions, hence the strong dependence of this flux on plage activity.

Measurements were made on the same rocket flights using slit scans of the solar disk with two detectors in each case, one for 8 to 15 Å, the other for 44 to 60 Å. The slit resolution was about 1 arc-minute for each channel. It was found on the first flight that emission peaks from active regions were in the same positions for both wavelength ranges. Some active regions were apparently 1 arc-minute or smaller on the solar disk, while the observed structure was finer in the 8 to 15 Å band than in the 44 to 60 Å band. This latter conclusion is consistent with the fact that all the shorter wavelength radiation was observed to originate in active regions, while only about half of the 44 to 60 Å emission did so. No appreciable limb brightening was observed. On the second flight the wavelength range of the 8 to 15 Å detector was increased to 8 to 20 Å, and it was found that an appreciable contribution from inactive solar regions was observable. On the first flight the 8 to 15 Å radiation was practically all from disturbed regions.

Pinhole Camera Measurements

An Aerobee rocket was launched from White Sands Missile Range on June 23, 1965. (See Kitt Peak National Observatory monthly report for July and August 1965.) X-ray pinhole photographs were

taken in which five discrete X-ray sources were detected, the two most intense being outside the visible limb of the Sun. Close correlation was obtained between the various sources and calcium and microwave spectroheliograms.

X-ray pinhole photographs were taken from Skylark rockets on August 11 and December 17, 1964 (Russell, 1965, refs. 6 and 7), and showed good correlation with calcium and microwave spectroheliographs. However, appreciable limb brightening was observable and on one of the pinhole photographs (for December 17), one of the sources on the limb of the solar disk did not coincide with any plage area on the Fraunhofer Institute solar map for that day. A plage area in that position on the next day's map indicated that the X-ray-emitting region was outside the solar limb and therefore visible before the plage area underneath.

Solar Corona

OSO I, in viewing the solar EUV spectrum, observed nine successive stages of ionization of iron. Combining these data with Ca II plage observations and limb observations of coronal forbidden lines, Neupert in 1965 obtained physical conditions in the coronal region associated with a type E sunspot group at various stages in its development. An electron temperature of 4.2×10^6 ° K was determined and a density increase of approximately 10 times quiet coronal values at the time of maximum development was inferred. For the region above the residual plage, after all spots had disappeared, a temperature of 3×10^6 ° K and a density of two to three times quiet coronal values was obtained.

The solar chromosphere and corona were also investigated using instrumentation on board the Skylark rocket flight of April 9, 1965 (Burton and Wilson, 1965, ref. 14). A spectrograph was set to cover the wavelength range 950 to 2950 Å, and the alinement system stabilized an image of the Sun so that the spectrograph slit was set 10 arcsec outside the solar limb. This permitted viewing the chromospheric and coronal layers separately from the bright solar disk and enabled the spectrograph to record new emission lines originating in the chromosphere and corona at wavelengths where the solar spectrum is normally dominated by emission from the photosphere. A preliminary analysis showed many features of interest, including some emission lines between 2000 and 2400 Å which are probably due to forbidden transitions in highly ionized atoms.

In addition to the space-flight program, there was of course the extensive series of measurements performed from the ground and by airborne expeditions in connection with the solar eclipse of May 30, 1965. Some results of the University of Hawaii-Sacramento Peak

Observatory program was recently reported by Curtis, Dunn, and Orrall (1965, ref. 23). Two identical spectrographs were used, one aboard the research aircraft and one on Bellingshausen Island. A number of excellent spectra in the range 3000 to 9000 Å were obtained at exposure times ranging from 1 sec to 70 sec (ground-based instrument) and 239 seconds (airborne instrument). One set of results was tabulated and presented as a list of observed coronal emission lines. Nine lines were observed whose presence was apparently never before recorded, while the existence of four lines reported only once previously was confirmed.

In addition to line identification, the intensity of the continuum and of some representative coronal lines was determined as a function of position angle around the limb. The red line Fe X 6374 Å is typical of Class I lines (in the scheme of classification devised by Shajn and Lyot). The green line Fe XIV 5303 Å is typical of Class II, while Ni XV 6702 Å and Ca XIII 4086 Å belong to Class III. The yellow line Ca XV 5694 Å is the strongest known line of Class IV. The lines of Classes I and II were visible at all position angles around the limb but strongly enhanced in the coronal condensation on the west limb. The lines of Class III were much more strongly enhanced in the condensation. The yellow line (Class IV) is visible only in the condensation. The increasing concentration of Classes III and IV lines to the center of condensation may be construed as evidence that the temperature, as well as density, increases toward the center.

Measurements of the polarization of coronal lines during the eclipse were reported by Pepin et al. (in a private communication in 1965) and also by Hyder (1965, ref. 24). In the first case, a specially designed camera was used to obtain photographic data of the brightness and polarization of the F-corona in the region 3 to 14 solar radii from the center of the Sun. Evaluation of the data has not been completed, but there seem to be two generally apparent characteristics. First, there exists a minimum in the percentage of polarization ranging in position from 4 to 6 solar radii from the Sun. Second, polarization in the polar regions (only a few percent) is much lower than in the ecliptic regions where it often has values of more than 10 percent.

Hyder's work (making use of the coronal green line) showed that the polarization vector is generally radial. There are notable exceptions, one on the NW limb and perhaps one on the NE limb. If anything, the deviated direction of the polarization appears to be perpendicular to the lines along the coronal arches at the NW limb (this is expected if the coronal arch magnetic fields be along the arches). The degree of polarization apparently varied from between 1.5 and 5 percent within 1 minute of arc from the limb to between 12.5 and 25

percent at distances greater than the 0.4 solar radius above the limb. Details of polarization mechanisms and upper limits on the degrees of polarization that might be expected from several coronal emission lines are treated further in a separate theoretical discussion (Hyder, 1965, ref. 24).

In two additional theoretical studies, Athay (1965, refs. 25 and 26) has considered the excitation of chromospheric He II and hydrogen and he has also computed intensities for chromospheric lines and their continua. The observed solar radiation field was used to compute radiative transition rates and solutions were obtained for varying degrees of departure from radiative detailed balance. The results were used in computing the expected intensities of the resonance series lines for hydrogen and He II. Good agreement was obtained with observed fluxes using a relatively simple chromosphere model consistent with eclipse observations and with previous radio data.

A concept for future detailed studies of the corona and chromosphere has recently been suggested by Kastner and Wolff (1965, ref. 27). The method makes use of the Earth as an occulting disk to obscure the solar disk and to determine the altitudes in the solar atmosphere at which various EUV emission lines originate. It appears that with a proper choice of trajectories for a spacecraft, about 10 hours of observing time from within the Earth's shadow may be obtained.

The variation in intensity of chromospheric emission lines, due to partial eclipse by the Earth, was calculated along trajectries within the Earth's umbra. The emission lines were assumed to originate in spherical shells, and to have a gaussian distribution of intensity about a height of maximum intensity. Discrimination appears possible between several emission lines originating at altitudes above the photosphere differing by less than 10 000 kilometers, and is best if the spacecraft is sent out toward the apex of the Earth's shadow cone.

Infrared and Long-Wavelength Observations

Infrared eclipse observations were made from the NASA aircraft with a Michelson-type scanning interferometer spectrometer by R. Stockhausen and J. Mangus in 1965. They used a lead sulfide detector to obtain spectral observations in the 1 to 3.5 μ range.

The results show a number of newly observed emission lines. Up to the present time, several lines of the hydrogen Paschen and Brackett series have been identified along with the 10 830 Å line of helium. A number of lines are still unidentified. The time variations of these lines seem to indicate that they originate either from the chromosphere or from a number of prominences visible on the limb of the Sun.

Solar emission in the millimeter-wavelength region also originates in the chromosphere and thus may provide fundamental information regarding active regions on the Sun. In the past, observations at these wavelengths have been hampered by the poor resolving power of the available radio telescopes. Recent work by Simon (1965, ref. 28), using a telescope of 3-arc-minute beam width, has yielded data concerning solar brightness temperature and limb brightening and has provided a correlation of observed radio emissions with optical data. The active regions on H-alpha photographs correlate very well with the regions of enhanced radio emission, but the correlation is even better between the regions of enhanced 3.2-millimeter emission and those of strong magnetic fields. In addition, it was noted that active regions that later flared were consistently enhanced some 200° K above the background for a day or more prior to the flare. No bursts were observed during this time. After the flare, the enhancement generally subsided.

Additional work by Anderson (1965, ref. 29) has suggested that the well-known 10.7-centimeter flux from the Sun may not be a good index of solar EUV as was previously assumed. It is shown that no exact causal relationship between the emissions at these two different wavelength regions has really been given. Although it is true that both radiations issue from the upper chromosphere and lower corona, our knowledge of the details of their origin is very deficient. At present, there seem to be no theoretical grounds for an exact relationship.

Future Planning

A major step was taken at the Woods Hole Summer Study of the Space Science Program where solar astronomers active in the NASA program reviewed current projects and indicated logical directions for near- and distant-future planning. One of the exciting possibilities is the application of manned systems to obtain solar observations. Manned missions can provide possible opportunities for solar astronomers which complement rather than duplicate or substitute for the unmanned satellites like OSO. For example, a 3-week manned mission can bring back vast quantities of photographic observations, permitting very high picture rates to study the rapid development of sunspots and flares. The limited data storage and telemetry capability of even our most advanced unmanned satellites would preclude such high-resolution observations. Nevertheless, we need the automatic unmanned satellites to maintain specialized instruments in orbit, ever ready to record the onset and full lifetime development of unpredictable transient phenomena like flares.

In order to utilize certain planned manned missions such as Earth-orbiting Apollo flights for solar astronomy, it is necessary to mount telescopes on the spacecraft, to point them at the Sun with sufficient precision and steadiness, to enable the astronaut to control and operate them during the flight, and to retrieve the observations. A system to do this, called the Apollo Telescope Mount (ATM), is currently under study as is development of a number of solar telescopes which might fly on ATM.

In the long-range view, astronomers see eventual application of manned space flight to the erection of significantly larger telescopes in orbit, which might subsequently operate in an unmanned mode for an extended period of time. Astronauts would make regular visits to collect the data, to replenish expendable supplies, to adjust or repair the telescope, or for particular purposes to provide manual operation. In order to identify the scientific requirements of such systems, and to examine in detail the feasibility and technological developments needed to attain them, a series of studies of future manned orbiting telescope systems has been started.

REFERENCES

1. Hinteregger, H. E.: Absolute Intensity Measurements in the Extreme Ultraviolet Spectrum of Solar Radiation. Space Sci. Rev., vol. IV, 1965, pp. 461–497.
2. Ederer, D. L.; and Tomboulian, D. H.: Photoionization Cross Section of Neon in the 80 to 600 Å Region. Phys. Rev., vol. 133A, 1964, pp. 1525–1532.
3. Samson, J. A. R.; and Kelly, F. L.: Planetary Physics III: Photoionization Cross Sections of the Rare Gases. NASA CR-55940, 1964.
4. Codling, K.; and Madden, R. P.: Phys. Rev. Letters, vol. 12, 1964, p. 106.
5. Neupert, W. M.; Underwood, J. H.; and Lindsay, J. C.: An Extreme Ultraviolet Spectroheliograph for Advanced Orbiting Solar Observatory. NASA Report X-614, 65-310, 1965.
6. Russell, P. C.: Soft X-ray Image of the Sun. (Letter) Nature, vol. 205, 1965, pp. 684–685.
7. Russell, P. C.: Further Soft X-ray Images of the Sun. (Letter) Nature, vol. 206, 1965, pp. 281–282.
8. Blake, R. L.; Chubb, T. A.; Friedman, H.; and Unzicker, A. E.: Spectral and Photometric Measurements of Solar X-Ray Emission Below 60 A. Astrophys. J., vol. 142, 1965, pp. 1–12.
9. Muney, W. S.; Neupert, W. M.; Underwood, J. H.; and Lindsay, J. C.: A Proposal for an X-Ray Spectroheliograph (7–25 A) for Advanced Orbiting Solar Observatory, 1965.
10. Hicks, D. B.; and Ried, L., Jr.: X-Ray Telescope for an Orbiting Solar Observatory. IEEE Transactions on Nuclear Science, vol. NS-12, 1965, pp. 54–65.

11. YOUNG, R. M.; AND STOBER, A. K.: A Soft X-Ray Photoionization Detector. NASA TN-D-3169, 1965.
12. VAN ALLEN, J. A.; FRANK, L. A.; AND MAEHLUM, B.: Solar X-ray Observations by Injun 1. J. Geophys. Res., vol. 70, 1965, pp. 1639–1645.
13. HALL, L. A.; SCHWEIZER, W.; HEROUX, L.; AND HINTEREGGER, H. E.: Solar XUV Spectrum of March, 1964. Astrophys. J., vol. 142, 1965, pp. 13–15.
14. BURTON, W. M.; AND WILSON, R.: Observations of the Sun in the Extreme Ultra-violet made from a Stabilized Skylark Rocket. (Letter) Nature, vol. 207, 1965, pp. 61–62.
15. FELDMAN, U.; FRAENKEL, B. S.; AND HOORY, S.: Identifications of Solar Ultraviolet Lines Resulting From a Study of the Ar I and K I Isoelectronic Sequences. Astrophys. J., vol. 142, 1965, pp. 719–723.
16. COWAN, ROBERT D.; AND PEACOCK, NICOL J.: Identification of Some Intense Iron Lines in the Solar Spectrum Near 170 A. (Letter) Astrophys. J., vol. 142, 1965, pp. 390–396.
17. GOLDBERG, L.; PARKINSON, W. H.; AND REEVES, E. M.: Carbon Monoxide in the Ultraviolet Solar Spectrum. (Letter) Astrophys. J., vol. 141, 1965, pp. 1293–1295.
18. HESSER, JAMES E.; AND DRESSLER, KURT: Absolute Transition of Probabilities in the Ultraviolet Spectrum of CO. (Letter) Astrophys. J., vol. 142, 1965, pp. 389–390.
19. KODAIRA, K.: Paper presented at 6th International Space Science Symposium, Buenos Aires, Argentina, May 13–19, 1965.
20. WILLIAMS, ROBERT E.: The Size of a Solar H II Region. Astrophys. J., vol. 142, 1965, pp. 314–320.
21. POUNDS, K. A.: Recent Solar X-Ray Studies in the United Kingdom. Ann. Astrophys., vol. 28, 1965, pp. 132–145.
22. ACTON, LOREN W.: Contribution of Characteristic X-rays to the Radiation of Solar Flares. Nature, vol. 207, 1965, pp. 737–738.
23. CURTIS, G. W.; DUNN, R. B.; AND OBRALL, F. Q.: Coronal Emission Spectrum. Presented at the Solar Eclipse Symposium, Ames Research Center, California, Dec. 16, 1965.
24. HYDER, CHARLES L.: The Polarization of Emission Lines in Astronomy. III. The Polarization of Coronal Emission Lines. Astrophys. J., vol. 141, 1965, pp. 1382–1389.
25. ATHAY, R. GRANT: Theoretical Line Intensities. II. Excitation of Chromospheric He II and Hydrogen. Astrophys. J., vol. 142, 1965, pp. 732–754.
26. ATHAY, R. GRANT: Theoretical Line Intensities. III. Solar UV Lines and Continua of H, He I, and He II and the Chromospheric Model. Astrophys. J., vol. 142, pp. 755–766.
27. KASTNER, S. O.; AND WOLFF, C. L.: On the Determination of Solar EUV Emission Altitudes Using the Earth as an Occulting Disk. NASA TM X-55314, 1965.
28. SIMON, MICHAL: Solar Observations at 3.2 MM. Astrophys. J., vol. 141, 1965, pp. 1413–1522.
29. ANDERSON, ALBERT D.: Long-Term (Solar Cycle) Variation of the Extreme Ultraviolet Radiation and 10.7-Centimeter Flux from the Sun. J. Geophys. Res., vol. 70, 1965, pp. 3231–3234.

BIBLIOGRAPHY

GABRIEL, A. H.; SWAIN, J. R.; AND WALLER, W. A.: A Two-Metre Grazing-Incidence Spectrometer for Use in the Range 5–950 Å. J. Sci. Instr., vol. 42, 1965, pp. 94–97.

HYDER, C. L.: Polarization of the Coronal Green Line. Presented at NASA Eclipse Symposium, Dec. 16, 1965.

RICH, JOHN C.: Presented at 120th Meeting of AAS, Berkeley, Calif., Dec. 1965.

U.S. GOVERNMENT PRINTING OFFICE : 1967—O-245-015